https://doi.org/10.15388/vu.thesis.628
https://orcid.org/0000-0001-8604-2604

VILNIUS UNIVERSITY
CENTER FOR PHYSICAL SCIENCES AND TECHNOLOGY

Benediktas Brasiūnas

The use of Metal and Metal Oxide Nanostructures for the Detection of Biologically Active Materials

DOCTORAL DISSERTATION

Natural Sciences,
Chemistry (N 003)

VILNIUS 2024

The dissertation was prepared between 2019 and 2023 at Faculty of Chemistry and Geosciences, Vilnius University. The research was supported by the Research Council of Lithuania.

Academic supervisor – Prof. Dr. Almira Ramanavičienė
(Vilnius University, Natural Sciences, Chemistry – N 003)

This doctoral dissertation will be defended in a public meeting of the Dissertation Defence Panel:

Chairman – Prof. Habil. Dr. Audrius Padarauskas (Vilnius University, Natural Sciences, Chemistry – N 003).
Members:
Dr. Sigita Jurkonienė (The Nature Research Centre, Natural Sciences, Biology – N 010),
Dr. Vilius Poškus (Vilnius University, Natural Sciences, Chemistry – N 003),
Dr. Vladimir Sivakov (The Leibniz Institute of Photonic Technology, Natural Sciences, Chemistry – N 003),
Prof. Dr. Aleksej Žarkov (Vilnius University, Natural Sciences, Chemistry – N 003).

The dissertation shall be defended at a public meeting of the Dissertation Defence Panel at 12:00 on the 2nd of July 2024 in the Inorganic chemistry auditorium of Vilnius University, Faculty of Chemistry and Geosciences.
Address: Naugarduko st. 24, 141(NChA), Vilnius, Lithuania.
Tel. +370 5 219 3105; e-mail: info@chgf.vu.lt

The text of this dissertation can be accessed at the libraries of Vilnius University, and the library of Center for Physical sciences and Technology, as well as on the website of Vilnius University:
www.vu.lt/lt/naujienos/ivykiu-kalendorius

https://doi.org/10.15388/vu.thesis.628
https://orcid.org/0000-0001-8604-2604

VILNIAUS UNIVERSITETAS
FIZINIŲ IR TECHNOLOGIJOS MOKSLŲ CENTRAS

Benediktas Brasiūnas

Metalinių ir metalo oksidų nanostruktūrų taikymas biologiškai aktyvių medžiagų nustatymui

DAKTARO DISERTACIJA

Gamtos mokslai,
Chemija (N 003)

VILNIUS 2024

Disertacija rengta 2019 – 2023 metais Vilniaus universitete.
Mokslinius tyrimus rėmė Lietuvos mokslo taryba.

Mokslinė vadovė – Prof. dr. Almira Ramanavičienė (Vilniaus universitetas, gamtos mokslai, chemija – N 003)

Gynimo taryba:
Pirmininkas – Prof. habil. dr. Audrius Padarauskas (Vilniaus universitetas, gamtos mokslai, chemija – N 003)
Nariai:
Dr. Sigita Jurkonienė (Gamtos tyrimų centras, gamtos mokslai, biologija – N 010),
Dr. Vilius Poškus (Vilniaus universitetas, gamtos mokslai, chemija – N 003),
Dr. Vladimir Sivakov (The Leibniz Institute of Photonic Technology, gamtos mokslai, chemija – N 003),
Prof. dr. Aleksej Žarkov (Vilniaus universitetas, gamtos mokslai, chemija – N 003).

Disertacija ginama viešame Gynimo tarybos posėdyje 2024 m. liepos mėn. 2 d. 12 val. Vilniaus universiteto, chemijos ir geomokslų fakulteto, neorganinės chemijos auditorijoje. Adresas: Naugarduko g. 24, 141(NChA), Vilnius, Lietuva. tel. +370 5 219 3105; el. paštas info@chgf.vu.lt

Disertaciją galima peržiūrėti Vilniaus universiteto, Fizinių ir technologijos mokslų centro bibliotekose ir VU interneto svetainėje adresu:
https://www.vu.lt/naujienos/ivykiu-kalendorius

ACKNOWLEDGMENTS

I express sincerest gratitude to my supervisor Almira Ramanavičienė and my dear colleague Anton Popov, for unending support and encouragement over the years of collaboration. You made the process of scientific research fun and engaging!

To the colleagues I worked with in the faculty and the laboratory, thank you for making my days brighter!

Finally, I would like to thank my friends and family for encouraging me to seek a scientific path, while reminding me to enjoy everyday life.

LIST OF INCLUDED PUBLICATIONS

Paper 1	A. Popov, **B. Brasiunas**, A. Damaskaite, I. Plikusiene, A. Ramanavicius, A. Ramanaviciene. Electrodeposited gold nanostructures for the enhancement of electrochromic properties of PANI–PEDOT film deposited on transparent electrode, Polymers, 12(12), (2020), 2778. https://doi.org/10.3390/polym12122778
Paper 2	**B. Brasiunas**, A. Popov, G. Kraujelyte, A. Ramanaviciene, The effect of gold nanostructure morphology on label-free electrochemical immunosensor design, Bioelectrochemistry, 156, (2024), 108638. https://doi.org/10.1016/j.bioelechem.2023.108638
Paper 3	A. Ramanaviciene, A. Popov, E. Baliunaite, **B. Brasiunas**, A. Kausaite-Minkstimiene, U. Tamer, G. Kirdaite, E. Bernotiene, A. Mobasheri, Magneto-immunoassay for the detection and quantification of human growth hormone, Biosensors, 12(2), (2022), 65. https://doi.org/10.3390/bios12020065
Paper 4	**B. Brasiunas**, A. Popov, A. Ramanavicius, A. Ramanaviciene. Gold nanoparticle based colorimetric sensing strategy for the determination of reducing sugars, Food Chemistry, 351, (2021), 129238. https://doi.org/10.1016/j.foodchem.2021.129238
Paper 5	A. Popov, **B. Brasiunas**, A. Kausaite-Minkstimiene, A. Ramanaviciene, Metal nanoparticle and quantum dot tags for signal amplification in electrochemical immunosensors for biomarker detection, Chemosensors, 9(4), (2021), 85. https://doi.org/10.3390/chemosensors9040085
Paper 6	**B. Brasiunas**, A. Popov, V. Lisyte, A. Kausaite-Minkstimiene, A. Ramanaviciene, ZnO nanostructures: A promising frontier in immunosensor development, Biosensors and Bioelectronics, 246, (2024), 115848. https://doi.org/10.1016/j.bios.2023.115848

CONTRIBUTION TO INCLUDED PUBLICATIONS

Paper 1	Performed the electrodeposition of various gold nanostructures and polymeric layers onto transparent electrodes. Analyzed the electrochemical and electrochromic properties of produced layers. Contributed to the drafting and editing of the publication manuscript.
Paper 2	Performed the electrodeposition of various gold nanostructures on graphite rod electrodes. Employed these modified electrodes for the development of label-free electrochemical immunosensor. Analyzed the analytical and electrochemical properties of the produced immunosensor. Contributed to the drafting and editing of the publication manuscript.
Paper 3	Conducted the synthesis of magnetic nanoparticles coated with gold. Participated in the development of magneto-immunoassay. Contributed to the drafting and editing of the publication manuscript.
Paper 4	Carried out the validation of a colorimetric sensing strategy used to detect reducing sugars by analyzing the underlying gold nanoparticle formation reaction. The reaction was applied to detect various reducing sugars in the model and real samples. Contributed to the drafting and editing of the publication manuscript.
Paper 5	Participated in the conceptualization, drafting, and editing of the publication, which reviews the use of various metal nanoparticles and quantum dots for signal amplification of electrochemical immunosensors used to detect biomarkers.
Paper 6	Participated in the conceptualization, drafting, and editing of the publication, which reviews the use of various ZnO nanostructures for the development of immunosensors.

TABLE OF CONTENTS

LIST OF ABBREVIATIONS

11-MUA	11-mercaptoundecanoic acid
AuNPs	Gold nanoparticles
AuNSs	Gold nanostructures
BSA	Bovine serum albumin
CTAB	Cetyltrimethylammonium bromide
DPV	Differential pulse voltammetry
EASA	Electroactive surface area
EDC	1-ethyl-3-(3-dimethylaminopropyl)carbodiimide
ELISA	Enzyme-linked immunosorbent assay
GR	Graphite rod
ITO	Indium-tin oxide
LSPR	Local surface plasmon resonance
MNPs	Magnetic nanoparticles
MNPs-Au	Magnetic nanoparticles coated by gold
NHS	N-hydroxysuccinimide
PANI	Polyaniline
PBS	Phosphate-buffered saline
PEDOT	Poly(3,4-ethylenedioxythiophene)
S-HRP	Streptavidin labeled horse radish peroxidase
SAM	Self-assembled monolayer
SEM	Scanning electron microscopy
TEM	Tunneling electron microscopy
TMB	3,3’,5,5’-tetramethylbenzidine
hGH	Human growth hormone
m-anti-hGH	Monoclonal antibodies against hGH
p-anti-hGH-B	Biotinylated polyclonal antibodies against hGH
p-anti-BSA	Polyclonal antibodies against bovine serum albumin

INTRODUCTION

The science of analytical chemistry has always been moving forward, striving to detect analytes at miniscule concentrations and from the smallest possible sample volumes. In order to achieve those goals, the sensitivity of the sensors being produced had to improve significantly over the years, with the detection of femtomolar or even attomolar concentrations being possible nowadays. This growth has been achieved by various means, including improvements in the capabilities of employed equipment such as detectors. However, significant advances in sensors' performance can be attributed to the development of the field of nanotechnology. The ability to produce various organic and inorganic structures at nanometric dimensions allows us to use these materials to cleverly design analytical sensors, which can take advantage of unique material properties arising due to the size of these structures. In the present day, a profound number of nanostructures have been synthesized and employed for use in analytical chemistry. Two main applications of nanomaterials could be distinguished. These structures can be employed to improve the analytical parameters by enhancing the analytical signal already generated by the sensor. For example, due to the improved electrical or optical characteristics resulting from the use of nanostructures. On the other hand, nanomaterials can be the basis for the detection itself where the presence or absence of nanostructures is the core analytical signal generator. With the extensive field of nanotechnology being an integral part of analytical chemistry, this doctoral dissertation presents how specific metal and metal oxide nanoparticles can be used for the detection of biologically active compounds, mainly focusing on the employment of these materials in the design of immunosensors and the reducing sugar sensor. The doctoral dissertation will present three distinct analytical sensing strategies based on different metal or metal oxide structures showing unique ways to take advantage of nanomaterial properties.

Firstly, the development of a label-free electrochemical immunosensor utilizing AuNSs for the detection of p-anti-BSA will be presented. The electrodeposition process is used to modify the underlying electrode with AuNSs of various morphologies. This research analyzes the less understood effects that the morphology of electrodeposited AuNSs have on immunosensor performance. It was observed that the AuNS morphology on the graphite electrode surface has a significant effect on label-free electrochemical immunosensor response. New knowledge was revealed in this field, showing that out of 3 distinct morphologies, the one consisting of smaller but more numerous AuNSs was preferred. Deliberations as to why the specific morphology enhances the analytical response are provided.

Secondly, the development of optical magneto-immunoassay for the detection of hGH, based on MNPs-Au, will be discussed. This research presents a new way to use core-shell nanoparticles, made of a magnetic core and a gold shell, for the design of magneto-immunoassay. The magnetic properties of the synthesized MNPs-Au can significantly simplify and improve the process of making and using the immunoassay, since a magnet can be used to collect these structures. This allows to design an innovative preconcentration step for the immunoassay, where these particles, modified with the detection antibody, can be inserted into the analyte sample in order to bind the analyte. Afterwards, the nanoparticles with the bound analyte can be concentrated and extracted from the analyte sample using a magnet. Magnetic properties also simplify the immunoassay procedure by allowing for easier nanoparticle washing or buffer exchange. In addition, the gold coating can bring additional benefits by facilitating the use of different protein immobilization techniques, as well as improving the stability of such nanoparticles.

Furthermore, an optical reducing sugar quantification strategy will be presented. This research illustrates how the formation of AuNPs can be indirectly used to detect reducing sugars concentration. Due to the unique optical properties of AuNPs, the formation of these structures can be monitored spectrophotometrically. This allows us to analyze the kinetic process of the oxidation-reduction reaction between the gold precursor and the reducing sugar. The novelty of this research lies in the specific use of spectrophotometric data, to relate the formation of AuNPs with the concentration of reducing sugar participating in the reaction. In addition, deliberations about the reaction mechanism are provided.

Overall, the research presented in the doctoral dissertation deals with the synthesis of specific metal and metal oxide nanomaterials and the integration of these structures to form complex analytical systems. It will be shown how nanomaterials can be used in various ways, such as to enhance the analytical sensor response, facilitate a simpler detection process, or even be the basis for the detection itself.

The aim of this study:

To employ various metal and metal oxide nanostructures for the development of analytical systems designed to detect biologically active materials.

The objectives of this study:

1. To electrodeposit various AuNSs onto GR electrodes and employ modified electrodes for the design of a label-free electrochemical immunosensor, establishing the effects of AuNS morphology on the immunosensor response.
2. To synthesize and employ MNPs-Au for the development of an optical sandwich type magneto-immunoassay used to determine hGH.
3. To develop the optical reducing sugar quantification method, based on the AuNP formation, for the determination of fructose, glucose, lactose, and mannose.

The statements for the defense:

1. GR electrodes with electrodeposited AuNSs can be employed for the development of a label-free electrochemical immunosensor.
2. MNPs-Au can be employed for the development of optical magneto-immunoassay used to determine hGH.
3. The AuNP formation process can be used to indirectly quantify reducing sugar concentrations.

1. LITERATURE REVIEW

1.1. The synthesis of nanomaterials

There exists a multitude of ways to synthesize nanomaterials of many shapes and sizes. Depending on the material in question, specific synthesis techniques can be chosen. Those techniques can be divided into 2 main categories – top-down and bottom-up approaches [1]. The basis of a top-down approach is the division of bulk material into smaller nanostructures. The most common techniques used for the top-down approach are mechanical milling [2,3], laser ablation [4], etching [5], sputtering [6], and electrospinning [7]. On the other hand, for the bottom-up approach, nanostructures are grown from the molecular level. The most commonly utilized techniques are chemical vapor deposition [8], hydrothermal growth [9], sol-gel synthesis [10], oxidation-reduction reaction based synthesis [11,12], electrodeposition [13], pyrolysis [14], and biological synthesis methods [15]. The following subsections will provide a short literature overview of the techniques used to produce metal and metal oxide nanostructures presented in this dissertation.

1.1.1. The electrodeposition of AuNSs

One of the convenient ways to synthesize nanostructures directly onto the electrically conductive surface is to use the electrodeposition process. For this technique, the electric current is used to convert the material precursor to a solid state, usually through the reduction process, and force the nucleation and growth of nanostructures directly attached to the electrode surface [16]. In the case of the AuNS electrodeposition, the most commonly used precursor is a complex $[AuCl_4]^-$ ion, which can be reduced to form gold nanostructures based on the following reaction (Eq. 1.1) [17].

$$AuCl_{4\,(aq)}^{-} + 3e^{-} \rightarrow Au_{(s)} + 4Cl^{-} \qquad (1.1)$$

The standard reduction potential for this electrodeposition process is at around +1 V [18]. This allows for the use of a wide range of working electrode potentials while still facilitating the reduction process. The electrodeposition of noble metal nanostructures, including AuNSs, is very widely used for the nanostructurization of the working electrode for many reasons. The electrodeposition process yields nanostructures that attach and grow directly on the electrode surface, providing better surface stability. In addition, the electrodeposition process can be tightly controlled by varying the applied working electrode potential, by changing the electrodeposition time, and concentration of the precursor, by exchanging supporting electrolytes, pH, and ionic strength, or by utilizing various electrochemical techniques. This superb control of the electrodeposition conditions can facilitate the synthesis of nanostructures with various sizes and shapes [17,19–22].

One of the crucial factors affecting the morphology of produced structures is the composition of the electrodeposition solution. Firstly, the concentration of $[AuCl_4]^-$ governs the rate of AuNS growth, with higher concentrations facilitating the formation of bigger structures during the same synthesis time. Secondly, the supporting electrolyte can be added to the synthesis solution to affect the morphology of produced AuNSs. These electrolytes can affect the pH of the synthesis solution, which in turn affects the ionic structure of the Au precursor dominant in the aqueous medium since the $[AuCl_4]^-$ ion can undergo hydrolysis by exchanging Cl^- ligand for OH^-. It has been reported that a higher degree of hydrolysis decreases the reactivity of Au(III) complex ion and in turn reduces the nucleation rate for AuNS formation [19]. This would mean that a lower pH of the electrodeposition solution would suppress the hydrolysis of $[AuCl_4]^-$ ions and in turn increase the nucleation rate, leading to the formation of a higher number of AuNSs on the electrode surface. However, information can be found showing that the nature of the supporting electrolyte has a significantly bigger effect on the morphology of produced structures compared to the pH of the synthesis solution [17]. Although, the effects from the use of different supporting electrolytes are poorly understood. There is some indication that an increase in supporting salt concentration can suppress the formation of dendritic structures due to the increase of ionic strength. However, this effect is only observed for some specific supporting electrolytes [22]. Furthermore, surfactants can be employed to drastically change the electrodeposition process. Surfactants can bind to specific crystal facets of the growing AuNSs and block the growth of these structures at that particular facet, thus significantly affecting the morphology of produced structures [21].

In summary, the electrodeposition process, and the resulting morphology of produced AuNSs, is very sensitive to the electrodeposition solution composition, the electrochemical deposition parameters, and the electrical properties of the electrode. This makes it difficult to determine the morphology of the resulting AuNSs prior to synthesis. Thus, a more practical approach is usually taken, where SEM is used to determine the morphology of produced structures after the electrodeposition. However, once the desired morphology is achieved, repeating the electrodeposition process under identical conditions reliably produces nanostructured electrodes with minimal morphological variability.

1.1.2. The synthesis of core-shell MNPs-Au

The synthesis of core-shell nanoparticles allows to create structures that combine the unique properties of different materials. This extends the use cases for these structures by allowing to tune optical or electrochemical properties to desired specifications using different shell materials while maintaining other properties associated with the core material. For the synthesis of such structures, the bottom-up approach is more convenient and more commonly used. Usually, the synthesis of core-shell nanostructures consists of two steps. Firstly, the core is synthesized and afterwards the encapsulation or direct growth of a shell is performed. In principle, the core-shell structures can be multilayered, having many cores and shells [23].

One of the most commonly used cores for core-shell structures is made out of Fe_3O_4. This material is employed as a core due to its underlying magnetic properties. Although, other types of magnetic materials like cobalt [24] or nickel [25] can also be employed for the development of a magnetic core. Using a magnetic core for core-shell nanoparticle design is very useful since it allows to manipulate the synthesized structures using a magnet.

There exist various ways to synthesize magnetic Fe_3O_4 cores, including coprecipitation, hydrothermal decomposition, hydrothermal and sonochemical formation. Out of all of these synthesis methods, coprecipitation is most commonly employed. The synthesis requires combining ferric and ferrous ions, usually in a 2:1 molar ratio, at room temperature or elevated temperatures in strongly alkaline solutions. The shape and size of produced core particles are sensitive to the reaction conditions and can be tuned by modifying parameters such as employed salt type (chlorides, sulphates, nitrates, perchlorates, etc.), the ratio of ferric to ferrous ions, reaction temperature, ionic strength of the media, pH value, and other reaction parameters like stirring rate and injection speed of the base solution [26,27]. The general reaction equation for co-precipitation is provided below (Eq. 1.2) [28,29]. The synthesized magnetic iron oxide nanoparticles can be collected using a magnet, and then a shell structure can be applied to the magnetic core.

$$Fe^{2+}_{(aq)} + 2Fe^{3+}_{(aq)} + 8OH^{-} \rightarrow Fe_3O_{4(s)} + 4H_2O \qquad (1.2)$$

Shell synthesis techniques can be mainly divided into two groups – direct and seeded. The direct synthesis of a shell onto the core structure becomes possible when the crystal lattices of the shell and core materials are similar. However, if the crystal lattices are mismatched, the seeded shell formation approach is employed. For this technique, firstly, very small seeds, made from the same material as the intended shell, are adsorbed on the core structure to provide nucleation sites for the growth of the shell material [30].

Due to the superb electrical and unique optical properties, as well as high stability, noble metals are commonly used as shell materials. Noble metal shells are also employed due to the ease of synthesis. Gold shells are commonly formed by the reduction of complex Au(III) ions using various reducing agents, such as trisodium citrate at high temperatures [31] and sodium borohydride at room temperature [29]. Surfactants are used to stabilize the formed structures. In addition, sonication of the colloidal suspension before, during, and after the synthesis is commonly employed in order to improve synthesized nanoparticle uniformity [29,32,33]. Due to the similar crystal lattice structure between gold and Fe_3O_4, a gold shell can be grown on the magnetic core using both direct and seeded techniques. The gold shell of MNPs-Au presented in this dissertation has been synthesized by reducing $[AuCl_4]^-$ using hydroxylamine. The use of hydroxylamine as a reducing agent has an added advantage for the synthesis of core-shell structures. That is, the reduction mechanism using hydroxylamine favors the formation of a gold layer on the existing surface rather than initiating the self-nucleation of new nanostructures within the solution medium, leading to a more uniform final colloidal solution [34,35]. The principle reaction for $[AuCl_4]^-$ reduction with hydroxylamine is presented below (Eq 1.3) [36].

$$AuCl_4^- + 3NH_2OH \rightarrow Au^0 + 3NH_2OH^{+\bullet} + 4Cl^- \qquad (1.3)$$

1.1.3. The synthesis of AuNPs using reducing sugars

The synthesis of gold nanoparticles has been extensively studied and many different techniques can be used to produce AuNPs. These nanostructures are usually produced using a bottom-up approach by the reduction of $[AuCl_4]^-$ using various reducing agents, among which sodium citrate, sodium borohydride, and ascorbic acid are the most commonly used.[37].

The formation of AuNPs can also be facilitated using various reducing sugars, such as glucose, fructose, and galactose [38]. The reaction mechanism between $[AuCl_4]^-$ and reducing sugars is not sufficiently understood. Research by some authors implies that monosaccharides participate in the oxidation-reduction reaction directly through the open-chain conformation, which is present in the solution medium only in very small concentrations [38,39]. That would mean that in a basic or acidic medium, fructose would first undergo Lobry de Bruyn-Alberda van Eckenstein transformation completely into glucose or mannose (Fig. 1) and only then would participate in the reaction as either of these reducing sugars [40–42]. However, other authors show that the oxidation of reducing sugars using metal ions in a base medium proceeds through a reducing sugar enediol intermediate [43–45]. In addition, the research provided in this dissertation also hints that the reaction is more likely to take place through the enediol intermediate rather than directly through an open-chain conformation. In any case, if reducing sugars are used for the synthesis, the addition of surfactants is required to stabilize the resulting AuNPs. CTAB was used as a surfactant for the work presented in this dissertation.

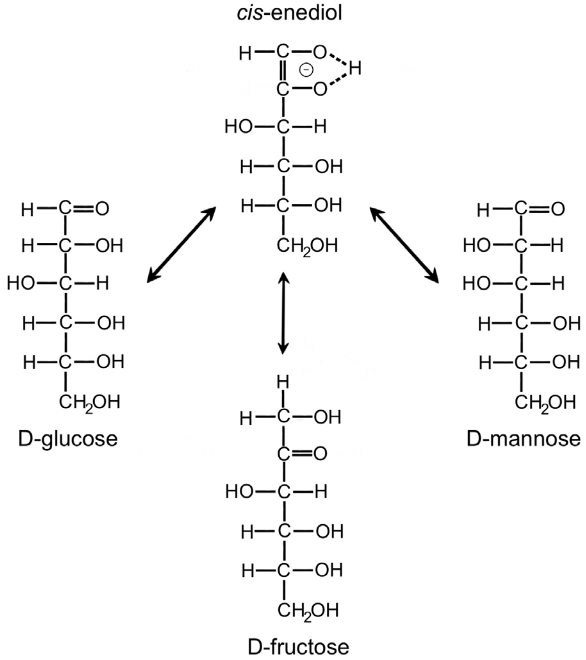

Fig. 1. Lobry de Bruyn-Alberda van Eckenstein transformations.

1.2. The analytes

The following subsections provide information about the analytes studied in the dissertation. The analyte properties and the most common detection methods are reviewed.

1.2.1. Human growth hormone

Human growth hormone, also known as somatotropin, is a heterogeneous protein produced by anterior pituitary gland, which stimulates growth, cell reproduction, and regeneration in humans. In addition, hGH also promotes the production of insulin-like growth factor 1 [46]. The hGH can be present in the blood in various isoforms. The predominant isoform, making up approximately 50% of all found hGH, has a molecular weight of 22 kDa and is made of 191 amino acids. The second isoform has the weight of 20 kDa and makes up around 5-9%. The remaining portion of hGH is present in dimer and oligomer forms or as hGH fragments [47–49]. Maintaining a proper concentration of hGH in the blood is crucial for regular body growth and a number of biological processes, such as the metabolism of lipids, carbohydrates, and proteins [50]. The deficiency of hGH can develop both in children and adults, however, it is usually more detrimental to children, leading to stunted growth. In adults, the deficiency is associated with changes to metabolism, reduced muscle and bone mass [51,52]. On the other hand, the presence of excess amount of hGH can cause gigantism [53], insulin resistance [54], and diabetes [55]. Furthermore, hGH is often used as a doping agent by unethical professional athletes. As a result, both the determination of deficiency and excess of hGH should be considered when developing analytical systems to detect this hormone.

The standard concentration of hGH in blood varies depending on gender and age but is usually in the range from $0.4\ \mathrm{ng \cdot mL^{-1}}$ ($0.018\ \mathrm{nmol \cdot L^{-1}}$) to $50\ \mathrm{ng \cdot mL^{-1}}$ ($2.273\ \mathrm{nmol \cdot L^{-1}}$) [56]. It is complicated to achieve robust detection of hGH due to the presence of isoforms, as some detection methods only detect the specific isoform, whereas other methods are sensitive to all isoforms present in the sample [48]. Through the years, various hGH concentration determination methods have been developed. Although, currently, immunoassays are mainly employed for clinical measurements. Radioimmunoassay [57], immunofluorometric assay [58], immunochemiluminescent assay [59], and enzyme-linked immunoassay (ELISA) [56] are used for the detection of hGH, with ELISA being the most popular technique currently. The described immunoassays are usually sensitive to all hGH isoforms. However, for anti-doping measures, simply determining the hGH concentration in blood is not sufficient due to the wide range of concentrations being allowed for athletes due to significant biological variance among people. For this purpose, specific differential immunoassays were developed based on the determination of different hGH isoforms [60]. Since the recombinant hGH (rhGH), used for doping, is only analogous to the main hGH isoform of 22 kDa, the consumption of rhGH changes the natural ratio between various hGH isoforms in favor of the primary isoform. Differential immunoassays are used to determine the ratios between these isoforms, allowing to detect doping since the natural ratio between isoforms is mostly consistent in human population. However, the detection procedure for these differential immunoassays is highly complex, requiring up to 11 blood sample measurements. As a result, an alternative indirect hGH doping determination method was developed in the early 2000, based on the detection of hGH biomarkers [61]. Specifically, the monitoring of insulin-like growth factor 1 and procollagen III N-terminal peptide concentrations in blood were chosen as markers for hGH doping. Currently, the analysis of hGH biomarker concentrations is also used in clinical laboratories for a more accurate diagnosis of the underlying cause of hGH deficiency or excess. In the last decade, the quantification of hGH using various chromatography-mass spectrometry methods has been gaining prominence [62–66].

1.2.2. Reducing sugars

From a historical perspective, carbohydrates have been the main subjects of study in the fields of organic chemistry and biochemistry, promoting the development of these sciences and being among the first organic compounds whose chemical structure was determined. Reducing carbohydrates, commonly called reducing sugars, are any carbohydrates that are capable of acting as a reducing agent in an oxidation-reduction reaction. All monosaccharides are reducing sugars, as well as some disaccharides and polysaccharides. Due to the presence in dietary products, reducing sugars such as glucose, fructose, galactose, mannose, and lactose are the most known and studied [41,67].

Depending on whether the carbonyl group is part of the aldehyde group or part of ketone, the sugars are divided into aldoses and ketoses, respectively. Sugars are also chiral compounds, and depending on the spatial arrangement of the asymmetric carbon farthest from the carbonyl group, they can be found in different enantiomeric forms designated using a prefix L– or D– in reference to L– and D– glyceraldehyde. Even though enantiomers behave identically from a chemical standpoint, they are not equivalent biologically, with D– carbohydrates being predominant. Furthermore, for monosaccharides containing more than 3 carbon atoms, in addition to the enantiomeric carbon, other non-terminal carbon atoms are also asymmetrical, thus providing the basis for the formation of stereoisomers, called epimers. For example, D–glucose and D–galactose are epimers at position C4 [41,67].

In the solution, due to the intramolecular forces, sugars undergo rearrangement into cyclic structures. After cyclization, the hydroxyl group attached to the carbonyl carbon can point either up or down, designating the compound as α or β anomer. In the α form, the hydroxyl group resides on the opposite side of the ring compared to the CH_2OH group of the chiral carbon responsible for determining the D– or L– configuration. Conversely, in the β form, the hydroxyl group is situated on the same side of the ring (Fig. 2). In aqueous solutions, anomers can freely intraconvert between α or β forms. Due to the chirality, most sugars are optically active and can rotate the plane polarized light [41,67].

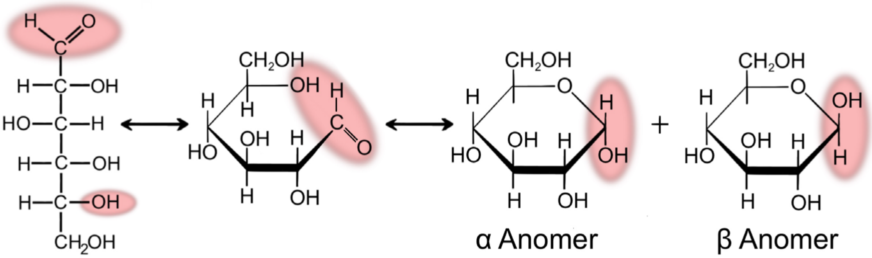

Fig. 2. The cyclization of glucose yielding both α and β anomers.

After undergoing intramolecular rearrangement, hexoses, containing the most common reducing sugars, usually form six-membered rings with the hemiacetal oxygen. These ring structures are called pyranoses. Occasionally, five-membered rings may also form, called furanoses, although they typically represent minor structures unless the formation of a six-membered ring is impossible. All these different forms of the same sugar, including the open-chain, are present in the solution once equilibrium is reached. Even if a pure compound of a specific form is dissolved in water, a complex series of reactions take place to give an equilibrium mixture containing all the forms. This process is called mutarotation. At room temperature and neutral pH this process is slow, taking hours to reach equilibrium. However, both acid and base can catalyze mutarotation, with basic conditions resulting in faster transformations compared to acidic pH. The equilibrium structures of the five forms of D-glucose in the solution [41,67,68] are provided below (Fig. 3).

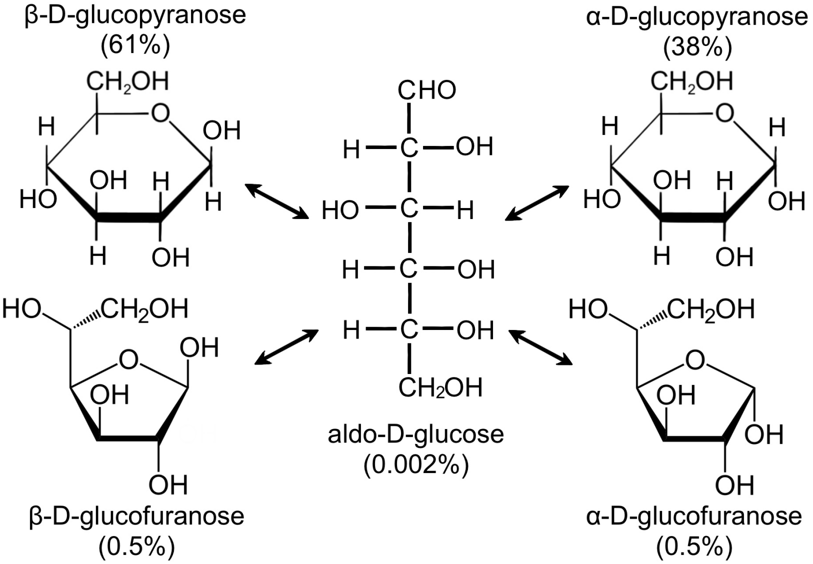

Figure 3. Equilibrium mixture of D–glucose solution at 30°C.

Excessive sugar intake is widely recognized as the predominant factor contributing to various global healthcare issues, including diabetes, obesity, tooth decay, heart diseases, weakened immunity, and others. Reducing sugars can be naturally found in food and drinks or added artificially. Since these compounds have such a significant impact on human health, the monitoring of reducing sugar concentrations in food, drinks, and bodily fluids is required.

The methods for determining reducing sugars are usually optical or electrochemical. The optical techniques for reducing sugar determination can measure absorbance, refractive index, or the rotation angle of plane-polarized light. For electrochemical methods, amperometry, potentiometry, or conductometry are usually employed. Detection methods can be divided into 3 main groups, depending on whether all carbohydrate content is measured from the sample, or only reducing sugars are detected, or a specific sugar is determined [69,70].

When the determination of the total carbohydrate content in the sample is required, the most commonly employed analysis method uses phenol-sulfuric acid. Under strongly acidic conditions and high temperatures, degradation of the carbohydrates occurs, yielding various furan derivatives. These products can condense with numerous phenolic substances to produce colored compounds which can be detected spectrophotometrically [69]. Most commonly, the condensation is performed with the phenol itself, producing a yellow-orange complex for which the absorbance is measured at 490 nm. This method is frequently employed as a qualitative test to determine the presence of carbohydrates. However, for the quantitative analysis, the standard curves need to be tailored for specific samples due to the non-stoichiometric nature of these reactions. In addition, if the ratio between carbohydrates in the sample is not known beforehand, extra measurement error is introduced [71].

Another group of methods can be used to specifically determine the total reducing sugar content in the samples. These methods are based on the reducing properties of these sugars. The most commonly used Samogyi-Nelson method has been developed in the 1944 [72]. This method relies on the ability of reducing sugars to participate in redox reactions with Cu^{2+} ions in an alkaline environment and at high temperature. The reaction yields Cu^{+} ions, which can further reduce the arsenomolybdate complex, resulting in a blue-colored compound, the absorption of which is measured at 520 nm. Some other detection methods are based on the precipitation of Cu_2O from Cu^{+} ions produced after the Cu^{2+} reaction with reducing sugars [69]. The same problem of non-stoichiometry exists for these reducing sugar content determination methods, meaning that standard curves need to be adapted specifically for desired samples. This is crucial when ketoses are present in the unknown sample since these compounds participate in the reaction at significantly different rates. In addition, since the detection is based on the reducing nature of these sugars, other reducing agents can interfere with the analysis. Although usually, the concentrations of reducing sugars in the unknown sample are significantly higher than other reducing agents, resulting in minimal error.

The methods mentioned above can determine the total amount of carbohydrates or reducing sugars in the sample, however, they cannot specifically quantify only one desired sugar. For this purpose, specific determination methods have been developed, which can be mainly divided into chromatographic and enzyme-based.

Both high-performance liquid chromatography (HPLC) and gas chromatography (GC) are employed for the detection of specific sugars. Various HPLC modes have been employed, including anion-exchange, cation-exchange, normal phase and reverse phase chromatography. HPLC methods have an added advantage that usually, no derivatization is required, which is not the case for gas chromatography due to the non-volatile nature of sugars. For GC analysis, aldoses are usually first reduced to alcohols and then converted to acetate esters or trimethylsilyl ethers. After the separation using chromatography methods, various detectors can be used for the detection itself. The most prevalent detectors include the refractive index detector, pulsed-amperometric detector, and mass spectrometry detector. If the derivatization is performed, spectrophotometric and flame ionization detectors can also be employed [69,73].

Finally, enzymatic methods can be used for the specific detection of desired sugars. Enzymatic methods typically exhibit specificity towards a particular sugar, however, sometimes enzymes can react with a couple of different sugars, although usually not at the same rate. Both optical and electrochemical detection are possible, with the latter being more prevalent.

Due to the clinical importance, special attention should be given to glucose detection. Enzymatic glucose detection is usually based on the enzyme glucose oxidase, which oxidizes D–glucose quantitatively to D–glucono-1,5-lactone, with the byproduct being H_2O_2. When an optical detection is performed, peroxidase enzyme is usually added to the sample as well as some colorless dye which can be oxidized to a colored one. In this case, the H_2O_2 produced during the enzymatic oxidation of β-D–glucose is employed by the peroxidase to oxidize the dye into a colored product which can be detected spectrophotometrically. In the case of electrochemical detection, three different generations of amperometric glucose biosensors can be distinguished based on electron transfer mechanisms. The first generation of glucose biosensors measures the electrochemically active substrate or a product formed during the enzymatic reaction. Usually, the anodic current resulting from the oxidation of H_2O_2, which was produced during the enzymatic reaction on the electrode, is measured. A high working electrode potential is required for such detection, raising the risk of interference from other compounds found in the sample, such as ascorbic and uric acids. However, the consumption of oxygen can also be monitored, although the detection is sensitive to fluctuations in the amount of dissolved oxygen. For the second generation of glucose biosensors, additional redox mediators are added, which outcompete oxygen and become responsible for electron transfer from the enzyme's active center to the electrode. In this case, the oxidation of the mediator, which was reduced in the enzyme active center, is registered at the working electrode. The third generation amperometric glucose biosensors are designed to work without a redox mediator. They are based on detecting direct electron transfer from the enzyme's active center to the electrode. However, since the active center for glucose oxidase is deep inside the enzyme globule, a complicated biosensor design is required for direct electron transfer to be possible [69,70,74,75].

1.3. Metal and metal oxide nanostructures in the design of optical and electrochemical immunosensors

A deep dive into this topic is provided in review articles **Paper 5** and **Paper 6**, presenting various ways in which metal nanoparticles, quantum dots, and ZnO nanomaterials can be used in the design of electrochemical as well as optical immunosensors. Thorough and up to date information is provided on various protein immobilization methods, as well as how these structures can be used to amplify the analytical signal, or how it can be the basis for the detection itself.

2. METHODS

2.1. Instruments

UV-vis spectrophotometer Lambda 25 (Perkin Elmer, Shelton, WA, USA). Microplate spectrophotometer Spectra-Max i3 (Molecular Devices, San Jose, CA, USA). Transmission electron microscope Tecnai F20 X-TWIN (Eindhoven, The Nederlands). Scanning electron microscope SU-70 (Hitachi, Krefeld, Germany). X-ray diffraction (XRD) measurements were performed using a MiniFlex II diffractometer (Rigaku, Japan). The diffractograms were recorded in the 2θ range from 10° to 80° using CuK_{α} $\lambda = 1.5406$ Å radiation.

2.2. The electrodeposition of AuNSs

All electrochemical measurements were performed using a three-electrode cell and a potentiostat/galvanostat PGSTAT30/Autolab from ECOChemie (Utrecht, Netherlands). A platinum electrode was used as a counter electrode, while $Ag/AgCl_{3M\ KCl}$ was used as a reference. The working electrode was either an ITO or GR.

GR electrodes were polished using fine (P120), very fine (P320), and ultra-fine grit (P2000) sandpaper and washed using deionized water. The side surface of the GR was isolated using a silicone tube to control the working surface area, resulting in an area of 0.071 cm^2.

Subsequent ultrasonic cleaning was performed for 15 minutes using acetone and deionized water for the ITO electrode. In addition, the ITO electrode underwent electrochemical pretreatment by cycling the working electrode potential from 0 to +1 V for 30 times in 50 mM PBS, pH 6, containing 0.1 M KCl, followed by rinsing with deionized water.

The electrodeposition process of AuNSs was performed at a constant −0.2 V potential for 60 s for both ITO and GR electrodes. The electrodeposition solution composition was varied in order to produce AuNSs of different morphologies. The solution consisted of $HAuCl_4$ at various concentrations of 3, 10, or 15 mM, and different supporting electrolytes. H_2SO_4 at a concentration of 0.1 or 0.2 M was used as a supporting electrolyte as well as KNO_3 with a concentration of 0.1, 0.2, or 1 M.

2.3. The synthesis of MNPs-Au

Magnetic gold coated nanoparticles were produced in two steps: the Fe_3O_4 MNPs synthesis and the gold shell growing procedure. MNPs were produced using the co-precipitation method (Eq. 1.2). To form MNPs, 125 mL of 1 M NaOH solution was slowly added to a 10 mL solution containing 1.28 M $FeCl_3$ and 0.64 M $FeSO_4$ using vigorous stirring. The resulting precipitate was gathered using a magnet, washed three times with deionized water, and subsequently immersed in a 2 M $HClO_4$ solution overnight under an argon atmosphere. The color of the solution becomes brown after the formation of MNPs. The produced nanoparticles were washed 3 times using deionized water and 1 time using ethanol by centrifuging at 12000 × g for 20 min. After centrifuging one additional time, the MNPs were left to dry in the air.

The growth of a gold shell onto the MNPs was then performed. Initially, 5 mg of dried magnetic nanoparticles underwent sonication in 5 mL of deionized water until completely dispersed. Next, 10 mL of 0.27 M EDTA solution, prepared in 1 M NaOH, was introduced. The particles were then collected using a magnet and dispersed in a 10 mL solution consisting of 0.1 M CTAB and 0.01 M $HAuCl_4$. Afterwards, 150 mg of hydroxylamine hydrochloride was added to the MNPs solution under vigorous stirring in order to facilitate the reduction of Au(III) complex ions to Au^0 on the surface of MNPs (Eq. 1.3). The color of the solution changes from brown to dark red.

2.4. The synthesis of AuNPs using reducing sugars

The formation of AuNPs occurs due to an oxidation-reduction process between the Au(III) complex ion and a reducing sugar at room temperature and high pH, with CTAB serving as a surfactant to stabilize the formed nanoparticles. The reaction mixture consisted of 0.1 M NaOH, 3.7 mM CTAB, and 1 mM of $HAuCl_4$ with various concentrations of different reducing sugars such as glucose, fructose, lactose, and mannose. The reaction was performed directly in a cuvette with a mixture volume of 1 mL. The change in the absorbance of the reaction mixture was registered at various times after the start of the reaction.

When real samples were used for the synthesis of AuNPs in order to determine reducing sugar concentrations in those samples, additional sample preparation steps were required for milk and saliva samples. For the milk sample, proteins were precipitated by adding $CuSO_4$ up to a 0.5% mass concentration and waiting for 10 min under vigorous mixing. Afterwards, the mixture was centrifuged at 17000 × g for 15 min, and the supernatant was collected and directly added to the reaction mixture. For the saliva sample, the mouth was rinsed with water for 2 min. Following this, saliva was collected using a cotton roll, which was chewed for 1 min. The saliva was subsequently extracted from the cotton roll using a sterile syringe through a 0.23 μm PVDF filter to separate proteins. The resulting saliva extract was then directly added to the reaction mixture. For the Coca-Cola and Coca-Cola Zero beverages, no additional sample preparation was required.

2.5. Covalent immobilization of BSA onto GR modified with AuNSs

BSA was covalently immobilized onto an AuNS-modified GR electrode using EDC/NHS chemistry through the formed self-assembled monolayer on the gold nanostructures. Initially, electrodes with electrodeposited AuNS were immersed in a 1 mM 11-MUA methanol solution for 2 h. Afterwards, the electrodes were washed by subsequently immersing them in methanol and deionized water for 15 min with mixing. Then, electrodes with the self-assembled monolayer were inserted into a 250 µL solution containing 200 mM EDC and 50 mM NHS for 15 min. Following this, modified electrodes with activated carboxylic groups were rinsed with deionized water and inserted in a 250 µL solution of 100 $\mu g \cdot mL^{-1}$ BSA for 20 min to facilitate the covalent immobilization of BSA onto the modified electrode surface. Finally, electrodes with immobilized BSA were washed by immersing them in a deionized water solution for 15 min with mixing.

2.6. Covalent immobilization of m-anti-hGH onto MNPs-Au

To effectively immobilize m-anti-hGH antibodies, it was necessary to first eliminate the CTAB present on the MNPs-Au surface. The removal of CTAB was based on the methodology by He et al. [76]. Firstly, 800 µL of 30 mM $NaBH_4$ was added to 1.6 mL of 0.2 $mg \cdot mL^{-1}$ solution of MNPs-Au. The mixture was stirred for 1 h. The CTAB-free nanoparticles were then washed with deionized water and used for the covalent immobilization of monoclonal antibodies. Firstly, a self-assembled monolayer was formed on MNPs-Au by transferring nanoparticles to a 1 mM solution of 11-MUA using a magnet and waiting for 2 h. Afterwards, MNPs-Au/11-MUA nanoparticles were washed with deionized water. The carboxyl groups of 11-MUA were activated by placing the particles in a mixture comprising of 200 mM EDC and 50 mM NHS for 15 min. Afterwards, the solution containing varying concentrations of m-anti-hGH antibodies (200, 330, 660, and 984 nM) was introduced onto magnetically retrieved MNPs-Au/11-MUA. Following a 2 h incubation, MNPs-Au with immobilized m-anti-hGH were washed 3 times with a 10 mM PBS solution, pH 7.4. After washing, the solution containing 1% BSA in 10 mM PBS, pH 7.4, was introduced. Nanoparticles were held at room temperature for 1 h and overnight at +4°C to block the unreacted activated esters and the free surface.

2.7. Electrochemical characterization methods

2.7.1. The determination of electroactive gold surface area

The electrochemically active area (EASA) of formed AuNS can be determined using the cyclic voltammetry method. For this purpose, the electrode with electrodeposited AuNS was immersed in 0.5 M H_2SO_4 solution, and the working electrode potential was cycled between 0 and +1.4 V at the potential sweep rate of 50, 100, and 150 $mV \cdot s^{-1}$. The 3rd cycle of cyclic voltammograms was used for the evaluation of EASA. The electrochemically active area (Γ), in cm^2, was calculated using the following equation [77,78].

$$\Gamma = \frac{A}{v \times 400\,\mu C \cdot cm^{-1}} \tag{2.1}$$

where A – the area of the cathodic current; v – the potential sweep rate in $V \cdot s^{-1}$; $400\,\mu C \cdot cm^{-1}$ – the charge density per unit area associated with the electrochemical reduction of a monolayer of chemisorbed oxygen on polycrystalline gold [79].

2.7.2. The determination of electroactive electrode surface area

The EASA of the total electrode surface, instead of just gold, can be determined using the cyclic voltammetry method by performing measurements in a 10 mM PBS solution containing 2.5 mM $[Fe(CN)_6]^{3-/4-}$. For this purpose, the potential was cycled between −0.2 and +0.7 V while the potential sweep rate was varied (10, 25, 50, 75, 100, and 150 $mV \cdot s^{-1}$). The 3rd cycle of cyclic voltammograms was used for the evaluation of EASA. The area was evaluated using the Randles-Sevcik equation at 25°C [79].

$$i_p = 2.69 \times 10^5 \cdot n^{\frac{3}{2}} \cdot A \cdot D^{\frac{1}{2}} \cdot C \cdot v^{\frac{1}{2}} \tag{2.2}$$

where i_p – maximum peak current in A; n – number of electrons transferred in the redox event; A – EASA in cm^2; D – diffusion coefficient in $cm^2 \cdot s^{-1}$ ($6.40 \cdot 10^{-6}\ cm^2 \cdot s^{-1}$ for ferrocyanide); C – concentration of electroactive species in $mol \cdot cm^{-3}$; v – potential sweep rate in $V \cdot s^{-1}$. Because the charge transfer in the cathodic region is slower compared to the anodic region for a $[Fe(CN)_6]^{3-/4-}$ redox pair, the peak anodic current values were utilized to determine the electroactive surface area [80]. The EASA was evaluated from the slope of $v^{1/2}$ *vs.* peak anodic current of $[Fe(CN)_6]^{3-4-}$ redox probe.

2.7.3. The determination of heterogeneous electron transfer rate constant

The heterogeneous electron transfer rate constant (k^0) can be determined based on the Nicholson-Lavagnini approach using the cyclic voltammetry method [81,82]. Measurements are performed identically as written in Section 2.7.2. The dimensionless kinetic parameter (Ψ) can be calculated using the following empirical equation (Eq. 2.3).

$$\Psi = \frac{-0.6288 + 0.0021 \cdot X}{1 - 0.0017 \cdot X} \tag{2.3}$$

where X – the system's peak potential separation (ΔE_p) multiplied by the number of electrons involved in the electrochemical reaction (n). Once the parameter Ψ is calculated, the k^0 can be determined using the following equation (Eq. 2.4).

$$\Psi = k^0 \cdot \left(\frac{\pi \cdot D \cdot n \cdot v \cdot F}{R \cdot T}\right)^{-\frac{1}{2}} \tag{2.4}$$

where k^0 – heterogeneous electron transfer rate constant in $cm \cdot s^{-1}$; D – diffusion coefficient in $cm^2 \cdot s^{-1}$; n – number of electrons transferred in the redox event; v – potential sweep rate in $V \cdot s^{-1}$; F – Faraday constant of 98485 $C \cdot mol^{-1}$; R – universal gas constant of 8.31446 $J \cdot mol^{-1} \cdot K^{-1}$; T – temperature in K. The heterogeneous electron transfer rate constant was evaluated from the slope of $v^{-1/2}$ *vs.* Ψ.

3. RESULTS AND DISCUSSION

This results and discussion section is divided into 3 main subsections. Subsection 3.1., based on **Paper 1** and **Paper 2**, describes how an easy electrodeposition procedure can be used to synthesize AuNSs of different morphologies directly onto the electrode, improving the electrode's electrical and electrochemical parameters. The electrodeposited AuNSs can enhance the electrochromic properties of conducting polymer layers or can be adapted for the development of a label-free electrochemical immunosensor. Subsection 3.2., based on **Paper 3**, presents how MNPs-Au nanoparticles can be used for the development of optical magneto-immunoassay for the detection of hGH. Finally, Subsection 3.3., based on **Paper 4**, shows how the AuNP formation process can be used to quantify reducing sugars optically.

3.1. The use of electrodeposited AuNSs for the development of a label-free electrochemical immunosensor

3.1.1. Electrodeposition and characterization of AuNSs on ITO electrodes

AuNSs of different morphologies were electrodeposited onto the ITO coated glass slide depending on the composition of the synthesis solution. The electrodeposition was performed at a constant −0.2 V potential *vs.* Ag/AgCl$_{3M\ KCl}$ for 60 s. AuNS$_I$ were produced when the electrodeposition solution consisted of 3 mM $HAuCl_4$ and 0.1 M H_2SO_4, while AuNS$_{II}$ were produced when the composition was 15 mM $HAuCl_4$ and 1 M KNO_3. The electrodeposition of AuNSs was clearly visible on the transparent ITO electrode due to the appearance of a colored layer, which intensified during the synthesis process. The colors of the electrode after the electrodeposition of AuNS$_I$ and AuNS$_{II}$ were light grey and intense dark orange, respectively. The electrode morphology, after the electrodeposition of AuNSs, was evaluated using SEM imaging technique (Fig. 4). Produced AuNS$_I$ were "hedgehog" shaped, ranging in size from 200 to 500 nm, however, even smaller structures were present. These AuNS$_I$ were positioned sporadically at different distances from each other. In the case of AuNS$_{II}$, the resulting structures were noticeably larger and dendritic, containing branches.

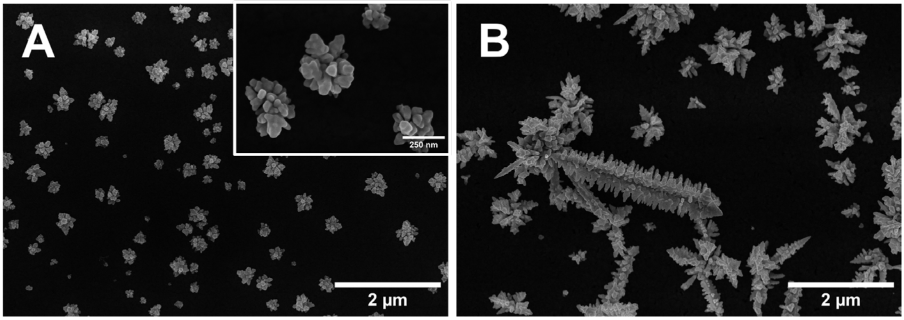

Fig. 4. SEM images of (**A**) ITO/AuNS$_I$ and (**B**) ITO/AuNS$_{II}$ electrodes. Inset: A higher magnification image of the ITO/AuNS$_I$ surface.

Similar but more densely packed structures to AuNS$_{II}$ were reported on ITO electrode by Shu et al. when the electrodeposition was performed from a 10 mM $HAuCl_4$ and 0.1 M KNO_3 solution at −0.3 V *vs.* Ag/AgCl but for a much more extended period of 60 minutes [83]. As mentioned in the literature review section 1.1.1., many different factors can affect the morphology of produced AuNSs. When it comes to electrodeposition solution, the pH, $[AuCl_4]^-$ concentration, as well as the nature and concentration of supporting electrolyte should be taken into consideration. The increase in $[AuCl_4]^-$ usually does not significantly affect the nucleation rate for new nanostructure growth points on the electrode surface but instead increases the growth rate for already formed structures. On the other hand, pH is considered to be a strong factor affecting the nucleation rate and the morphology of produced AuNSs. This is due to the fact that the complex $[AuCl_4]^-$ ion undergoes pH-dependent hydrolysis by exchanging the Cl^- for OH^-. It has been suggested that the AuNS nucleation rate depends on the degree of hydrolysis of $[AuCl_4]^-$ ion, with lower pH facilitating a higher nucleation rate [19,20]. However, some research suggests that the nature of the supporting electrolyte itself has a substantially more significant impact on the morphology of produced AuNS compared to the solution pH [17]. The morphological analysis of AuNS$_I$ and AuNS$_{II}$ also showed that a higher nucleation rate was indeed achieved at lower pH since the AuNS$_I$-modified electrode exhibited a greater number of individualized structures on the electrode in comparison to the AuNS$_{II}$-modified ITO.

XRD measurements were performed on AuNS-modified ITO electrodes. It was revealed that both AuNS$_I$ and AuNS$_{II}$ were polycrystalline, showing the reflection lines of Au(111), Au(200), Au(220), and Au(311) crystal faces. With this knowledge, oxygen chemisorption measurements were performed to determine the electroactive Au surface area of the AuNS-modified ITO electrodes based on the methodology provided in Section 2.7.1. The electroactive surface area of gold was found to be 0.19 ± 0.03 cm^2 and 1.44 ± 0.17 cm^2 for $AuNS_I$ and $AuNS_{II}$, respectively. The geometric electrode area was 0.8 cm^2. The electroactive area of gold for $AuNS_I$, being around 4 times lower compared to the geometric area, is likely the result of the low gold nanostructure density on the electrode, leaving much of the underlying ITO exposed. In addition, the lower $HAuCl_4$ concentration also leads to a lower amount of gold being electrodeposited. In the end, even though the separate structures were less numerous for $AuNS_{II}$, the branched and dendritic nature of these structures leads to the electroactive area of gold being significantly higher, even above that of the geometric electrode area.

The electrodeposition of AuNSs onto ITO electrodes improved electroactive surface area, electric properties, and altered optical characteristics. These enhancements were used to improve the electrochromic properties of the PANI-PEDOT conductive polymer layer. More detailed information is provided in **Paper 1**, showing that the electrodeposition of the AuNS layer onto the ITO electrode can help to improve optical contrast by 22%, coloration efficiency by 50%, and shorten the switching time between colored states by 17% while improving electrochromic cycling stability. However, after observing the enhancements that electrodeposited AuNSs bring to conductive polymer layers, it was decided to test how such electrodeposited structures could be employed for the development and improvement of electrochemical immunosensors based on graphite rod electrodes.

3.1.2. Electrodeposition and characterization of AuNSs on GR electrodes

Depending on the electrodeposition solution, various AuNS morphologies were achieved on the GR electrodes. 6 different synthesis solutions were tested. The electrodeposition was performed in the same way as for ITO electrodes by applying −0.2 V potential to the GR electrodes *vs.* $Ag/AgCl_{3M\ KCl}$ for 60 s duration. SEM images of AuNS-modified electrodes are presented in Fig. 5. The observed structures showed significant morphological differences compared to AuNS-modified ITO electrodes.

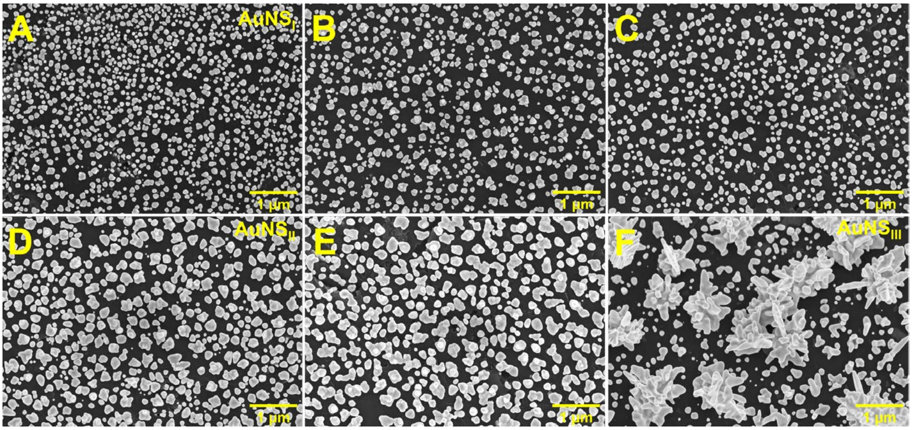

Fig. 5. SEM images of GR electrodes modified with AuNS electrodeposited from a solution containing (**A**) 3 mM $HAuCl_4$ and 0.2 M H_2SO_4 (**AuNS$_I$**), (**B**) 3 mM $HAuCl_4$ and 0.1 M KNO_3, (**C**) 3 mM $HAuCl_4$ and 0.2 M KNO_3, (**D**) 10 mM $HAuCl_4$ and 0.1 M KNO_3 (**AuNS$_{II}$**), (**E**) 10 mM $HAuCl_4$ and 0.2 M KNO_3, (**F**) 15 mM $HAuCl_4$ and 1 M KNO_3 (**AuNS$_{III}$**).

The analysis of SEM images shows a similar pH dependent trend as was observed when AuNSs were electrodeposited on ITO electrodes. AuNS$_I$, synthesized from the solution containing 0.2 M H_2SO_4, contained a higher number of separate structures in comparison to all KNO_3 based structures, indicating a higher nucleation rate, likely due to the lower degree of hydrolysis of $[AuCl_4]^-$ ions. When 0.1 or 0.2 M KNO_3 was employed instead of H_2SO_4, fewer separate particles were formed, however, the formed structures tended to be slightly larger even though the same $[AuCl_4]^-$ concentration was used. This likely occurs because Au(III) complex ions at the electrode surface can be more readily consumed to grow the already existing nanoparticles rather than form new nucleation points. When comparing electrodeposition with 0.1 or 0.2 M KNO_3, but with different $[AuCl_4]^-$ concentrations, larger structures were observed for higher gold precursor concentrations, however, the overall number of separate particles stayed mostly similar. Although, it was observed that some closely located gold nanoparticles merged into single structures during growth. Finally, the effects of KNO_3 concentration on AuNSs morphology are less clear. On one hand, when KNO_3 concentration was increased from 0.1 to 0.2 M, the formed structures appeared slightly less jagged with better surface uniformity, although the effect is not very significant. On the other hand, when the concentration was increased further to 1 M, substantial branching was observed, forming large dendritic structures (AuNS$_{III}$). In my opinion, it is likely that the ratio between the concentration of $HAuCl_4$ and the supporting electrolyte has an effect on the morphology of produced AuNSs. However, no analysis of such effects has been found in the literature for AuNS electrodeposition.

Significant differences can be observed when the morphology of AuNSs, electrodeposited under similar conditions on ITO and GR electrodes, is compared. For AuNS$_I$-modified GR electrode, substantially larger number of smaller structures were electrodeposited compared to AuNS$_I$-modified ITO electrode. In addition, nanoparticles were mostly circular, while in the case of ITO, the structures were “hedgehog” shaped. When comparing nanostructures synthesized from an identical 15 mM $HAuCl_4$ and 1 M KNO_3 solution, some similarities in the nanostructure morphology can be observed, with dendritic structures forming on both surfaces. However, again significantly higher nanostructure population density is observed on GR surface. These results could be due to the differences in electrical properties and crystal structure of the electrode surface. For example, Bleiji et al. showed, that depending on the crystalline structure of ITO surface, different reduction potentials for AgNS electrodeposition were achieved. In addition, significant nucleation overpotentials were required to achieve a higher nanoparticle surface population [84].

AuNS-modified GR electrodes with 3 distinct surface morphologies (AuNS$_I$, AuNS$_{II}$, AuNS$_{III}$) were selected for further determination of electroactive electrode surface area and heterogeneous electron transfer rate constant based on methodologies provided in Section 2.7.2. and Section 2.7.3. using a $[Fe(CN)_6]^{3-/4-}$ redox pair. Calculated values for EASA and k^0 are given in Table 1.

Table 1. Calculated EASA and heterogeneous electron transfer rate constant. Error bars are expressed as sample standard deviation (n=4).

Electrodes	**Electroactive surface area, cm^2**	**Heterogeneous electron transfer rate constant, cm·s^{-1}**
GR	0.077 ± 0.012	$1.80 \cdot 10^{-3} \pm 0.73 \cdot 10^{-3}$
GR/AuNS$_I$	0.213 ± 0.019	$4.77 \cdot 10^{-3} \pm 0.73 \cdot 10^{-3}$
GR/AuNS$_{II}$	0.116 ± 0.006	$4.26 \cdot 10^{-3} \pm 0.57 \cdot 10^{-3}$
GR/AuNS$_{III}$	0.110 ± 0.011	$4.33 \cdot 10^{-3} \pm 0.25 \cdot 10^{-3}$

The determined EASA of unmodified GR electrode (0.077 ± 0.012 cm^2) corresponds well with the geometric area of GR, which is 0.071 cm^2. All AuNS electrodeposition techniques produced surfaces with higher EASA compared to unmodified GR. AuNS$_I$-modified GR electrode exhibited the highest EASA, almost 2 times higher than electrodes modified with other AuNSs. The differences in the morphology of the structures might explain these results. For AuNS$_{I}$-modified electrode, sufficient gaps between nanostructures likely allow for less restricted diffusion of the redox probe as well as for the increase in the surface area participating in electrochemical conversion, since both the underlying GR surface and additional AuNS surface can interact with the redox probe. The AuNS$_{II}$-modified electrode, having smaller number but bigger particles, had an EASA of 0.116 cm^2. For the GR/AuNS$_{III}$ electrode, while branched nanostructures should increase the surface area, the calculated EASA of 0.110 cm^2 suggests a similar electrochemical conversion area to the AuNS$_{II}$-modified electrode. It could be that the more exposed flat graphite rod surface surrounding the branched particles offsets the gain in surface area coming from the dendritic geometry.

The heterogeneous electron transfer rate constant describes the efficiency of the electron transfer process happening at the electrode-solution interface. The variability of k^0 for $[Fe(CN)_6]^{3-/4-}$ using polished graphite electrodes is quite large, mainly due to differences in electrode quality and surface preparation, but is usually in the range of 10^{-2} – 10^{-3} cm·s^{-1} [85–92]. The k^0 evaluated in this research for unmodified GR ($1.80 \cdot 10^{-3} \pm 0.73 \cdot 10^{-3}$ cm·s^{-1}) is also in this range. The modification of GR with any AuNSs increased the electron transfer rate by a similar degree. On average, electrodes with electrodeposited AuNS exhibited a 2.5-fold increase in k^0 value compared to unmodified GR. M. Drobysh et al. reported a similar increase for screen-printed electrodes with AuNSs electrodeposited in a similar manner [93]. Directly comparing the heterogeneous electron transfer rate constant values between different research papers is challenging due to the kinetic effects of specific electrode materials and variations in the supporting electrolytes used for determining k^0 [85]. However, when the technique is used under the same conditions, the changes in estimated values can be attributed to specific changes on the electrode surface. Due to the high standard deviation among samples presented in this research, it is difficult to accurately determine which AuNS electrodeposition technique produces electrodes with the fastest electron transfer rate. However, it has been observed that the nature of the electrode material plays a more substantial role for electron transfer rate compared to the surface morphology of AuNS, since all AuNS-modified electrodes exhibit similar k^0 values.

3.1.3. The determination of BSA immobilization efficiency

The characterized GR electrodes, modified with AuNSs of different morphologies, were tested for the development of a label-free electrochemical immunosensor. The underlying immunosensor design is presented in Fig. 6. Bovine serum albumin and polyclonal antibodies against bovine serum albumin were chosen as a model antigen and antibody pair. The effects that different AuNSs morphologies have on the immunosensor performance were analyzed. The 10 mM PBS solution containing 2.5 mM $[Fe(CN)_6]^{3-/4-}$ redox pair was used as a probe.

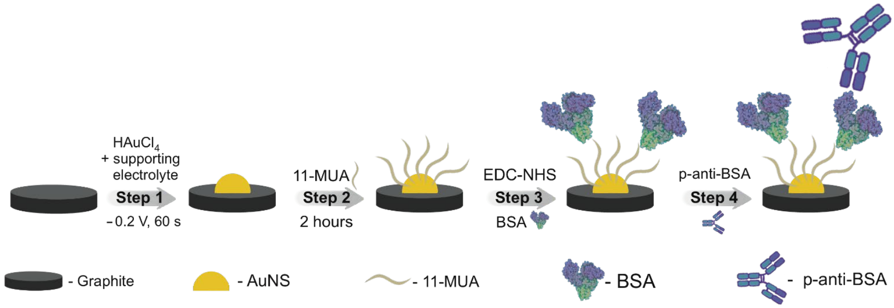

Fig. 6. Immunosensor preparation scheme. Step 1 – electrodeposition of AuNSs; Step 2 – formation of 11-MUA monolayer; Step 3 – surface activation using EDC/NHS and covalent BSA immobilization; Step 4 – the detection of p-anti-BSA antibodies. Additional surface blocking was performed using a control blood serum when working with real samples.

The covalent immobilization method, using a 11-MUA self-assembled monolayer and EDC/NHS chemistry, was chosen for the immobilization of BSA onto the AuNS-modified GR electrodes. The 11-MUA self-assembly proceeds due to thiol-gold interaction creating Au-S. After sufficient time, a dense monolayer can be formed on the gold surface. However, for the purpose of label-free electrochemical detection using redox probes, it is important to have a sufficiently conductive electrode surface. The formation of 11-MUA on the surface of AuNSs hinders the redox probe diffusion toward the gold surface, as well as nearby graphite surface. If the formation of 11-MUA is allowed to proceed to complete and uniform monolayer formation on the AuNS surface, which happens after around 18 h formation time at room temperature, the AuNS surface becomes almost completely insulated. This would lead to a very significant decrease in registered redox probe oxidation/reduction currents. An example of this effect on a planar gold electrode is presented by Drobysh et al. [94]. As such, a shorter 11-MUA formation time is required for successful label-free immunosensor development based on redox probe oxidation/reduction detection. 2 h monolayer formation time was chosen empirically, where enough functional groups are introduced to the gold surface for efficient protein immobilization, without significantly reducing the registered redox probe oxidation/reduction currents.

Covalent immobilization of BSA onto 11-MUA happens through a three-step reaction with the help of EDC/NHS resulting in amide bonds forming between the carboxyl groups of the 11-MUA and the primary amine groups of BSA [95]. The amount of BSA bound to the electrode surface was determined based on the depletion method, where BSA concentration was estimated in the solution which remains after the immobilization [96]. Bradford assay was used to determine BSA concentration in the solution using Roti®Nanoquant reagent. The starting concentration of BSA in the immobilization solution was 100 µg·mL^{-1}. The results from BSA immobilization efficiency measurements are presented in Table 2.

Table 2. Calculations to determine the amount of bound BSA on pre-modified electrodes using Bradford assay. Error bars are expressed as sample standard deviation (n=4).

Electrode	**Determined BSA concentration in the solution remaining after immobilization, µg·mL^{-1}**	**Weight of bound BSA, µg**
GR/AuNS$_I$/11-MUA/BSA	77.0 ± 1.17	5.75 ± 0.29
GR/AuNS$_{II}$/11-MUA/BSA	78.5 ± 1.05	5.37 ± 0.26
GR/AuNS$_{III}$/11-MUA/BSA	81.8 ± 0.05	4.55 ± 0.01

These results indicate that GR, modified with smaller, rounder, and more numerous nanoparticles (AuNS$_I$ and AuNS$_{II}$), facilitated more efficient BSA immobilization compared to the bigger branched gold nanostructures. Various factors may contribute to the observed differences. One of factors affecting the efficiency of BSA immobilization is the amount of 11-MUA monolayer formed on the surface of AuNSs. While the initial 11-MUA formation occurs rapidly, achieving a dense and uniform monolayer on AuNS typically necessitates a much longer SAM formation time of approximately one day [97]. However, the 11-MUA formation time of 2 hours does not result in a full coverage of AuNS surface with the 11-MUA monolayer. Therefore, the amount of 11-MUA formed on the surface is likely directly proportional to the surface area of AuNSs available at the start of formation. Another factor worth considering is steric hinderance. Since the 11-MUA monolayer is less than 2 nm thick [98] and the hydrodynamic radius of BSA is ~7 nm [99], it is reasonable to assume that the covalent immobilization of BSA on the AuNS surface may impede further protein binding nearby. Overall, it is difficult to attribute which of the factors play the most significant role, however, the results show a trend where electrodes modified with smaller but more uniformly distributed $AuNS_I$ and $AuNS_{II}$ exhibited significantly better BSA immobilization efficiencies compared to $AuNS_{III}$-modified electrode containing sparsely placed but bigger branched structures. In addition, when comparing electrodes modified with $AuNS_I$ and $AuNS_{II}$, the surface with even smaller and more numerous $AuNS_I$ promoted a slightly higher BSA immobilization efficiency.

3.1.4. Evaluation of the effects of AuNS morphology on the label-free immunosensor performance

The effects that different AuNSs morphologies have on the immunosensor performance were analyzed. For this reason, differential pulse voltammetry (DPV) measurements were performed with all BSA-modified electrodes before and then after the 30 min interaction with 5 nM of p-anti-BSA in PBS solution, pH 7.4. For DPV analysis, the 10 mM PBS solution containing 2.5 mM $[Fe(CN)_6]^{3-/4-}$ redox pair was used. The measured potential range was from −0.15 V to +0.5 V while pulse height was 25 mV, pulse width – 0.05 s, pulse period – 0.5 s, and potential step – 5 mV. All DPV measurements were baseline corrected. The change in peak anodic current, as a result of 30 min interaction between BSA and p-anti-BSA, was chosen as an analytical signal. Results are provided in Fig. 7.

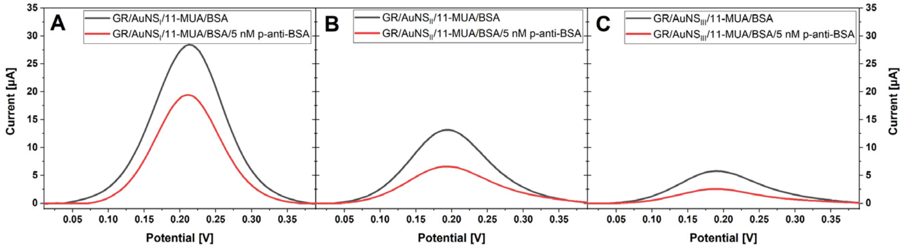

Fig. 7. Differential pulse voltammetry measurements in a PBS solution containing 2.5 mM $[Fe(CN)_6]^{3-/4-}$ before and after 30 min long interaction with 5 nM of p-anti-BSA for GR premodified with (**A**) $AuNS_I$, (**B**) $AuNS_{II}$, (**C**) $AuNS_{III}$.

The highest peak anodic current before the interaction with p-anti-BSA, at 28.4 ± 1.4 µA, was recorded for electrodes modified with AuNS$_{\mathrm{I}}$. For AuNS$_{\mathrm{II}}$, it was 12.8 ± 0.5 µA, and for AuNS$_{\mathrm{III}}$ it was 7.1 ± 1.9 µA. The primary factor influencing the peak anodic current observed before the interaction with p-anti-BSA is likely the electroactive surface area that remains available following the immobilization of BSA. AuNS$_{\mathrm{I}}$ and AuNS$_{\mathrm{II}}$ modified electrodes bound a similar amount of BSA, however, before the immobilization of BSA, the AuNS$_{\mathrm{I}}$-modified GR had a significantly higher EASA. It is reasonable to assume that after the immobilization of a similar amount of BSA, more EASA would be left exposed for AuNS$_{\mathrm{I}}$-modified GR, thus resulting in higher registered peak anodic current. However, for AuNS$_{\mathrm{III}}$-modified electrode significantly lower anodic peak current was observed than anticipated, based on the BSA immobilization efficiency and EASA measurement data. Since AuNS$_{\mathrm{III}}$-modified electrode had a similar EASA to AuNS$_{\mathrm{II}}$-modified GR and bound a lower amount of BSA, a similar or even slightly higher peak anodic current was expected to be observed. However, this was not the case implying that other factors affect the observed currents. Since covalent immobilization happens on 11-MUA monolayer which only forms on the gold surface, it could be reasoned that extra steric hinderance is introduced when BSA is immobilized on dense branched structures (AuNS$_{\mathrm{III}}$) instead of a more spread out and smaller gold nanoparticles (AuNS$_{\mathrm{I}}$ or AuNS$_{\mathrm{II}}$). This additional steric hindrance could also explain why a smaller amount of BSA was bound to on AuNS$_{\mathrm{III}}$-modified GR compared to AuNS$_{\mathrm{II}}$-modified GR even though both electrodes showed similar EASA before BSA immobilization.

The incubation of GR/AuNS/11-MUA/BSA electrodes in a solution containing 5 nM p-anti-BSA leads to the decrease of registered anodic DPV peak currents. This decrease occurs because the antibodies bind to the immobilized BSA, which reduces the EASA available for electrochemical redox probe oxidation-reduction and impedes the diffusion of the redox probe toward the electrode surface. The reduction in anodic peak current was selected as the analytical signal for the detection of p-anti-BSA. The results indicate that the electrode modified with AuNS$_{\mathrm{I}}$ exhibited the highest decrease in peak anodic current, measuring 8.9 ± 1.8 µA. The AuNS$_{\mathrm{II}}$-modified electrode showed a decrease of 6.6 ± 0.5 µA, while the AuNS$_{\mathrm{III}}$-modified electrode had a decrease of 4.1 ± 1.2 µA. The differences in the decrease of peak anodic currents can occur due to multiple reasons. To start with, the quantity of immune complexes formed on the electrode exerts some influence. In this case, a higher amount of bound BSA likely increases the chance for successful immune complex formation. However, following the interaction with p-anti-BSA, GR modified with $AuNS_I$ and $AuNS_{II}$, despite having a comparable amount of bound BSA, exhibited a notably different reduction in peak anodic current. Specifically, the $AuNS_I$-modified electrode experienced a 35% greater decrease compared to the $AuNS_{II}$-modified electrode. Two factors could explain the observed results. Firstly, the decrease in anodic current would likely be higher for $AuNS_I$-modified electrode since this surface feasibly had a higher EASA beforehand. As a result, it is likely that even if the same number of immune complexes are formed on $AuNS_I$ and $AuNS_{II}$ modified electrodes, more electroactive surface area could be blocked for $AuNS_I$ based electrode. Secondly, the availability of the BSA epitopes for the immune complex formation could differ. Since antibodies are larger than BSA, the immune complex formation between BSA and p-anti-BSA likely hinders further immune complex formation with nearby immobilized BSA molecules. Non-planar geometry and well-spaced nanostructures help to alleviate these steric hindrances. For instance, Haddada et al. discovered that, compared to a planar gold layer, a nanostructured surface increases the analytical signal by up to 56%, despite identical antibody coverage and antigen concentrations in both cases. This improvement is attributed to the enhanced accessibility of the recognition sites on the nanostructured sensor compared to the planar one. [100].

GR modified with $AuNS_I$, consisting of smaller but more numerous and nanoparticles, showed superior label-free immunosensing performance compared to other AuNS-modified electrodes. It should also be noted that the immunosensor response using $AuNS_{III}$-modified GR electrode, containing bigger but less populous branched gold structures, was significantly poorer. As such, it was decided to use GR modified with $AuNS_I$ for further label-free immunosensor development.

3.1.5. Analytical response for the detection of p-anti-BSA

GR/$AuNS_I$/11-MUA/BSA electrode was first tested for the detection of p-anti-BSA in the concentration range from 1 to 50 nM. For this reason, antibodies were dissolved in 10 mM PBS solution, pH 7.4, and the electrode was immersed in p-anti-BSA solution for 30 min. DPV measurements were performed before and after the incubation. However, it was observed that the DPV response for all tested p-anti-BSA concentrations showed a significant standard deviation between the registered signals of the same samples indicating that some non-specific binding was likely taking place. As a result, it was decided to perform an additional blocking step after the immobilization of BSA in order to reduce non-specific binding. Since the immunosensor was designed for the detection of antibodies, in order to block the free electrode surface and reduce the effects from the sample matrix, the blocking was performed using 10 times diluted human blood serum. This was performed by immersing GR/AuNS$_I$/11-MUA/BSA electrode in the diluted serum solution for 30 min. Afterwards, the electrode was washed with deionized water and DPV measurements were performed in order to establish the new baseline anodic peak current (I_{blank}). It was observed that anodic peak current was reduced by 10% as a result of the blocking procedure. This indicates that some compounds from the serum were adsorbed on the electrode surface. The additional blocking procedure significantly improved the stability of DPV response to various p-anti-BSA concentrations solving the measurement repeatability issue. Finally, the determination of p-anti-BSA concentration in diluted serum, as a model real sample, was performed using the fabricated sensor. The analytical response was chosen as peak anodic current of GR/AuNS$_I$/11-MUA/BSA electrode, registered after the blocking procedure, minus anodic peak current of the electrode after the interaction with p-anti-BSA ($I_{blank} – I_c$). The calibration curves are presented in Fig. 8.

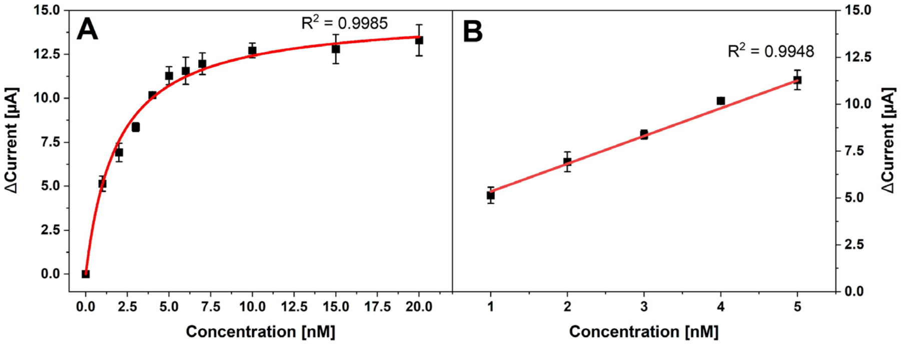

Fig. 8. Calibration plot with different concentrations of p-anti-BSA in human serum. (**A**) The wide concentration range and (**B**) the linear range of the calibration curve. Relative response was calculated based on DPV measurements performed in a PBS solution containing 2.5 mM $[Fe(CN)_6]^{3-/4-}$.

It can be seen that the increase in the concentration of p-anti-BSA leads to a decrease in the recorded peak anodic current (higher ΔCurrent in Fig. 8). As mentioned beforehand, this occurs as a result of multiple factors due to the formation of immune complex. As expected, as the concentration of p-anti-BSA increases, more antibodies bind to the BSA immobilized on the electrode surface. This results in an increasing obstruction of EASA, and a hinderance of redox probe diffusion towards the electrode, ultimately leading to a further decrease in the registered peak anodic currents. Analyzing the results in Fig. 8, only a slight increase in registered relative response was observed for p-anti-BSA concentrations above 7 nM. This is likely the result of the saturation happening at the surface of the electrode, with most of the available active centers for immune complex formation being employed. The linear calibration range was quite narrow, from 1 to 5 nM. The calculated limit of detection was 0.71 nM.

3.2. The use of MNPs-Au for the development of optical magneto-immunoassay used to detect hGH

3.2.1. The synthesis and characterization of MNPs-Au

MNPs-Au were synthesized in two steps. Firstly, co-precipitation was used to produce magnetic Fe_3O_4 nanoparticles (MNPs). Secondly, a gold shell was coated onto MNPs by reducing $[AuCl_4]^-$ onto the particles using hydroxylamine. TEM was used to analyze the produced structures. The images are provided in Fig. 9.

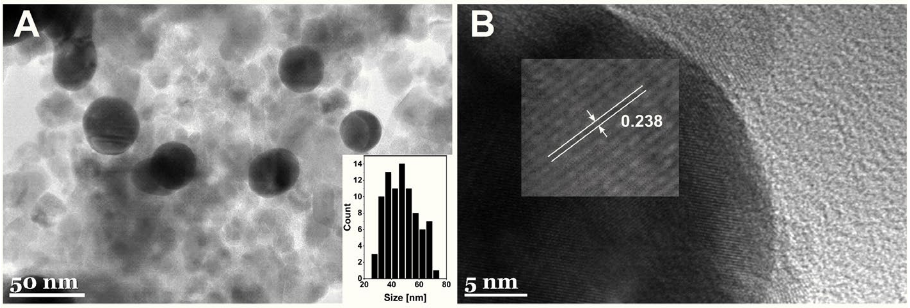

Fig. 9. TEM images of synthesized MNPs-Au under different magnification. Insets: (**A**) the particle size distribution histogram and (**B**) HRTEM image demonstrating the Au lattice spacing.

Both spherical coated and non-coated MNPs were observed in TEM images. MNPs-Au appear darker in the images due to the higher electron density for gold in comparison to iron oxide [29]. These results are similar to previously published work by Tamer et al. [101]. The average diameter of synthesized MNPs-Au was equal to 47.6 ± 11.3 nm. The analysis of interplanar spacing in TEM images for MNPs-Au, revealed a spacing of 2.38 Å, which is attributed to fcc-structured gold (111) plane.

In addition to TEM analysis, crystallographic XRD and optical UV-Vis spectroscopy measurements were performed to confirm successful MNPs-Au synthesis. The results are shown in Fig. 10.

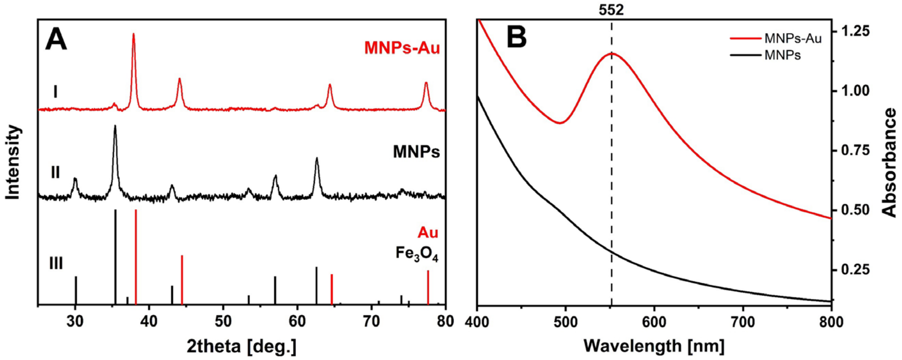

Fig. 10. (**A**) XRD patterns of (**I**) MNPs-Au, (**II**) MNPs, and (**III**) standards of Au (ICDD 00-004-0784) and Fe_3O_4 (ICDD 00-019-0629); (**B**) absorbance spectra of magnetic nanoparticles (MNPs) before and after coating with the gold layer.

Crystallographic XRD analysis revealed that synthesized MNPs were made from magnetite, Fe_3O_4, with all the diffraction peaks matching well with the standard (ICDD 00-019-0629). In the case of MNPs-Au, additional diffraction peaks, observed at 38.12°, 44.14°, 64.4°, and 77.38°, were assigned respectively to (111), (200), (220), and (311) reflections of the face-centered cubic structure of metallic gold. In the XRD pattern of MNPs-Au, certain Fe_3O_4 peaks are also visible. The low intensity of these peaks and the lack of other magnetite peaks can be attributed to the heavy atom effect of Au [102].

The analysis of absorbance spectra of MNPs-Au shows a surface plasmon band with the maximum at 552 nm characteristic of local surface plasmon resonance (LSPR) of spherical gold nanoparticles [103]. In comparison, as expected no absorbance peak is observed in the spectra of MNPs [102]. The presence of characteristic LSPR band corroborates successful synthesis of MNPs-Au.

3.2.2. The optimization of magneto-immunoassay procedure

The procedure for optical hGH detection involves multiple steps (Fig. 11). Firstly, an 11-MUA monolayer is allowed to form onto the synthesized MNPs-Au (Step 1). Next, capture m-anti-hGH antibodies are covalently immobilized by employing EDC/NHS chemistry. After immobilization, the modified particles are placed in 1% BSA solution overnight to block the unreacted activated esters and the free gold surface in order to reduce non-specific interactions (Step 2). The capture of hGH out of the sample is performed using a magnet. hGH is bound by m-anti-BSA due to the immune complex formation (Step 3). p-anti-hGH-B detection antibodies, labeled with biotin, are introduced and allowed to form the immune complex with hGH captured by m-anti-hGH (Step 4). Streptavidin labeled horseradish peroxidase (S-HRP) is introduced and allowed to bind to p-anti-hGH-B due to the streptavidin-biotin affinity interaction (Step 5). The magnetic modified particles are concentrated. The substrate to horseradish peroxidase is added and the colored product of the enzymatic reaction is measured using a microplate spectrophotometer. Specifically, HRP active center is first oxidized by H_2O_2 and then reduced by 3,3',5,5'-tetramethylbenzidine (TMB). After the enzymatic reaction is allowed to proceed for 10 min, the STOP solution containing H_2SO_4 is added. The change in pH turns the oxidized blue-green TMB into a stable yellow compound, which is determined at 450 nm (Step 6).

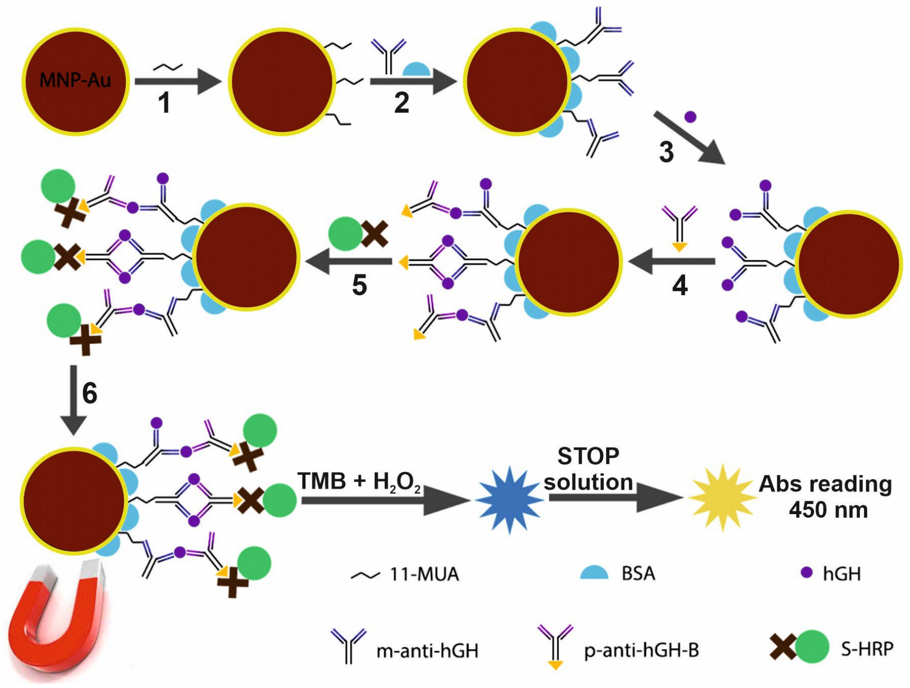

Fig. 11. A schematic illustrating the design of the sandwich-type magneto-immunoassay for the detection of human growth hormone (hGH). The magnet was used in all steps to collect and wash modified MNPs-Au.

The employment of magnetic structures in the design of immunoassay has multiple advantages. It is much easier to manipulate such structures during the immunoassay procedure. Instead of using centrifugation in order to exchange the solution in which the particles reside, a magnet can be used to collect the magnetic nanoparticles, which allows for an easy washing or solution exchange. This reduces the loss of particles coming from centrifugation as well as significantly speeds up the immunoassay procedure. In addition, magnetic collection, compared to centrifugation, is also less likely to cause particle aggregation or damage to proteins. Finally, when using MNPs-Au, the magnet can be used to easily reduce the volume of the solution the particles reside in, thus concentrating the analyte.

Since the presence of m-anti-hGH on the surface of the MNPs-Au is required in order to capture and concentrate the hGH present in the sample, the surface concentration of these monoclonal antibodies plays a significant role in the final response of the optical immunoassay. As such, the optimization of m-anti-hGH concentration, used for immobilization onto MNPs-Au, was undertaken (Fig. 12A).

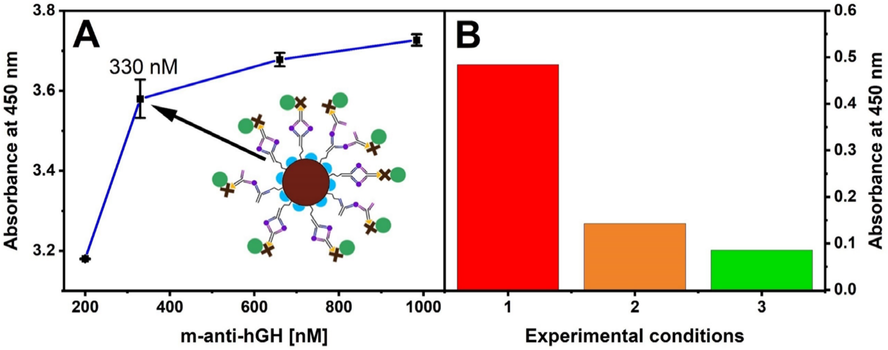

Fig. 12. (**A**) Dependence of the immunoassay response at 450 nm on the concentration of m-anti-hGH used for covalent immobilization onto MNPs-Au. (**B**) The reduction in the non-specific interactions during the magneto-immunoassay. The absorbance of the blank samples: 1 – using only 10 mM·L^{-1} PBS; 2 – after blocking test tubes walls with 1% BSA in 10 mM·L^{-1} PBS; 3 – after blocking of test tubes walls with 1% BSA in 10 mM·L^{-1} PBS and using dilution and washing solutions consisting of 0.1% BSA in 10 mM·L^{-1} PBS.

For this optimization a constant 400 nM hGH and 990 nM p-anti-hGH-B concentrations were used, while m-anti-hGH immobilization concentration varied between 200, 330, 660, and 980 mM. A significant increase in the optical response was observed when the concentration was increased from 200 to 330 nM, however, only a slight improvement was observed for higher immobilization concentrations. Since usually better response can be achieved with analytical systems containing lower antibody surface concentrations [104], and due to the desire to reduce the immunoassay costs, the chosen concentration for m-anti-hGH immobilization was 330 nM.

During the development of the magneto-immunoassay a significant optical response was measured for blank samples containing no hGH (Fig. 12B-1). In theory, in the absence of hGH, no optical response should be observed for this immunoassay, however, registered results indicate that significant non-specific binding is happening on MNPs-Au/m-anti-hGH particles or container walls, with either p-anti-hGH-B or S-HRP adsorbing on the surfaces. In order to reduce the response for the blank sample and to decrease non-specific interactions, some blocking procedures were tested. Since the whole immunoassay procedure is performed in a single container it was decided to block the inside walls of the test tube to reduce adsorption of p-anti-hGH-B or S-HRP. To accomplish this, a 1% BSA solution in 10 mM PBS buffer, pH 7.4, was added to the test tube before the start of the immunoassay and held for 1 h. It should be noted that the employed test tubes were "low-binding" to begin with, and were specifically pretreated by the manufacturer to reduce the non-specific binding of proteins. Even then, the additional treatment of test tube walls with BSA allowed to reduce the non-specific binding further as indicated by ~3 times lower optical response for blank samples. Finally, it was decided to include BSA into the washing procedures, which are performed 3 times between each immunoassay step from steps 3 to 5. A 0.1% BSA solution in 10 mM PBS, pH 7.4, was used for these washing procedures. This, in combination with the treatment of test tube inside surfaces, allowed to further reduce the absorbance of the blank sample by ~5.7 times, compared to no treatment, making the immunoassay more reliable. The final background signal was subtracted from the responses registered with different hGH concentrations.

3.2.3. Analytical response for the detection of hGH

The developed sandwich-type optical magneto-immunoassay was successfully used to detect hGH in the concentration range from 0.1 to 50 nM. The lower concentration of 100 nM for p-anti-hGH-B was used for these measurements. The dependence of absorbance at 450 nm on different concentrations of hGH under optimized conditions is presented in Fig. 13.

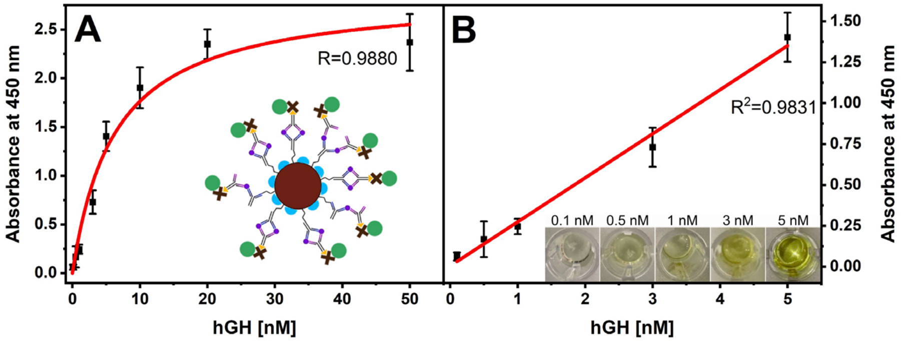

Fig. 13. (**A**) Dependence of absorbance at 450 nm on the concentration of hGH. (**B**) The linear range of the developed sandwich-type magneto-immunoassay for hGH detection using MNPs-Au. Conditions: 0.2 mg·mL^{-1} of MNPs-Au modified with 330 nM concentration of m-anti-hGH; 100 nM concentration of p-anti-hGH-B; 0.1 – 5.0 nM concentrations of hGH.

The linear range for hGH quantification was determined to be from 0.1 to 5 nM. The limit of detection, defined as an analytical signal greater than the background plus 3 σ, was calculated to be 0.082 nM. These analytical parameters show that this magneto-immunoassay can be used for the quantification of hGH in the normal concentration range found in blood. In addition, compared to traditional sandwich-type ELISA, this magneto-immunoassay has a wider linear range allowing to quantify hGH at higher concentrations, facilitating the detection of excess hormone. In order to evaluate the magneto-immunoassay for the detection of hGH in real samples the analysis of a human serum spiked with 3.5 nM of hGH was performed. The recovery of hGH was found to be 95%.

3.3. The evaluation of AuNP formation reaction for the optical detection of reducing sugars

3.3.1. The principle of optical reducing sugar detection method based on AuNP formation

Reducing sugar detection is based on the oxidation-reduction reaction between the reducing sugar and the complex Au(III) ions. During this reaction, Au(III) ions are reduced to Au(0) by the reducing sugar resulting in the formation of AuNPs, which are stabilized due to the presence of CTAB surfactant in the reaction mixture. In neutral pH this oxidation reaction is slow, however, both basic and acidic conditions can be used to increase the reaction rate due to faster mutarotation. In this work, the reaction was performed in

0.1 M NaOH since the mutarotation proceeds faster under basic pH than acidic. The principal reaction scheme is presented in Fig. 14.

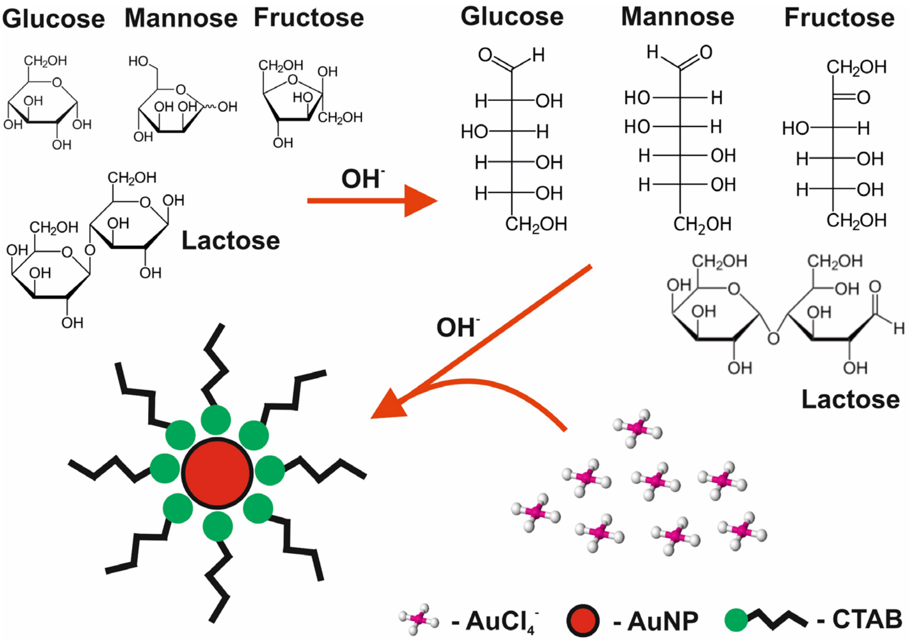

Fig. 14. The principle of gold nanoparticle based colorimetric assay for the determination of reducing sugars.

The mechanism of this reaction is not fully understood. Research by some authors implies that the reaction takes place through the open-chain conformation, where ketoses such as fructose first undergo a complete Lobry de Bruyn-Alberda van Eckenstein transformation into glucose or mannose and participate in the reaction as either of those sugars [38,39]. However, other authors present that oxidation of reducing sugars with metal ions in a basic medium usually proceeds through a reducing sugar enediol intermediate [43–45], which would not require ketoses to first fully convert to aldoses. It also should be noted that since this reaction is performed at basic pH, due to hydrolysis of $[AuCl_4]^-$, AuNP formation likely occurs through the intermediates of $[AuCl(OH)_3]^-$ or $[Au(OH)_4]^-$. Because of this, at high pH, the nucleation rate for AuNP formation is slower compared to acidic conditions [105], however, the mutarotation is quicker [41], which could lead to a faster overall AuNP formation rate.

The produced AuNPs, due to the LSPR effect, absorb visible light. This allows us to evaluate the AuNP formation using a spectrophotometer. The oxidation-reduction reaction rate varies depending on the concentration of reducing sugar, leading to the formation of different amounts of AuNPs over the same duration. This kinetic dependence on reducing sugar concentration in conjunction with spectrophotometric measurements can be used as a basis for development of an optical system used to determine reducing sugar concentrations. To begin with, spectrophotometric monitoring of the reaction mixture over time was performed. The absorbance spectra of the reaction mixture containing 1 mM glucose, 3.7 mM CTAB, 1 mM $HAuCl_4$ and 0.1 M NaOH at various times from the start of the reaction is presented in Fig. 15.

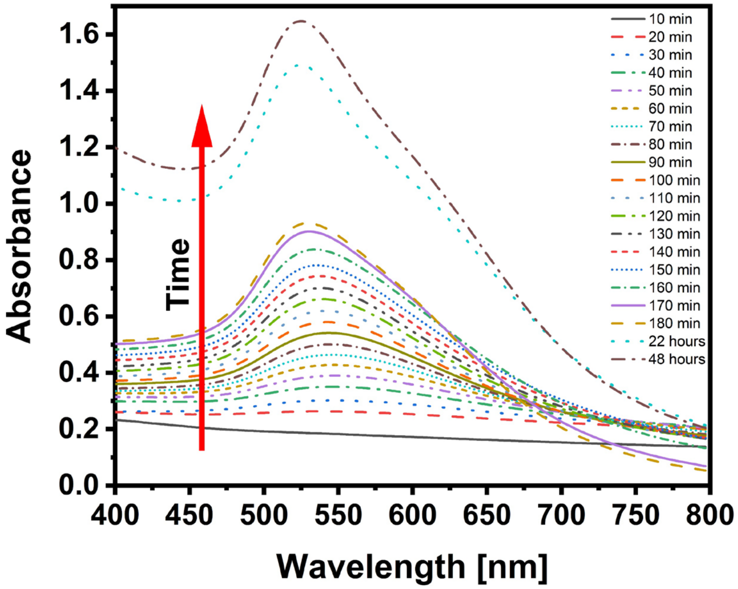

Fig. 15. Absorbance spectra of the reaction mixture with 1 mM glucose dependence on the reaction time. Reaction mixture consists of 3.7 mM CTAB, 1 mM $HAuCl_4$ and 0.1 M NaOH.

Based on the results it was observed that LSPR peak of formed AuNPs appeared ~550 nm at the start of the reaction, however, as the reaction proceeded further, the LSPR peak slowly shifted to shorter wavelengths settling at ~525 nm. The observed blue shift might be attributed to the attachment of gold atoms as co-ions in the electronic double layer of the seed particles at the initial stage of AuNP growth [106]. Furthermore, it can be seen that the reaction with 1 mM of glucose was slow, with the formation of AuNPs still ongoing even 24 h after the start of the reaction, although significantly slower, only stopping at around 48 h mark. However, more than half of the final peak absorbance value was achieved in the first 3 h of the reaction.

3.3.2. Evaluation of AuNP formation using different reducing sugars

When analyzing the absorbance spectra of the reaction mixture containing different concentrations of one reducing sugar, it was observed that the increase in reducing sugar concentration led to the faster AuNP formation rate. This was represented as a higher peak absorbance value measured after a fixed amount of time. This kinetic dependence on reducing sugar concentration was explored to indirectly determine reducing sugar concentration. After reviewing the absorbance spectra at different reducing sugar concentrations, it was observed that absorbance at 525 nm had the best linearity on reducing sugar concentration in the mixture. Since the reducing sugar detection is based on the kinetic AuNP formation reaction, the calibration curves for the specific sugar can be constructed after a different amount of time has passed since the start of the reaction. The detection of reducing sugars was tested out with fructose, glucose, lactose, and mannose 20, 40, and 60 min after the start of the reaction, with the reaction mixture consisting of 3.7 mM CTAB, 1 mM $HAuCl_4$, and 0.1 M NaOH. The results are presented in Fig. 16.

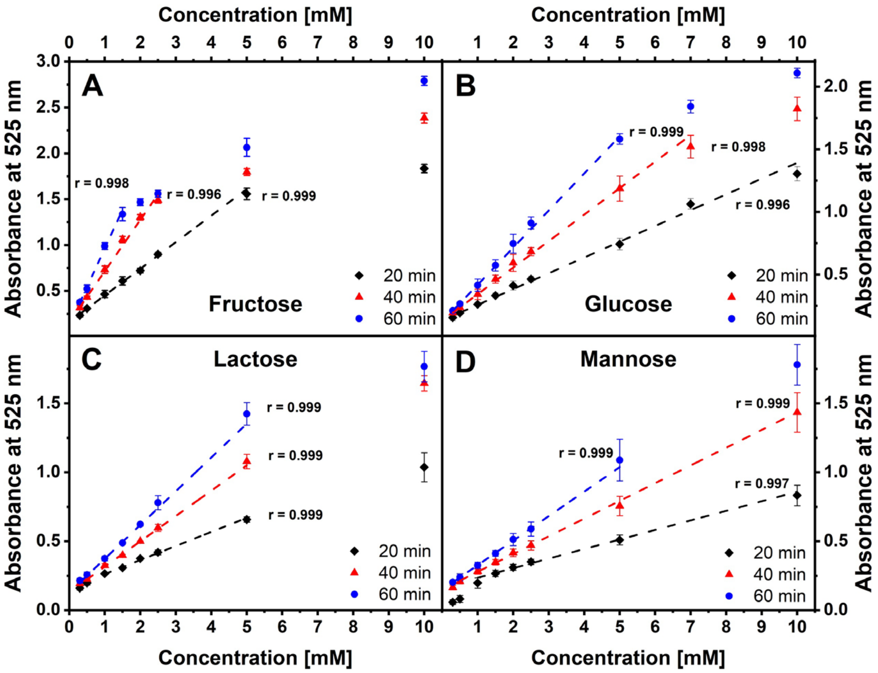

Fig. 16. The absorbance at 525 nm dependence on (**A**) fructose, (**B**) glucose, (**C**) lactose, and (**D**) mannose concentration in the reaction mixture measured 20, 40, and 60 min after the start of the reaction.

Some trends can be observed from the results presented in the figure above. Firstly, higher analytical sensitivity is achieved for all reducing sugars when the absorbance is measured later from the start of the reaction, allowing to detect lower reducing sugar concentration. This is likely because, with smaller concentrations, longer durations are required for the formation AuNPs to begin. In addition, the linear range of the calibration curve also changes with time. However, in this case, the absorbance values measured for higher reducing sugar concentrations deviate from the linear relationship. For example, when measured after 20 min, the absorbance of the mixture containing 10 mM of glucose is still in the linear range of the calibration curve, however, if measured after 40 min, the absorbance value is no longer in the linear range. This means that as the reaction is allowed to proceed for a longer duration, lower concentrations of the reducing sugar can be detected, however, higher concentrations might no longer be in the linear calibration range. This effect can be in theory adapted to conveniently detect the reducing sugar concentration in the desired range by changing the reaction duration. If the detection of higher reducing sugar concentration is required, the analysis time can be shortened, while for lower reducing sugar concentrations the reaction can be allowed to proceed longer.

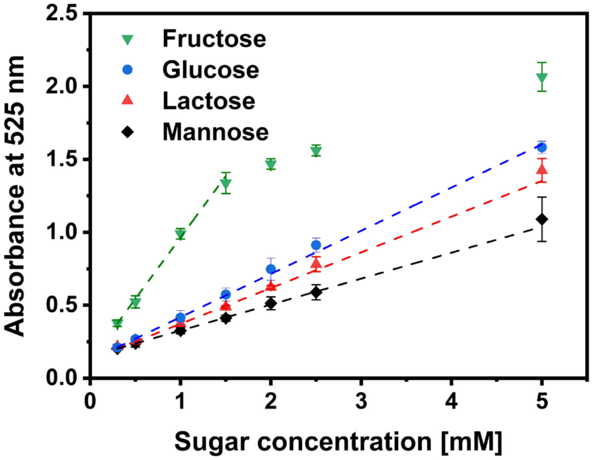

Fig. 17. The absorbance at 525 nm dependence on the concentration of different reducing sugars measured after 60 min from the start of the reaction.

A comparison between the calibration curves for different reducing sugars, measured 60 min from the start of the reaction, is provided in Fig. 17. It can be seen that the AuNP formation rate and in turn the absorbance value at 525 nm also depended on the nature of the reducing sugar participating in the reaction. It was discovered that the reaction with fructose had the quickest AuNP formation rate, followed by glucose, lactose, and mannose. Depending on the reaction mechanism, some explanations could be given to describe these results.

Research by some authors implies that reducing sugars participate in the oxidation-reduction reaction with complex Au(III) ions directly through the open-chain conformation [38,39]. For example, glucose in open-chain form could be directly oxidized to gluconic acid, by the Au(III) ions, while mannose to mannonic acid. However, a ketose like fructose would first need to undergo Lobry de Bruyn-Alberda van Eckenstein transformations to glucose or mannose and could only then participate in the reaction as either of these reducing sugars. Under such a reaction mechanism, the rate of AuNP formation could depend on these sugars' reduction potential. It is also possible that different mutarotation rates for the specific reducing sugars play a role in this process. Since only a very small percentage of reducing sugars in a solution exist in an open-chain conformation, upon the start of the reaction the concentration of this form decreases and is replenished only due to the mutarotation of the reducing sugar from other conformations into the open-chain. It has indeed been published that mutarotation rates differ depending on the nature of the reducing sugar [107]. It was highlighted that ketoses have noticeably higher rates of mutarotation in comparison to aldoses. Although, when comparing mutarotation rates just for aldoses, including disaccharides, only a slight variation in mutarotation rate is observed. This might explain the observed results in Fig. 17, where the reaction with fructose displayed a significantly higher rate of AuNP formation in comparison to aldoses, which showed less distinct reaction rates. However, most of the published mutarotation studies are performed at neutral pH. Higher pH can catalyze the process significantly increasing the rate of mutarotation. Unfortunately, no research was found where mutarotation rates at higher pH are compared, thus it is unclear if mutarotation rates differ between sugars at those conditions. Furthermore, another factor that should affect the AuNP formation rate is the proportion of open-chain conformation present in the solution. For example, at ~25°C fructose is present in open-chain conformation at a percentage of 0.8% in comparison to other conformations, while mannose, and glucose are only found at 0.005%, and 0.002%, respectively [41,108]. It is likely that higher open-chain concentrations would lead to faster AuNP formation and growth rates. However, results in Fig. 17 show quicker AuNP formation rate with glucose than with mannose even though glucose open-chain concentration is slightly lower than mannose, indicating that other factors, apart from open-chain concentration, affect the reaction.

On the other hand, other authors report that the oxidation of reducing sugars using metal ions in a base medium proceeds through a common reducing sugar enediol intermediate instead of directly through the open-chain conformation [43–45]. In this case, reducing sugars such as glucose, fructose, and mannose would participate in the oxidation-reduction reaction by first being transformed into a common cis-enediol intermediate [42]. The authors have suggested that sugar enolization process is the rate limiting step for oxidation-reduction reactions with various metal ions. Under such a reaction mechanism, the reduction potential of different sugars is of no concern, and instead the enolization rate likely governs the AuNPs formation process. It has been reported that the isomerization rate, indicative of the enolization rate, is fastest for fructose, followed by glucose, and mannose [109]. The same trend is observed for the AuNP formation rates with those sugars, as presented in Fig. 17.

3.3.3. Evaluation of AuNP formation using reducing sugar mixtures

The AuNP formation reaction with reducing sugar mixtures was also performed and analyzed. The results for a 1 mM glucose-fructose 1:1 mixture are provided in Fig. 18.

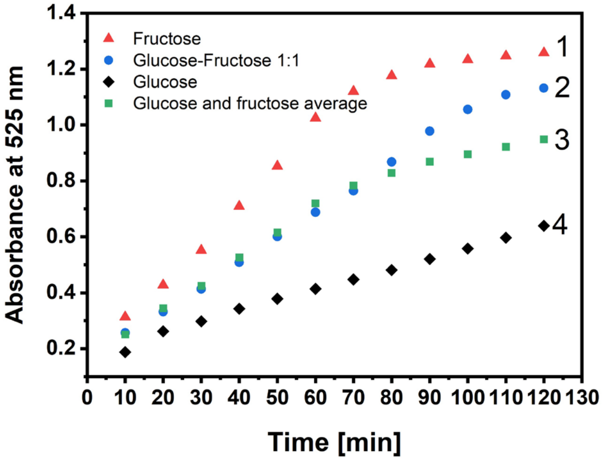

Fig. 18. The dependence of absorbance at 525 nm on the reaction duration in the solution containing 1 mM of fructose (**1**), 1 mM of glucose (**4**), and an overall 1 mM mixture of glucose and fructose at the ratio of 1:1 (**2**). The mathematical average (**3**) was calculated using the absorbance values for solutions containing 1 mM of fructose (**1**) and 1 mM of glucose (**4**).

As can be seen in the figure above, three different samples were tested comprising of 1 mM of fructose (**1**), 1 mM of glucose (**4**), and a mixture containing 1 mM overall sugar content with fructose and glucose at 1:1 ratio (**2**). The monitoring of absorbance at 525 nm was performed over time for these samples. The analysis of the results showed that for the AuNP formation between 10 and 70 min, the absorbance for the sample containing a 1:1 mixture of fructose and fructose was around the middle between the absorbance values registered for samples containing only one of these sugars. In fact, when the average absorbance values, derived from samples containing only one sugar, are plotted (**3**), it becomes evident that these averages align very closely with the actual absorbance values recorded for the mixture (**2**).

The observed results could be better explained if the reaction mechanism relies on a common enediol intermediate. In this case, both glucose and fructose would need to be first converted to the same cis enediol intermediate. The introduction of both sugars in the reaction mixture would establish a new equilibrium for the enolization process, altering the overall AuNP formation rate. It is conceivable that the effects of different sugars on the overall mixture enolization process are stoichiometric.

If that were the case, this trend could be explored for the analysis of reducing sugar mixtures. Typically, when quantifying reducing sugar mixtures using any of the oxidation-reduction detection methods, calibration curves must be individualized for specific samples because of the non-stoichiometric nature of these reactions. However, in the case of AuNP formation reaction, it might be possible to avoid this problem and mathematically create calibration curves for the desired sugar ratios. For example, if a sample contains two reducing sugars, such as glucose and fructose, at the ratio of 3:1, the calibration curve for such a sample could be obtained by combining the separate calibration curves of glucose and fructose together and adjusting for the required sugar ratio mathematically. However, a more comprehensive analysis is required to prove this hypothesis.

3.3.4. The evaluation of optical reducing sugar quantification method using real samples

The proposed optical reducing sugar quantification method was tested for the determination of various reducing sugars in real samples. The method was used to detect lactose in milk, fructose and glucose detection in Coca-Cola beverage, and for glucose detection in saliva.

For the detection of lactose in milk, due to the opaque nature of the sample, an additional procedure, described in Section 2.4., was performed in order to precipitate milk proteins and make the sample transparent. The calibration curves for lactose, shown in Fig. 16C, were used for the determination of lactose concentration. The detected average lactose concentration in the sample varied, measuring 0.161 ± 0.014 M after 20 min, 0.153 ± 0.011 M after 40 min, and 0.135 ± 0.010 M after 60 min, with a 99% confidence interval. The lactose concentration provided on the package was 0.13 M. Both the accuracy and precision of the measurement improved when the reaction was allowed to proceed for a longer duration.

For the detection of glucose and fructose in Coca-Cola beverage no additional sample preparation was required. The calibration curves were adjusted mathematically for a 55:45 ratio of fructose to glucose using the calibration curves in Fig. 16A and 16B. This adjustment was made to accommodate for the high-fructose corn syrup commonly used to sweeten the beverage [110]. The determined total amount of reducing sugars, using the mathematically adjusted calibration curve, was 20% lower compared to the value provided on the package. This error could be explained by the non-consistent ratio of fructose to glucose found in sweetener due to variations in the production [111]. Or it could be the effects from the sample matrix, or the presence of other reducing agents. In order to assess the latter effects, the analysis of Coca-Cola Zero sample was performed. Since no reducing sugars are present in this sample, no formation of AuNPs was expected. This was indeed the case, as no absorbance peak was detected after the reaction was allowed to proceed for 1 h. This indicates that the error for detecting the total reducing sugar content in the Coca-Cola sample likely comes from the unknown actual ratio of fructose to glucose, or some other unforeseen phenomena.

Furthermore, the analytical system was tested for the detection of glucose in a saliva sample. The saliva sample collection procedure is described in Section 2.4. The glucose concentration in the saliva varies in the range from 0.03 to 0.07 mM [112], which is slightly below the detection limit of glucose after the 60 min reaction duration. Thus, as expected no AuNPs were formed and in turn, no absorbance peak was observed in the first 60 min when measuring the reaction mixture containing the saliva sample. However, allowing for the reaction to take place for a longer period of time revealed the slow formation of an absorbance peak at ~550 nm, which is indicative of the synthesis of AuNPs. As previously mentioned, nearly half of the final analytical signal is achieved within the initial 3 h of the reaction. Therefore, it is expected that the glucose calibration curve created 3 h after the start of the reaction should allow us to determine the glucose concentration in the saliva sample precisely.

CONCLUSIONS

1. The morphology of electrodeposited AuNSs differed significantly for GR and ITO electrodes, even when identical electrodeposition conditions were used. $AuNS_I$-modified GR electrode, consisting of smaller but more numerous circular structures, provided up to 2 times higher EASA, and bound up to 26% more BSA in comparison to other AuNS-modified electrodes. In addition, GR modification with $AuNS_I$ also facilitated up to 2.1 times higher immunosensing response.
2. MNPs-Au were synthesized and employed for the development of optical magneto-immunoassay used to detect hGH. Under optimized conditions, the limit of detection was 0.082 nM, with the linear range of the calibration curve being from 0.1 to 5 nM. This is suitable for the determination of normal and excess concentrations of hGH found in blood serum.
3. AuNP formation process, as a result of an oxidation-reduction reaction with reducing sugars, was employed for the indirect quantification of fructose, glucose, lactose, and mannose concentration. Lower reducing sugar concentrations could be determined if the reaction was allowed to proceed for a longer duration. The rate of AuNP formation depended on the nature of the reducing sugar and decreased in the following order: fructose, glucose, lactose, and mannose.

REFERENCES

[1] N. Baig, I. Kammakakam, W. Falath, Nanomaterials: a review of synthesis methods, properties, recent progress, and challenges, Mater. Adv. 2 (2021) 1821–1871. https://doi.org/10.1039/D0MA00807A.

[2] M. Seyedi, S. Haratian, J.V. Khaki, Mechanochemical Synthesis of Fe2O3 Nanoparticles, Procedia Mater. Sci. 11 (2015) 309–313. https://doi.org/10.1016/j.mspro.2015.11.093.

[3] V.I. Merupo, S. Velumani, K. Ordon, N. Errien, J. Szade, A.H. Kassiba, Structural and optical characterization of ball-milled copper-doped bismuth vanadium oxide (BiVO4), CrystEngComm 17 (2015) 3366–3375. https://doi.org/10.1039/C5CE00173K.

[4] S. Zhang, Y. Tang, B. Vlahovic, A Review on Preparation and Applications of Silver-Containing Nanofibers, Nanoscale Res. Lett. 11 (2016) 80. https://doi.org/10.1186/s11671-016-1286-z.

[5] A. Solanki, H. Um, Top-Down Etching of Si Nanowires, in: S. Mokkapati, C. Jagadish (Eds.), Nanowires Energy Appl., Elsevier, 2018: pp. 71–149. https://doi.org/10.1016/bs.semsem.2018.04.001.

[6] J.H. Nam, M.J. Jang, H.Y. Jang, W. Park, X. Wang, S.M. Choi, B. Cho, Room-temperature sputtered electrocatalyst WSe2 nanomaterials for hydrogen evolution reaction, J. Energy Chem. 47 (2020) 107–111. https://doi.org/10.1016/j.jechem.2019.11.027.

[7] M. Abid, S. Sayegh, I. Iatsunskyi, E. Coy, G. Lesage, A. Ramanavicius, A. Ben Haj Amara, M. Bechelany, Design of halloysite-based nanocomposites by electrospinning for water treatment, Colloids Surfaces A Physicochem. Eng. Asp. 651 (2022) 129696. https://doi.org/10.1016/j.colsurfa.2022.129696.

[8] L. Sun, G. Yuan, L. Gao, J. Yang, M. Chhowalla, M.H. Gharahcheshmeh, K.K. Gleason, Y.S. Choi, B.H. Hong, Z. Liu, Chemical vapour deposition, Nat. Rev. Methods Prim. 1 (2021) 5. https://doi.org/10.1038/s43586-020-00005-y.

[9] G. Gasparotto, J.P.C. Costa, P.I. Costa, M.A. Zaghete, T. Mazon, Electrochemical immunosensor based on ZnO nanorods-Au nanoparticles nanohybrids for ovarian cancer antigen CA-125 detection, Mater. Sci. Eng. C 76 (2017) 1240–1247. https://doi.org/10.1016/j.msec.2017.02.031.

[10] I. Bogdanoviciene, A. Beganskiene, K. Tõnsuaadu, J. Glaser, H.-J. Meyer, A. Kareiva, Calcium hydroxyapatite, Ca10(PO4)6(OH)2 ceramics prepared by aqueous sol–gel processing, Mater. Res. Bull. 41 (2006) 1754–1762. https://doi.org/10.1016/j.materresbull.2006.02.016.

[11] Y. Gao, L. Torrente-Murciano, Mechanistic insights of the reduction of gold salts in the Turkevich protocol, Nanoscale 12 (2020) 2740–2751. https://doi.org/10.1039/C9NR08877F.

[12] B. Brasiunas, A. Popov, A. Ramanavicius, A. Ramanaviciene, Gold nanoparticle based colorimetric sensing strategy for the determination

of reducing sugars, Food Chem. 351 (2021) 129238. https://doi.org/10.1016/j.foodchem.2021.129238.

[13] B. Brasiunas, A. Popov, G. Kraujelyte, A. Ramanaviciene, The effect of gold nanostructure morphology on label-free electrochemical immunosensor design, Bioelectrochemistry 156 (2024) 108638. https://doi.org/10.1016/j.bioelechem.2023.108638.

[14] A. Tricoli, N. Nasiri, H. Chen, A.S. Wallerand, M. Righettoni, Ultra-rapid synthesis of highly porous and robust hierarchical ZnO films for dye sensitized solar cells, Sol. Energy 136 (2016) 553–559. https://doi.org/10.1016/j.solener.2016.07.024.

[15] M. Guilger-Casagrande, R. de Lima, Synthesis of Silver Nanoparticles Mediated by Fungi: A Review, Front. Bioeng. Biotechnol. 7 (2019) 287. https://doi.org/10.3389/fbioe.2019.00287.

[16] U.S. Mohanty, Electrodeposition: a versatile and inexpensive tool for the synthesis of nanoparticles, nanorods, nanowires, and nanoclusters of metals, J. Appl. Electrochem. 41 (2011) 257–270. https://doi.org/10.1007/s10800-010-0234-3.

[17] N.D. Zakaria, M.H. Omar, N.N. Ahmad Kamal, K. Abdul Razak, T. Sönmez, V. Balakrishnan, H.H. Hamzah, Effect of Supporting Background Electrolytes on the Nanostructure Morphologies and Electrochemical Behaviors of Electrodeposited Gold Nanoparticles on Glassy Carbon Electrode Surfaces, ACS Omega 6 (2021) 24419–24431. https://doi.org/10.1021/acsomega.1c02670.

[18] M.D. Đurović, R. Puchta, Ž.D. Bugarčić, R. van Eldik, Studies on the reactions of [AuCl4]− with different nucleophiles in aqueous solution, Dalt. Trans. 43 (2014) 8620–8632. https://doi.org/10.1039/C4DT00247D.

[19] M. Tran, C. Mundt, T. Lan, S. Padalkar, Electrodeposition of Gold Nanostructures Having Controlled Morphology, J. Nanosci. Nanotechnol. 18 (2018) 3492–3498. https://doi.org/10.1166/jnn.2018.14633.

[20] K. Terao, C. Kakita, N. Nagase, N. Miyanishi, T. Suzuki, H. Takao, F. Shimokawa, F. Oohira, Evaluation of Electrodeposited Gold Nanostructures for Applications in QCM Sensing, Anal. Sci. 28 (2012) 291–294. https://doi.org/10.2116/analsci.28.291.

[21] C. Zhu, Q. Zhao, D. Huo, X. Hu, X. Wang, Electrodeposition of rough gold nanoarrays for surface-enhanced Raman scattering detection, Mater. Chem. Phys. 263 (2021) 124388. https://doi.org/10.1016/j.matchemphys.2021.124388.

[22] A.K. Pearson, P. Kao, A.P. O’Mullane, A.I. Bhatt, Investigating the effect of ionic strength on the suppression of dendrite formation during metal electrodeposition, Phys. Chem. Chem. Phys. 19 (2017) 14745–14760. https://doi.org/10.1039/C7CP00839B.

[23] R. Ghosh Chaudhuri, S. Paria, Core/Shell Nanoparticles: Classes, Properties, Synthesis Mechanisms, Characterization, and

Applications, Chem. Rev. 112 (2012) 2373–2433. https://doi.org/10.1021/cr100449n.

[24] W. Lee, M.G. Kim, J. Choi, J.-I. Park, S.J. Ko, S.J. Oh, J. Cheon, Redox−Transmetalation Process as a Generalized Synthetic Strategy for Core−Shell Magnetic Nanoparticles, J. Am. Chem. Soc. 127 (2005) 16090–16097. https://doi.org/10.1021/jp052084.

[25] T. Seto, H. Akinaga, F. Takano, K. Koga, T. Orii, M. Hirasawa, Magnetic Properties of Monodispersed Ni/NiO Core−Shell Nanoparticles, J. Phys. Chem. B 109 (2005) 13403–13405. https://doi.org/10.1021/jp052084+.

[26] N. Ajinkya, X. Yu, P. Kaithal, H. Luo, P. Somani, S. Ramakrishna, Magnetic Iron Oxide Nanoparticle (IONP) Synthesis to Applications: Present and Future, Materials (Basel). 13 (2020) 4644. https://doi.org/10.3390/ma13204644.

[27] W. Wu, Q. He, C. Jiang, Magnetic Iron Oxide Nanoparticles: Synthesis and Surface Functionalization Strategies, Nanoscale Res. Lett. 3 (2008) 397. https://doi.org/10.1007/s11671-008-9174-9.

[28] A.K. Gupta, M. Gupta, Synthesis and surface engineering of iron oxide nanoparticles for biomedical applications, Biomaterials 26 (2005) 3995–4021. https://doi.org/10.1016/j.biomaterials.2004.10.012.

[29] U. Tamer, Y. Gündoğdu, İ.H. Boyacı, K. Pekmez, Synthesis of magnetic core–shell Fe3O4–Au nanoparticle for biomolecule immobilization and detection, J. Nanoparticle Res. 12 (2010) 1187–1196. https://doi.org/10.1007/s11051-009-9749-0.

[30] E.A. Kwizera, E. Chaffin, Y. Wang, X. Huang, Synthesis and properties of magnetic-optical core–shell nanoparticles, RSC Adv. 7 (2017) 17137–17153. https://doi.org/10.1039/C7RA01224A.

[31] T.T. Hien Pham, C. Cao, S.J. Sim, Application of citrate-stabilized gold-coated ferric oxide composite nanoparticles for biological separations, J. Magn. Magn. Mater. 320 (2008) 2049–2055. https://doi.org/10.1016/j.jmmm.2008.03.015.

[32] C. Yang, G. Wang, Z. Lu, J. Sun, J. Zhuang, W. Yang, Effect of ultrasonic treatment on dispersibility of Fe3O4 nanoparticles and synthesis of multi-core Fe3O4/SiO2 core/shell nanoparticles, J. Mater. Chem. 15 (2005) 4252. https://doi.org/10.1039/b505018a.

[33] J. Liu, M.-J. Chang, B. Gao, Z.-G. Xu, H.-L. Zhang, Sonication-assisted synthesis of multi-functional gold nanorod/silica core–shell nanostructures, J. Alloys Compd. 551 (2013) 405–409. https://doi.org/10.1016/j.jallcom.2012.11.042.

[34] K.R. Brown, D.G. Walter, M.J. Natan, Seeding of Colloidal Au Nanoparticle Solutions. 2. Improved Control of Particle Size and Shape, Chem. Mater. 12 (2000) 306–313. https://doi.org/10.1021/cm980065p.

[35] K.R. Brown, M.J. Natan, Hydroxylamine Seeding of Colloidal Au Nanoparticles in Solution and on Surfaces, Langmuir 14 (1998) 726–

728. https://doi.org/10.1021/la970982u.

[36] J.D.S. Newman, G.J. Blanchard, Formation of Gold Nanoparticles Using Amine Reducing Agents, Langmuir 22 (2006) 5882–5887. https://doi.org/10.1021/la060045z.

[37] C. Daruich De Souza, B. Ribeiro Nogueira, M.E.C.M. Rostelato, Review of the methodologies used in the synthesis gold nanoparticles by chemical reduction, J. Alloys Compd. 798 (2019) 714–740. https://doi.org/10.1016/j.jallcom.2019.05.153.

[38] M. Scampicchio, A. Arecchi, S. Mannino, Optical nanoprobes based on gold nanoparticles for sugar sensing, Nanotechnology 20 (2009) 135501. https://doi.org/10.1088/0957-4484/20/13/135501.

[39] K. Pacławski, B. Streszewski, W. Jaworski, M. Luty-Błocho, K. Fitzner, Gold nanoparticles formation via gold(III) chloride complex ions reduction with glucose in the batch and in the flow microreactor systems, Colloids Surfaces A Physicochem. Eng. Asp. 413 (2012) 208–215. https://doi.org/10.1016/j.colsurfa.2012.02.050.

[40] J.C. Speck, The Lobry De Bruyn-Alberda Van Ekenstein Transformation, in: M.L. Wolfrom (Ed.), Academic Press, 1958: pp. 63–103. https://doi.org/10.1016/S0096-5332(08)60352-5.

[41] J.F. Robyt, Essentials of Carbohydrate Chemistry, 1st ed., Springer-Verlag New York, 1998. https://doi.org/10.1007/978-1-4612-1622-3.

[42] S.J. Angyal, The Lobry de Bruyn-Alberda van Ekenstein Transformation and Related Reactions, in: A.E. Stütz (Ed.), Springer Berlin Heidelberg, Berlin, Heidelberg, 2001: pp. 1–14. https://doi.org/10.1007/3-540-44422-X_1.

[43] S.V. Singh, O.C. Saxena, M.P. Singh, Mechanism of copper(II) oxidation of reducing sugars. I. Kinetics and mechanism of oxidation of D-xylose, L-arabinose, D-glucose, D-fructose, D-mannose, D-galactose, L-sorbose, lactose, maltose, cellobiose, and melibiose by copper(II) in alkaline medium, J. Am. Chem. Soc. 92 (1970) 537–541. https://doi.org/10.1021/ja00706a020.

[44] H.S. Singh, A. Gupta, A.K. Singh, B. Singh, Kinetics and mechanism of the oxidation of reducing sugars by osmium tetroxide in alkaline medium, Transit. Met. Chem. 23 (1998) 277–281. https://doi.org/10.1023/A:1015756732447.

[45] E.O. Odebunmi, O.A. Oyetunji, H. Marufu, The kinetics and mechanism of oxidation of D-glucose, and D-sorbitol by KMnO4 and hexachloroiridate (IV). Nig, J. Sci 33 (1999) 133–143.

[46] M.B. Ranke, J.M. Wit, Growth hormone — past, present and future, Nat. Rev. Endocrinol. 14 (2018) 285–300. https://doi.org/10.1038/nrendo.2018.22.

[47] G.P. Baumann, Growth hormone isoforms, Growth Horm. IGF Res. 19 (2009) 333–340. https://doi.org/10.1016/j.ghir.2009.04.011.

[48] V. Popii, G. Baumann, Laboratory measurement of growth hormone, Clin. Chim. Acta 350 (2004) 1–16.

https://doi.org/10.1016/j.cccn.2004.06.007.

[49] M. Saugy, N. Robinson, C. Saudan, N. Baume, L. Avois, P. Mangin, Human growth hormone doping in sport, Br. J. Sports Med. 40 (2006) i35–i39. https://doi.org/10.1136/bjsm.2006.027573.

[50] N. Møller, J.O.L. Jørgensen, Effects of Growth Hormone on Glucose, Lipid, and Protein Metabolism in Human Subjects, Endocr. Rev. 30 (2009) 152–177. https://doi.org/10.1210/er.2008-0027.

[51] J. Ayuk, M.C. Sheppard, Growth hormone and its disorders, Postgrad. Med. J. 82 (2006) 24–30. https://doi.org/10.1136/pgmj.2005.036087.

[52] M.T. Dattani, N. Malhotra, A review of growth hormone deficiency, Paediatr. Child Health (Oxford). 29 (2019) 285–292. https://doi.org/10.1016/j.paed.2019.04.001.

[53] N. Rhee, K. Jeong, E.M. Yang, C.J. Kim, Gigantism caused by growth hormone secreting pituitary adenoma, Ann. Pediatr. Endocrinol. Metab. 19 (2014) 96–99. https://doi.org/10.6065/apem.2014.19.2.96.

[54] J. Fowelin, S. Attvall, H. von Schenck, B.-Å. Bengtsson, U. Smith, I. Lager, Effect of prolonged hyperglycemia on growth hormone levels and insulin sensitivity in insulin-dependent diabetes mellitus, Metabolism 42 (1993) 387–394. https://doi.org/10.1016/0026-0495(93)90092-3.

[55] F. Salomon, R. Cuneo, P.H. Sönksen, Growth Hormone and Protein Metabolism, Horm. Res. 36 (1991) 41–43. https://doi.org/10.1159/000182187.

[56] Human Growth Hormone ELISA Kit, https://www.antibodies.com/human-growth-hormone-elisa-kit-a33015 (accessed May 1, 2024).

[57] E.O. Reiter, A.H. Morris, M.H. Macgillivray, D. Weber, Variable Estimates of Serum Growth Hormone Concentrations by Different Radioassay Systems, J. Clin. Endocrinol. Metab. 66 (1988) 68–71. https://doi.org/10.1210/jcem-66-1-68.

[58] K. Albertsson-Wikland, C. Jansson, S. Rosberg, A. Novamo, Time-resolved immunofluorometric assay of human growth hormone., Clin. Chem. 39 (1993) 1620–5. http://www.ncbi.nlm.nih.gov/pubmed/8353947.

[59] A. Iranmanesh, B. Grisso, J.D. Veldhuis, Low basal and persistent pulsatile growth hormone secretion are revealed in normal and hyposomatotropic men studied with a new ultrasensitive chemiluminescence assay, J. Clin. Endocrinol. Metab. 78 (1994) 526–535. https://doi.org/10.1210/jcem.78.3.8126122.

[60] M. Bidlingmaier, J. Suhr, A. Ernst, Z. Wu, A. Keller, C.J. Strasburger, A. Bergmann, High-Sensitivity Chemiluminescence Immunoassays for Detection of Growth Hormone Doping in Sports, Clin. Chem. 55 (2009) 445–453. https://doi.org/10.1373/clinchem.2008.112458.

[61] P. Sönksen, The International Olympic Committee (IOC) and GH-2000, Growth Horm. IGF Res. 19 (2009) 341–345. https://doi.org/10.1016/j.ghir.2009.04.015.

[62] G. Such-Sanmartín, N. Bache, J. Bosch, R. Gutiérrez-Gallego, J. Segura, O.N. Jensen, Detection and differentiation of 22kDa and 20kDa Growth Hormone proteoforms in human plasma by LC-MS/MS, Biochim. Biophys. Acta - Proteins Proteomics 1854 (2015) 284–290. https://doi.org/10.1016/j.bbapap.2014.12.022.

[63] M. Thevis, M. Bredehöft, M. Kohler, W. Schänzer, Mass Spectrometry-Based Analysis of IGF-1 and hGH, in: D. Thieme, P. Hemmersbach (Eds.), Springer Berlin Heidelberg, Berlin, Heidelberg, 2009: pp. 201–207. https://doi.org/10.1007/978-3-540-79088-4_9.

[64] C.G. Arsene, J. Kratzsch, A. Henrion, Mass Spectrometry – an Alternative in Growth Hormone Measurement, Bioanalysis 6 (2014) 2391–2402. https://doi.org/10.4155/bio.14.196.

[65] K.-S. Wong, G.H.M. Chan, E.N.M. Ho, T.S.M. Wan, Simultaneous detection of recombinant growth hormones in equine plasma by liquid chromatography/high-resolution tandem mass spectrometry for doping control, J. Chromatogr. A 1478 (2016) 35–42. https://doi.org/10.1016/j.chroma.2016.11.032.

[66] C.G. Arsene, A. Henrion, N. Diekmann, J. Manolopoulou, M. Bidlingmaier, Quantification of growth hormone in serum by isotope dilution mass spectrometry, Anal. Biochem. 401 (2010) 228–235. https://doi.org/10.1016/j.ab.2010.03.005.

[67] C.W. Pratt, K. Cornely, Essential biochemistry, 5th ed., John Wiley & Sons, 2023.

[68] S.J. Angyal, The Composition of Reducing Sugars in Solution: Current Aspects, in: B. Horton (Ed.), Academic Press, 1991: pp. 19–35. https://doi.org/10.1016/S0065-2318(08)60180-8.

[69] S. Nielsen, Food Analysis, 4th ed., Springer US, Boston, MA, 2010. https://doi.org/10.1007/978-1-4419-1478-1.

[70] V.A. Buzanovskii, Methods for the determination of glucose in blood. Part 1, Rev. J. Chem. 5 (2015) 30–81. https://doi.org/10.1134/S207997801501001X.

[71] M. DuBois, K.A. Gilles, J.K. Hamilton, P.A. Rebers, F. Smith, Colorimetric Method for Determination of Sugars and Related Substances, Anal. Chem. 28 (1956) 350–356. https://doi.org/10.1021/ac60111a017.

[72] N. Nelson, A Photometric Adaptation of The Somogyi Method for The Determination of Glucose, J. Biol. Chem. 153 (1944) 375–380. https://doi.org/10.1016/S0021-9258(18)71980-7.

[73] L.A. Kartsova, A. V Maliushevska, E.A. Kolobova, Analytical Capabilities of the Determination of Carbohydrates by Chromatographic and Electrophoretic Methods, J. Anal. Chem. 78 (2023) 144–161. https://doi.org/10.1134/S1061934823020041.

[74] V. Scognamiglio, Nanotechnology in glucose monitoring: Advances and challenges in the last 10 years, Biosens. Bioelectron. 47 (2013) 12–25. https://doi.org/10.1016/j.bios.2013.02.043.

[75] C. Chen, Q. Xie, D. Yang, H. Xiao, Y. Fu, Y. Tan, S. Yao, Recent advances in electrochemical glucose biosensors: a review, RSC Adv. 3 (2013) 4473. https://doi.org/10.1039/c2ra22351a.

[76] J. He, S. Unser, I. Bruzas, R. Cary, Z. Shi, R. Mehra, K. Aron, L. Sagle, The facile removal of CTAB from the surface of gold nanorods, Colloids Surfaces B Biointerfaces 163 (2018) 140–145. https://doi.org/10.1016/j.colsurfb.2017.12.019.

[77] K. Nikolaev, S. Ermakov, Y. Ermolenko, E. Averyaskina, A. Offenhäusser, Y. Mourzina, A novel bioelectrochemical interface based on in situ synthesis of gold nanostructures on electrode surfaces and surface activation by Meerwein's salt. A bioelectrochemical sensor for glucose determination, Bioelectrochemistry 105 (2015) 34–43. https://doi.org/10.1016/j.bioelechem.2015.05.004.

[78] J.C. Hoogvliet, M. Dijksma, B. Kamp, W.P. van Bennekom, Electrochemical Pretreatment of Polycrystalline Gold Electrodes To Produce a Reproducible Surface Roughness for Self-Assembly: A Study in Phosphate Buffer pH 7.4, Anal. Chem. 72 (2000) 2016–2021. https://doi.org/10.1021/ac991215y.

[79] S. Trasatti, O.A. Petrii, Real surface area measurements in electrochemistry, J. Electroanal. Chem. 327 (1992) 353–376. https://doi.org/10.1016/0022-0728(92)80162-W.

[80] V. Liustrovaite, M. Drobysh, A. Rucinskiene, A. Baradoke, A. Ramanaviciene, I. Plikusiene, U. Samukaite-Bubniene, R. Viter, C.-F. Chen, A. Ramanavicius, Towards an Electrochemical Immunosensor for the Detection of Antibodies against SARS-CoV-2 Spike Protein, J. Electrochem. Soc. 169 (2022) 037523. https://doi.org/10.1149/1945-7111/ac5d91.

[81] R.S. Nicholson, Theory and Application of Cyclic Voltammetry for Measurement of Electrode Reaction Kinetics., Anal. Chem. 37 (1965) 1351–1355. https://doi.org/10.1021/ac60230a016.

[82] I. Lavagnini, R. Antiochia, F. Magno, An Extended Method for the Practical Evaluation of the Standard Rate Constant from Cyclic Voltammetric Data, Electroanalysis 16 (2004) 505–506. https://doi.org/10.1002/elan.200302851.

[83] H. Shu, L. Cao, G. Chang, H. He, Y. Zhang, Y. He, Direct Electrodeposition of Gold Nanostructures onto Glassy Carbon Electrodes for Non-enzymatic Detection of Glucose, Electrochim. Acta 132 (2014) 524–532. https://doi.org/10.1016/j.electacta.2014.04.031.

[84] Y. Bleiji, M. Dieperink, I. Schuringa, H. Sun, E. Alarcon-Llado, Influence of the crystallographic texture of ITO on the electrodeposition of silver nanoparticles, RSC Adv. 13 (2023) 6490–6497. https://doi.org/10.1039/D3RA00577A.

[85] W.J. Blaedel, G.W. Schieffer, A hydrodynamic voltammetric study of the ferricyanide/ferrocyanide system with convective electrodes of platinum, gold, glassy carbon, carbon film, and boron carbide, J.

Electroanal. Chem. Interfacial Electrochem. 80 (1977) 259–271. https://doi.org/10.1016/S0022-0728(77)80048-X.

[86] M.T. McDermott, C.A. McDermott, R.L. McCreery, Scanning tunneling microscopy of carbon surfaces: relationships between electrode kinetics, capacitance, and morphology for glassy carbon electrodes, Anal. Chem. 65 (1993) 937–944. https://doi.org/10.1021/ac00055a017.

[87] R. Bowling, R.T. Packard, R.L. McCreery, Mechanism of electrochemical activation of carbon electrodes: role of graphite lattice defects, Langmuir 5 (1989) 683–688. https://doi.org/10.1021/la00087a022.

[88] R.J. Rice, N.M. Pontikos, R.L. McCreery, Quantitative correlations of heterogeneous electron-transfer kinetics with surface properties of glassy carbon electrodes, J. Am. Chem. Soc. 112 (1990) 4617–4622. https://doi.org/10.1021/ja00168a001.

[89] A.P. Washe, P. Lozano-Sánchez, D. Bejarano-Nosas, I. Katakis, Facile and versatile approaches to enhancing electrochemical performance of screen printed electrodes, Electrochim. Acta 91 (2013) 166–172. https://doi.org/10.1016/j.electacta.2012.12.110.

[90] I.F. Hu, D.H. Karweik, T. Kuwana, Activation and deactivation of glassy carbon electrodes, J. Electroanal. Chem. Interfacial Electrochem. 188 (1985) 59–72. https://doi.org/10.1016/S0022-0728(85)80050-4.

[91] R.O. Kadara, N. Jenkinson, C.E. Banks, Characterisation of commercially available electrochemical sensing platforms, Sensors Actuators B Chem. 138 (2009) 556–562. https://doi.org/10.1016/j.snb.2009.01.044.

[92] C. Saby, B. Ortiz, G.Y. Champagne, D. Bélanger, Electrochemical Modification of Glassy Carbon Electrode Using Aromatic Diazonium Salts. 1. Blocking Effect of 4-Nitrophenyl and 4-Carboxyphenyl Groups, Langmuir 13 (1997) 6805–6813. https://doi.org/10.1021/la961033o.

[93] M. Drobysh, V. Liustrovaite, A. Baradoke, R. Viter, C.-F. Chen, A. Ramanavicius, A. Ramanaviciene, Determination of rSpike Protein by Specific Antibodies with Screen-Printed Carbon Electrode Modified by Electrodeposited Gold Nanostructures, Biosensors 12 (2022) 593. https://doi.org/10.3390/bios12080593.

[94] M. Drobysh, V. Liustrovaite, A. Baradoke, A. Rucinskiene, A. Ramanaviciene, V. Ratautaite, R. Viter, C.-F. Chen, I. Plikusiene, U. Samukaite-Bubniene, R. Slibinskas, E. Ciplys, M. Simanavicius, A. Zvirbliene, I. Kucinskaite-Kodze, A. Ramanavicius, Electrochemical Determination of Interaction between SARS-CoV-2 Spike Protein and Specific Antibodies, Int. J. Mol. Sci. 23 (2022) 6768. https://doi.org/10.3390/ijms23126768.

[95] M.J.E. Fischer, Amine Coupling Through EDC/NHS: A Practical

Approach BT - Surface Plasmon Resonance: Methods and Protocols, in: N.J. Mol, M.J.E. Fischer (Eds.), Humana Press, Totowa, NJ, 2010: pp. 55–73. https://doi.org/10.1007/978-1-60761-670-2_3.

[96] A. Popov, A. Stirke, N. Bakute, B. Brasiunas, A. Ramanavicius, A. Ramanaviciene, Efficiency of granulocyte colony-stimulating factor immobilized on magnetic microparticles on proliferation of NFS-60 cells, Colloids Surfaces A Physicochem. Eng. Asp. 578 (2019) 123580. https://doi.org/10.1016/j.colsurfa.2019.123580.

[97] D.K. Schwartz, Mechanisms and Kinetics of Self-Assembled Monolayer Formation, Annu. Rev. Phys. Chem. 52 (2001) 107–137. https://doi.org/10.1146/annurev.physchem.52.1.107.

[98] F.S. Damos, R.C.S. Luz, L.T. Kubota, Determination of Thickness, Dielectric Constant of Thiol Films, and Kinetics of Adsorption Using Surface Plasmon Resonance, Langmuir 21 (2005) 602–609. https://doi.org/10.1021/la0487038.

[99] G. Yohannes, S.K. Wiedmer, M. Elomaa, M. Jussila, V. Aseyev, M.-L. Riekkola, Thermal aggregation of bovine serum albumin studied by asymmetrical flow field-flow fractionation, Anal. Chim. Acta 675 (2010) 191–198. https://doi.org/10.1016/j.aca.2010.07.016.

[100] M. Ben Haddada, M. Salmain, S. Boujday, Gold colloid-nanostructured surfaces for enhanced piezoelectric immunosensing of staphylococcal enterotoxin A, Sensors Actuators B Chem. 255 (2018) 1604–1613. https://doi.org/10.1016/j.snb.2017.08.180.

[101] U. Tamer, D. Cetin, Z. Suludere, I. Boyaci, H. Temiz, H. Yegenoglu, P. Daniel, İ. Dinçer, Y. Elerman, Gold-Coated Iron Composite Nanospheres Targeted the Detection of Escherichia coli, Int. J. Mol. Sci. 14 (2013) 6223–6240. https://doi.org/10.3390/ijms14036223.

[102] Z. Xu, Y. Hou, S. Sun, Magnetic Core/Shell Fe3O4/Au and Fe3O4 /Au/Ag Nanoparticles with Tunable Plasmonic Properties, J. Am. Chem. Soc. 129 (2007) 8698–8699. https://doi.org/10.1021/ja073057v.

[103] S. Moraes Silva, R. Tavallaie, L. Sandiford, R.D. Tilley, J.J. Gooding, Gold coated magnetic nanoparticles: from preparation to surface modification for analytical and biomedical applications, Chem. Commun. 52 (2016) 7528–7540. https://doi.org/10.1039/C6CC03225G.

[104] A. Makaraviciute, T. Ruzgas, A. Ramanavicius, A. Ramanaviciene, Antibody fragment immobilization on planar gold and gold nanoparticle modified quartz crystal microbalance with dissipation sensor surfaces for immunosensor applications, Anal. Methods 6 (2014) 2134–2140. https://doi.org/10.1039/C4AY00070F.

[105] N.T.K. Thanh, N. Maclean, S. Mahiddine, Mechanisms of Nucleation and Growth of Nanoparticles in Solution, Chem. Rev. 114 (2014) 7610–7630. https://doi.org/10.1021/cr400544s.

[106] M. Wuithschick, A. Birnbaum, S. Witte, M. Sztucki, U. Vainio, N. Pinna, K. Rademann, F. Emmerling, R. Kraehnert, J. Polte, Turkevich

in New Robes: Key Questions Answered for the Most Common Gold Nanoparticle Synthesis, ACS Nano 9 (2015) 7052–7071. https://doi.org/10.1021/acsnano.5b01579.

[107] A.E. Flood, S. Srisa-nga, Mutarotation Rates and Equilibrium of Simple Carbohydrates, Asian Pacific Confed. Chem. Eng. Congr. Progr. Abstr. 2004 (2004) 110. https://doi.org/10.11491/apcche.2004.0.110.0.

[108] R.E. Wrolstad, Food Carbohydrate Chemistry, 1st ed., Wiley, 2012. https://doi.org/10.1002/9781118688496.

[109] H.S. El Khadem, S. Ennifar, H.S. Isbell, Contribution of the reaction pathways involved in the isomerization of monosaccharides by alkali, Carbohydr. Res. 169 (1987) 13–21. https://doi.org/10.1016/0008-6215(87)80238-0.

[110] G.A. Bray, S.J. Nielsen, B.M. Popkin, Consumption of high-fructose corn syrup in beverages may play a role in the epidemic of obesity, Am. J. Clin. Nutr. 79 (2004) 537–543. https://doi.org/10.1093/ajcn/79.4.537.

[111] E.E. Ventura, J.N. Davis, M.I. Goran, Sugar Content of Popular Sweetened Beverages Based on Objective Laboratory Analysis: Focus on Fructose Content, Obesity 19 (2011) 868–874. https://doi.org/10.1038/oby.2010.255.

[112] W. Zhang, Y. Du, M.L. Wang, Noninvasive glucose monitoring using saliva nano-biosensor, Sens. Bio-Sensing Res. 4 (2015) 23–29. https://doi.org/10.1016/j.sbsr.2015.02.002.

SANTRAUKA

SANTRUMPOS

11-MUR	11-merkaptoundekano rūgštis
AuND	Aukso nanodalelės
AuNS	Aukso nanostruktūros
CTAB	Cetiltrimetilamonio bromidas
DPV	Diferencinė pulsinė voltamperometrija
EDC	1-etil-3-(3-dimetilaminopropil)karbodiimidas
GS	Grafito strypelis
IAO	Indžio alavo oksidu dengtas stiklas
JSA	Jaučio serumo albuminas
MND-Au	Auksu padengtos magnetinės nanodalelės
NHS	N-Hidroksisukcinimidas
S-KP	Streptavidinu modifikuota krienų peroksidazė
TMB	3,3’,5,5’-tetrametilbenzidinas
m-anti-ŽAH	Monokloniniai antikūnai prieš žmogaus augimo hormoną
p-anti-ŽAH-B	Biotinu modifikuoti polikloniniai antikūnai prieš žmogaus augimo hormoną
p-anti-JSA	Polikloniniai antikūnai prieš jaučio serumo albuminą
ŽAH	Žmogaus augimo hormonas

ĮVADAS

Analizinės chemijos mokslo sritis nuolat tobulėja, siekiant aptikti kuo mažesnes analitės koncentracijas, panaudojant kuo mažesnius mėginių tūrius. Tam, kad būtų pasiekti šie tikslai, bėgant metams analizinių sistemų jautrumas turėjo gerokai išaugti. Dabar galima aptikti femtomoliarines ar net atomoliarines medžiagų koncentracijas mėginiuose. Šį tobulėjimą skatino įvairūs veiksniai, pvz., detektorių jautrumo padidėjimas. Vis dėlto, reikšminga pažanga atsirado dėl nanotechnologijų mokslo srities plėtros. Įvairių organinių ir neorganinių nanostruktūrų sintezės metodų vystymasis leido sukurti plataus spektro, dydžio bei formų nanostruktūras. Šios struktūros gali būti pritaikytos analizinėse sistemose, pasitelkiant unikalias medžiagų savybes, atsirandančias dėl itin mažo šių struktūrų dydžio. Galima išskirti dvi pagrindines nanomedžiagų taikymo sritis analizinėje chemijoje. Šios struktūros gali būti panaudojamos siekiant pagerinti analizinius sistemos parametrus, sustiprinant jau esamą jutiklio registruojamą signalą. Pavyzdžiui, dėl pagerėjusių elektrinių ar optinių jutiklio savybių. Kita vertus, nanostruktūros gali būti analizinės sistemos detekcijos pagrindas. Šiuo atveju nanostruktūrų suteikiamos savybės ar jų pokytis yra pagrindinis analizinio signalo šaltinis. Šioje disertacijoje bus plačiau aptariama kaip metalinės ir metalo oksidų nanostruktūros gali būti panaudotos analizinėse sistemose siekiant jautriai nustatyti biologiškai aktyvias medžiagas. Ypatingas dėmesys skiriamas šių medžiagų panaudojimui įvairių imuninių jutiklių ir redukuotų cukrų jutiklių kūrimui.

Pirmiausia, bus pristatytas elektrocheminis imuninis jutiklis be papildomų žymenų, skirtas p-anti-JSA aptikimui. Elektrocheminis nusodinimas yra naudojamas siekiant sukurti skirtingų morfologijų AuNS modifikuotus elektrodus. Šis tyrimas gilinasi į mažiau suprantamą AuNS morfologijos poveikį imuninio jutiklio veikimui. Pastebėta, kad AuNS morfologija ant GS elektrodo paviršiaus turi reikšmingos įtakos elektrocheminiam imuninio jutiklio atsakui. Buvo atskleista, kad iš trijų skirtingų morfologijų, didesnis jutiklio atsakas buvo pasiektas kai GS elektrodo paviršius buvo modifikuotas didesniu kiekiu mažesnių AuNS. Disertacijoje pateikiami svarstymai, kodėl ši specifinė morfologija labiausiai sustiprina analizinį atsaką.

Toliau bus aptarta unikaliomis MND-Au savybėmis pagrįsta optinė imunoanalizinė sistema, skirta ŽAH nustatymui. Šis tyrimas pristato naują būdą panaudoti šerdies-apvalkalo (angl. *Core-shell*) nanodaleles, kuriant magnetinių dalelių pagalba veikiančią imunoanalizinę sistemą. Šių dalelių šerdis pagaminta iš magnetinėmis savybėmis pasižyminčio geležies oksido, o apvalkalas iš aukso. Susintetintų MND-Au magnetinės savybės leidžia ženkliai supaprastinti ir pagerinti imunoanalizinės sistemos gamybos bei naudojimo procesą, nes šios struktūros gali būti surenkamos panaudojant magnetą. Tai leidžia sukurti naujovišką analitės sukoncentravimo etapą. Analitė gali būti sukoncentruota iš mėginio, įnešant šias aptikimo antikūnais modifikuotas daleles į mėginį. Įvykus giminingai antikūno sąveikai su analite, šios dalelės gali būti surenkamos panaudojant magnetą, taip išgaunant analitę iš tiriamojo mėginio. MND-Au magnetinės savybės taip pat supaprastina analizinės sistemos gamybos ir naudojimo procedūras, nes palengvina plovimo ir tirpalo keitimo etapus. Be to, magnetinių nanodalelių padengimas aukso apvalkalu suteikia papildomos naudos. Dėl padengimo aukso sluoksniu galima panaudoti įvairesnius baltymų imobilizavimo metodus, taip pat, aukso apvalkalo suformavimas padidina tokių nanodalelių stabilumą.

Dar toliau bus pristatyta optinė įvairių redukuojančių cukrų nustatymui skirta analizinė sistema. Šis tyrimas parodo, kaip AuND susidarymas gali būti panaudotas netiesioginiam redukuojančių cukrų koncentracijos nustatymui. Dėl unikalių AuND optinių savybių, šių struktūrų susidarymą galima stebėti spektrofotometriškai. Tai leidžia analizuoti oksidacijos-redukcijos procesą tarp kompleksinių Au(III) jonų ir redukuojančių cukrų, įvertinant kinetinius šios reakcijos aspektus. Šio tyrimo naujumas atsiskleidžia siekyje susieti AuND susidarymą su reakcijoje dalyvaujančio redukuojančių cukrų koncentracija. Disertacijoje taip pat pateikiami pasvarstymai apie šios oksidacijos-redukcijos reakcijos mechanizmą.

Apibendrinant, disertacijoje pateiktuose tyrimuose nagrinėjami specifinių metalinių ir metalo oksidų nanostruktūrų sintezė ir šių struktūrų integravimas į sudėtingas analizines sistemas. Parodomi įvairūs nanomedžiagų panaudojimo būdai. Nanostruktūros panaudojamos imunoanalizinės sistemos atsako stiprinimui, analizės proceso supaprastinimui, ar net yra analizinio signalo šaltinis.

Darbo tikslas:

Panaudoti įvairias metalines ir metalo oksidų nanostruktūras analizinių sistemų, skirtų biologiškai aktyvių medžiagų nustatymui, kūrimui.

Darbo uždaviniai:

1. Elektrochemiškai nusodinti įvairias AuNS ant GS elektrodų, bei panaudoti modifikuotus elektrodus elektrocheminio imuninio jutiklio be žymenų, kūrimui. Įvertinti AuNS morfologijos įtaką imuninio jutiklio atsakui.
2. Susintetinti ir panaudoti MND-Au optinės imunoanalizinės sistemos, skirtos nustatyti ŽAH, kūrimui.
3. Sukurti optinį redukuojančių cukrų kiekybinį nustatymo metodą, pagrįstą AuND susidarymu, skirtą fruktozės, gliukozės, laktozės ir manozės nustatymui.

Ginamieji teiginiai:

1. GS elektrodai su elektrochemiškai nusodintomis AuNS gali būti pritaikyti elektrocheminio imuninio jutiklio be žymenų, kūrimui.
2. MND-Au gali būti pritaikytos optinės imunoanalizinės sistemos, skirtos nustatyti ŽAH, kūrimui.
3. AuND susidarymo procesas gali būti naudojamas netiesioginiam redukuojančių cukrų koncentracijos nustatymui.

LITERATŪROS APŽVALGA

Nanomedžiagų sintezė

Egzistuoja daugybė būdų, kaip susintetinti įvairių formų ir dydžių nanomedžiagas. Šioms struktūroms sukurti naudojami įvairūs sintezės metodai. Šie metodai gali būti suskirstyti į dvi pagrindines kategorijas – „iš viršaus į apačią“ ir „iš apačios į viršų“ [1]. „Iš viršaus į apačią“ metodas yra pagrįstas didesnių medžiagų dalelių smulkinimu į mažesnes nanostruktūras. Dažniausiai naudojami „iš viršaus į apačią“ metodai apima mechaninį malimą [2,3], lazerinę abliaciją [4], ėsdinimą [5], išpurškimą [6] ir elektroverpimą [7]. Kita vertus, taikant metodą „iš apačios į viršų“, nanostruktūros auginamos nuo molekulinio lygmens. Dažniausiai naudojami metodai apima cheminį nusodinimą iš garų fazės [8], hidroterminį auginimą [9], zolio-gelio sintezę [10], oksidacijos-redukcijos reakcija pagrįstą sintezę [11,12], nusodinimą elektrocheminiu būdu [13], pirolizę [14] ir biologinius sintezės metodus [15].

Elektrocheminis AuNS nusodinimas

Elektrocheminis nusodinimas yra patogus būdas tiesiogiai susintetinti nanostuktūras ant elektrai laidžių paviršių [16]. Šiuo metodu elektros srovė panaudojama oksiduoti arba redukuoti tirpale esančias medžiagas, skatinant nanostruktūrų susidarymą ir augimą ant elektrodo paviršiaus. Kompleksinis Au(III) jonas dažnai naudojamas kaip AuNS elektrocheminio nusodinimo pirmtakas [17]. Elektrocheminis nusodinimo procesas gali būti labai tiksliai kontroliuojamas keičiant indikatorinio elektrodo potencialą, nusodinimo laiką, pirmtako koncentraciją, keičiant pagalbinius elektrolitus, pH ir joninę jėgą [17,19–22]. Gautų struktūrų morfologijai didelę įtaką turi elektrocheminiam nusodinimui naudojamo tirpalo sudėtis. Kai šis procesas atliekamas su didesnėmis metalų pirmtako koncentracijomis, susidariusios struktūros taip pat būna didesnės. Tuo tarpu pagalbiniai elektrolitai daro įtaką tirpalo pH, paveikdami AuNS susidarymo ir augimo greitį [19]. Paviršiaus aktyviosios medžiagos taip pat gali pakeisti elektrocheminio nusodinimo procesą, prisijungdamos prie specifinių kristalinių briaunų taip sustabdydamos struktūros augimą ties ta kristaline briauna [21]. Nuspėti susidariusių struktūrų morfologiją ant elektrodo paviršiaus gana sudėtinga, todėl morfologijai įvertinti dažnai naudojama skenuojanti elektroninė mikroskopija.

MND-Au sintezė

Šerdies-apvalkalo nanodalelių sintezė, leidžia sukurti tokias nanostuktūras, kurios gali turėti kelių skirtingų medžiagų savybes. Tai leidžia išplėsti tokių nanodalelių pritaikymo galimybes. Gautų struktūrų optinės bei elektrocheminės savybės gali būti keičiamos, priklausomai nuo šerdies ar apvalkalo sintezei naudojamų medžiagų. Dažniausiai šerdies-apvalkalo nanodalelių formavimui naudojami „iš apačios į viršų“ sintezės metodai. Sintezė paprastai susideda iš dviejų žingsnių. Iš pradžių susintetinama norimo dydžio šerdis, o po to atliekamas šerdies padengimas apvalkalu. Galimi du padengimo apvalkalu mechanizmai. Jei šerdies ir apvalkalo kristalinė struktūra panaši, apvalkalas dažniausiai gali būti užauginamas tiesiogiai ant šerdies paviršiaus. Tuo atveju jei medžiagų kristalinės struktūros skirtingos, ant šerdies paviršiaus iš pradžių adsorbuojamos itin mažos nanodalelės (angl. *nanoseeds*), kurios yra pagamintos iš tos pačios medžiagos kaip ir planuojamas apvalkas. Adsorbuotos nanodalelės veikia kaip kristalizacijos taškai, o tai leidžia atlikti tolimesnį šerdies padengimą apvalkalu. Iš principo, šerdies-apvalkalo nanodalelės gali turėti keletą apvalkalų sluoksnių [23,30].

Šerdies sintezei dažnai naudojamos magnetinėmis savybėmis pasižyminčios medžiagos, tokios kai Fe_3O_4, ar kobalto bei nikelio junginiai. Magnetinių medžiagų panaudojimas šerdies sintezei leidžia sukurti tokias nanodaleles kurios gali būti manipuliuojamos panaudojant magnetą. Fe_3O_4 sintezė gali būti atliekama įvairiais būdais, tačiau populiariausias yra koprecipitacijos metodas. Šiuo metodu, Fe(II) ir Fe(III) jonai sumaišomi santykiu 1:2 bazinėje terpėje. Susidariusių nanodalelių dydis bei forma priklauso nuo įvairių faktorių, tokių kaip pagalbinių anijonų prigimties ir koncentracijos, geležies jonų santykio, reakcijos mišinio temperatūros, joninės jėgos, pH, ir įvairių kitų kriterijų, kaip bazinio tirpalo lašinimo ir maišymo greitis [26-29].

Dėl unikalių optinių ir puikių elektrinių savybių, dažnai apvalkalo sintezei naudojami taurieji metalai, iš kurių populiariausias auksas. Aukso apvalkalo suformavimo procesas nėra itin sudėtingas, o gautos struktūros yra stabilios ilgą laiko tarpą. Dažniausiai aukso apvalkalas formuojamas redukuojant kompleksinius Au(III) jonus, įvairiais reduktoriais, tokiais kaip trinatrio citratas aukštoje temperatūroje [31], ar natrio borohidridas kambario temperatūroje [29]. Paviršiaus aktyviosios medžiagos naudojamos stabilizuoti susidariusias šerdies-apvalkalo nanodaleles. Aukso apvalkalo sintezė ant šerdies pagamintos iš Fe_3O_4 yra palanki, nes abiejų šių medžiagų kristalinės gardelės panašios, o tai leidžia atlikti tiesioginį aukso apvalkalo auginimą ant šerdies paviršiaus. Kompleksinių Au(III) jonų redukcija taip pat gali būti atliekama panaudojant hidroksilaminą. Šis reduktorius, palyginus su kitais, palankus tuo, kad skatina aukso apvalkalo augimą ant tirpale jau esančių Fe_3O_4 šerdies dalelių, vietoj naujų auksinių nanodalelių susidarymo [34-36].

AuND sintezė naudojant redukuojančius cukrus

Aukso nanodalelių sintezė yra genėtinai plačiai ištirta. Dažniausiai šių struktūrų sintezei taikomas „iš apačios į viršų“ metodas. Redukuoti $[AuCl_4]^-$ jonus yra naudojamos tokios medžiagos kaip trinatrio citratas, natrio borohidridas, ar askorbo rūgštis [37]. Redukuojantys cukrai, tokie kaip gliukozė, fruktozė ir galaktozė, taip pat gali būti panaudoti AuND sintezei [38]. Tačiau tikslus $[AuCl_4]^-$ ir redukuojančių cukrų reakcijos mechanizmas nėra visiškai aiškus. Kai kurie tyrimai rodo, kad monosacharidai dalyvauja reakcijoje tiesiogiai per atviros grandinės konformaciją [38,39]. Tačiau kiti autoriai teigia, kad redukuojančių cukrų oksidacija naudojant metalų jonus bazinėje terpėje vyksta per tarpinę redukuojančių cukrų enediolio struktūrą [43–45]. Šioje disertacijoje pateikti tyrimai taip pat rodo, kad labiau tikėtina, kad reakcija vyksta per tarpinį enediolį, o ne tiesiogiai per atviros grandinės konformaciją. Bet kuriuo atveju, sintezei naudojant redukuojančius cukrus, yra reikalinga gautų AuND stabilizacija. Šiam tikslui papildomai pridedama paviršiaus aktyviųjų medžiagų. Šiame darbe AuND stabilizacijai buvo naudojamas CTAB.

Žmogaus augimo hormonas

ŽAH arba somatotropinas yra priekinės hipofizės gaminamas baltymas, būtinas žmogaus augimui, ląstelių dauginimuisi ir audinių atstatymui reguliuoti. Be to, jis skatina į insuliną panašaus augimo faktoriaus 1 gamybą [46]. Kraujyje ŽAH yra randamas įvairių izoformų. Pagrindinė izoforma, sudaranti maždaug pusę viso ŽAH, yra 22 kDa ir susideda iš 191 aminorūgšties. Kitos izoformos dydis yra 20 kDa ir ją sudaro maždaug 5–9% viso ŽAH. Be šių pagrindinių formų, ŽAH gali egzistuoti kaip dimeras ar oligomeras. Taip pat kraujo serume aptinkamas skilęs į mažesnės molekulinės masės fragmentus [47–49].

Normaliam žmogaus augimui ir medžiagų apykaitos funkcijoms, įskaitant lipidų, angliavandenių ir baltymų apykaitą, labai svarbu palaikyti optimalią ŽAH koncentraciją kraujyje [50]. Nepakankama ŽAH koncentracija kraujyje gali sulėtinti tiek suaugusiųjų, tiek vaikų, augimą. Suaugusiesiems ŽAH trūkumas pasireiškia medžiagų apykaitos sutrikimais, raumenų ir kaulų masės sumažėjimu bei kitais fiziologiniais pokyčiais [51,52]. Priešingai, per didelis ŽAH kiekis gali sukelti tokias ligas kaip gigantizmas bei diabetas [53–55]. ŽAH taip pat dažnai yra vartojamas neetiškų sportininkų, siekiant įgauti pranašumą prieš kitus sportininkus. Dėl šių priežasčių, ŽAH analizės metodai yra svarbūs ir gali būti pritaikyti klinikinėje medicinoje bei dopingo prevencijos srityse.

Standartinė ŽAH koncentracija kraujyje skiriasi priklausomai nuo lyties ir amžiaus, tačiau įprastai svyruoja nuo 0,4 ng·mL^{-1} (0,018 nmol·L^{-1}) iki 50 ng·mL^{-1} (2,273 nmol·L^{-1}) [56]. Tačiau dėl įvairių ŽAH izoformų egzistavimo, šio hormono nustatymas kelia iššūkių. Yra reikalingi nustatymo metodai, galintys identifikuoti specifinių izoformų koncentracijas arba registruoti bendrą visų mėginyje esančių izoformų koncentraciją [48]. ŽAH nustatymui dažniausiai yra naudojami įvairūs imunologiniai tyrimai, įskaitant radioimuninį, imunofluorometrinį, ar imunochemiliuminescencinį tyrimą bei imunofermentinę analizę. Iš paminėtų metodų imunofermentinė analizė yra plačiausiai naudojama [56–59].

Redukuojantys cukrai

Angliavandeniai buvo tarp pirmųjų organinių junginių, kurių cheminė struktūra buvo nustatyta. Redukuojantys angliavandeniai, dažniausiai vadinami redukuojančiais cukrais, yra junginiai, kurie oksidacijos-redukcijos reakcijose gali dalyvauti kaip reduktoriai. Šiai kategorijai priklauso visi monosacharidai, taip pat kai kurie disacharidai ir polisacharidai. Svarbu paminėti, kad redukuojantys cukrai, tokie kaip gliukozė, fruktozė, galaktozė, manozė bei laktozė, yra plačiausiai žinomi ir ištirti, nes šie angliavandeniai randami įvairiuose maisto produktuose [41,67].

Angliavandeniai pasižymi struktūrine įvairove, atsižvelgiant į tai, ar jie turi aldehido (aldozės) ar ketono (ketozės) grupę. Be to, šie cukrai savo struktūroje turi chiralinių centrų, todėl jie gali egzistuoti įvairių enantiomerinių formų. Cukrai, turintys daugiau nei tris anglies atomus, gali sudaryti stereoizomerus, žinomus kaip epimerai. Pavyzdys yra D–gliukozė ir D–galaktozė, kurių chirališkumas skiriasi C4 padėtyje. Tirpaluose cukrai dėl tarpmolekulinių jėgų persitvarko, sudarydami ciklines struktūras. Priklausomai nuo hidroksilo grupės, prijungtos prie anomerinės anglies, orientacijos susidarius ciklinėms struktūroms gaunami α arba β anomerai. Anomerinės struktūros vandeniniuose tirpaluose gali laisvai keistis tarpusavyje (2 pav., 21 psl.). Šis reiškinys, vadinamas mutarotacija, prisideda prie skirtingų cukraus formų pusiausvyros nusistovėjimo tirpale (3 pav., 21 psl.) [41,67]. Per didelis cukraus vartojimas plačiai pripažįstamas kaip vienas pagrindinių įvairių pasaulio sveikatos problemų šaltinių, įskaitant diabetą, nutukimą bei širdies ir kraujagyslių ligas. Todėl būtina stebėti redukuojančių cukrų koncentracijas maisto produktuose, gėrimuose, ir kūno skysčiuose. Redukuojančių cukraus koncentracijų nustatymo metodai paprastai apima optinius arba elektrocheminius metodus. Juos galima suskirstyti į 3 pagrindines grupes, priklausomai nuo to, ar mėginyje nustatomas visas angliavandenių kiekis, ar nustatomi tik redukuojantys cukrai, ar nustatomas specifinis cukrus [69,70].

Bendra redukuojančių cukrų koncentracija mėginyje dažniausiai nustatoma remiantis šių medžiagų savybe dalyvauti oksidacijos-redukcijos reakcijose. Itin plačiai paplitęs Samogyi-Nelson metodas, sukurtas 1944 metais [72]. Metodas pagrįstas oksidacijos-redukcijos reakcija tarp redukuojančių cukrų ir Cu^{2+} jonų bazinėje terpėje ir aukštoje temperatūroje. Reakcijos metu susidarę Cu^{+} jonai gali dalyvauti kitoje oksidacijos-redukcijos reakcijoje su papildomai pridėtu arsenomolibdato kompleksu, susidarant mėlynos spalvos junginiui, kurio absorbcija registruojama ties 520 nm. Kiti panašūs redukuojančių cukrų nustatymo metodai paremti Cu_2O nuosėdų susidarymu [69]. Kadangi šie metodai pagrįsti nestechiometrinėmis reakcijomis, kalibracinės kreivės turi būti specifiškai pritaikytos atitinkamiems mėginiams analizuoti. Ypač jei mėginiuose yra ketozių. Kiti reduktoriai esantys mėginyje gali iškreipti analizės rezultatus, tačiau dažniausiai redukuojančių cukrų koncentracija mėginyje yra žymiai didesnė nei kitų reduktorių, todėl šių medžiagų įtaka analizei dažniausiai nėra didelė.

Metalinių ir metalo oksidų nanostruktūrų taikymas optinių ir elektrocheminių imuninių jutiklių kūrimui

Ši tema yra plačiau apžvelgiama šiuose publikacijose: **Straipsnis 5, Straipsnis 6**. Publikacijose pristatomi įvairūs būdai, kaip metalinės nanodalelės, kvantiniai taškai ir ZnO nanostruktūros gali būti naudojamos kuriant elektrocheminius ir optinius imuninius jutiklius. Pateikiama išsami ir naujausia informacija apie įvairius baltymų imobilizacijos metodus. Įvardijami būdai, kaip šias struktūras galima panaudoti analizinio signalo stiprinimui arba kaip šios struktūros gali sukurti analizinį signalą.

TYRIMO METODIKA

AuNS elektrocheminis nusodinimas

Visi elektrocheminiai tyrimai buvo atliekami trijų elektrodų celėje, naudojant potenciostatą/galvanostatą PGSTAT30/Autolab pagamintą ECOChemie (Ultrechtas, Olandija). Pagalbinis elektrodas buvo pagamintas iš platinos, o lyginamasis – $Ag/AgCl_{3M\ KCl}$. GS elektrodai prieš naudojimą buvo poliruojami įvairaus šiurkštumo poliravimo popieriumi (P120, P320, P2000). Po poliravimo elektrodai nuplaunami dejonizuotu vandeniu. IAO elektrodas prieš naudojimą buvo plaunamas ultragarso vonelėje, 15 min. acetone ir 15 min. dejonizuotame vandenyje. Papildomai IAO elektrodas valytas elektrochemiškai ciklinės voltamperometrijos metodu. Elektrodas buvo pamerktas į 50 mM fosfatinį buferinį tirpalą turintį 0,1 M KCl, pH 6, ir potencialas buvo skleidžiamas intervale nuo 0 iki +1 V, 30 kartų.

AuNS elektrocheminis nusodinimas buvo atliekamas indikatoriniam elektrodui suteikiant −0,2 V potencialą 60 sek. Elektrocheminio nusodinimo tirpalai buvo sudaryti iš skirtingų koncentracijų $HAuCl_4$ ir pagalbinio elektrolito (KNO_3 ir H_2SO_4).

MND-Au sintezė

MND sintezė: Į 1,28 M $FeCl_3$ ir 0,64 M $FeSO_4$ tirpalą, esant stipriam maišymui, buvo lėtai sulašinta 125 mL 1 M NaOH. Naudojantis magnetu, susintetintos MND buvo 3 kartus praplautos dejonizuotu vandeniu. Po to dalelės buvo patalpintos į 2 M $HClO_4$ tirpalą esant argono atmosferai ir laikytos +4°C 12 val. Gautos MND buvo 3 kartus praplautos dejonizuotu vandeniu ir 1 kartą etanoliu. Toliau dalelės buvo nucentrifuguotos ir išdžiovintos ore.

MND padengimas aukso sluoksniu: 5 mg išdžiovintų MND disperguojamos 5 mL dejonizuoto vandens, panaudojant ultragarsą. Į šią dispersiją supilami 5 mL 1 M NaOH ir 0,27 M EDTA tirpalų mišinio. Dalelės surenkamos magnetu ir supernatantas pakeičiamas 10 mL 0,1M CTAB ir 0,01 M $HAuCl_4$ tirpalu. Stipriai maišant dispersinį tirpalą, į jį suberiama 150 mg hidroksilamino.

AuND sintezė panaudojant redukuojančius cukrus

Kiuvetėjė tirpalai sumaišomi taip, kad galutinė medžiagų koncentracija reakcijos mišinyje būtų 0,1 M NaOH, 3,7 mM CTAB, 1 mM $HAuCl_4$ ir nuo 0,1 iki 10 mM redukuojančio cukraus.

Kai reakcija atliekama su realiai mėginiais, reikia atlikti išankstinį mėginio paruošimą. Pieno mėginiui atliekamas baltymų išsodinimas, į mėginį pridedant $CuSO_4$ kol pasiekiama 0,5 % koncentracija. Mėginys maišomas 10 min., ir tada 15 min. centrifuguojamas esant 17000 × g. Analizei toliau naudojamas supernatantas. Prieš surenkant seilių mėginį burna 2 min. skalaujama vandeniu. Seilės surenkamos vatos gumulėlį laikant burnoje 1 min. Seilės iš vatos gumulėlio švirkštu filtruojamos panaudojant 0,23 µm PVDF filtrą. Analizei toliau naudojamas seilių filtratas.

Kovalentinis JSA imobilizavimas ant AuNS modifikuoto GS elektrodo

AuNS modifikuotas GS elektrodas 2 valandom pamerkiamas į 1 mM 11-MUR metanolio tirpalą. Po to elektrodas 15 min. plaunamas, pamerkiant elektrodą į maišomą metanolio tirpalą ir 15 min. – į dejonizuotą vandenį.

Toliau elektrodas pamerkiamas į 250 µL 200 mM EDC ir 50 mM NHS tirpalų mišinį, ir laikomas 15 min. Elektrodas nuplaunamas dejonizuotu vandeniu, pamerkiamas į 250 µL 100 $\mu g \cdot mL^{-1}$ JSA tirpalą ir laikomas 20 min. Po to elektrodas 15 min. plaunamas, pamerkiant elektrodą į maišomą dejonizuotą vandenį.

Kovalentinis m-anti-ŽAH imobilizavimas ant MND-Au

Į 1,6 mL 0,2 $mg \cdot mL^{-1}$ MND-Au tirpalą įpilama 800 µL 30 mM $NaBH_4$ tirpalo. Mišinys maišomas 1 val., tada MND-Au dalelės praplaunamos dejonizuotu vandeniu. MND-Au surenkamos panaudojant magnetą ir supernatantas pakeičiamas į 1 mM 11-MUR metanolio tirpalą. MND-Au laikomos šiame tirpale 2 val. Toliau MND-Au/11-MUR praplaunamos dejonizuotu vandeniu ir užpilamos 200 mM EDC ir 50 mM NHS tirpalų mišiniu. Dalelės laikomos mišinyje 15 min., tada praplaunamos dejonizuotu vandeniu. MND-Au/11-MUR dalelės surenkamos panaudojant magnetą ir supernatantas pakeičiamas 330 nM m-anti-ŽAH tirpalu. Dalelės laikomos antikūnų tirpale 2 val. Po kovalentinės antikūnų imobilizacijos, nanodalelės 3 kartus praplaunamos su 10 mM fosfatiniu buferiniu tirpalu, pH 7,4. Toliau, panaudojant magnetą, supernatantas pakeičiamas 1 % JSA tirpalu, ištirpintu 10 mM fosfatiniame buferiniame tirpale, pH 7,4. Nanodalelių tirpalas laikomas +4°C temperatūroje 12 val.

Elektroaktyvaus aukso paviršiaus ploto nustatymas

Elektroaktyvaus aukso paviršiau plotas nustatomas naudojantis ciklinės voltamperometrijos metodą. AuNS dengti IAO elektrodai pamerkiami į 0,5 M H_2SO_4 tirpalą ir indikatorinio elektrodo potencialas skleidžiamas nuo 0 iki +1,4 V tris kartus, esant skirtingam potencialo skleidimo greičiui (50, 100, ir 150 $mV \cdot s^{-1}$). Elektroaktyvus aukso paviršiaus plotas įvertinamas remiantis chemiškai adsorbuoto deguonies monosluoksnio redukcijos srove [77,78].

Elektroaktyvaus elektrodo paviršiaus ploto nustatymas

Elektroaktyvaus aukso paviršiau plotas nustatomas naudojant ciklinės voltamperometrijos metodą. AuNS dengti GS elektrodai pamerkiami į 2,5 mM $[Fe(CN)_6]^{3-/4-}$ tirpalą ir indikatorinio elektrodo potencialas skleidžiamas nuo −0,2 iki +0,7 V tris kartus, esant skirtingam potencialo skleidimo greičiui (10, 25, 50, 75, 100, ir 150 $mV \cdot s^{-1}$). Elektroaktyvus elektrodo paviršiaus plotas įvertinamas naudojant Randles-Sevcik lygtį esant 25°C, pagal maksimalios anodinės srovės priklausomybės nuo $\nu^{1/2}$ nuolinkio kampą [79].

Heterogeninės elektronų pernašos greičio konstantos nustatymas

Heterogeninė elektronų pernašos greičio konstanta nustatoma naudojant ciklinės voltamperometrijos metodą. AuNS dengti GS elektrodai pamerkiami į 2,5 mM $[Fe(CN)_6]^{3-/4-}$ tirpalą ir indikatorinio elektrodo potencialas skleidžiamas nuo −0,2 iki +0,7 V tris kartus, esant skirtingam potencialo skleidimo greičiui (10, 25, 50, 75, 100, ir 150 $mV \cdot s^{-1}$). Heterogeninė elektronų pernašos greičio konstanta įvertinama naudojant Nicholson-Lavagnini metodiką [81,82].

REZULTATŲ APTARIMAS

AuNS modifikuotų GS elektrodų panaudojimas elektrocheminio jutiklio be žymenų kūrimui

Elektrocheminiam AuNS nusodinimui buvo naudojamas pastovus −0,2 V potencialas $Ag/AgCl_{3M\ KCl}$ lyginamojo elektrodo atžvilgiu. Potencialas buvo suteikiamas 60 sek. laiko tarpą. Priklausomai nuo tirpalo naudojamo elektrocheminiam nusodinimui koncentracijos, buvo nusodintos skirtingos morfologijos AuNS ant IAO ir GS elektrodų (4 pav., 32 psl. ir 5 pav., 34 psl.). Pastebėta, kad nusodinimo tirpale esant didesnei $HAuCl_4$ koncentracijai, ant elektrodų paviršiaus susidaro didesnės AuNS. Taip pat, kai elektrocheminis nusodinimas atliekamas panaudojant tirpalą kurio pH žemas, ant elektrodo paviršiaus susidaro didesnis kiekis mažesnių AuNS. Palyginus ant skirtingų elektrodų tokiomis pačiomis sąlygomis susintetintas AuNS pastebėta, kad jų morfologijos stipriai skiriasi. Elektrochemiškai nusodintos AuNS buvo polikristalinės. Tolimesniems tyrimams buvo pasirinkti GS elektrodai, modifikuoti $AuNS_I$, susintetintomis panaudojant 3 mM $HAuCl_4$ ir 0,2 M H_2SO_4 tirpalą, $AuNS_{II}$ – 10 mM $HAuCl_4$ ir 0,1 M KNO_3, ir $AuNS_{III}$ – 15 mM $HAuCl_4$ ir 1 M KNO_3.

Buvo įvertinti AuNS modifikuotų GS elektrodų elektroaktyvūs paviršiaus plotai bei heterogeninės elektronų pernašos greičio konstantos. Pastebėta, kad didžiausiu elektroaktyviu paviršiaus plotu pasižymėjo $AuNS_I$ modifikuoti GS elektrodai ($0,213 \pm 0,019\ cm^2$). $AuNS_{II}$ ir $AuNS_{III}$ modifikuoti elektrodai turėjo mažesnį, bet panašų elektroaktyvų paviršiaus plotą, atitinkamai 0.116 ± 0.006 ir $0.110 \pm 0.011\ cm^2$. Įvertinta, kad heterogeninė elektronų pernašos greičio konstantos vertė nepriklausė nuo AuNS modifikuotų elektrodų paviršiaus morfologijos ir buvo ~2,5 karto didesnė palyginus su nemodifikuotam GS elektrodui apskaičiuota verte (1 lentelė, 35 psl.).

Ant AuNS modifikuotų elektrodų atlikus kovalentinį JSA imobilizavimą, buvo įvertintas prisijungusio prie elektrodo JSA kiekis. Ant $AuNS_I$ ir $AuNS_{II}$

modifikuotų elektrodų prisijungė panašus ir ~20 % didesnis JSA kiekis lyginant su $AuNS_{III}$ modifikuotu elektrodu (2 lentelė, 38 psl.). Pastebėta, kad GS elektrodai padengti didesniu kiekiu apvalių pavienių dalelių ($AuNS_{I}$ ir $AuNS_{II}$) efektyviau prisijungė JSA, lyginant su didelėmis šakotomis struktūromis ($AuNS_{III}$) dengtais elektrodais.

AuNS modifikuoti elektrodai su imobilizuotu JSA buvo pritaikyti p-anti-JSA antikūnų nustatymui (6 pav., 37 psl.). Modifikuotiems elektrodams charakterizuoti buvo pasitelktas DPV metodas. Matavimai buvo atliekami tirpale turinčiame 2,5 mM $[Fe(CN)_6]^{3-/4-}$ ir 10 mM fosfatinio buferinio tirpalo, pH 7,4. Potencialas buvo skleidžiamas nuo −0,15 V iki +0,5 V, kai impulso dydis buvo 25 mV, impulso laikas – 0,05 sek., impulso periodas – 0,5 sek, o potencialo žingsnis – 5 mV. Didžiausia anodinė srovė prieš sąveiką su p-anti-JSA buvo užregistruota naudojant $AuNS_{I}$ modifikuotą elektrodą (28.4 ± 1.4 μA), tuo tarpu maksimalios anodinės srovės naudojant $AuNS_{II}$ ir $AuNS_{III}$ modifikuotus elektrodus atitinkamai buvo 12.8 ± 0.5 μA ir 7.1 ± 1.9 μA (7 pav., 39 psl.). Toliau buvo vertinamas anodinės srovės stiprio pokytis, po 30 min. sąveikos su 5 nM p-anti-JSA. Po sąveikos su p-anti-JSA registruojama anodinė srovė sumažėjo, nes prie modifikuoto elektrodo paviršiaus prisijungę antikūnai trukdė redokso mediatoriaus difuzijai link elektrodo paviršiaus ir sumažino elektroaktyvaus paviršiaus plotą. Šis anodinės srovės pokytis buvo pasirinktas kaip analizinis signalas antikūnų koncentracijos nustatymui. Didžiausias srovės pokytis po sąveikos su 5 nM p-anti-JSA buvo registruojamas naudojant $AuNS_{I}$ modifikuotą elektrodą (8,9 ± 1.8 μA), tuo tarpu pokytis naudojant $AuNS_{II}$ ir $AuNS_{III}$ modifikuotus elektrodus atitinkamai buvo 6.6 ± 0.5 μA ir 4.1 ± 1.2 μA. Elektrocheminis imuninis jutiklis toliau buvo analizuojamas naudojant $AuNS_{I}$ modifikuotą GS elektrodą.

Atliekant tyrimus ir siekiant nustatyti skirtingas p-anti-JSA koncentracijas, buvo pastebėtas didelis analizinės sistemos atsako išsibarstymas, signalą registruojant esant tai pačiai p-anti-JSA koncentracijai. Nuspręsta po JSA imobilizacijos atlikti papildomą laisvo elektrodo paviršiaus ploto blokavimo žingsnį. Šiam tikslui po JSA imobilizavimo, modifikuotas elektrodas buvo pamerkiamas į 10 kartų skiestą kraujo serumo tirpalą ir laikomas tirpale 30 min. Po elektrodo paviršiaus blokavimo buvo stebimas 10 % analizinio signalo sumažėjimas, parodantis, kad medžiagos esančios kraujo serume nespecifiškai prisijungė prie elektrodo paviršiaus. Papildomas paviršiaus blokavimo etapas leido pasiekti žymiai geresnį elektrocheminio imuninio jutiklio atsako pakartojamumą. Buvo įvertinta sukurto jutiklio signalo priklausomybė nuo 10 kartų skiestame kraujo serume ištirpintos p-anti-JSA koncentracijos (8 pav., 42 psl). Analizinio signalo tiesinis intervalas buvo nuo 1 iki 5 nM p-anti-JSA, o apskaičiuota aptikimo riba buvo 0,71 nM.

MND-Au panaudojimas optinės imunoanalizinės sistemos, skirtos nustatyti ŽAH, kūrimui

MND-Au nanodalelės buvo susintetintos dviem etapais. Iš pradžių buvo atlikta MND sintezė panaudojant koprecipitacijos metodą. Gautos MND buvo padengtos aukso sluoksniu, atliekant $[AuCl_4]^-$ redukciją hidroksilaminu. Aukso sluoksnio susiformavimas ant MND buvo patvirtintas transmisijos elektroniniu mikroskopu (9 pav., 43 psl.), rentgeno spinduliuotės difrakcijos metodu bei spektrofotometriškai (10 pav., 44 psl.). Gautos MND-Au buvo 47.6 ± 11.3 nm dydžio.

Šios MND-Au buvo pritaikytos optinės imunoanalizinės sistemos, skirtos nustatyti ŽAH, kūrimui (11 pav., 45 psl.). Ant MND-Au paviršiaus buvo 2 val. formuojamas 11-MUR savitvarkis monosluoksnis. Ant MND-Au/11-MUR kovalentiškai imobilizuojami m-anti-ŽAH, kurie gali būti panaudojami analitę surinkti iš mėginio. Į MND-Au/11-MUR/m-anti-ŽAH/ŽAH dalelių tirpalą įpilami p-anti-ŽAH-B antikūnai. Po sąveikos ir dalelių praplovimo, į tirpalą įpilama S-KP. Pridėjus TMB substrato, bei leidus fermentinei reakcijai vykti 10 min., papildomai įpilamas „STOP“ tirpalas. Spektrofotometriškai ties 450 nm bangos ilgiu registruojamas atsiradęs geltonos spalvos junginys. Šviesos absorbcija didėja, anlizuojamame tirpale esant didesnei ŽAH koncentracijai.

Buvo atliktas sukurtos optinės imunoanalizinės sistemos paruošimo optimizavimas (12 pav., 46 psl.). m-anti-ŽAH imobilizacijai pasirinkta optimaliausia koncentracija buvo 330 nM. Atliekant tyrimą panaudojant kontrolinio mėginį, neturintį ŽAH, buvo registruota pakankamai didelė absorbcijos vertė, ~0,5. Siekiant kuo labiau sumažinti su kontrolinio mėginiu registruojamą atsaką, buvo atliktos dvi skirtingos nespecifinę sąveiką sumažinti padedančios procedūros. Pirma, atliktas mėgintuvėlio, kuriame vykdome imunoanalizės etapus, vidinio paviršiaus blokavimas naudojant 1 % JSA tirpalą, paruoštą 10 mM fosfatiniame buferiniame tirpale. Blokavimas buvo atliekamas 1 val. prieš visą imunoanalizės proceso pradžią. Šis blokavimo etapas leido su kontroliniu mėginiu registruojamą atsaką sumažinti ~3 kartus. Toliau buvo nuspręsta į praplovimo tirpalą, sudaryta iš 10 mM fosfatinio buferinio tirpalo, papildomai įdėti 0,1 % JSA. Naudojant abi blokavimo procedūras, su kontroliniu mėginiu registruojamas atsakas buvo sumažintas ~5,7 karto.

Sukurta optinė imunoanalizinė sistema panaudojant MND-Au buvo pritaikyta skirtingai ŽAH koncentracijai nustatyti intervale nuo 0,1 iki 50 nM

(13 pav., 48 psl.). Tiesinis atsako priklausomybės nuo ŽAH koncentracijos intervalas buvo nuo 0,1 iki 5 nM. Apskaičiuota ŽAH aptikimo riba buvo 0,082 nM. Optinė imunoanalizinė sistema panaudojant MND-Au įvertinta nustatant kraujo serume ištirpintą ŽAH. Registruota ŽAH išgava buvo 95 %.

AuND susidarymo proceso panaudojimas redukuojančių cukrų koncentracijai nustatyti

Redukuojančių cukrų koncentracijos nustatymo metodas yra paremtas AuND susidarymu, vykstant oksidacijos-redukcijos reakcijai tarp kompleksinių Au(III) jonų ir redukuojančių cukrų (14 pav., 49 psl.). Reakcija atliekama bazinėje terpėje, o susidariusių AuND stabilizacijai naudojamas CTAB. AuND susidarymas buvo stebimas spektrofotometriškai, registruojant AuND būdingą lokalaus paviršiaus plazmonų rezonanso absorbcijos smailę.

Atliekant AuND susidarymo reakcijos su redukuojančiais cukrais analizę, pastebėta, kad AuND spektre absorbcijos smailės maksimumas iš pradžių susidaro ties ~550 nm, o reakcijos eigoje slenkasi link trumpesnių bangos ilgių, kol nusistovi ties ~525 nm. Reakcijos eigoje absorbcijos vertė ties absorbcijos smailės maksimumu didėja, kol ši vertė nusistovi praėjus ~48 val. nuo reakcijos pradžios (15 pav., 50 psl.).

Analizuojant rezultatus pastebėta, kad absorbcijos vertė ties 525 nm tiesiškai priklausė nuo redukuojančio cukraus koncentracijos (16 pav., 51 psl.). Priklausomai nuo absorbcijos registracijos po reakcijos pradžios laiko tarpo, tiesinis priklausomybės intervalas ir analizinės sistemos jautris buvo skirtingi. Analizę atliekant ilgesnį laiko tarpą didėjo analizinės sistemos jautris, todėl buvo galima nustatyti mažesnę redukuojančių cukrų koncentraciją. Tačiau, tiesiškumo intervalas signalą registruojant po ilgesnio laiko tarpo buvo siauresnis. Tiriant reakciją su skirtingais redukuojančiais cukrais pastebėta, kad AuND susidarymo greitis priklausė nuo redukuojančio cukraus prigimties ir mažėjo šia tvarka: fruktozė, gliukozė laktozė, manozė (17 pav., 52 psl.).

Buvo tiriama AuND susidarymo reakcija, panaudojant gliukozės-fruktozės redukuojančių cukrų mišinį. Šiame mišinyje bendra redukuojančių cukrų koncentracija buvo 1 mM, o gliukozės ir fruktozės santykis buvo 1:1. AuND susidarymas, reaguojant su šiuo redukuojančiu cukrų mišiniu, buvo palygintas su rezultatu, kai reakcija vykdoma su 1 mM koncentracijos pavieniais gliukozės ir fruktozės tirpalais (18 pav., 54 psl). Pastebėta, kad AuND susidarymo greitis, reakciją vykdant su gliukozes-fruktozės mišiniu, atitiko reakcijos greičių su pavieniais redukuojančiais cukrais vidurkį.

Analizinė sistema skirta redukuojančių cukrų koncentracijos nustatymui buvo įvertinta panaudojant realius mėginius. Buvo įvertinta gliukozės-fruktozės koncentracija gaiviajame gėrime „Coca-Cola“, laktozės koncentracija piene bei gliukozės koncentracija seilėse.

Kalibracinė kreivė skirta nustatyti gliukozės-fruktozės mišinio koncentracijai, kuriame gliukozės ir fruktozės santykis 45:55, buvo sudaryta matematiškai, remiantis pavienių redukuojančių cukrų kalibracinėmis kreivėmis (16 pav., A ir B dalis, 51 psl.). Nustatyta bendra redukuojančių cukrų mišinio koncentracija buvo 20 % mažesnė nei vertė nurodyta ant gaiviojo gėrimo „Coca-Cola“ pakuotės. Gaiviojo gėrimo matricos įtakos analiziniam signalui įvertinimui buvo atlikta AuND susidarymo reakcija, panaudojant redukuojančių cukrų neturintį gaivųjį gėrimą „Coca-Cola Zero“. Per pirmą reakcijos valandą AuND susidarymas nebuvo stebimas.

Remiantis laktozės kalibracinėmis kreivėmis (16 pav., C dalis, 51 psl.), buvo nustatyta laktozės koncentracija piene. Po 20 min nustatyta vidutinė laktozės koncentracija piene buvo 0,161 ± 0,014 M, po 40 min – 0,153 ± 0,011 M, o po 60 min – 0,135 ± 0,010 M. Ant pakuotės nurodyta laktozės koncentracija buvo 0,13 M.

Taip pat buvo vykdoma AuND susidarymo reakcija naudojant seilių mėginį. Kaip ir tikėtasi, per pirmą reakcijos valandą AuND susidarymas nebuvo stebimas, nes gliukozės koncentracija seilėse buvo mažesnė nei gliukozės aptikimo riba po 60 min. laiko tarpo. Tačiau reakciją su seilių mėginiu vykdant ilgesnį laiko tarpą, AuND susidarymas buvo stebimas. Manoma, kad gliukozės koncentraciją seilėse būtų galima nustatyti sudarius gliukozės kalibracinę kreivę po 3 val. nuo reakcijos pradžios.

IŠVADOS

1. Elektrochemiškai identiškomis sąlygomis nusodinus AuNS ant ITO ir GS elektrodo, susidarė skirtingos morfologijos struktūros. GS elektrodas modifikuotas didesniu kiekiu mažesnių apvalių $AuNS_I$, pasižymėjo iki 2 kartų didesniu elektroaktyviu paviršiaus plotu, o ant šio elektrodo paviršiaus prisijungė iki 26 % daugiau jaučio serumo albumino, lyginant su kitais AuNS modifikuotais elektrodais. Taip modifikuotas elektrodas pasižymėjo iki 2,1 karto didesniu imuninio jutiklio atsaku.
2. MND-Au buvo susintetintos ir panaudotos optinės imunoanalizinės sistemos, skirtos nustatyti ŽAH, kūrimui. Optimaliomis analizės sąlygomis ŽAH aptikimo riba buvo 0,082 nM, o tiesinis kalibravimo kreivės intervalas buvo nuo 0,1 iki 5 nM. Tai leidžia nustatyti normalią ir perteklinę kraujo serume randamą ŽAH koncentraciją.

3. AuND susidarymas, vykstantis dėl oksidacijos-redukcijos reakcijos su redukuojančiais cukrais, buvo panaudotas netiesiogiai nustatyti fruktozės, gliukozės, laktozės ir manozės koncentracijai. Ilginant reakcijos trukmę nustatoma mažesnė redukuojančio cukraus koncentracija. AuND susidarymo greitis priklauso nuo redukuojančio cukraus prigimties ir mažėja šia tvarka: fruktozė, gliukozė, laktozė, manozė.

CURRICULUM VITAE

PERSONAL INFORMATION

Name, Surname	Benediktas Brasiūnas
Email	benediktas.brasiunas@chgf.vu.lt

EDUCATION

2013 – 2017	Bachelor of Chemistry, Vilnius University.
2017 – 2019	Master of Chemistry, Vilnius University.
2019 – 2023	PhD studies, Vilnius University

PROFFESIONAL EXPERIENCE

2017-09 – 2023-09	Faculty of Chemistry and Geosciences, Vilnius university, Laboratory assistant.
2023-09 - Present	Faculty of Chemistry and Geosciences, Vilnius university, Junior assistant.
2023-09 - Present	Faculty of Chemistry and Geosciences, Vilnius university, Junior researcher.

TRAINING

2019-10	Secondment to a company “Osteoplant R&D” in Dębica, Poland. Worked and trained with electrospinning equipment. Scientific mentor: Dr. Maksym Pogorielov
2020-07	Summer school “Supramolecular and Colloid Chemistry and Physics for the Life Sciences“
2021-10 – 2021-12	Secondment to a company “Biosensors” in Rome, Italy. Worked and trained in biosensors development focusing on field deployment. Scientific mentor: Dr. Maria Teresa Giardi
2022-05	Secondment to a company “Nano Prime Sp. z o. o.” in Dębica, Poland. Worked and trained in electrochemical biosensor development. Scientific mentor: Dr. Maksym Pogorielov
2022-09 – 2022-11	Secondment to a company “Biosensors” in Rome, Italy. Worked and trained in portable biosensor development. Scientific mentor: Dr. Maria Teresa Giardi
2023-05 – 2023-06	Secondment to a company “Nano Prime Sp. z o. o.” in Dębica, Poland. Training in electrospinning techniques. Scientific mentor: Dr. Maksym Pogorielov
2023-08 – 2023-09	Secondment to a company “3D STRONG SIA” in Riga, Latvia. Training in ZnO electrodeposition techniques. Scientific mentor: Dr. Marija Korabovska
2023-11 – 2023-12	Secondment to a company “3D STRONG SIA” in Riga, Latvia. Training in integrating microfluidic systems into biosensor design. Scientific mentor: Dr. Marija Korabovska

PARTICIPATION IN CONFERENCES

1. **B. Brasiunas**, A. Popov, A. Ramanavicius, A. Ramanaviciene. Optical sensor based on gold nanoparticle formation for reducing sugar determination. 22-nd International Conference – School “Advanced Materials and Technologies 2020”, August 24-28, 2020, Palanga, Lithuania, Book of Abstracts p. 60.
2. **B. Brasiunas**, A. Popov, A. Ramanavičiene. The evaluation of kinetic optical reducing sugar sensor based on gold nanoparticle formation. „64th International Conference for Students of Physics and Natural Sciences – Open Readings“, May 16-19, 2021, Vilnius, Lithuania, Abstract Book, p. 124.
3. **B. Brasiunas**, A. Popov, A. Ramanaviciene. Unique gold nanostructures for use in electrochemical immunosensor design. „Advances in Surfaces, Interfaces and Interphases 2022“, May 15-18, 2022.
4. **B. Brasiunas**, A. Popov, A. Ramanaviciene. Sensor for the reducing sugar mixture detection based on the gold nanoparticle formation, „11th International Colloids Conference“, June 12-15, 2022, Lisbon, Portugal, Book of Abstracts, p 28.
5. **B. Brasiunas**, A. Popov, A. Ramanaviciene, Exploring the influence of various gold nanostructures on the efficiency of label-free electrochemical immunosensor design, „12th International Colloids Conference“, June 11-14, 2023, Palma, Spain.

CO-AUTHORED SCIENTIFIC PUBLICATIONS

The list of co-authored scientific publications, which are not part of the dissertation:

1. A. Ramanaviciene, A. Kausaite-Minkstimiene, A. Popov, **B. Brasiunas**, A. Ramanavicius, Chapter 12 - Design of immunosensors for rapid and sensitive detection of biomarkers, Academic Press, 2012, p. 303-333.
2. V. Liustrovaite, D. Karoblis, **B. Brasiunas**, A. Popov, A. Katelnikovas, A. Kareiva, A. Ramanavicius, R. Viter, M.T. Giardi, D. Erts, A. Ramanaviciene. Electrochemical immunosensor for the determination of antibodies against prostate-specific antigen based on ZnO nanostructures, Int. J. Mol. Sci., 2023, 24(6), 5803.
3. I. Morkvenaite-Vilkonciene, A. Kisieliute, W. Nogala, A. Popov, **B. Brasiunas**, M. Kamarauskas, A. Ramanavicius, S. Linfield, A. Ramanaviciene. Scanning electrochemical microscopy: Glucose oxidase as an electrochemical label in sandwich format immunoassay, Electrochimica Acta, 2023, 463, 142790.
4. L. Sakalauskiene, **B. Brasiunas**, A. Popov, A. Kausaite-Minkstimiene, A. Ramanaviciene. The development of reagentless amperometric glucose biosensor based on gold nanostructures, prussian blue and glucose oxidase, biosensors, 2023, 13(10), 942.
5. M. Drobysh, V. Liustrovaite, Y. Kanetski, **B. Brasiunas**, A. Zvirbliene, A. Rimkute, D. Gudas, I. Kucinskaite-Kodze, M. Simanavicius, S. Ramanavicius, R. Slibinskas, E. Ciplys, I. Plikusiene, A. Ramanavicius. Electrochemical biosensing based comparative study of monoclonal antibodies against SARS-CoV-2 nucleocapsid protein, Science of The Total Environment, 2024, 908, 168154.
6. E. Brazys, V. Ratautaite, **B. Brasiunas**, A. Ramanaviciene, L. Rodriguez, A. Pinto, D. Milea, U. Prentice, A. Ramanavicius. Molecularly imprinted polypyrrole-based electrochemical melamine sensors, Microchemical Journal, 2024, 199, 109890.
7. A. Popov, B**. Brasiunas**, K. Blazevic, A. Kausaite-Minkstimiene, A. Ramanaviciene. Ultra-sensitive electrochemical immunosensors for clinically important biomarker detection: Prospects, opportunities, and global trends, Current Opinion in Electrochemistry, In-press, 101524.

COPIES OF INCLUDED PUBLICATIONS

Paper 1

Electrodeposited gold nanostructures for the enhancement of electrochromic properties of PANI–PEDOT film deposited on transparent electrode

A. Popov, **B. Brasiunas**, A. Damaskaite, I. Plikusiene, A. Ramanavicius,
A. Ramanaviciene

Polymers, 2020, 12(12), 2778
doi.org/10.3390/polym12122778

polymers

MDPI

Article

Electrodeposited Gold Nanostructures for the Enhancement of Electrochromic Properties of PANI–PEDOT Film Deposited on Transparent Electrode

Anton Popov [1], Benediktas Brasiunas [1], Anzelika Damaskaite [1], Ieva Plikusiene [1], Arunas Ramanavicius [1,2] and Almira Ramanaviciene [1,*]

[1] NanoTechnas—Center of Nanotechnology and Materials Science, Institute of Chemistry, Faculty of Chemistry and Geosciences, Vilnius University, Naugarduko st. 24, LT-03225 Vilnius, Lithuania; anton.popov@chgf.vu.lt (A.P.); benediktas.brasiunas@chgf.vu.lt (B.B.); damaskaite@gmail.com (A.D.); ieva.plikusiene@chgf.vu.lt (I.P.); arunas.ramanavicius@chf.vu.lt (A.R.)

[2] Division of Materials Science and Electronics, State Scientific Research Institute Center for Physical Sciences and Technology, Savanorių ave. 231, LT-02300 Vilnius, Lithuania

* Correspondence: almira.ramanaviciene@chf.vu.lt; Tel.: +370-5-219-3115

Received: 10 November 2020; Accepted: 21 November 2020; Published: 24 November 2020

Abstract: Conjugated polymers (CPs) are attractive materials for use in different areas; nevertheless, the enhancement of electrochromic stability and switching time is still necessary to expand the commercialization of electrochromic devices. To our best knowledge, this is the first study demonstrating the employment of electrodeposited gold nanostructures (AuNS) for the enhancement of CPs' electrochromic properties when a transparent electrode is used as a substrate. Polyaniline–poly(3,4-ethylenedioxythiophene) (PANI-PEDOT) films were electrodeposited on a transparent indium tin oxide glass electrode, which was pre-modified by two different methods. AuNS were electrodeposited at −0.2 V constant potential for 60 s using both the 1st method (synthesis solution consisted of 3 mM $HAuCl_4$ and 0.1 M H_2SO_4) and 2nd method (15 mM $HAuCl_4$ and 1 M KNO_3) resulting in an improvement of optical contrast by 3% and 22%, respectively. Additionally, when using the 1st method, the coloration efficiency was improved by 50% while the switching time was reduced by 17%. Furthermore, in both cases, the employment of AuNS resulted in an enhancement of the electrochromic stability of the CPs layer. A further selection of AuNS pre-modification conditions with the aim to control their morphology and size can be a possible stepping stone for the further improvement of CPs electrochromic properties.

Keywords: electrochromic polymers; gold nanostructures; polyaniline; poly(3,4-ethylenedioxythiophene); conducting polymers

1. Introduction

Conjugated polymers (CPs) stand out among other electrochromic materials due to their environmental stability, flexibility, biocompatibility, and convenient electrochemical or chemical synthesis [1,2]. Such properties allow CPs to be employed in the design of displays, bioelectronics, smart windows, and electrochromic color-changing textiles [3–7]. However, further investigations of electrochromic materials including CPs are needed to change electrochromic devices such as smart windows from an expensive item to a widely used commodity [8].

A joint utilization of nanostructures with CPs can be the way to improve the desired properties of electrochromic materials. Various nanostructures such as graphene oxide [9], metal oxides [10], MXenes [11], etc. can be used in the fabrication of electrochromic devices. For instance, polyaniline (PANI) layer deposited on indium tin oxide coated glass (ITO) with graphene oxide shows an enhancement of electrochromic stability and improvement of other kinetic parameters [12]. In this context, plasmonic nanostructures are a rather promising candidate for the enhancement of desired CPs properties [13,14]. For instance, the incorporation of metallic nanoparticles into the structure of CPs can be accomplished during the synthesis by the simultaneous reduction of metal salts. Ten nm spherical gold nanoparticles (AuNPs) embedded to electrodeposited nanocomposites of polypyrrole and dye—indigo carmine—enable the enhancement of electrochromic properties such as optical contrast and switching time. In addition, higher electroactivity and lower band-gap energy have been achieved [15]. The incorporation of AuNPs and silver nanoparticles (AgNPs) to the nanocomposite of well-known and widely studied polythiophene derivative poly(3,4-ethylenedioxythiophene) (PEDOT) was performed during oxidative polymerization by Mumtaz et al. [16]. PEDOT–metal particle composites possessed increased coloration efficiency, 3–4 times enhanced contrast ratio, and 4–5 times faster switching between bleached and colored states.

Mixing nanoparticles with polymer solutions is another option of nanocomposite formation. Such a nanocomposite of PEDOT/poly(styrene sulfonate) with 3.2 nm AuNPs or 6.5 nm AgNPs possessed modified colors in colored/bleached states [13]. The incorporation of AuNPs into the structure of PANI copolymerized with *p*-aminothiophenol in the presence of poly(styrene sulfonate) (PSS) was performed by Xiong et al. [17]. Such nanohybrids possessed improved electrochemical activity and shorter switching time. The possibility to control plasmonic resonance by the insertion of gold nanocubes or nanorods to an electrochromic polymer matrix was shown previously [18,19]. An alternative approach is based on plasmonic nanostructures that are deposited on the surface. The usage of gold nanomesh structures as substrate allows for the moderation of a deposited thin PANI layer color under electrochemical switching [20]. The electrochromic polymer layer color change was monitored where an Au film with etched nanoholes [21], and Au or Al nanoslit arrays [22], were used as substrates for polymer deposition. Furthermore, a PANI layer on a metallic nanoslit exhibits faster electrochromic switching, and its color can be controlled by changing slit dimensions.

Gold nanostructures (AuNS) can be electrodeposited on the surface of various electrodes [23], wherein the morphology of deposited AuNS could be easily controlled to some extent by choosing deposition conditions, such as synthesis time, electrode potential, and the composition of the synthesis solution [24]. It is well known that optical and electrochemical properties depend on the size and morphology of AuNS [25]. According to previously discussed articles, various AuNS affect the optical and electrochromic properties of CPs differently. It can be assumed that the interaction between CPs and AuNS may vary depending on the size and morphology of AuNS.

The enhancement of electrochromic performance and stability is needed for a wider application of CPs in different areas such as smart windows and display devices [26]. Plasmonic nanostructures, which negligibly affect substrate transparency and have a positive impact on CPs' electrochromic properties, are a potentially interesting object to study.

In this work, we investigated how plasmonic nanostructures affect the electrochromic properties of CPs. To our knowledge, the effects of AuNS deposited on a transparent electrode were investigated for the first time. AuNS were synthesized on an ITO electrode and polyaniline-poly(3,4-ethylenedioxythiophene) (PANI-PEDOT) films were electrodeposited on top of ITO/AuNS substrate.

2. Experimental

2.1. Materials and Methods

3,4-Ethylenedioxythiophene (EDOT), tetrachloroauric acid trihydrate ($HAuCl_4 \cdot 3H_2O$), and ITO (15–25 Ω cm^{-1}) were purchased from Sigma-Aldrich (Steinheim, Germany). Aniline (ANI) and sodium dihydrogen phosphate monohydrate were bought from Fluka (Buchs, Switzerland). Sulfuric acid was obtained from Roth (Karlsruhe, Germany). Potassium chloride were purchased from Merck. Lithium perchlorate and acetone were bought from Alfa Aesar (Karlsruhe, Germany). Aniline was distilled once before use. All aqueous solutions were prepared with deionized water (18 MΩ·cm^{-1}).

2.2. Pre-Treatment of ITO Electrode

All electrochemical measurements were performed using a three-electrode cell and a potentiostat PGSTAT30/Autolab from ECOChemie (Utrecht, Netherlands) with GPES 4.9 software. An ITO electrode, which was cut to required size rectangles, was used as a working electrode. A platinum electrode served as a counter electrode and an $Ag/AgCl_{(3M\ KCl)}$ electrode from CH Instruments (Austin, TX, USA) was used as a reference. Before synthesis, the ITO electrode was washed with acetone and then sequentially treated by ultrasound for 15 min each in acetone and water. Additionally, the ITO electrode was cleaned by potential cycling between 0 and +1 V in 50 mM phosphate-buffered saline (PBS), pH 6, with 0.1 M KCl and then rinsed with deionized water.

2.3. Electrodeposition of Gold Nanostructures

AuNS were electrodeposited at −0.2 V constant potential for 60 s. Two aqueous synthesis solutions were used for the formation of AuNS differing in morphology and shape. For the 1st synthesis method, the solution from which $AuNS_I$ were formed consisted of 3 mM $HAuCl_4$ and 0.1 M H_2SO_4, while the 2nd synthesis method solution consisted of 15 mM $HAuCl_4$ and 1 M KNO_3 ($AuNS_{II}$). After AuNS were formed on an ITO electrode, the layer was carefully washed with deionized water and left to dry in air.

2.4. Preparation of Polymer Films

PANI-PEDOT films were electrodeposited using the cyclic voltammetry method with a three-electrode electrochemical cell by our previously reported method [3]. Electrodeposition was performed from a water-based solution consisting of 0.2 M ANI, 0.01 M EDOT, 0.2 M H_2SO_4, and 0.1 M $LiClO_4$ as the supporting electrolyte. The voltage was swept between 0 and +1.1 V with a potential sweep rate of 50 mV s^{-1} for 10 cycles. After electrodeposition, synthesized polymer films were gently rinsed with deionized water to remove the oligomers and inorganic salt from the surface of the polymer layer.

2.5. Characterization of AuNS and PANI-PEDOT Films

An electrochemically active area of formed AuNS was determined for both synthesis methods using the cyclic voltamperometry method where the ITO/AuNS electrode was submerged in 0.5 M H_2SO_4 solution and the potential was cycled between 0 and +1.4 V at the potential sweep rate of 50, 100, and 150 mV s^{-1}. The electrochemically active area (Γ) was calculated using this equation [27]:

$$\Gamma = \frac{A}{\nu \cdot 400\ \mu C\ cm^{-1}} \tag{1}$$

where A—the area of the cathodic current, ν—the potential sweep rate, and 400 µC cm^{-1}—the charge density per unit area associated with the electrochemical reduction of a monolayer of chemisorbed oxygen on polycrystalline gold [28].

The color of electrodeposited AuNS was evaluated using a Flame spectrometer with a tungsten halogen light source HL 2000 (OceanOptics, Dunedin, FL, USA). A white standard WS-1-SL and reflection probe QR400-7-VIS-NIR were used for calibrating the flame spectrometer before measurements. The CIELAB 1976 color space coordinates [29] were selected for the evaluation of the ITO/AuNS sample color.

The polycrystallinity of AuNS was determined by performing the X-ray diffraction method (XRD) using MiniFlex II diffractometer (Rigaku, Tokyo, Japan). XRD was performed in the angle range of

10° to 80° with a rate of 5° per minute. The shape of gold nanostructures for both synthesis methods and the morphology of PANI/PEDOT films deposited on ITO/AuNS were analyzed using scanning electron microscope SU-70 (SEM) (Hitachi, Krefeld, Germany).

The absorbance spectra of AuNS and PANI-PEDOT films were determined using a UV-Vis spectrometer Lambda 25 (Perkin Elmer, Waltham, MA, USA) and were registered in the range from 400 to 1100 nm. The thickness of the polymer layers was evaluated by atomic force microscope BioScope Catalyst (Bruker, Billerica, MA, USA). A gold-coated silicon nitride cantilever (spring constant 0.06 N m^{-1}, resonant frequency 24 kHz) was used. AFM measurements were performed in contact mode at the junction of the polymer and ITO left after scratching polymer layers with a soft plastic stick.

2.6. Electrochromic Switching

Measurements of electrochromic performance of PANI-PEDOT layers were performed using the same potentiostat and 3-electrode system, which was used for AuNS and polymers deposition. Potential was cycled between −0.1 and +0.5 V, while the absorbance of PANI-PEDOT layers was registered at the same time. PANI-PEDOT layers deposited on a bare and AuNS-coated ITO electrode were compared using an absorbance value at λ_{max} of the polymer's colored state.

3. Results

AuNS with different shapes and morphology were electrodeposited onto a pre-cleaned ITO electrode using two methods. During the 1st synthesis method, deposition was performed from a water-based solution consisting of 3 mM $HAuCl_4$ and 0.1 M H_2SO_4 ($AuNS_I$), while the 2nd method used 15 mM $HAuCl_4$ and 1 M KNO_3 ($AuNS_{II}$). In both cases, electrochemical deposition was performed at a constant −0.2 V working electrode potential vs. $Ag/AgCl_{(3M\ KCl)}$ reference electrode for 60 s. The chronoamperograms registered during electrochemical deposition are presented in Figure 1. During the synthesis, there was a clear visual indication that AuNS were depositing on ITO because the color of the formed AuNS layer was becoming more intensive with time using both AuNS formation methods. After the synthesis, colors of $AuNS_I$ and $AuNS_{II}$ were light gray (L* = 47.2, a* = −2.1, b* = 10.3) and intense dark-orange (L* = 50.6, a* = 20.0, b* = 20.6), respectively.

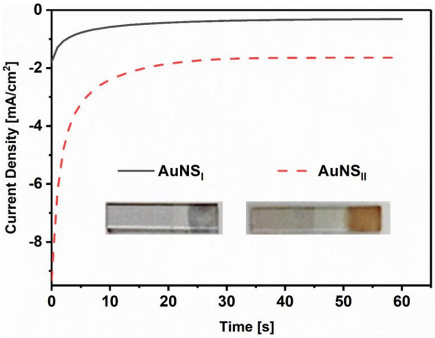

Figure 1. Electrochemical deposition of gold nanostructures (AuNS) on an indium tin oxide (ITO) electrode. Inset: Photographic pictures of ITO/AuNS electrodes after electrodeposition from different solutions.

The morphology of synthesized AuNS was evaluated using the SEM imaging technique (Figure 2). Using the 1st method, anisotropic "hedgehog" shape AuNS, which were around 200–500 nm in size, were deposited on an ITO electrode. AuNS were located randomly at various distances apart from one another. On the contrary, significantly larger dendritic microstructures with branches were observed after AuNS synthesis using the 2nd method. Higher $HAuCl_4$ concentration in the case of the 2nd method possibly had an impact on the formation of larger AuNS. Similar structures were registered when AuNS were electrodeposited on an ITO electrode by applying −0.3 V for 3600 s [30]. It is well known that the morphology and shape of AuNS depend on the applied potential, deposition time, and the composition of the synthesis solution [24]. In our case, the reason for such a difference in AuNS morphology possibly lies in the choice of supporting electrolyte and the pH value of the initial solution. On the other hand, initial $HAuCl_4$ concentration is likely to influence the size of the AuNS rather than the morphology. The replacement of Cl^- ligands by OH^- groups in $AuCl_4{}^-$ ion tends to decrease the nucleation rate and since the gold complex degree of hydrolysis depends on the pH, more reactive Au complexes are present in acidic solutions. In turn, this leads to the formation of a larger number of synthesis nuclei at acidic conditions [31]. Therefore, as expected, a larger number of smaller AuNS were deposited using the 1st method.

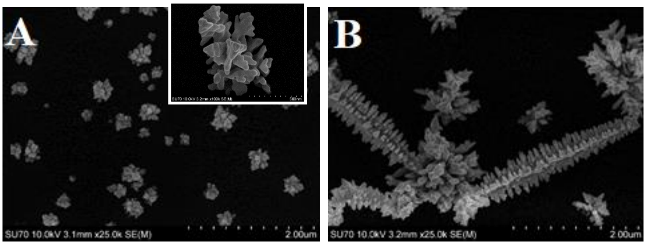

Figure 2. SEM images of (**A**) ITO/$AuNS_I$ and (**B**) ITO/$AuNS_{II}$ deposited at −0.2 V for 60 s from a water-based solutions.

Oxygen adsorption measurements were chosen to determine the electroactive surface area of synthesized AuNS [32]. Figure 3 represents ITO/AuNS cyclic voltammograms collected in 0.5 M H_2SO_4 solution. Electrochemical gold oxide formation and subsequent reduction were observed. The electroactive surface area was found to be 0.19 ± 0.03 cm^2 and 1.44 ± 0.17 cm^2 for AuNS synthesized using the 1st and 2nd method respectively.

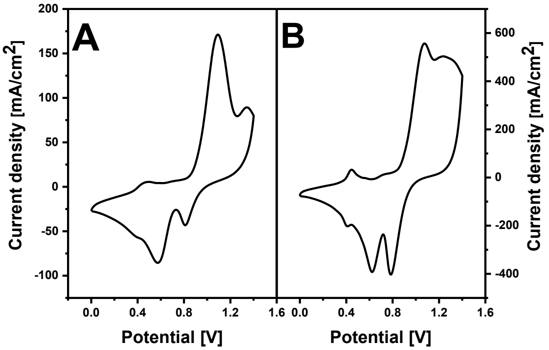

Figure 3. Cyclic voltammograms of (**A**) ITO/$AuNS_I$ and (**B**) ITO/$AuNS_{II}$ recorded in 0.5 M H_2SO_4 solution. The potential sweep rate was 150 mV s^{-1}.

Cyclic voltammograms also displayed a broad region of gold oxide reduction. In both cases, three oxidation and three reduction peaks were registered. This fact reveals the polycrystalline nature of synthesized AuNS [33]. The position of oxidation/reduction peaks depends on the crystallographic orientation of the gold surface [34]. The oxidation peak observed with both methods at around +1.3 V is attributed to the Au (111) plane [35]. Additional XRD measurements were performed for the determination of the AuNS crystalline structure (Figure 4). The results clearly indicate that the formed AuNS are polycrystalline. All patterns have the lines of Au(111), Au(200), Au(220), and Au(311) crystal faces. It illustrates the fcc crystalline structure of AuNS [35]. In both cases, the intensity of the Au(111) diffraction peak was much stronger when compared to others. The ratio of gold and ITO facets intensities was higher for ITO/AuNS$_{II}$. These results coincide with CV measurements and indicate that a higher amount of gold was deposited using the 2nd method.

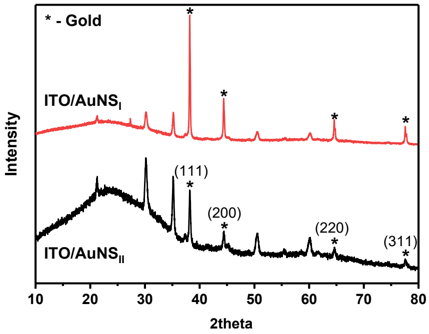

Figure 4. XRD patterns of AuNS deposited on an ITO electrode.

Since electrodeposition was performed on a transparent ITO electrode, the optical properties of AuNS could be conveniently studied using the UV-Vis-NIR spectroscopy method. Absorption spectra were recorded in the range from 400 to 1100 nm (Figure 5). In the absorption spectra of AuNS$_I$, three maxima at 460, 590, and 960 nm were registered. In the case of AuNS$_{II}$, only two peaks at 584 nm and 980 nm were observed. The broad peaks at 960 nm for AuNS$_I$ and at 980 nm for AuNS$_{II}$ are present due to in-plane dipole resonance, whereas peaks at visible parts of the spectrum are attributed to the out-of-plane dipole resonance [36]. In comparison, surface plasmon resonance (SPR) peaks at 550 nm and at about 940 nm were registered in the spectra of Au nanoplates synthesized on an ITO electrode [37,38]. Differences in the absorbance intensity of AuNS and the position of λ_{max} can be explained by the distinctions in shape, morphology, aspect ratio, and sizes of AuNS synthesized using different methods [39,40]. For instance, local roughness can affect the AuNS optical properties [41]. In addition, the broad absorption throughout the whole visible spectra can likely be attributed to an uneven AuNS size on the surface, resulting in continuous absorption and diffraction at various wavelengths. Furthermore, our results showed that the active surface area of AuNS synthesized using the 2nd method was much larger, which possibly represents the differences in AuNS absorbance intensity between synthesis methods.

PANI-PEDOT layers were electrochemically deposited on the surface of ITO/AuNS$_I$ and ITO/AuNS$_{II}$ substrates (Figure 6). Moreover, the synthesis of the polymer layer was also performed on the surface of a bare ITO electrode without AuNS to be used as a control sample. Typical cyclic voltammograms were monitored during PANI-PEDOT electrodeposition on ITO/AuNS [3]. The formation of a "nucleation loop" during the first few cycles can be associated with the reaction between PANI and PEDOT monomers and the formation of their oligomers [42]. PANI polymerization is confirmed by the presence of oxidation peaks at +0.55 V and +0.75 V in the case of electrodeposition on ITO/AuNS$_I$ and at +0.61 V and +0.80 V in the case of an ITO/AuNS$_{II}$ substrate. The first peak in both cases represents the formation of breakdown products such as p-benzoquinone and hydroquinone [43]. Oxidation peaks at +0.75 V and +0.80 V are related to the formation of a PANI polymerization chain by the generation of diradical–dications, while at potential higher than +0.80 V, an interaction of diradical–dications and PANI monomers takes place [44]. It is also worth noting that PEDOT polymerization occurs in the range from +1 to +1.1 V [45]. According to our previous work [3], a PANI and PEDOT composite is formed during polymerization, since the formation of aniline radicals and EDOT polymerization take place at significantly different potentials.

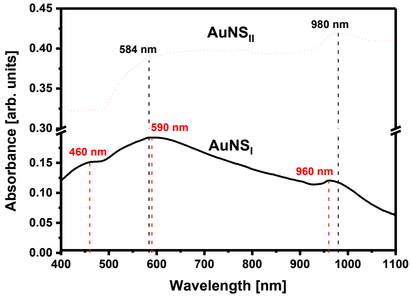

Figure 5. Absorption spectra of AuNS deposited on an ITO electrode.

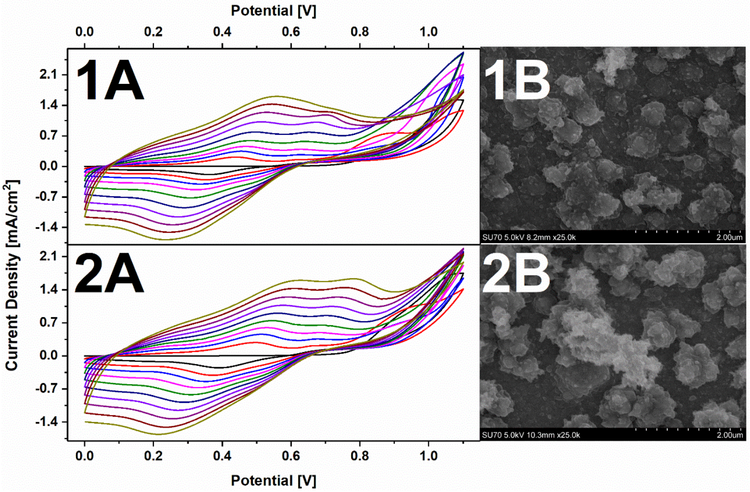

Figure 6. (**A**) Cyclic voltammograms obtained during the synthesis and (**B**) SEM images of polyaniline–poly(3,4-ethylenedioxythiophene) (PANI-PEDOT) films on (**1**) ITO/AuNS$_I$ and (**2**) ITO/AuNS$_{II}$ electrodes. Electrochemical synthesis was performed in 0.2 M H_2SO_4 solution containing 0.1 M $LiClO_4$, the sweep rate of the electrode potential was 50 mV s^{-1}.

The morphology of the synthesized PANI-PEDOT layers did not change regardless of the method used for AuNS formation (Figure 6). Moreover, the surface of the electrodeposited nanocomposite was similar to the surface of the PANI-PEDOT layer deposited on the bare ITO electrode. Observed globular structures are attributed to the PEDOT polymer, wherein lump-like and fibrous clumps are characteristic features of PANI structures [3].

Since the deposition of PANI-PEDOT layers was performed under the same conditions for the bare ITO electrode and ITO/AuNS electrodes, it was theorized that the thickness of the polymer layers will be the same regardless of the increase in surface area observed due to the formation of AuNS, since the growth after a first few electrodeposition cycles continues on the freshly formed polymer layer. AFM measurements in contact mode (Figure 7) were performed to confirm this statement.

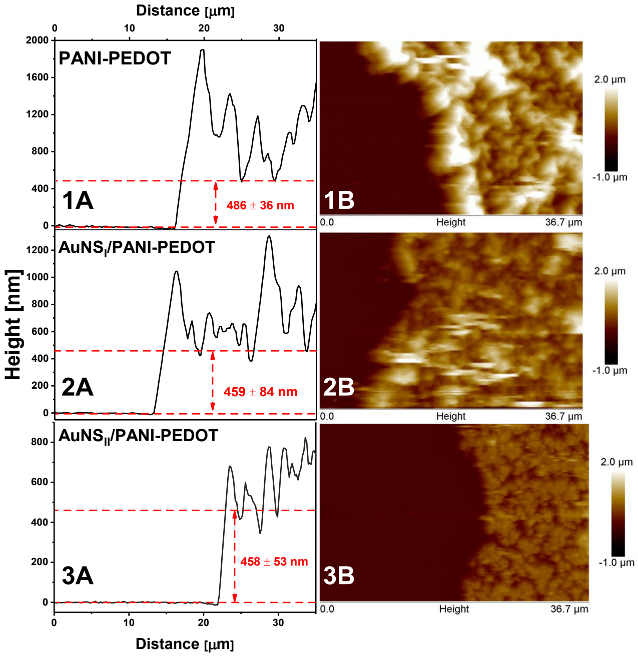

Figure 7. The surface topography evaluation of a PANI-PEDOT layer deposited on (**1**) ITO, (**2**) ITO/AuNS$_I$, and (**3**) ITO/AuNS$_{II}$ obtained by AFM. The surface section (**A**) and 2D AFM image (**B**) are presented.

Morphology typical for electrodeposited polymers was determined. A large number of irregularities were present in all cases on the PANI-PEDOT surface, resulting in relatively rough polymer layers. The layer thickness was similar for all different substrates. For bare ITO, ITO/AuNS$_I$, and ITO/AuNS$_{II}$, it was equal to 486 ± 36 nm, 459 ± 84 nm, and 458 ± 53 nm, respectively. The same effect was observed in the literature where the PANI layer was electrochemically deposited on a flat gold surface and gold nanomesh substrates [20].

The electrochromic performance of the prepared polymer layers was investigated by the spectrochronoamperometry method. Primarily, absorbance spectra were registered after applying

−0.1 or +0.5 V potential to the polymer layers (Figure 8A). After applying +0.5 V (colored state), a slight shift in the position of absorption maximum from 623 to 628 nm was observed in the case of the PANI-PEDOT layer deposited on the AuNS$_{II}$ substrate compared with other substrates. A similar effect for the absorption minimum was monitored while in a bleached state (−0.1 V) wherein a more significant λ_{min} red shift from 501 to 541 nm was detected. A similar large red shift of absorbance maximum in the colored state was reported by Shahabuddin et al. where the PANI layer was deposited on nanomesh gold structures [20]. Those results were obtained in reflection mode, and the red shift was observed in comparison with the PANI layer deposited on a flat gold surface. It clearly illustrates that such an effect is achieved due to the presence of gold nanostructures. However, in our case, only AuNS$_{II}$ resulted in such a shift. It could possibly be explained by the different interaction between polymers and AuNS.

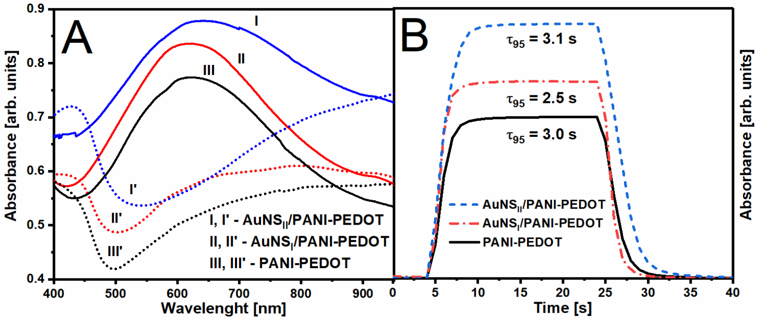

Figure 8. (**A**) Absorbance spectra of the PANI-PEDOT layer deposited on different substrates under (**dotted lines**) −0.1 V and (**solid lines**) +0.5 V applied potential. (**B**) Absorbance at λ_{max} dependency on time during electrochromic switching between −0.1 and +0.5 V potential (measurements were done in 0.2 M H_2SO_4 and 0.1 M $LiClO_4$ solution when potential was applied vs. Ag/AgCl electrode).

Switching time (τ_{95}) is an important kinetic parameter for comparing electrochromic materials. In this study, the response was calculated as the time that is needed for an optical change of 95% to happen between colored and bleached states (Figure 8B). The optical change was monitored at λ_{max}, which was observed in the colored state (+0.5 V) of the PANI-PEDOT layers. In the case of the ITO/AuNS$_{II}$ substrate, the switching time slightly increases from 3.0 to 3.1 s when compared to PANI-PEDOT on a bare ITO electrode, wherein τ_{95} using AuNS$_I$ on the contrary decreases to 2.5 s. A comparable reduction of switching time was obtained after the incorporation of gold nanoparticles to the nanocomposite of indigo carmine-doped polypyrrole [15]. The usage of AuNS in both cases led not only to the increase of background absorbance (Figure 8A) but also to the improvement of optical contrast (ΔT) (Table 1). This difference can be associated with the variation in size and surface concentration of gold nanostructures.

Table 1. Electrochromic properties of the PANI-PEDOT layer deposited on different substrates.

Substrate	N	Q [mC cm^{-2}]	T_c/T_b [%]	ΔT [%]	CE [cm^2 C^{-1}]
ITO	1	5.6	29.4/20.7	8.7	21.7
	150	2.3	28.6/26.0	2.6	14.3
ITO/AuNS$_I$	1	4.8	24.9/15.9	9.0	32.8
	150	2.5	25.1/21.0	4.1	24.5
ITO/AuNS$_{II}$	1	10.0	23.8/13.2	10.6	20.5
	150	3.8	23.5/18.8	4.7	14.5

Additional experiments were done for the evaluation of the influence of AuNS on polymer's electrochromic performance and cycling stability. Electrochromic switching between −0.1 and +0.5 V was performed for 150 cycles (Figure 9). Optical change was monitored at the same wavelengths as were used in the previous experiment. Coloration efficiency (*CE*) was calculated according to the following Equations [46]:

$$\Delta QD = log\left(\frac{T_b}{T_c}\right) \qquad\qquad CE = \frac{\Delta QD}{Q} \tag{2}$$

where ΔQD is optical density change, which was calculated using transmittance values of polymer's bleached (T_b) and colored (T_c) states, and Q is the electronic charge consumed per unit area.

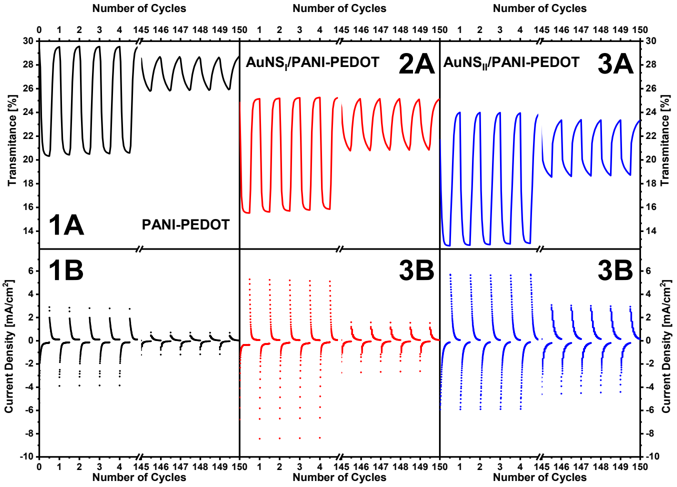

Figure 9. (**A**) Transmittance curves at λ_{max} and (**B**) chronoamperometry results of PANI-PEDOT layers synthesized on (**1**) ITO, (**2**) ITO/AuNS$_I$ and (**3**) ITO/AuNS$_{II}$ registered in 0.2 M H_2SO_4 with 0.1 M $LiClO_4$ solution. First 5 and last 146–150 cycles are displayed. The potential was switched between −0.1 V and +0.5 V vs. Ag/AgCl for 10 s at each step.

It can obviously be seen that AuNS affect the electrochromic performance of the PANI-PEDOT layer. The addition of AuNS$_I$ to the system results in an increase of *CE* value from 21.7 to 32.8 cm^2 C^{-1}. The value of ΔT improves from 8.7% to 9.0% when compared with PANI-PEDOT on a bare ITO electrode. On the other hand, optical contrast was higher (10.6%) when AuNS$_{II}$ were used; however, the calculated *CE* value was practically the same compared with PANI-PEDOT on a bare ITO electrode. These results go hand in hand with the data from switching time measurements, with AuNS$_I$ providing the best results. A minor decrease in the transmittance of the investigated layers is monitored due to the AuNS interaction with light (absorbance, diffraction, etc.). Additionally, samples with AuNS showed better electrochromic stability. After 150 cycles of electrochromic switching, the ΔT value of the PANI-PEDOT layer deposited on the bare ITO electrode decreases about 1.5 times more in comparison with that determined for the polymer layers deposited on ITO/AuNS, wherein *CE* values decrease relatively equally. The observable and expected decrease of optical contrast is associated with dopants leaching out of the polymer during electrochromic switching accompanied by changes in structure and conformation due to the accumulation of extra charges in the chains [15].

The deposition of plasmonic nanostructures typically allows for the increase of electrode surface area, thereby possibly affecting charge transport kinetics due to interface effects [20,47]. These effects are related to a quite low work function value for AuNS. For instance, gold nanoparticles with values of 3.4 eV and 3.6 eV were recently described in the literature [48,49]. In our case, it is important to pay attention to the work function value of ITO being approximately equal to 4.5 eV [50], while that of PANI is 4.42 eV [51], and PEDOT in the form of a mixture with PSS has been reported from 4.7 to 5.4 eV [52]. Therefore, the change in electrochromic properties due to the formation of the depletion layer and Schottky barrier in polymers, which are p-type semiconductors, is expected [20]. Different effects on electrochromic properties can be associated with a distinct work function for particular gold nanostructures. Previously, it was shown that the work function [53] and electron affinity [54] of gold clusters depend on their size.

4. Conclusions

The enhancement of the electrochromic properties of the PANI-PEDOT layer, which was provided by AuNS deposited on an ITO electrode, has been observed. Such an easy and low-cost method of substrate pre-modification can be used for further improvements of various electrochromic devices based on conducting polymers. This research demonstrated that the electrochemical and optical properties of AuNS can be controlled by changing electrodeposition parameters. We believe that future investigations will allow for the selection of AuNS synthesis conditions that result in better optical transmittance while possessing enough significant positive effects on the electrochromic properties of conducting polymers. In addition, the possibility to increase the optical contrast and to control the color of the CPs layer could reduce the need for combining several CPs to achieve a full-color gamut during the fabrication of electrochromic devices. Moreover, the electrodeposition of other plasmonic nanostructured materials can potentially be used to tune the electrochromic properties of CPs. Thus, the use of transparent substrates with nanostructures can allow extending possible areas of CPs' application in smart windows and flexible electrochromic displays.

Author Contributions: Conceptualization, A.P. and A.R. (Almira Ramanaviciene); methodology, A.P., B.B., A.R. (Arunas Ramanavicius) and A.R. (Almira Ramanaviciene); software, A.P., B.B. and I.P.; validation, A.P. and B.B.; formal analysis, A.P. and B.B.; investigation, A.P., A.D. and B.B.; resources, A.R.(Almira Ramanaviciene); data curation, A.P. and B.B.; writing—original draft preparation, A.P., B.B., I.P., A.R. (Arunas Ramanavicius) and A.R. (Almira Ramanaviciene); writing—review and editing, A.P., B.B., I.P., A.R. (Arunas Ramanavicius) and A.R. (Almira Ramanaviciene); visualization, A.P., B.B and I.P.; supervision, A.P. and A.R. (Almira Ramanaviciene); project administration, A.R. (Almira Ramanaviciene); funding acquisition, A.R. (Arunas Ramanavicius). All authors have read and agreed to the published version of the manuscript.

Funding: This project has received funding from European Regional Development Fund (project No 01.2.2-LMT-K-718-01-0063) under grant agreement with the Research Council of Lithuania (LMTLT).

Conflicts of Interest: The authors declare no conflict of interest.

References

1. Spychalska, K.; Zajac, D.; Baluta, S.; Halicka, K.; Cabaj, J. Functional polymers structures for (Bio)sensing application—A review. *Polymers* **2020**, *12*, 1154. [CrossRef] [PubMed]
2. Deshmukh, M.A.; Gicevicius, M.; Ramanaviciene, A.; Shirsat, M.D.; Viter, R.; Ramanavicius, A. Hybrid electrochemical/electrochromic Cu(II) ion sensor prototype based on PANI/ITO-electrode. *Sens. Actuators B Chem.* **2017**, *248*, 527–535. [CrossRef]
3. Popov, A.; Brasiunas, B.; Mikoliunaite, L.; Bagdziunas, G.; Ramanavicius, A.; Ramanaviciene, A. Comparative study of polyaniline (PANI), poly(3,4-ethylenedioxythiophene) (PEDOT) and PANI-PEDOT films electrochemically deposited on transparent indium thin oxide based electrodes. *Polymer* **2019**, *172*, 133–141. [CrossRef]
4. Mantione, D.; del Agua, I.; Sanchez-Sanchez, A.; Mecerreyes, D. Poly(3,4-ethylenedioxythiophene) (PEDOT) derivatives: Innovative conductive polymers for bioelectronics. *Polymers* **2017**, *9*, 354. [CrossRef]

5. Le, T.-H.; Kim, Y.; Yoon, H. Electrical and electrochemical properties of conducting polymers. *Polymers* **2017**, *9*, 150. [CrossRef]
6. Celiesiute, R.; Ramanaviciene, A.; Gicevicius, M.; Ramanavicius, A. Electrochromic sensors based on conducting polymers, metal oxides, and coordination complexes. *Crit. Rev. Anal. Chem.* **2019**, *49*, 195–208. [CrossRef]
7. Wang, H.; Yao, C.-J.; Nie, H.-J.; Yang, L.; Mei, S.; Zhang, Q. Recent progress in integrated functional electrochromic energy storage devices. *J. Mater. Chem. C* **2020**. [CrossRef]
8. Kraft, A. Electrochromism: A fascinating branch of electrochemistry. *ChemTexts* **2019**, *5*, 1. [CrossRef]
9. Shi, Y.; Zhang, Y.; Tang, K.; Song, Y.; Cui, J.; Shu, X.; Wang, Y.; Liu, J.; Wu, Y. In situ growth of PEDOT/graphene oxide nanostructures with enhanced electrochromic performance. *RSC Adv.* **2018**, *8*, 13679–13685. [CrossRef]
10. Zheng, J.; Chen, L.; Liu, S.; Sun, C.; Hu, X.; Zhou, S. MoO3@PEDOT coaxial heterostructure nanobelts by in situ polymerization with enhanced electrochromic performance. *Mater. Res. Express* **2019**, *6*, 1150h8. [CrossRef]
11. Li, J.; Levitt, A.; Kurra, N.; Juan, K.; Noriega, N.; Xiao, X.; Wang, X.; Wang, H.; Alshareef, H.N.; Gogotsi, Y. MXene-conducting polymer electrochromic microsupercapacitors. *Energy Storage Mater.* **2019**, *20*, 455–461. [CrossRef]
12. Zhao, L.; Zhao, L.; Xu, Y.; Qiu, T.; Zhi, L.; Shi, G. Polyaniline electrochromic devices with transparent graphene electrodes. *Electrochim. Acta* **2009**, *55*, 491–497. [CrossRef]
13. Pacios, R.; Marcilla, R.; Pozo-Gonzalo, C.; Pomposo, J.A.; Grande, H.; Aizpurua, J.; Mecerreyes, D. Combined electrochromic and plasmonic optical responses in conducting polymer/metal nanoparticle films. *J. Nanosci. Nanotechnol.* **2007**, *7*, 2938–2941. [CrossRef] [PubMed]
14. Mikoliunaite, L.; Kubiliute, R.; Popov, A.; Voronovič, J.; Šakirzanovas, S.; Ramanavičiene, A.; Ramanavičius, A. Development of gold nanoparticle-polypyrrole nanocomposites. *Chemija* **2014**, *25*, 63–69.
15. Loguercio, L.F.; Alves, C.C.; Thesing, A.; Ferreira, J. Enhanced electrochromic properties of a polypyrrole-indigo carmine-gold nanoparticles nanocomposite. *Phys. Chem. Chem. Phys.* **2015**, *17*, 1234–1240. [CrossRef]
16. Mumtaz, M.; Ouvrard, B.; Maillaud, L.; Labrugere, C.; Cloutet, E.; Cramail, H.; Delville, M.-H. Hybrid PEDOT-metal nanoparticles—New substitutes for PEDOT:PSS in electrochromic layers—Towards improved performance. *Eur. J. Inorg. Chem.* **2012**, *2012*, 5360–5370. [CrossRef]
17. Xiong, S.; Lan, J.; Yin, S.; Wang, Y.; Kong, Z.; Gong, M.; Wu, B.; Chu, J.; Wang, X.; Zhang, R.; et al. Enhancing the electrochromic properties of polyaniline via coordinate bond tethering the polyaniline with gold colloids. *Sol. Energy Mater. Sol. Cells* **2018**, *177*, 134–141. [CrossRef]
18. König, T.A.F.; Ledin, P.A.; Kerszulis, J.; Mahmoud, M.A.; El-Sayed, M.A.; Reynolds, J.R.; Tsukruk, V.V. Electrically tunable plasmonic behavior of nanocube-polymer nanomaterials induced by a redox-active electrochromic polymer. *ACS Nano* **2014**, *8*, 6182–6192. [CrossRef]
19. Ledin, P.A.; Jeon, J.W.; Geldmeier, J.A.; Ponder, J.F.; Mahmoud, M.A.; El-Sayed, M.; Reynolds, J.R.; Tsukruk, V.V. Design of hybrid electrochromic materials with large electrical modulation of plasmonic resonances. *ACS Appl. Mater. Interfaces* **2016**, *8*, 13064–13075. [CrossRef]
20. Shahabuddin, M.; McDowell, T.; Bonner, C.E.; Noginova, N. Enhancement of electrochromic polymer switching in plasmonic nanostructured environment. *ACS Appl. Nano Mater.* **2019**, *2*, 1713–1719. [CrossRef]
21. Zhang, S.; Yu, S.; Zhou, J.; Ponder, J.F.; Smith, M.J.; Reynolds, J.R.; Tsukruk, V.V. Heterogeneous forward and backward scattering modulation by polymer-infused plasmonic nanohole arrays. *J. Mater. Chem. C* **2019**, *7*, 3090–3099. [CrossRef]
22. Xu, T.; Walter, E.C.; Agrawal, A.; Bohn, C.; Velmurugan, J.; Zhu, W.; Lezec, H.J.; Talin, A.A. High-contrast and fast electrochromic switching enabled by plasmonics. *Nat. Commun.* **2016**, *7*, 1–6. [CrossRef] [PubMed]
23. Feng, L.; Niu, M.; Wen, Z.; Hao, X. Recent advances of plasmonic organic solar cells: Photophysical investigations. *Polymers* **2018**, *10*, 123. [CrossRef] [PubMed]
24. Terao, K.; Kakita, C.; Nagase, N.; Miyanishi, N.; Suzuki, T.; Takao, H.; Shimokawa, F.; Oohira, F. Evaluation of electrodeposited gold nanostructures for applications in QCM sensing. *Anal. Sci.* **2012**, *28*, 291–294. [CrossRef] [PubMed]
25. Li, Y.; Shi, G. Electrochemical growth of two-dimensional gold nanostructures on a thin polypyrrole film modified ITO electrode. *J. Phys. Chem. B* **2005**, *109*, 23787–23793. [CrossRef] [PubMed]
26. Yu, F.; Liu, W.; Ke, S.-W.; Kurmoo, M.; Zuo, J.-L.; Zhang, Q. Electrochromic two-dimensional covalent organic framework with a reversible dark-to-transparent switch. *Nat. Commun.* **2020**, *11*, 5534. [CrossRef]

27. Nikolaev, K.; Ermakov, S.; Ermolenko, Y.; Averyaskina, E.; Offenhäusser, A.; Mourzina, Y. A novel bioelectrochemical interface based on in situ synthesis of gold nanostructures on electrode surfaces and surface activation by Meerwein's salt. A bioelectrochemical sensor for glucose determination. *Bioelectrochemistry* **2015**, *105*, 34–43. [CrossRef]
28. Trasatti, S.; Petrii, O.A. Real surface area measurements in electrochemistry. *J. Electroanal. Chem.* **1992**, *327*, 353–376. [CrossRef]
29. Stojkoski, V.; Kert, M. Design of pH responsive textile as a sensor material for acid rain. *Polymers* **2020**, *12*, 2251. [CrossRef]
30. Shu, H.; Cao, L.; Chang, G.; He, H.; Zhang, Y.; He, Y. Direct electrodeposition of gold nanostructures onto glassy carbon electrodes for non-enzymatic detection of glucose. *Electrochim. Acta* **2014**, *132*, 524–532. [CrossRef]
31. Tran, M.; Mundt, C.; Lan, T.; Padalkar, S. Electrodeposition of gold nanostructures having controlled morphology. *J. Nanosci. Nanotechnol.* **2017**, *18*, 3492–3498. [CrossRef] [PubMed]
32. Oesch, U.; Janata, J. Electrochemical study of gold electrodes with anodic oxide films-I. Formation and reduction behaviour of anodic oxides on gold. *Electrochim. Acta* **1983**, *28*, 1237–1246. [CrossRef]
33. Plowman, B.J.; O'Mullane, A.P.; Bhargava, S.K. The active site behaviour of electrochemically synthesised gold nanomaterials. *Faraday Discuss.* **2011**, *152*, 43–62. [CrossRef] [PubMed]
34. Hamelin, A. Cyclic voltammetry at gold single-crystal surfaces. Part 1. Behaviour at low-index faces. *J. Electroanal. Chem.* **1996**, *407*, 1–11. [CrossRef]
35. Tian, Y.; Liu, H.; Zhao, G.; Tatsuma, T. Shape-controlled electrodeposition of gold nanostructures. *J. Phys. Chem. B* **2006**, *110*, 23478–23481. [CrossRef] [PubMed]
36. Millstone, J.E.; Park, S.; Shuford, K.L.; Qin, L.; Schatz, G.C.; Mirkin, C.A. Observation of a quadrupole plasmon mode for a colloidal solution of gold nanoprisms. *J. Am. Chem. Soc.* **2005**, *127*, 5312–5313. [CrossRef]
37. Sajanlal, P.R.; Pradeep, T. Growth of anisotropic gold nanostructures on conducting glass surfaces. *J. Chem. Sci.* **2008**, *120*, 79–85. [CrossRef]
38. Goy-López, S.; Castro, E.; Taboada, P.; Mosquera, V. Block copolymer-mediated synthesis of size-tunable gold nanospheres and nanoplates. *Langmuir* **2008**, *24*, 13186–13196. [CrossRef]
39. Yu, K.; Kelly, K.L.; Sakai, N.; Tatsuma, T. Morphologies and surface plasmon resonance properties of monodisperse bumpy gold nanoparticles. *Langmuir* **2008**, *24*, 5849–5854. [CrossRef]
40. Yu, Y.Y.; Chang, S.S.; Lee, C.L.; Wang, C.R.C. Gold nanorods: Electrochemical synthesis and optical properties. *J. Phys. Chem. B* **1997**, *101*, 6661–6664. [CrossRef]
41. Wang, H.; Goodrich, G.P.; Tam, F.; Oubre, C.; Nordlander, P.; Halas, N.J. Controlled texturing modifies the surface topography and plasmonic properties of Au nanoshells. *J. Phys. Chem. B* **2005**, *109*, 11083–11087. [CrossRef] [PubMed]
42. Zhou, C.; Liu, Z.; Du, X.; Ringer, S.P. Electrodeposited PEDOT films on ITO with a flower-like hierarchical structure. *Synth. Met.* **2010**, *160*, 1636–1641. [CrossRef]
43. Mirmohseni, A.; Wallace, G. Preparation and characterization of processable electroactive polyaniline–polyvinyl alcohol composite. *Polymer* **2003**, *44*, 3523–3528. [CrossRef]
44. Chen, W.-C.; Wen, T.-C.; Gopalan, A. Negative capacitance for polyaniline: An analysis via electrochemical impedance spectroscopy. *Synth. Met.* **2002**, *128*, 179–189. [CrossRef]
45. Sakmeche, N.; Aeiyach, S.; Aaron, J.-J.; Jouini, M.; Lacroix, J.C.; Lacaze, P.-C. Improvement of the electrosynthesis and physicochemical properties of poly(3,4-ethylenedioxythiophene) using a sodium dodecyl sulfate micellar aqueous medium. *Langmuir* **1999**, *15*, 2566–2574. [CrossRef]
46. Yue, H.; Kong, L.; Wang, B.; Yuan, Q.; Zhang, Y.; Du, H.; Dong, Y.; Zhao, J. Synthesis and characterization of novel D-A type neutral blue electrochromic polymers containing pyrrole[3-c]pyrrole-1,4-diketone as the acceptor units and the aromatics donor units with different planar structures. *Polymers* **2019**, *11*, 2023. [CrossRef] [PubMed]
47. Runnerstrom, E.L.; Llordés, A.; Lounis, S.D.; Milliron, D.J. Nanostructured electrochromic smart windows: Traditional materials and NIR-selective plasmonic nanocrystals. *Chem. Commun.* **2014**, *50*, 10555–10572. [CrossRef]
48. Zhang, Y.; Pluchery, O.; Caillard, L.; Lamic-Humblot, A.F.; Casale, S.; Chabal, Y.J.; Salmeron, M. Sensing the charge state of single gold nanoparticles via work function measurements. *Nano Lett.* **2015**, *15*, 51–55. [CrossRef]

49. Pluchery, O.; Zhang, Y.; Benbalagh, R.; Caillard, L.; Gallet, J.J.; Bournel, F.; Lamic-Humblot, A.F.; Salmeron, M.; Chabal, Y.J.; Rochet, F. Static and dynamic electronic characterization of organic monolayers grafted on a silicon surface. *Phys. Chem. Chem. Phys.* **2016**, *18*, 3675–3684. [CrossRef]
50. Park, Y.; Choong, V.; Gao, Y.; Hsieh, B.R.; Tang, C.W. Work function of indium tin oxide transparent conductor measured by photoelectron spectroscopy. *Appl. Phys. Lett.* **1996**, *68*, 2699–2701. [CrossRef]
51. Abdulrazzaq, O.; Bourdo, S.E.; Saini, V.; Watanabe, F.; Barnes, B.; Ghosh, A.; Biris, A.S. Tuning the work function of polyaniline via camphorsulfonic acid: An X-ray photoelectron spectroscopy investigation. *RSC Adv.* **2015**, *5*, 33–40. [CrossRef]
52. Nardes, A.M.; Kemerink, M.; de Kok, M.M.; Vinken, E.; Maturova, K.; Janssen, R.A.J. Conductivity, work function, and environmental stability of PEDOT:PSS thin films treated with sorbitol. *Org. Electron.* **2008**, *9*, 727–734. [CrossRef]
53. Abdellatif, M.H.; Ghosh, S.; Liakos, I.; Scarpellini, A.; Marras, S.; Diaspro, A.; Salerno, M. Effect of nanoscale size and medium on metal work function in oleylamine-capped gold nanocrystals. *J. Phys. Chem. Solids* **2016**, *89*, 7–14. [CrossRef]
54. Roduner, E. Size matters: Why nanomaterials are different. *Chem. Soc. Rev.* **2006**, *35*, 583–592. [CrossRef]

Paper 2

The effect of gold nanostructure morphology on label-free electrochemical immunosensor design

B. Brasiunas, A. Popov, G. Kraujelyte, A. Ramanaviciene

Bioelectrochemistry, 2024, 156, 108638
doi.org/10.1016/j.bioelechem.2023.108638

Bioelectrochemistry 156 (2024) 108638

Contents lists available at ScienceDirect

Bioelectrochemistry

journal homepage: www.journals.elsevier.com/bioelectrochemistry

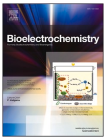

The effect of gold nanostructure morphology on label-free electrochemical immunosensor design

Benediktas Brasiunas, Anton Popov, Gabija Kraujelyte, Almira Ramanaviciene [*]

NanoTechnas - Center of Nanotechnology and Materials Science, Institute of Chemistry, Faculty of Chemistry and Geosciences, Vilnius University, Naugarduko str. 24, LT-03225 Vilnius, Lithuania

ARTICLE INFO

Keywords:
Gold nanostructures
Immunosensor
Label-free
Electroactive surface area
Heterogeneous electron transfer rate constant
Electrochemical sensor

ABSTRACT

In this research, various electrodeposition techniques were used to form gold nanostructures (AuNSs) on the surface of graphite rod electrode (GE). Three distinct AuNS morphologies on GE have been achieved based on the composition of electrodeposition solution. The use of H_2SO_4 as a supporting electrolyte resulted in the formation of smaller but more numerous $AuNS_I$ with a modified electrode's electroactive surface area (EASA) of 0.213 cm^2. Exchanging the supporting electrolyte to KNO_3 and increasing $HAuCl_4$ concentration facilitated the formation of bigger $AuNS_{II}$ particles with electrode EASA of 0.116 cm^2. Finally, a partial coverage of GE by branched gold nanostructures ($AuNS_{III}$) was achieved with an estimated EASA of 0.110 cm^2, when the $HAuCl_4$ and KNO_3 concentrations were increased further. Estimated values of heterogeneous electron transfer rate constant did not depend on AuNS morphology. Electrode modified with $AuNS_I$ exhibited the highest bovine serum albumin (BSA) immobilization efficiency and the highest relative response for the detection of specific polyclonal antibodies against BSA (p-anti-BSA) compared to other modified electrodes. The limit of p-anti-BSA detection in PBS buffer was calculated as 0.63 nM, while in blood serum it was 0.71 nM. Linear ranges were from 1 to 7 nM and from 1 to 5 nM, respectively.

1. Introduction

Nowadays, the use of nanomaterials in analytical sensor design is very promising. Various nanostructures can be employed to make analytical systems more sensitive and robust [1] as well as shorten the analysis time [2]. In other cases, nanomaterials are the groundwork for the design of the analytical sensing system playing a crucial part in the generation of the analytical signal [3] or even being basis for the detection itself [4,5].

Biosensors are specific analytical sensors that employ the biological recognition element in order to detect the desired analyte. The interaction of the analyte with the biological recognition element is converted through a signal transducer to a measurable signal that is proportional to the concentration of the analyte. Immunosensors are a branch of biosensors, where the biological recognition element is antibodies or antigens. Immunosensors are specifically designed to register the affinity interaction between the antibody and the antigen. When properly designed immunosensors are characterized by high sensitivity, stability, selectivity, and even the possibility to detect multiple analytes. However, the development of these analytical devices is subject to issues and considerations such as the amount and type of the immobilized antibodies, the proper antibody orientation on the surface to facilitate interaction with the antigen, as well as the remaining activity of antigen binding sites after immobilization. As such, factors like the biocompatibility of employed materials, proper immobilization method, and the preparation of underlying surface play an important role in the design of immunosensors [6]. The use of nanomaterials in the design of these devices can help to significantly affect beforementioned factors to our advantage. Surfaces can be nanostructured using different nanomaterials in order to improve biocompatibility [7] or enhance analytical signals [8]. Nanostructures can act as carriers transporting immobilized biomolecules to the desired location [3,9,10]. Additionally, nanomaterials can be used for labelling antibodies or antigens in order to enable detection [5,11] or improve analytical signals [7,12]. Finally, various nanostructures can act as scaffolds used for the immobilization of other analytical signal producing molecules, like enzymes, in order to improve the surface coverage of said molecules [13–17].

Electrochemical immunosensors use traditional voltammetric, impedimetric, potentiometric, amperometric, or conductometric signal detection methods in order to detect antibodies or antigens.

---

* Corresponding author.
E-mail address: almira.ramanaviciene@chf.vu.lt (A. Ramanaviciene).

https://doi.org/10.1016/j.bioelechem.2023.108638
Received 29 October 2023; Received in revised form 13 December 2023; Accepted 28 December 2023

Electrochemical immunosensors can be divided into two main groups [6]. Label-free electrochemical immunosensors employ the oxidation or reduction of the electroactive substance, like $[Fe(CN)_6]^{3-/4-}$, on the surface of the electrode [18]. In this case, the antibody-antigen interaction results in a decrease of the registered current for the oxidation/reduction of the redox probe, since the formed immunocomplex interferes with the redox probe diffusion towards the working electrode as well as hinders electron transfer [19]. The other group of electrochemical immunosensors employ antigens or antibodies with electrochemically active labels, usually enzymes such as horseradish peroxidase [16] or alkaline phosphatase [17], however, other electroactive labels can also be employed [20,21]. In this case, usually, the sandwich immunosensing format is used, where the detection antibody is conjugated with electroactive label. Labelled antibodies bind to the analyte and then are detected electrochemically either directly, or after further addition of activating molecules, like substrates in the case of enzyme labels. Although labelled electrochemical immunosensors usually exhibit higher sensitivity, the use of additional labelled antibodies significantly complicates immunosensor design. In addition, in some cases, labelled antibodies are not available for purchase or are too costly to produce. Label-free electrochemical detection is preferred due to the simpler immunosensor design as well as lower sensor production cost. In addition, produced sensors exhibit short analysis time and could be made portable and easy to use for non-professionals. Furthermore, the analysis can be performed in opaque samples, where optical detection could prove difficult [22]. On the other hand, for analysis of some analytes, label-free electrochemical immunosensors might lack the sensitivity required if the analyte is present at very low concentrations. However, the sensitivity of label-free electrochemical immunosensors can be significantly improved using nanomaterials, eliminating the major weak point.

For electrochemical detection methods, the nanostructurization of the working electrode is one of the simple ways to enhance the registered electrical signals [23]. Various different materials can be used for electrode modification, however, for electrochemical detection materials like graphene-based carbon nanotubes, or noble metal nanostructures are desirable due to their superior electrical properties which can significantly improve the electrochemical characteristics of the working electrode [24,25]. Furthermore, the use of distinct materials for the production of the underlying electrode surface and for the nanostructurization of the electrode can result in the electrode containing different surface chemistries. For example, a graphite electrode can be modified with gold nanostructures (AuNS). The presence of gold is especially useful since different techniques for biomolecule immobilization on the gold surface can be used in comparison to graphite surface. Namely, the simple covalent immobilization using self-assembled monolayers containing carboxyl groups and 1-ethyl-3-(3-dimethylaminopropyl)carbodiimide (EDC) and N-hydroxysuccinimide (NHS) chemistry [26]. Furthermore, by the development of well-placed nanostructures on the electrode surface, it is possible to form protein islands. In this way, localized immobilization of the protein is achieved, which can help in the development of SECM based immunoassays [27]. Electrodeposition is one of the straightforward techniques used to modify the working electrode with nanostructures of various shapes and sizes. Since any conductive electrode material can be used for the electrodeposition of nanostructures, cheap and simple to produce materials such as graphite can be employed, and electrically superior noble metal nanostructures can be formed on top. The electrodeposition of AuNS is simple and usually performed using aqueous solutions of $HAuCl_4$ containing various supporting electrolytes [19,24,25,28]. Different electrochemical methods can be used for AuNS electrodeposition, however, the most common are chronoamperometry and cyclic voltammetry (CV) [29,30]. During electrodeposition, $HAuCl_4$ is reduced on the working electrode through nucleation and growth processes, resulting in the formation of AuNS on the surface. Depending on the solution pH, ionic strength, the nature and concentration of supporting electrolyte, as well as electrochemical synthesis method conditions AuNS of various shapes, sizes, and morphologies can be achieved [31–34].

Regrettably, there is insufficient understanding regarding how various morphologies of nanostructured electrodes affect the response of label-free electrochemical immunosensors. As such, in this work, six solutions containing $HAuCl_4$ and different supporting electrolytes were used to electrodeposit AuNS on polished graphite rod electrodes (GE). Nanostructured electrodes with 3 distinct surface morphologies were chosen and analyzed further. Electroactive surface area and heterogeneous electron transfer rate constant were determined and compared for unmodified GE and for GE modified with various electrodeposited AuNS. Bovine serum albumin (BSA) immobilization efficiency was assessed using all electrodes with electrodeposited AuNS in order to compare how it differs depending on the surface morphology. Furthermore, all electrodes with various electrodeposited AuNS were evaluated for use in the design of label-free electrochemical immunosensing platform using BSA and specific polyclonal antibodies (p-anti-BSA) as a model antigen and antibody pair. The effects of AuNS morphology on the immunosensing platform design were explored.

2. Experimental

2.1. Materials

Hydrogen tetrachloroaurate(III) trihydrate ($HAuCl_4{\cdot}3H_2O$), 11-mercaptoundecanoic acid (11-MUA), methanol (CH_3OH), potassium ferricyanide ($K_3[Fe(CN)_6]$), and potassium ferrocyanide ($K_4[Fe(CN)_6]$) were acquired from Sigma-Aldrich (Steinheim, Germany). 1-ethyl-3-(3-dimethylaminopropyl) carbodiimide hydrochloride (EDC), sulfuric acid (H_2SO_4), PBS tablets (0.14 M NaCl, 0.0027 M KCl, 0.01 M phosphate buffer (pH 7.4)), bovine serum albumin (BSA) and Roti NanoQuant reagent were purchased from Carl Roth (Karlsruhe, Germany). N-hydrosuccinimide (NHS), and potassium nitrate (KNO_3) were obtained from Merck (Darmstadt, Germany). Graphite rods (diameter 3.0 mm, purity – 99.999 %) were purchased from Sigma-Aldrich (St. Louis, MO, USA). Polyclonal rabbit antibodies against bovine serum albumin (p-anti-BSA) were acquired from Immunology Consultants Laboratory, Inc (Portland, USA). Human blood serum was obtained from Sigma-Aldrich (St. Louis, MO, USA). All aqueous solutions were prepared with deionized water (18 MΩ·cm).

2.2. Pretreatment of the working electrode and electrodeposition of gold nanostructures

Graphite rod electrodes were polished using fine (P120), very fine (P320), and ultra-fine grit (P2000) sandpaper. Polished electrodes were washed with deionized water and dried at room temperature. The side surface of the GE was isolated using a silicone tube in order to control the working surface area resulting in an area of 0.071 cm^2. All electrochemical measurements, including electrodeposition, were performed using potentiostat/galvanostat Autolab PGSTAT30 (EcoChemie, The Netherlands) with NOVA 2.0 software. Polished GE was used as a working electrode, $Ag/AgCl_{3M\ KCl}$ was used as a reference, and Pt wire as a counter electrode. All electrochemical characterization measurements were performed in a solution consisting of 2.5 mM $K_{3/4}[Fe(CN)_6]^{3-/4-}$ and 10 mM PBS, pH 7.2.

Electrochemical deposition of AuNS was performed on polished GE by applying −0.2 V constant potential to the working electrode vs. $Ag/AgCl_{3M\ KCl}$ for 60 s. Six different synthesis solutions were tested containing different concentrations of $HAuCl_4$ and various supporting electrolytes (Fig. S1). Three synthesis solutions, resulting in distinct AuNS morphologies, were chosen for further analysis. The solution No. 1 consisted of 3 mM $HAuCl_4$ and 0.2 M H_2SO_4 and resulted in the formation of $AuNS_I$. $AuNS_{II}$ was prepared from solution No. 2 containing 10 mM $HAuCl_4$ and 0.1 M KNO_3, while $AuNS_{III}$ was electrodeposited from solution No. 3 containing 15 mM $HAuCl_4$ and 1 M KNO_3. Afterwards, modified electrodes were thoroughly washed with deionized water. The surface morphology of electrodeposited AuNS was assessed using a scanning electron microscope SU-70 (SEM) (Hitachi, Krefeld, Germany).

2.3. Electrochemical characterization of electrodes

In order to evaluate electroactive surface area (EASA) and heterogeneous electron transfer rate constant (k^0) for unmodified and AuNS-modified electrodes CV measurements were performed in a 10 mM PBS solution containing 2.5 mM $[Fe(CN)_6]^{3-/4-}$. The potential was swept between −0.2 and 0.7 V vs. $Ag/AgCl_{3M\ KCl}$ while the potential sweep rate was varied (10, 25, 50, 75, 100, and 150 $mV \cdot s^{-1}$). The 3rd cycle of cyclic voltammograms was used for the evaluation of EASA and k^0.

EASA was evaluated based on Randles-Sevcik equation at 25 °C (Eq. (1)) [35]:

$$i_p = 2.69 \times 10^5 \cdot n^{\frac{3}{2}} \cdot A \cdot D^{\frac{1}{2}} \cdot C \cdot \nu^{\frac{1}{2}} \tag{1}$$

where i_p – maximum peak current in A; n – number of electrons transferred in the redox event; A – EASA in cm^2; D – diffusion coefficient in $cm^2 \cdot s^{-1}$ ($6.40 \cdot 10^{-6}$ $cm^2 \cdot s^{-1}$ for ferrocyanide); C – concentration of electroactive species in $mol \cdot cm^{-3}$; υ – potential sweep rate in $V \cdot s^{-1}$. Since charge transfer in the cathodic region is slower than in the anodic region [36] the values of peak anodic current were used for determining electroactive surface area. EASA was evaluated from the slope of $\upsilon^{1/2}$ vs. peak anodic current of $[Fe(CN)_6]^{3-/4-}$ redox probe.

The heterogeneous electron transfer rate constant was determined based on Nicholson-Lavagnini approach [37,38]. Dimensionless kinetic parameter Ψ was calculated based on empirical equation (2):

$$\Psi = \frac{-0.6288 + 0.0021 \cdot X}{1 - 0.0017 \cdot X} \tag{2}$$

where X – the peak potential separation (ΔE_p) of the system multiplied by the number of electrons involved in the electrochemical reaction (n). Following the calculation of Ψ, the k^0 could be determined using the equation (3):

$$\Psi = k^0 \cdot \left(\frac{\pi \cdot D \cdot n \cdot \nu \cdot F}{R \cdot T}\right)^{-\frac{1}{2}} \tag{3}$$

where k^0 – heterogeneous electron transfer rate constant in $cm \cdot s^{-1}$; D - diffusion coefficient in $cm^2 \cdot s^{-1}$; n – number of electrons transferred in the redox event; υ – potential sweep rate in $V \cdot s^{-1}$; F – Faraday constant of 98,485 $C \cdot mol^{-1}$; R – universal gas constant of 8.31446 $J \cdot mol^{-1} \cdot K^{-1}$; T – temperature in K. Heterogeneous electron transfer rate constant was evaluated from the slope of $\upsilon^{-1/2}$ vs. Ψ.

2.4. Covalent binding of BSA

Bovine serum albumin was covalently immobilized on AuNS-modified electrodes by employing EDC/NHS chemistry through the formation of a self-assembled monolayer on gold nanostructures. Electrodes with electrodeposited AuNS were immersed in 1 mM 11-MUA methanol solution for 2 h. Afterwards, the electrodes were washed by subsequently immersing them in methanol and deionized water for 15 min using mixing. Furthermore, electrodes with the formed self-assembled monolayer were put in 250 μL of 1:1 mixture of 0.4 M EDC and 0.1 M NHS for 15 min. Finally, the modified electrodes with activated carboxylic groups were rinsed with deionized water and immersed in 250 μL of 100 $\mu g \cdot mL^{-1}$ BSA solution for 20 min to covalently immobilize BSA on the modified electrode surface. Electrodes with immobilized BSA were washed by immersing them in a deionized water solution for 15 min with mixing.

The amount of bound BSA was assessed using a depletion method [39]. Bradford assay was performed using Roti Nanoquant reagent. In order to determine BSA concentration in the solution, which was left after immobilization, firstly a calibration curve for BSA was constructed in the range from 1 to 100 $\mu g \cdot mL^{-1}$. The concentration of BSA in the solution left after immobilization was estimated based on this calibration curve. The amount of BSA bound to the surface of the electrode was calculated based on the depletion method, knowing the BSA concentration in the initial BSA immobilization solution (100 $\mu g \cdot mL^{-1}$) and determining the BSA concentration in the solution remaining after immobilization.

2.5. p-anti-BSA quantification in PBS solution and human blood serum

Electrodes with covalently immobilized BSA were tested for the detection and quantification of p-anti-BSA in 10 mM PBS solution and in spiked human blood serum. Differential pulse voltammetry (DPV) measurements were performed in a PBS solution containing 2.5 mM $[Fe(CN)_6]^{3-/4-}$ before and after the interaction with p-anti-BSA. For DPV measurements the potential range from −0.15 V to 0.5 V was used while pulse height was 25 mV, pulse width – 0.05 s, pulse period – 0.5 s, and potential step – 5 mV. All DPV measurements were baseline corrected. A decrease in peak anodic current after the interaction with p-anti-BSA was chosen as an analytical signal, defined as I_{blank} minus I_c, where I_{blank} is peak anodic current registered before the interaction with p-anti-BSA, and I_c – peak anodic current obtained after 30 min long interaction with p-anti-BSA. Calibration curves for quantification of p-anti-BSA were obtained in the range from 1 nM to 50 nM when measurements were performed in 10 mM PBS solution (pH 7.4), and in the range from 1 nM to 20 nM for measurements in spiked human serum. Desired p-anti-BSA concentrations for calibration curves were achieved by the subsequent addition of p-anti-BSA solution. Before measurements with spiked human serum, additional surface blocking step was performed. Electrodes modified with BSA were immersed in non-spiked human blood serum for 30 min in order to block the free surface and reduce non-specific binding for the detection of p-anti-BSA. The coefficient of determination (R^2) was evaluated using the least square method. The limit of detection (LOD) was calculated based on equation (4).

$$LOD = \frac{3\sigma}{S} \tag{4}$$

where σ – standard deviation of the sample's with the lowest p-anti-BSA concentration response; S – slope of the calibration curve.

3. Results and discussion

In this work, a platform for label-free electrochemical immunosensor design is presented. The immunosensor preparation scheme is given in Fig. 1. Three distinct surface morphologies were tested to choose the most appropriate procedure for use in label-free electrochemical immunosensor design. The detection of p-anti-BSA was done by performing DPV measurements in a PBS solution containing 2.5 mM $[Fe(CN)_6]^{3-/4-}$ redox probe.

3.1. Electrodeposition of AuNS

Electrodeposition of AuNS was performed on GE. The principle reduction reaction happening during the electrodeposition is shown in equation (5) [34].

$$AuCl^-_{4(aq)} + 3e^- \rightarrow Au_{(s)} + 4Cl^- \tag{5}$$

Electrodeposition solutions and techniques were adapted based on prior research [2]. Various AuNS morphologies were achieved on the GE depending on a synthesis solution. 6 different synthesis solutions were tested (Fig. S1), 3 of which, with different surface morphologies, were

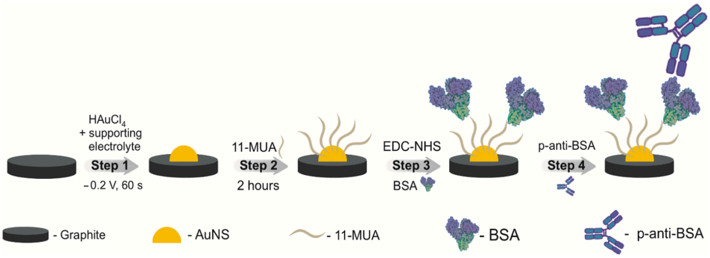

Fig 1. Immunosensor preparation scheme. Step 1 – electrodeposition of AuNS; Step 2 – formation of 11-MUA monolayer; Step 3 – surface activation using EDC/NHS and covalent BSA immobilization; Step 4 – the detection of p-anti-BSA antibodies. When working with real samples, additional surface blocking was performed using a control blood serum.

chosen for further analysis. The chosen solution No. 1 was composed of 3 mM $HAuCl_4$ and 0.2 M H_2SO_4 and led to the formation of $AuNS_I$. Solution No. 2 was made of 10 mM $HAuCl_4$ and 0.1 M KNO_3 ($AuNS_{II}$), while solution No. 3 was of 15 mM $HAuCl_4$ and 1 M KNO_3 ($AuNS_{III}$). In all cases, a constant potential of −0.2 V vs. $Ag/AgCl_{3M\ KCl}$ was applied to the GE electrode for 60 s. SEM images of GE with electrodeposited AuNS are provided in Fig. 2.

As can be seen from SEM images various AuNS morphologies can be achieved depending on synthesis solution composition. Using electrodeposition solution No. 1 (Fig. 2A), the obtained $AuNS_I$ are polydisperse and mostly circular in shape, however not the entire GE surface is covered by $AuNS_I$, leaving some of the underlying graphite rod electrode exposed. The increase in $HAuCl_4$ concentration and the use of KNO_3 as a supporting electrolyte (solution No. 2) leads to the formation of larger and less circular $AuNS_{II}$ particles compared to $AuNS_I$ (Fig. 2B). In addition, some of the AuNS particles consisted of merged smaller nanostructures. A further increase in $HAuCl_4$ and KNO_3 concentration (solution No. 3) results in the formation of a smaller number of significantly bigger branched gold structures with additional small nanoparticles created around the branched structures on GE surface ($AuNS_{III}$) (Fig. 2C). Larger magnification SEM images of GE/AuNS are provided in Fig. S2.

The analysis of all SEM images of GE modified with various electrodeposited AuNS (Fig. S1) reveals some trends for the synthesis of these nanostructures. Firstly, in the case of $AuNS_I$ electrodeposition, the use of H_2SO_4 is likely the cause of the formation of a larger number of smaller AuNS. $AuCl_4^-$ complex ion hydrolyses in aqueous solutions by exchanging Cl^- ligand for OH^- in turn decreasing the reactivity of Au (III) complex and the nucleation rate depending on the degree of hydrolysis. Since acidic condition lowers the degree of hydrolysis, during electrodeposition a larger number of smaller nanostructures are formed due to the higher nucleation rate [32]. Changing the supporting electrolyte from H_2SO_4 to KNO_3, increases the solution pH and in turn reduces the nucleation rate, leading to the formation of the lower number of particles which end up larger, since Au (III) complex ions at the electrode surface can be more readily consumed to grow already present nanoparticles instead of forming new nanoparticle nucleation points. Secondly, the use of a higher $HAuCl_4$ concentration only increases the rate of AuNS growth, leading to the formation of bigger gold nanoparticles with the overall number of particles staying mostly similar. However, it was observed that some closely located gold nanoparticles can merge into bigger structures during growth. Thirdly, the increase in KNO_3 from 0.1 to 0.2 M did not produce a significant change in the morphology of synthesized AuNS, although in the case of higher KNO_3 concentration, the surface of produced nanoparticles exhibited slightly higher uniformity and less branching. This effect seems to be more pronounced when the synthesis was performed with $HAuCl_4$ concentration of 3 mM. Finally, the significant increase in $HAuCl_4$ and KNO_3 concentrations to 15 mM and 1 M respectively facilitated the formation of bigger branched gold structures, but smaller nanoparticles were still present on GE surface.

3.2. Electrochemical characterization of electrodes

Graphite rod electrodes with various synthesized AuNS were characterized using CV method. The measurements were performed using $[Fe(CN)_6]^{3-/4-}$ redox probe while varying the potential sweep rate from 10 to 150 mV·s^{-1}. Results from CV measurements are provided in Fig. 3.

Assessing the data, it can be clearly seen that the electrodeposition of any type of AuNS on GE significantly increases recorded peak currents during oxidation and reduction of $[Fe(CN)_6]^{3-/4-}$ redox probe. Out of all AuNS electrodeposition techniques electrode modified with $AuNS_I$ showed the highest increase in registered peak currents at 2.3 times larger compared to unmodified GE (150 mV·s^{-1}), while GE/$AuNS_{II}$ and GE/$AuNS_{III}$ electrodes both produced lower but very similar current increases at 1.6 times larger than GE. Since the charge transfer in the cathodic region is slower than in the anodic region [36], the values of peak anodic current were used for determining electroactive surface

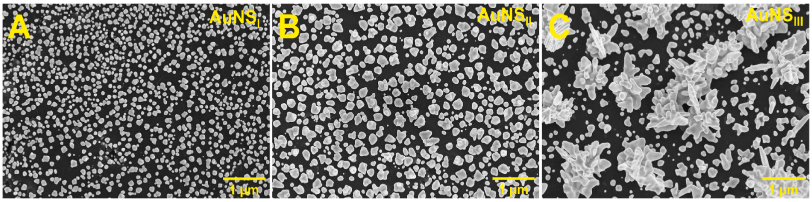

Fig 2. SEM images of GE modified with AuNS electrodeposited from (**A**) 3 mM $HAuCl_4$ and 0.2 M H_2SO_4 solution (**$AuNS_I$**), (**B**) 10 mM $HAuCl_4$ and 0.1 M KNO_3 solution (**$AuNS_{II}$**), and (**C**) 15 mM $HAuCl_4$ and 1 M KNO_3 solution (**$AuNS_{III}$**).

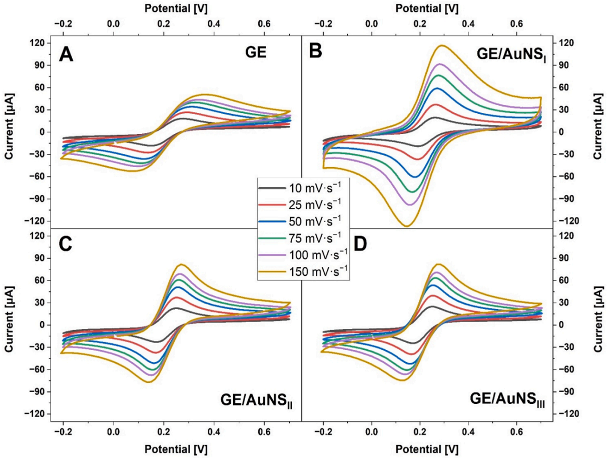

Fig 3. The 3rd cycle of cyclic voltammograms of (**A**) GE, (**B**) GE/AuNS$_I$, (**C**) GE/AuNS$_{II}$, and (**D**) GE/AuNS$_{III}$ recorded at different electrode potential sweep rates (from 10 to 150 mV·s^{-1}) in a PBS solution containing 2.5 mM $[Fe(CN)_6]^{3-/4-}$.

area using the Randles-Sevcik equation [35]. Using results from CV measurements, the $\upsilon^{1/2}$ vs. peak anodic current of $[Fe(CN)_6]^{3-/4-}$ redox probe was plotted in Fig. 4A. In order to determine the heterogeneous electron transfer rate constant Nicholson-Lavagnini approach was used [37,38]. The $\upsilon^{-1/2}$ vs. Ψ trend was plotted in Fig. 4B. Calculated values for electroactive surface area and heterogeneous electron transfer rate constants are given in Table 1.

Table 1
Calculated EASA and heterogeneous electron transfer rate constant. Error bars are expressed as sample standard deviation (n = 4).

Electrodes	Electroactive surface area, cm^2	Heterogeneous electron transfer rate constant, cm·s^{-1}
GE	0.077 ± 0.012	$1.80 \cdot 10^{-3} \pm 0.73 \cdot 10^{-3}$
GE/AuNS$_I$	0.213 ± 0.019	$4.77 \cdot 10^{-3} \pm 0.73 \cdot 10^{-3}$
GE/AuNS$_{II}$	0.116 ± 0.006	$4.26 \cdot 10^{-3} \pm 0.57 \cdot 10^{-3}$
GE/AuNS$_{III}$	0.110 ± 0.011	$4.33 \cdot 10^{-3} \pm 0.25 \cdot 10^{-3}$

The determined EASA of unmodified GE (0.077 ± 0.012 cm^2) correlates well with a geometric area of GE, which is 0.071 cm^2. Calculated EASA for electrodes with electrodeposited AuNS can be well explained by the surface morphologies provided in SEM images (Fig. 2). All AuNS electrodeposition techniques resulted in electrodes with higher EASA compared to unmodified GE. AuNS$_I$-modified GE exhibited the highest EASA, which was almost 2 times higher compared to electrodes modified with other AuNS. Looking back to SEM images, this tendency can be explained by the difference in nanostructure size and morphology. For AuNS$_I$-modified electrode sufficient gaps between nanostructures allow for unrestricted diffusion of the redox probe as well as for the increase in the surface area participating in electrochemical conversion, since both the underlying GE surface and additional AuNS surface can participate in the redox reaction. On the other hand, although the AuNS$_{II}$-modified electrode also exhibits a similar electrode surface morphology, the smaller number of larger gold nanoparticles can be attributed to the reduced EASA (0.116 cm^2) compared to the AuNS$_I$-modified electrode due to the loss of additional surface area provided by the larger number of smaller gold nanoparticles. In the case of GE/AuNS$_{III}$ electrode, we would expect the presence of branched nanostructures to significantly increase electrode surface area, however, the calculated EASA of 0.110 cm^2 indicates that the overall surface area for electrochemical conversion is similar to AuNS$_{II}$-modified electrode, likely because the extra surface area from the presence of branched gold nanostructures is negated by a more exposed flat graphite rod electrode surface around the branched particles and the lower overall number of particles.

The heterogeneous electron transfer rate constant can also be

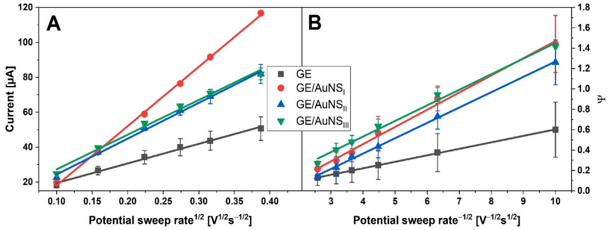

Fig 4. (**A**) The relationships between square root of the potential sweep rate and peak anodic current. (**B**) The plot of $\upsilon^{-1/2}$ vs. Ψ.

determined from CV measurements and used to evaluate the efficiency of the electron transfer process happening at the electrode-solution interface. The constants were determined for modified and unmodified electrodes with a $[Fe(CN)_6]^{3-/4-}$ redox probe. The variability of k^0 for $[Fe(CN)_6]^{3-/4-}$ using polished graphite electrodes [40–47] is large due to variations in the quality of the electrodes and their surface preparation but is often in the range of 10^{-2} – 10^{-3} cm·s^{-1}. The k^0 evaluated in this research for unmodified GE ($1.80 \cdot 10^{-3} \pm 0.73 \cdot 10^{-3}$ cm·s^{-1}) is also in this range. All AuNS electrodeposition techniques increased the electron transfer rate by a similar degree. For electrodes with electrodeposited AuNS, on average, k^0 value increased 2.5 times compared with unmodified GE. A similar increase was observed by M. Drobysh et. al. [24] when AuNS were electrodeposited on screen-printed carbon electrode. In our research, out of all AuNS electrodeposition techniques, the highest heterogeneous electron transfer rate constant on average was achieved for GE modified with AuNS$_I$ at $4.77 \cdot 10^{-3} \pm 0.73 \cdot 10^{-3}$ cm·s^{-1}, however, similar k^0 values were registered for GE/AuNS$_{II}$ and GE/AuNS$_{III}$ at $4.26 \cdot 10^{-3} \pm 0.57 \cdot 10^{-3}$ and $4.33 \cdot 10^{-3} \pm 0.25 \cdot 10^{-3}$ cm·s^{-1}, respectively. Other researchers using similar AuNS electrodeposition techniques registered comparable k^0 values for modified graphite electrodes. For example, A. Kamal et. al. reported k^0 of $1.24 \cdot 10^{-2} \pm 0.12 \cdot 10^{-2}$ cm·s^{-1} for glassy carbon electrode with electrodeposited AuNPs [19]. The direct comparison of heterogeneous electron transfer rate constants between different research papers remains difficult, due to the kinetic effects of specific electrode materials as well as the use of different supporting electrolytes for the determination of k^0 [47]. However, in our case, k^0 determination is performed with the same conditions for all measured electrodes as such the changes in the value of k^0 are the result of formed AuNS. Due to the high standard deviation between samples, it is not possible to accurately assess which AuNS electrodeposition technique produces electrodes, which have the quickest electron transfer rate, however, since all AuNS modified electrodes show similar k^0 values it can be concluded that the nature of the electrode material plays a more significant role compared to the surface morphology of AuNS. As such, when comparing the electrochemical performance of electrodes with AuNS of different morphologies, the electroactive surface area is likely the main factor to be taken into consideration.

3.3. Determination of BSA immobilization efficiency on electrodes modified with AuNS

All electrodes with electrodeposited AuNS were used to evaluate the efficiency of BSA immobilization. Firstly, an 11-MUA SAM was formed on the electrodes premodified with AuNS by immersing them in a 1 mM 11-MUA methanol solution for 2 h. The SAM forms due to thiol-gold interaction creating Au-S in turn forming a monolayer on the surface of AuNS. Afterwards, the carboxylic groups of the formed monolayer were activated by immersing the modified electrode in a 1:1 mixture of 0.4 M EDC and 0.1 M NHS for 15 min. Furthermore, the GE/AuNS/11-MUA electrodes with activated carboxylic groups were immersed in 100 µg·mL^{-1} BSA solution for 20 min [26]. Covalent immobilization of BSA onto 11-MUA happens through a three-step reaction with the help of EDC/NHS resulting in amide bonds forming between the carboxyl groups of the 11-MUA and the primary amine groups of BSA [48]. The amount of bound BSA was determined based on the depletion of BSA concentration in the solution remaining after immobilization (Section 2.4) [39]. Bradford assay was used to determine BSA concentration in the solution by using Roti®Nanoquant reagent (Fig. S3). The results of the Bradford assay (Table S1) indicated that the electrode modified with AuNS$_I$ bound 5.75 ± 0.29 µg of BSA, whereas the electrodes modified with AuNS$_{II}$ and AuNS$_{III}$ bound 5.37 ± 0.26 µg and 4.55 ± 0.01 µg of BSA, respectively. Reviewing the data from the Bradford assay it can be observed that the highest amount of BSA bound to the surface was recorded for AuNS$_I$-modified electrode. On the other hand, despite having 1.8 times lower EASA, the electrode modified with AuNS$_{II}$ bound a similar but slightly lower amount of BSA. However, the electrode with AuNS$_{III}$ linked 21 % less of BSA compared to the case of AuNS$_I$. The similarity between the amount of bound BSA for AuNS$_I$ and AuNS$_{II}$ modified electrodes, in comparison to AuNS$_{III}$, indicates that smaller and rounder nanoparticles at the surface of GE allow for higher BSA immobilization efficiency compared to the bigger branched gold nanostructures. Various reasons could be attributed to observed differences. One of the factors affecting the BSA immobilization efficiency is the amount of SAM formed on the surface of AuNS. Although the initial formation of the SAM is a quick process, in order to produce a dense and uniform monolayer on AuNS a significantly longer SAM formation time of around 1 day is required [49]. However, for label-free electrochemical immunosensors, a dense and uniform layer formation is undesired due to the significant electrical isolation, which happens after SAM formation, resulting in a drop in redox probe oxidation/reduction current. As such, shorter SAM formation times are required. In our case, the 11-MUA SAM formation time of 2 h did not lead to complete coverage of AuNS surface with 11-MUA monolayer, as such, the amount of 11-MUA SAM presence on the surface can likely be directly related to the AuNS surface area. Despite the high surface area of branched AuNS$_{III}$, the sparse number of these particles likely results in a lower overall AuNS surface area compared to other AuNS morphologies. Another factor to take into consideration is steric hindrance. With the thickness of the 11-MUA monolayer being <2 nm [50] and the hydrodynamic radius of BSA at ~7 nm [51] it is reasonable to assume the covalent immobilization of BSA on the AuNS surface can hinder additional binding of the protein in the vicinity.

In addition to the Bradford assay, BSA immobilization efficiency was also analyzed with the electrochemical impedance spectroscopy (EIS) method utilizing screen printed carbon electrodes due to the better EIS response. Results extracted from EIS measurements are provided in supplementary material Fig. S4 and Table S2 display similar trends observed with already provided BSA immobilization efficiency calculations based on the Bradford method. A change in R_{ct} value can be used as a good indication for the immobilization of proteins on the electrode surface [36]. EIS measurements showed that AuNS$_I$ and AuNS$_{II}$ modified electrodes exhibited a similar increase in R_{ct} value after BSA immobilization, while for AuNS$_{III}$-modified electrode the change in R_{ct} values was 20 % lower, which is in agreement with Bradford assay results.

Overall, it is difficult to attribute which of the factors plays the most significant role, however, the results show a trend where electrodes modified with smaller but more uniformly distributed AuNS$_I$ and AuNS$_{II}$ exhibited significantly better BSA immobilization efficiencies compared to AuNS$_{III}$-modified electrode containing sparsely placed but bigger branched structures. In addition, when comparing electrodes modified with AuNS$_I$ and AuNS$_{II}$, the surface with smaller but more numerous AuNS$_I$ promoted a slightly higher BSA immobilization efficiency.

3.4. Evaluation of the effects of different gold nanostructures on the analytical signal

To choose the most effective immunosensing platform for the detection of p-anti-BSA antibodies, it is necessary to first evaluate the impact of various AuNS on the analytical signal. For this task, DPV measurements were performed on all modified electrodes before and then after 30 min interaction with 5 nM of p-anti-BSA in PBS solution, pH 7.4. Results are provided in Fig. 5.

The highest peak anodic current before the interaction with p-anti-BSA, at 28.4 ± 1.4 µA, was recorded for electrodes modified with AuNS$_I$. For AuNS$_{II}$, it was 12.8 ± 0.5 µA, and for AuNS$_{III}$ it was 7.1 ± 1.9 µA. The difference in registered currents in the case of electrodes modified with AuNS$_I$ and AuNS$_{II}$ can likely be attributed to a significant difference in EASA measured before BSA immobilization since both modified electrodes bound a similar amount of BSA. However, despite having the least amount of bound BSA, the electrode modified with AuNS$_{III}$ displayed a significantly lower peak anodic current than anticipated, based on the BSA immobilization efficiency and EASA measurement data. These results suggest that AuNS$_{III}$ morphology, where the electrode surface is

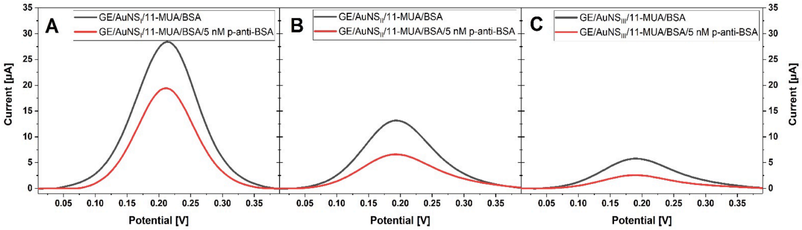

Fig 5. Differential pulse voltammetry measurements in a PBS solution containing 2.5 mM $[Fe(CN)_6]^{3-/4-}$ before and after 30 min long interaction with 5 nM of p-anti-BSA for GE modified with (**A**) AuNS$_I$, (**B**) AuNS$_{II}$, (**C**) AuNS$_{III}$.

sparsely populated with significantly bigger branched gold structures, is more easily blocked by the immobilization of a lower amount of BSA, making this type of electrode surface morphology less suited for label-free immunosensor design.

The DPV results after incubation in 5 nM p-anti-BSA solution exhibit a decrease in registered peak anodic currents. This decrease is observed because antibodies bind to the immobilized BSA and in turn reduce available EASA for redox probe oxidation–reduction, as well as hinder redox probe diffusion towards the electrode surface. This peak anodic current decrease was chosen as an analytical signal for p-anti-BSA detection. Results show that the highest decrease in peak anodic current of 8.9 ± 1.8 μA was registered in the case of electrode modified with AuNS$_I$. For AuNS$_{II}$-modified electrode, the decrease was 6.6 ± 0.5 μA, while for AuNS$_{III}$ it was 4.1 ± 1.2 μA. The differences in the decrease of peak anodic currents can occur due to multiple reasons. Firstly, the decrease can differ depending on the amount of antibodies participating in the immune complex formation. In this case, the higher amount of bound BSA likely creates more accessible epitopes for immune complex formation with antibodies. However, after interaction with p-anti-BSA electrodes with AuNS$_I$ and AuNS$_{II}$, having very similar amount of bound BSA, registered a significantly different decrease in peak anodic current, with AuNS$_I$-modified electrode registering 35 % higher decrease compared with AuNS$_{II}$-modified electrode. Two main factors could explain the results mentioned in this paragraph. Firstly, it is likely that even with the formation of the same number of immune complexes, the decrease in the peak anodic current will be greater in the case of AuNS$_I$. This is because the electrode modified with AuNS$_I$ had 1.8 times higher EASA compared to AuNS$_{II}$, meaning that in principle more of the electroactive surface area could be blocked by the formation of the same number of immune complexes. Another factor that could explain these results is the availability of the epitopes on the surface of BSA-modified electrode for the immune complex formation with p-anti-BSA. Since antibodies are larger than BSA, the immune complex formation between BSA and p-anti-BSA likely hinders further immune complex formation with nearby immobilized BSA molecules. Non-planar geometry and well-spaced nanostructures help to alleviate these steric hindrances. For example, Haddada et. al. [8] found that in comparison to the planar Au layer, a nanostructured surface provides an increase in analytical signal of up to 56 % even though antigen concentration and antibody coverage was the same in both cases, attributing the increase to improved accessibility of the recognition sites on the nanostructured sensor compared to the planar one. It is difficult to attribute which factor exhibits the highest influence based on presented data, however the combination of these factors could explain the observed results well with electrode modified with AuNS$_I$ resulting in the highest decrease of observed peak anodic current after interaction with p-anti-BSA.

In summary, the electrode modified with AuNS$_I$ exhibited the highest EASA and had the highest BSA immobilization efficiency. In addition, in the case of AuNS$_I$ the surface had the highest number of separate and smaller nanostructures. Furthermore, GE modified with AuNS$_I$/11-MUA/BSA produced the highest decrease in peak anodic current after interaction with 5 nM of p-anti-BSA in PBS solution, pH 7.4, compared to electrodes with other electrodeposited AuNS. As such, after this analysis, GE modified with AuNS$_I$ was chosen for further testing as a platform for successful label-free electrochemical immunosensor development.

3.5. Model of immunosensor for the detection of p-anti-BSA

GE/AuNS$_I$/11-MUA/BSA electrode was tested with different concentrations of p-anti-BSA (1 – 50 nM) to assess the analytical parameters of model immunosensing platform. Antibodies were dissolved in 10 mM PBS solution, pH 7.4. GE/AuNS$_I$/11-MUA/BSA modified electrode was immersed in p-anti-BSA solution for 30 min, and DPV measurements were done in 2.5 mM $[Fe(CN)_6]^{3-/4-}$ and 10 mM PBS solution, pH 7.4, after washing the electrode with deionized water. The results from DPV measurements and calibration curves for p-anti-BSA detection are presented in Fig. 6.

Analyzing the results, we can see that increasing the concentration of p-anti-BSA leads to a decrease in the recorded peak anodic current. As mentioned beforehand, this occurs as a result of multiple factors due to the formation of immune complex. As expected, as the concentration of p-anti-BSA increases, more antibodies bind to the BSA immobilized on the electrode surface. This results in an increasing obstruction of EASA, and a hinderance of redox probe diffusion towards the electrode, ultimately leading to a further decrease in the registered peak anodic currents. The relationship was explored to create a calibration curve for p-anti-BSA quantification. The analytical response was chosen as peak anodic current of GE/AuNS$_I$/11-MUA/BSA electrode minus peak anodic current of the electrode after the interaction with p-anti-BSA ($I_{blank} – I_c$). The results are presented in Fig. 6B. This immunosensing platform exhibited a linear range between 1 and 7 nM of p-anti-BSA concentration. At higher concentrations of p-anti-BSA, there was a significant increase in the registered signal standard deviation. In addition, for concentrations above 30 nM, only a slight increase in registered relative response was observed. This could be the result of the saturation happening at the surface of the electrode, with most of the available active centers for immune complex formation being employed. The LOD calculated using the calibration curve in PBS solution was 0.63 nM.

Additionally, the determination of p-anti-BSA diluted in serum was performed with a fabricated immunosensor and compared with the results in PBS solution. Since the calibration curve with different concentrations of p-anti-BSA in PBS solution showed a significant standard deviation between the registered signals of the same samples it was decided to perform an additional blocking step after BSA immobilization. This was performed by immersing GE/AuNS$_I$/11-MUA/BSA electrode in non-spiked serum solution for 30 min in order to block the free surface and minimize non-specific interactions. After the blocking in non-spiked serum the electrode was washed with deionized water and DPV measurements were performed in order to establish the new baseline (I_{blank}). The incubation of the GE/AuNS$_I$/11-MUA/BSA

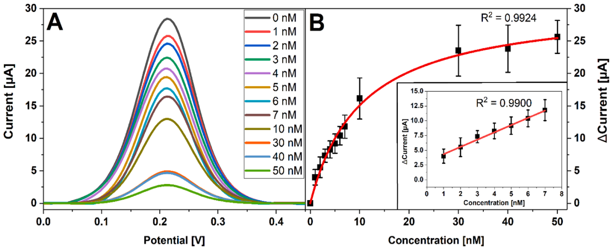

Fig 6. (**A**) DPV measurements before and after the bovine serum albumin modified electrode interaction with different concentrations of p-anti-BSA in the linear calibration range. (**B**) Calibration plot with different concentrations of p-anti-BSA in PBS solution. Relative response was calculated based on DPV measurements performed in a PBS solution containing 2.5 mM $[Fe(CN)_6]^{3-/4-}$. **Insert:** Linear range of the calibration curve.

electrode in non-spiked serum resulted in a 10 % decrease of the registered peak current of $[Fe(CN)_6]^{3-/4-}$ redox probe oxidation compared to before the blocking. This is within expectation since incubating GE/$AuNS_I$/11-MUA/BSA electrode in non-spiked serum results in some non-specific adsorption of proteins and other compounds from the blood serum in turn resulting in a lower registered peak anodic current due to the hindrance of redox probe diffusion and the obstruction of EASA. The following DPV measurements with spiked serum samples were performed in the same manner as for buffer samples. Calibration curves for p-anti-BSA quantification in human serum are provided in Fig. 7.

The same trend was registered from the analysis of results with spiked serum samples. The subsequent decrease in peak anodic current was observed as p-anti-BSA concentration increased. Compared to testing in PBS solution a couple of changes can be examined. Firstly, the linear range of the calibration curve was narrower and was within 1 and 5 nM of p-anti-BSA in serum compared to 1 and 7 nM in PBS solution. In addition, the saturation at the electrode surface was achieved at a lower p-anti-BSA concentration of ~10 nM. Finally, the maximum relative response achieved with spiked serum samples was 21 % lower compared to results achieved in PBS solution. These changes were likely the result of the additional blocking step performed with unspiked blood serum. The adsorption of proteins and other compounds present in serum to the electrode surface would reduce EASA and provide extra hindrance for redox probe diffusion, reducing the maximum achievable response compared to the samples in PBS solution. However, when comparing the relative response in the more important linear range of the calibration curve, almost no decrease in sensitivity is observed when comparing measurements in PBS solution and spiked serum. In addition, it can be observed that the extra blocking step significantly reduced standard error between different samples improving the reproducibility of the system. The estimated detection limit of 0.71 nM for the p-anti-BSA spiked serum samples was very similar to the LOD of 0.63 nM for the samples in PBS solution. Overall, these results indicate that the effect of the sample matrix can result in the narrowing of the linear range and the decrease of maximum relative response while having almost no effect on the sensitivity and the limit of detection at the same time improving the reproducibility of the immunoanalytical system.

4. Conclusions

In this work, a platform for label-free electrochemical immunosensor design consisting of various electrodeposited AuNS was presented. Distinct modified electrode surface morphologies were achieved based on the synthesis solution composition used for electrodeposition. The use of H_2SO_4 as a supporting electrolyte resulted in the formation of mostly circular, smaller, and more numerous AuNS. Exchanging the supporting electrolyte to KNO_3 and increasing $HAuCl_4$ concentration facilitated the formation of bigger nanoparticles some of which consisted of merged smaller nanostructures. Finally, partial coverage of GE by significantly bigger and branched AuNS was achieved when the $HAuCl_4$ and KNO_3 concentrations were increased further. EASA of electrodes with electrodeposited AuNS depended significantly on the morphology of formed nanostructures, with smaller but more numerous $AuNS_I$ providing up to 2 times higher EASA compared to other employed AuNS formation techniques. On the other hand, AuNS morphology did not seem to affect the heterogeneous electron transfer rate constants of modified electrodes with k^0 at around 2.5 times higher compared to unmodified graphite rod electrode in all cases. The study revealed that the morphology of AuNS significantly influenced the efficiency of BSA immobilization. Specifically, the GE surface, modified with smaller but more evenly distributed gold nanostructures ($AuNS_I$ and $AuNS_{II}$), exhibited an increase in the amount of bound BSA of up to 26 % compared to the GE surface modified with larger but more sparsely arranged branched structures. Compared to other electrodes with

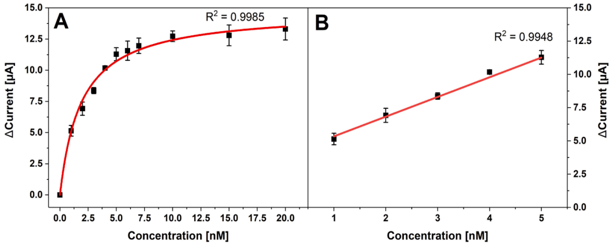

Fig. 7. Calibration plot with different concentrations of p-anti-BSA in human serum. (**A**) The wide concentration range and (**B**) the linear range of the calibration curve. Relative response was calculated based on DPV measurements performed in a PBS solution containing 2.5 mM $[Fe(CN)_6]^{3-/4-}$.

electrodeposited AuNS, those modified with AuNS$_I$ showed the highest peak anodic current for $[Fe(CN)_6]^{3-/4-}$ redox probe oxidation after BSA immobilization as well as the highest decrease in peak anodic current following the interaction with 5 nM of p-anti-BSA. Overall, results from this research showed that for the label-free electrochemical immunosensing platform design smaller, more numerous, and separated AuNS are desirable providing higher EASA, improving antigen immobilization efficiency, and reducing steric hindrance, in turn resulting in a more sensitive analytical system. Finally, it is within expectation that this immunosensing platform could be successfully adapted for use with different antibody and antigen pairs, enabling the development of various immunosensors.

CRediT authorship contribution statement

Benediktas Brasiunas: Conceptualization, Methodology, Formal analysis, Data curation, Validation, Visualization, Writing – original draft, Writing – review & editing. **Anton Popov:** Methodology, Formal analysis, Data curation, Writing – original draft, Writing – review & editing. **Gabija Kraujelyte:** Investigation, Methodology, Writing – review & editing. **Almira Ramanaviciene:** Conceptualization, Methodology, Formal analysis, Supervision, Project administration, Resources, Writing – original draft, Writing – review & editing.

Declaration of competing interest

The authors declare that they have no known competing financial interests or personal relationships that could have appeared to influence the work reported in this paper.

Data availability

Data will be made available on request.

Acknowledgments

This research was funded by a grant (No. S-MIP-22-46) from the Research Council of Lithuania.

Appendix A. Supplementary data

Supplementary data to this article can be found online at https://doi.org/10.1016/j.bioelechem.2023.108638.

References

[1] V. Mazeiko, A. Kausaite-Minkstimiene, A. Ramanaviciene, Z. Balevicius, A. Ramanavicius, Gold nanoparticle and conducting polymer-polyaniline-based nanocomposites for glucose biosensor design, Sensors Actuators B Chem. 189 (2013) 187–193, https://doi.org/10.1016/j.snb.2013.03.140.

[2] A. Popov, B. Brasiunas, A. Damaskaite, I. Plikusiene, A. Ramanavicius, A. Ramanaviciene, Electrodeposited Gold Nanostructures for the Enhancement of Electrochromic Properties of PANI–PEDOT Film Deposited on Transparent Electrode, Polymers (basel). 12 (2020) 2778, https://doi.org/10.3390/polym12122778.

[3] S.D. Soelberg, R.C. Stevens, A.P. Limaye, C.E. Furlong, Surface Plasmon Resonance Detection Using Antibody-Linked Magnetic Nanoparticles for Analyte Capture, Purification, Concentration, and Signal Amplification, Anal. Chem. 81 (2009) 2357–2363, https://doi.org/10.1021/ac900007c.

[4] B. Brasiunas, A. Popov, A. Ramanavicius, A. Ramanaviciene, Gold nanoparticle based colorimetric sensing strategy for the determination of reducing sugars, Food Chem. 351 (2021) 129238, https://doi.org/10.1016/j.foodchem.2021.129238.

[5] J. Neng, M.H. Harpster, W.C. Wilson, P.A. Johnson, Surface-enhanced Raman scattering (SERS) detection of multiple viral antigens using magnetic capture of SERS-active nanoparticles, Biosens. Bioelectron. 41 (2013) 316–321, https://doi.org/10.1016/j.bios.2012.08.048.

[6] A. Ramanaviciene, A. Kausaite-Minkstimiene, A. Popov, B. Brasiunas, A. Ramanavicius, Design of immunosensors for rapid and sensitive detection of biomarkers, in: S.A. Ozkan, N.K. Bakirhan, F.B.T.-T.D. of B. Mollarasouli (Eds.), Detect. Biomarkers, Elsevier, 2022: pp. 303–333. 10.1016/B978-0-12-822859-3.00009-2.

[7] Y. Lou, T. He, F. Jiang, J.J. Shi, J.J. Zhu, A competitive electrochemical immunosensor for the detection of human interleukin-6 based on the electrically heated carbon electrode and silver nanoparticles functionalized labels, Talanta. 122 (2014) 135–139, https://doi.org/10.1016/j.talanta.2014.01.016.

[8] M. Ben Haddada, M. Salmain, S. Boujday, Gold colloid-nanostructured surfaces for enhanced piezoelectric immunosensing of staphylococcal enterotoxin A, Sensors Actuators B Chem. 255 (2018) 1604–1613, https://doi.org/10.1016/j.snb.2017.08.180.

[9] M. Eguílaz, M. Moreno-Guzmán, S. Campuzano, A. González-Cortés, P. Yáñez-Sedeño, J.M. Pingarrón, An electrochemical immunosensor for testosterone using functionalized magnetic beads and screen-printed carbon electrodes, Biosens. Bioelectron. 26 (2010) 517–522, https://doi.org/10.1016/j.bios.2010.07.060.

[10] J. Zhou, N. Gan, T. Li, H. Zhou, X. Li, Y. Cao, L. Wang, W. Sang, F. Hu, Ultratrace detection of C-reactive protein by a piezoelectric immunosensor based on Fe3O4@SiO2 magnetic capture nanoprobes and HRP-antibody co-immobilized nano gold as signal tags, Sensors Actuators B Chem. 178 (2013) 494–500, https://doi.org/10.1016/j.snb.2013.01.013.

[11] J. Baniukevic, I. Hakki Boyaci, A. Goktug Bozkurt, U. Tamer, A. Ramanavicius, A. Ramanaviciene, Magnetic gold nanoparticles in SERS-based sandwich immunoassay for antigen detection by well oriented antibodies, Biosens. Bioelectron. 43 (2013) 281–288, https://doi.org/10.1016/j.bios.2012.12.014.

[12] J.-W. Choi, D.-Y. Kang, Y.-H. Jang, H.-H. Kim, J. Min, B.-K. Oh, Ultra-sensitive surface plasmon resonance based immunosensor for prostate-specific antigen using gold nanoparticle–antibody complex, Colloids Surfaces A Physicochem. Eng. Asp. 313–314 (2008) 655–659, https://doi.org/10.1016/j.colsurfa.2007.05.057.

[13] P. Samadi Pakchin, H. Ghanbari, R. Saber, Y. Omidi, Electrochemical immunosensor based on chitosan-gold nanoparticle/carbon nanotube as a platform and lactate oxidase as a label for detection of CA125 oncomarker, Biosens. Bioelectron. 122 (2018) 68–74, https://doi.org/10.1016/j.bios.2018.09.016.

[14] B. Kavosi, A. Salimi, R. Hallaj, F. Moradi, Ultrasensitive electrochemical immunosensor for PSA biomarker detection in prostate cancer cells using gold nanoparticles/PAMAM dendrimer loaded with enzyme linked aptamer as integrated triple signal amplification strategy, Biosens. Bioelectron. 74 (2015) 915–923, https://doi.org/10.1016/j.bios.2015.07.064.

[15] V. Mani, B.V. Chikkaveeraiah, V. Patel, J.S. Gutkind, J.F. Rusling, Ultrasensitive Immunosensor for Cancer Biomarker Proteins Using Gold Nanoparticle Film Electrodes and Multienzyme-Particle Amplification, ACS Nano. 3 (2009) 585–594, https://doi.org/10.1021/nn800863w.

[16] D. Tang, R. Yuan, Y. Chai, Ultrasensitive Electrochemical Immunosensor for Clinical Immunoassay Using Thionine-Doped Magnetic Gold Nanospheres as Labels and Horseradish Peroxidase as Enhancer, Anal. Chem. 80 (2008) 1582–1588, https://doi.org/10.1021/ac702217m.

[17] Z. Yin, Y. Liu, L.-P. Jiang, J.-J. Zhu, Electrochemical immunosensor of tumor necrosis factor α based on alkaline phosphatase functionalized nanospheres, Biosens. Bioelectron. 26 (2011) 1890–1894, https://doi.org/10.1016/j.bios.2010.03.025.

[18] X. Liu, W.-J. Li, L. Li, Y. Yang, L.-G. Mao, Z. Peng, A label-free electrochemical immunosensor based on gold nanoparticles for direct detection of atrazine, Sensors Actuators B Chem. 191 (2014) 408–414, https://doi.org/10.1016/j.snb.2013.10.033.

[19] N.N.A. Kamal, N.S. Anuar, R. Noordin, A. Rahumatullah, H.H. Hamzah, Electrodeposited Gold Nanoparticle (AuNP)-Film as a Nanoplatform for a Label-Free Electrochemical Strongyloidiasis Immunosensor, J. Electrochem. Soc. 169 (2022) 106514, https://doi.org/10.1149/1945-7111/ac9434.

[20] Q. Yan, L. Cao, H. Dong, Z. Tan, Q. Liu, W. Zhang, P. Zhao, Y. Li, Y. Liu, Y. Dong, Sensitive amperometric immunosensor with improved electrocatalytic Au@Pd urchin-shaped nanostructures for human epididymis specific protein 4 antigen detection, Anal. Chim. Acta. 1069 (2019) 117–125, https://doi.org/10.1016/j.aca.2019.04.023.

[21] L. Deng, G. Lai, L. Fu, C.-T. Lin, A. Yu, Enzymatic deposition of gold nanoparticles at vertically aligned carbon nanotubes for electrochemical stripping analysis and ultrasensitive immunosensing of carcinoembryonic antigen, Analyst. 145 (2020) 3073–3080, https://doi.org/10.1039/C9AN02633A.

[22] H. Haji-Hashemi, P. Norouzi, M.R. Safarnejad, M.R. Ganjali, Label-free electrochemical immunosensor for direct detection of Citrus tristeza virus using modified gold electrode, Sensors Actuators B Chem. 244 (2017) 211–216, https://doi.org/10.1016/j.snb.2016.12.135.

[23] A. Bhimji, A.A. Zaragoza, L.S. Live, S.O. Kelley, Electrochemical Enzyme-Linked Immunosorbent Assay Featuring Proximal Reagent Generation: Detection of Human Immunodeficiency Virus Antibodies in Clinical Samples, Anal. Chem. 85 (2013) 6813–6819, https://doi.org/10.1021/ac4009429.

[24] M. Drobysh, V. Liustrovaite, A. Baradoke, R. Viter, C.-F. Chen, A. Ramanavicius, A. Ramanaviciene, Determination of rSpike Protein by Specific Antibodies with Screen-Printed Carbon Electrode Modified by Electrodeposited Gold Nanostructures, Biosensors. 12 (2022) 593, https://doi.org/10.3390/bios12080593.

[25] J. Wang, L. Wang, J. Di, Y. Tu, Electrodeposition of gold nanoparticles on indium/tin oxide electrode for fabrication of a disposable hydrogen peroxide biosensor, Talanta. 77 (2009) 1454–1459, https://doi.org/10.1016/j.talanta.2008.09.034.

[26] A. Ramanaviciene, A. Popov, E. Baliunaite, B. Brasiunas, A. Kausaite-Minkstimiene, U. Tamer, G. Kirdaite, E. Bernotiene, A. Mobasheri, Magneto-Immunoassay for the Detection and Quantification of Human Growth Hormone, Biosensors. 12 (2022) 65, https://doi.org/10.3390/bios12020065.

[27] I. Morkvenaite-Vilkonciene, A. Kisieliute, W. Nogala, A. Popov, B. Brasiunas, M. Kamarauskas, A. Ramanavicius, S. Linfield, A. Ramanaviciene, Scanning electrochemical microscopy: Glucose oxidase as an electrochemical label in

sandwich format immunoassay, Electrochim. Acta. 463 (2023) 142790, https://doi.org/10.1016/j.electacta.2023.142790.

[28] M.S. El-Deab, T. Sotomura, T. Ohsaka, Morphological Selection of Gold Nanoparticles Electrodeposited on Various Substrates, J. Electrochem. Soc. 152 (2005) C730, https://doi.org/10.1149/1.2041948.

[29] I. Saldan, O. Dobrovetska, L. Sus, O. Makota, O. Pereviznyk, O. Kuntyi, O. Reshetnyak, Electrochemical synthesis and properties of gold nanomaterials, J. Solid State Electrochem. 22 (2018) 637–656, https://doi.org/10.1007/s10008-017-3835-5.

[30] U.S. Mohanty, Electrodeposition: a versatile and inexpensive tool for the synthesis of nanoparticles, nanorods, nanowires, and nanoclusters of metals, J. Appl. Electrochem. 41 (2011) 257–270, https://doi.org/10.1007/s10800-010-0234-3.

[31] C. Zhu, Q. Zhao, D. Huo, X. Hu, X. Wang, Electrodeposition of rough gold nanoarrays for surface-enhanced Raman scattering detection, Mater. Chem. Phys. 263 (2021) 124388, https://doi.org/10.1016/j.matchemphys.2021.124388.

[32] M. Tran, C. Mundt, T. Lan, S. Padalkar, Electrodeposition of Gold Nanostructures Having Controlled Morphology, J. Nanosci. Nanotechnol. 18 (2018) 3492–3498, https://doi.org/10.1166/jnn.2018.14633.

[33] A.K. Pearson, P. Kao, A.P. O'Mullane, A.I. Bhatt, Investigating the effect of ionic strength on the suppression of dendrite formation during metal electrodeposition, Phys. Chem. Chem. Phys. 19 (2017) 14745–14760, https://doi.org/10.1039/C7CP00839B.

[34] N.D. Zakaria, M.H. Omar, N.N. Ahmad Kamal, K. Abdul Razak, T. Sönmez, V. Balakrishnan, H.H. Hamzah, Effect of Supporting Background Electrolytes on the Nanostructure Morphologies and Electrochemical Behaviors of Electrodeposited Gold Nanoparticles on Glassy Carbon Electrode Surfaces, ACS, Omega. 6 (2021) 24419–24431, https://doi.org/10.1021/acsomega.1c02670.

[35] S. Trasatti, O.A. Petrii, Real surface area measurements in electrochemistry, J. Electroanal. Chem. 327 (1992) 353–376, https://doi.org/10.1016/0022-0728(92)80162-W.

[36] V. Liustrovaite, M. Drobysh, A. Rucinskiene, A. Baradoke, A. Ramanaviciene, I. Plikusiene, U. Samukaite-Bubniene, R. Viter, C.-F. Chen, A. Ramanavicius, Towards an Electrochemical Immunosensor for the Detection of Antibodies against SARS-CoV-2 Spike Protein, J. Electrochem. Soc. 169 (2022) 037523, https://doi.org/10.1149/1945-7111/ac5d91.

[37] R.S. Nicholson, Theory and Application of Cyclic Voltammetry for Measurement of Electrode Reaction Kinetics, Anal. Chem. 37 (1965) 1351–1355, https://doi.org/10.1021/ac60230a016.

[38] I. Lavagnini, R. Antiochia, F. Magno, An Extended Method for the Practical Evaluation of the Standard Rate Constant from Cyclic Voltammetric Data, Electroanalysis. 16 (2004) 505–506, https://doi.org/10.1002/elan.200302851.

[39] A. Popov, A. Stirke, N. Bakute, B. Brasiunas, A. Ramanavicius, A. Ramanaviciene, Efficiency of granulocyte colony-stimulating factor immobilized on magnetic microparticles on proliferation of NFS-60 cells, Colloids Surfaces A Physicochem. Eng. Asp. 578 (2019) 123580, https://doi.org/10.1016/j.colsurfa.2019.123580.

[40] C. Saby, B. Ortiz, G.Y. Champagne, D. Bélanger, Electrochemical Modification of Glassy Carbon Electrode Using Aromatic Diazonium Salts. 1. Blocking Effect of 4-Nitrophenyl and 4-Carboxyphenyl Groups, Langmuir. 13 (1997) 6805–6813, https://doi.org/10.1021/la961033o.

[41] R.O. Kadara, N. Jenkinson, C.E. Banks, Characterisation of commercially available electrochemical sensing platforms, Sensors Actuators B Chem. 138 (2009) 556–562, https://doi.org/10.1016/j.snb.2009.01.044.

[42] A.P. Washe, P. Lozano-Sánchez, D. Bejarano-Nosas, I. Katakis, Facile and versatile approaches to enhancing electrochemical performance of screen printed electrodes, Electrochim. Acta. 91 (2013) 166–172, https://doi.org/10.1016/j.electacta.2012.12.110.

[43] I.-F. Hu, D.H. Karweik, T. Kuwana, Activation and deactivation of glassy carbon electrodes, J. Electroanal. Chem. Interfacial Electrochem. 188 (1985) 59–72, https://doi.org/10.1016/S0022-0728(85)80050-4.

[44] R. Bowling, R.T. Packard, R.L. McCreery, Mechanism of electrochemical activation of carbon electrodes: role of graphite lattice defects, Langmuir. 5 (1989) 683–688, https://doi.org/10.1021/la00087a022.

[45] R.J. Rice, N.M. Pontikos, R.L. McCreery, Quantitative correlations of heterogeneous electron-transfer kinetics with surface properties of glassy carbon electrodes, J. Am. Chem. Soc. 112 (1990) 4617–4622, https://doi.org/10.1021/ja00168a001.

[46] M.T. McDermott, C.A. McDermott, R.L. McCreery, Scanning tunneling microscopy of carbon surfaces: relationships between electrode kinetics, capacitance, and morphology for glassy carbon electrodes, Anal. Chem. 65 (1993) 937–944, https://doi.org/10.1021/ac00055a017.

[47] W.J. Blaedel, G.W. Schieffer, A hydrodynamic voltammetric study of the ferricyanide/ferrocyanide system with convective electrodes of platinum, gold, glassy carbon, carbon film, and boron carbide, J. Electroanal. Chem. Interfacial Electrochem. 80 (1977) 259–271, https://doi.org/10.1016/S0022-0728(77)80048-X.

[48] M.J.E. Fischer, in: Amine Coupling through EDC/NHS: A Practical Approach BT - Surface Plasmon Resonance: Methods and Protocols, Humana Press, Totowa, NJ, 2010, pp. 55–73, https://doi.org/10.1007/978-1-60761-670-2_3.

[49] D.K. Schwartz, Mechanisms and Kinetics of Self-Assembled Monolayer Formation, Annu. Rev. Phys. Chem. 52 (2001) 107–137, https://doi.org/10.1146/annurev.physchem.52.1.107.

[50] F.S. Damos, R.C.S. Luz, L.T. Kubota, Determination of Thickness, Dielectric Constant of Thiol Films, and Kinetics of Adsorption Using Surface Plasmon Resonance, Langmuir. 21 (2005) 602–609, https://doi.org/10.1021/la0487038.

[51] G. Yohannes, S.K. Wiedmer, M. Elomaa, M. Jussila, V. Aseyev, M.-L. Riekkola, Thermal aggregation of bovine serum albumin studied by asymmetrical flow field-flow fractionation, Anal. Chim. Acta. 675 (2010) 191–198, https://doi.org/10.1016/j.aca.2010.07.016.

Paper 3

Magneto-immunoassay for the detection and quantification of human growth hormone

A. Ramanaviciene, A. Popov, E. Baliunaite, **B. Brasiunas**, A. Kausaite-Minkstimiene, U. Tamer, G. Kirdaite, E. Bernotiene, A. Mobasheri

Biosensors, 2022, 12(2), 65
doi.org/10.3390/bios12020065

biosensors

MDPI

Article

Magneto-Immunoassay for the Detection and Quantification of Human Growth Hormone

Almira Ramanaviciene [1,2,*], Anton Popov [1,2], Ema Baliunaite [2], Benediktas Brasiunas [2], Asta Kausaite-Minkstimiene [1,2], Ugur Tamer [3], Gailute Kirdaite [4], Eiva Bernotiene [5,6] and Ali Mobasheri [5,7,8,9,10]

[1] Department of Immunology, State Research Institute Centre for Innovative Medicine, LT-08406 Vilnius, Lithuania; anton.popov@imcentras.lt (A.P.); asta.minkstimiene@imcentras.lt (A.K.-M.)
[2] Nanotechnas—Center of Nanotechnology and Materials Science, Faculty of Chemistry and Geosciences, Institute of Chemistry, Vilnius University, LT-03225 Vilnius, Lithuania; emabaliunaite@gmail.com (E.B.); benediktas.brasiunas@chgf.vu.lt (B.B.)
[3] Department of Analytical Chemistry, Faculty of Pharmacy, Gazi University, Ankara TR-06330, Turkey; utamer@gazi.edu.tr
[4] Department of Experimental, Preventive and Clinical Medicine, State Research Institute Centre for Innovative Medicine, LT-08406 Vilnius, Lithuania; gailute.kirdaite@imcentras.lt
[5] Department of Regenerative Medicine, State Research Institute Centre for Innovative Medicine, LT-08406 Vilnius, Lithuania; eiva.bernotiene@imcentras.lt (E.B.); ali.mobasheri@oulu.fi (A.M.)
[6] Department of Chemistry and Bioengineering, The Faculty of Fundamental Sciences, Vilnius Gediminas Technical University, Vilnius-Tech, LT-10223 Vilnius, Lithuania
[7] Research Unit of Medical Imaging, Physics and Technology, Faculty of Medicine, University of Oulu, FI-90014 Oulu, Finland
[8] Departments of Orthopedics, Rheumatology and Clinical Immunology, University Medical Center Utrecht, 508 GA Utrecht, The Netherlands
[9] Department of Joint Surgery, The First Affiliated Hospital, Sun Yat-sen University, Guangzhou 510080, China
[10] World Health Organization Collaborating Center for Public Health Aspects of Musculoskeletal Health and Aging, Université de Liège, 4000 Liège, Belgium
* Correspondence: almira.ramanaviciene@imcentras.lt

Abstract: Physiological and endocrine maintenance of a normal human growth hormone (hGH) concentration is crucial for growth, development, and a number of essential biological processes. In this study, we describe the preparation and characterization of magnetic nanoparticles coated with a gold shell (MNPs-Au). The optimal surface concentration of monoclonal anti-hGH antibodies (m-anti-hGH) on magnetic nanoparticles, as well as conditions that decrease non-specific interactions during the magneto-immunoassay, were elaborated. After the selective recognition, separation, and pre-concentration of hGH by MNPs-Au/m-anti-hGH and the hGH interaction with specific polyclonal biotin-labeled antibodies (p-anti-hHG-B) and streptavidin modified horseradish peroxidase (S-HRP), the MNPs-Au/m-anti-hGH/hGH/p-anti-hGH-B/S-HRP immunoconjugate was formed. The concentration of hGH was determined after the addition of 3,3′,5,5′-tetramethylbenzidine and hydrogen peroxide substrate solution for HRP; the absorbance at 450 nm was registered after the addition of STOP solution. The developed sandwich-type colorimetric magneto-immunoassay is characterized by a clinically relevant linear range (from 0.1 to 5.0 nmol L^{-1}, R^2 0.9831), low limit of detection (0.082 nmol L^{-1}), and negligible non-specific binding of other antibodies or S-HRP. The obtained results demonstrate the applicability of the developed magneto-immunoassay for the concentration and determination of hGH in the serum. Additionally, important technical solutions for the development of the sandwich-type colorimetric magneto-immunoassay are discussed.

Keywords: human growth hormone; gold shell magnetic nanoparticles; sandwich-type colorimetric magneto-immunoassay

check for updates

Citation: Ramanaviciene, A.; Popov, A.; Baliunaite, E.; Brasiunas, B.; Kausaite-Minkstimiene, A.; Tamer, U.; Kirdaite, G.; Bernotiene, E.; Mobasheri, A. Magneto-Immunoassay for the Detection and Quantification of Human Growth Hormone. *Biosensors* **2022**, *12*, 65. https://doi.org/10.3390/bios12020065

Received: 19 December 2021
Accepted: 22 January 2022
Published: 25 January 2022

1. Introduction

Nanotechnology had a profound impact on different fields of research, including analytical systems for sensitive, selective, quick, and user-friendly detection of medically important biomolecules in the blood. Scientists face a great challenge when it comes to the detection of an ultralow concentration of the biomarkers in a relatively large sample volume. An effective strategy to solve this problem is the application of functionalized magnetic nanoparticles (MNPs) or magnetic beads (MBs) for the selective recognition, separation, and pre-concentration of the desired analyte from the sample. Metals (iron, cobalt, nickel), metal oxides (iron oxides and ferrites), or ferromagnetic alloy MNPs and MBs are characterized by a large active surface area for the immobilization of specific antibodies or receptors, the ability to maintain their magnetic properties after modification by biomolecules, and by the rapid separation of analyte from the mixture using an external magnetic field [1–3]. The increased sensitivity of analytical systems using different immunoassay formats and various techniques, the reduction in non-specific binding effect, and a shorter response time are major advantages rendered by the use of MNPs [4]. Improvement in the detection of circulating tumor cell phenotypes [5], microorganisms [6], nucleic acids [7], proteins [8], and small molecules [9] using MNPs was experimentally confirmed. Furthermore, MNPs serve for the separation and pre-concentration of different biomarkers or toxins present in the same sample, followed by the multiplex analysis using specific luminescent tags. Inorganic, semiconductor nanocrystals, quantum dots (QDs), immobilized on the detection antibody, are an ideal tag for the multiplex binding event evaluation and multiple biomarkers detections [10,11]. The excited QDs exhibit size and composition-dependent fluorescence emission spectra, allowing simultaneous detection of different biomarkers [12].

The concentration of hormones that are important for normal physiological functions is very low in blood and serum samples. The normal range for human growth hormone (hGH) (also known as somatotropin), one of several hormones secreted by the anterior pituitary gland in the brain, depends on gender and age and typically ranges from 0.4 ng mL^{-1} (0.018 nmol L^{-1}) to 50 ng mL^{-1} (2.273 nmol L^{-1}) [13]. hGH is a polypeptide hormone consisting of various circulating isoforms, between which the largely prevalent (~50%) is a 22 kDa hGH isoform consisting of 191 amino acids. The second most abundant form is 20 kDa hGH, only making up 5–9%. The rest of hGH is found in dimer and oligomer forms or as hGH fragments [14–16]. The normal concentration of hGH is essential for regular body growth and a number of biological processes, such as the metabolism of lipids, carbohydrates, and proteins [17]. An excess of this hormone was determined to cause gigantism [18], insulin resistance [19], and finally, diabetes [20], while deficiency results in growth retardation in children and deficiency syndrome in adults [21]. Thus, the determination of both the deficiency or excess of hGH in serum is very important for the evaluation of disorders in this hormone secretion and for the identification of various disorders that occur in people of different ages.

Different format immunoassays and various immunosensors based on different signal transducers were developed for the determination of hGH distinguished by the low limit of detection (LOD) and optimal linear range in a specific case, namely, standard double-antibody radioimmunoassay and immunoradiometric assay [22], immunofluorometric assay [23], immunochemiluminescent assay [24], sandwich enzyme-linked immunoassay (quantitative) (working range 2.5–600 pg mL^{-1}, sensitivity 4 pg mL^{-1}) [13], direct detection in serum using surface plasmon resonance (SPR) immunosensors based on the surface modified by site-directed oriented reduced half antibody fragments (LOD 0.0034 µmol L^{-1}, linear range 0.01–0.72 µmol L^{-1}) and whole antibody via protein G (LOD 0.99 nmol L^{-1}, linear range 3–9 nmol L^{-1}) [25,26], electrochemical impedance spectroscopy immunosensors (LOD 0.64 pg mL^{-1}, linear range 3–100 pg mL^{-1}) [27], and disposable electrochemical magneto-immunosensor (LOD 0.005 ng mL^{-1}, linear range 0.01–100 ng mL^{-1}) [28].

In this study, we describe the preparation of MNPs coated with gold shell (MNPs-Au) and modified with monoclonal anti-hGH antibodies (m-anti-hGH) for the application in a magneto-immunoassay for the detection of hGH. These MNP-Au nanoparticles were used for the selective recognition, separation, and pre-concentration of hGH from a sample and for further determination in a small volume by sandwich-type magneto-immunoassay using specific polyclonal biotin-labeled antibodies (p-anti-hHG-B), horseradish peroxidase modified with streptavidin (S-HRP), 3,3′,5,5′-tetramethylbenzidine (TMB), and hydrogen peroxide substrate solution for HRP. Technical solutions for the development of magneto-immunoassay were discussed. The performance of the developed colorimetric magneto-immunoassay for the detection and quantification of low concentrations of hGH in relatively large volume samples was evaluated. The further applications of the developed magneto-immunoassay were discussed.

2. Materials and Methods

2.1. Materials and Reagents

Recombinant human growth hormone from E. coli (hGH), mouse monoclonal anti-human growth hormone IgG2B antibodies (m-anti-hGH), and goat polyclonal anti-human growth hormone biotinylated IgG antibody (p-anti-hGH-B) were obtained from R&D Systems (Minneapolis, MN, USA). Steptavidin-HRP conjugate (S-HRP) and 3,3′,5,5′-tetramethylbenzidine (TMB) and hydrogen peroxide substrate for HRP, and 0.5 mol L^{-1} H_2SO_4 (STOP solution) were acquired from ELISA kit produced by BioVendor (Brno, Czech Republic). N-(3-dimethylaminopropyl)-N-ethylcarbodiimide hydrochloride (EDC), N-hydroxysuccinimide (NHS), methanol, hexadecyltrimethylammonium bromide (CTAB), and PBS tablets (0.01 M phosphate-buffered saline, pH 7.4) were purchased from Carl Roth (Karlsruhe, Germany). Hydrogen tetrachloroaurate trihydrate ($HAuCl_4 \cdot 3H_2O$) was received from Alfa Aesar (Karlsruhe, Germany). The 11-mercaptoundecanoic acid (11-MUA), perchloric acid, iron (II) sulfate heptahydrate ($FeSO_4 \cdot 7H_2O$), and bovine serum albumin (BSA) were received from Sigma-Aldrich (Steinheim, Germany). Iron (III) chloride hexahydrate ($FeCl_3 \cdot 6H_2O$) and ethylenediaminetetraacetic acid (EDTA) were obtained from AppliChem (Karlsruhe, Germany). Ethanol was acquired from Honeywell (North Carolina, USA), sodium borohydride ($NaBH_4$) was from Merck (Darmstadt, Germany), and hydroxylamine hydrochloride was from Lach-Ner (Neratovice, Czech Republic). All aqueous solutions were prepared in ultrapure deionized water.

2.2. Synthesis of Magnetic Nanoparticles

The synthesis of magnetic gold-coated nanoparticles consisted of two parts—iron oxide (Fe_3O_4) MNPs synthesis and gold shell coating procedure. MNPs were synthesized using the co-precipitation method according to the already published protocol [29,30]. Briefly, 125 mL of 1 mol L^{-1} NaOH solution was added dropwise under vigorous stirring into 10 mL of the solution consisting of 1.28 M $FeCl_3$ and 0.64 mol L^{-1} $FeSO_4$. The formed precipitate was collected with the help of a magnet, washed three times with deionized water, and then kept in 2 mol L^{-1} $HClO_4$ solution overnight under argon (Elme Messer Gaas, Lithuania) atmosphere to obtain Fe_3O_4 nanoparticles. The color of MNPs becomes brown. Subsequently, the nanoparticles were collected by centrifugation at 12,000× g for 20 min and washed three times with deionized water and once with ethanol, and finally, were left to dry in air.

2.3. Coating Magnetic Nanoparticles with a Gold Shell

Firstly, 5 mg of dried magnetic nanoparticles were sonicated in 5 mL of water until fully dispersed. Then, 10 mL of 0.27 mol L^{-1} EDTA solution prepared in 1 mol L^{-1} NaOH was added, and MNPs were re-suspended by using an ultrasonic bath. Particles were collected with a magnet and dispersed in a 10 mL mixture of 0.1 mol L^{-1} CTAB and 0.01 mol L^{-1} $HAuCl_4$ solution. Subsequently, the 150 mg hydroxylamine hydrochloride was added to the vigorously stirred solution in order to reduce $AuCl_4^-$ ions to Au(0) on the surface of MNPs. The color of the solution changed from brown to dark red, indicating the formation of nanoparticles with gold shells (MNPs-Au). These particles were characterized by UV-vis spectrophotometer Lambda 25 (Perkin Elmer, Shelton, WA, USA) and transmission electron microscope (TEM) Tecnai F20 X-TWIN (Eindhoven, The Nederland). X-ray diffraction (XRD) measurements were performed using a MiniFlex II diffractometer (Rigaku, Japan). The diffractograms were recorded in the 2θ range from 25° to 80° using CuK_α λ = 1.5406 Å radiation.

2.4. Modification of MNPs-Au by m-Anti-hGH Antibodies

In order to be able to immobilize m-anti-hGH antibodies successfully, the CTAB used in the synthesis procedure of the particles first had to be removed from the MNPs-Au surface [31]. Briefly, 800 µL of 30 mmol L^{-1} $NaBH_4$ was added to 1.6 mL 0.2 mg mL^{-1} MNPs-Au solution, and the mixture was stirred for 1 h. CTAB-free nanoparticles were washed with deionized water and further used for covalent immobilization of antibodies. Firstly, a self-assembled monolayer (SAM) was formed by keeping MNPs-Au in a 1 M 11-mercaptoundecanoic acid (11-MUA) solution for 2 h (Figure 1, step 1). After washing with H_2O, the carboxyl groups of 11-MUA were activated with a mixture consisting of 200 mmol L^{-1} EDC and 50 mmol L^{-1} NHS for 15 min. Magnetically collected MNPs-Au were added to the solutions consisting of different concentrations of m-anti-hGH antibodies (200, 330, 660, and 984 nmol L^{-1}). After 2 h MNPs-Au/m-anti-hGH particles were washed three times with 10 mM PBS solutions (pH 7.4) and kept in a solution of 1 % BSA made in 10 mmol L^{-1} PBS (pH 7.4) for 1 h at room temperature and overnight at +4 °C to block the unreacted activated esters and the free surface (Figure 1, step 2).

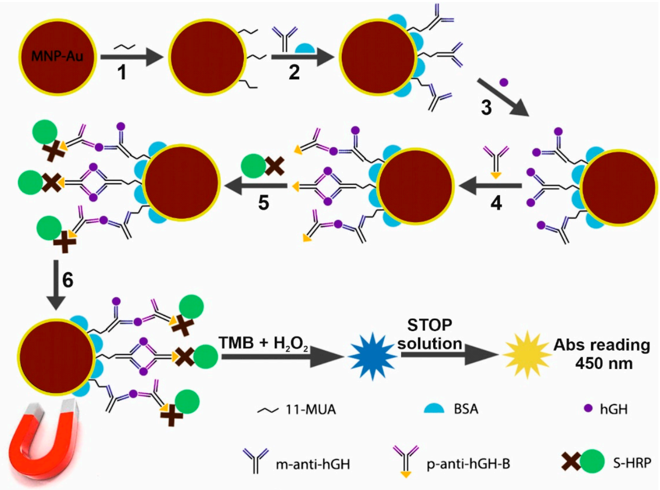

Figure 1. Schematic illustrating the design of the sandwich-type magneto-immunoassay for the detection of human growth hormone (hGH). The magnet was used in all steps for the collection of modified MNPs-Au.

Optimal m-anti-hGH concentration was determined by keeping MNPs-Au, which were modified with different m-anti-hGH concentrations, in solutions of 400 nmol L^{-1} hGH and 990 nmol L^{-1} p-anti-hGH-B, respectively. After the interaction with hGH and p-anti-hGH-B, immunoconjugates were washed three times using a 0.1% BSA solution in 10 mmol L^{-1} PBS (pH 7.4) and then left in 100 µL solution of S-HRP for 30 min. Another washing step was performed using 10 mmol L^{-1} PBS solution, and then a 100 µL of TMB substrate was added. An enzymatic reaction lasted for 10 min in the dark and was stopped by adding 100 µL of STOP solution. The absorbance of the formed yellow product was registered at 450 nm. After determining the optimal m-anti-hGH concentration for MNPs-Au modification, the analytical system based on the application of MNPs-Au for the collection and pre-concentration of hGH was designed.

2.5. Development of Sandwich Type Magneto-Immunoassay for hGH Detection Using MNPs-Au

An amount of 0.2 mg mL^{-1} of MNPs-Au was first modified using $NaBH_4$, then a SAM of 11-MUA was formed, and m-anti-hGHs at optimal concentration were covalently immobilized onto the MNPs-Au surface as described previously (Figure 1, steps 1–2). Afterward, MNPs-Au/m-anti-hGH interacted with different concentrations of hGH (Figure 1, step 3), followed by interaction with 100 nM p-anti-hGH-B (Figure 1, step 4) and S-HRP (Figure 1, step 5). The solution of 0.1% BSA in 10 mmol L^{-1} PBS (pH 7.4) was used for washing three times after each step of the interaction. After carrying out the enzymatic HRP reaction and stopping this reaction with STOP solution, the absorbance of the formed yellow product was registered at 450 nm after the removal of immunoconjugates from the solution. The scheme of magneto-immunoassay for the detection of hGH is provided in Figure 1. It should be mentioned that in order to reduce the non-specific adsorption of proteins and MNPs-Au surface, test tubes were coated with BSA using 1% solution for 1 h at room temperature and overnight at +4 °C.

3. Results and Discussion

3.1. Characterization of Magnetic MNPs-Au

A two-stage synthesis procedure was used for the preparation of MNPs-Au. The synthesized iron oxide nanoparticles were coated by a gold-layer shell. In order to demonstrate the formation of the gold layer around MNPs, UV-vis spectra were registered (Figure 2).

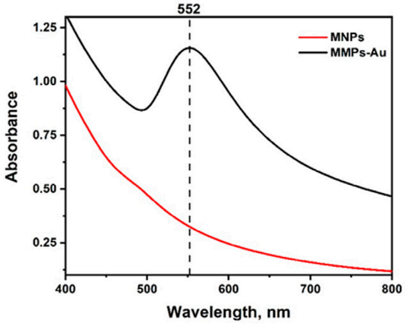

Figure 2. Absorbance spectra of magnetic nanoparticles (MNPs) before and after coating with the gold layer (MNPs-Au).

Absorption spectra for Fe_3O_4 nanoparticles [32], as expected, did not produce an absorption peak in the visible spectrum range. However, after the synthesis of a gold shell, a characteristic surface plasmon band with a maximum of 552 nm can be observed corresponding to the local surface plasmon resonance (LSPR) of spherical gold nanoparticles, confirming successful coating of MNPs by a gold layer [33]. Quite a high intensity of LSPR band can be explained by high extinction coefficient, which is characteristic for bigger gold nanoparticles, wherein broad band indicates polydispersity of the gold coatings [34].

The TEM micrographs of MNPs-Au are given in Figure 3. Spherical gold-coated nanoparticles surrounded by non-coated magnetic particles were observed. MNPs-Au appears darker in comparison with non-coated particles. This difference can be associated with higher electron density for gold versus iron oxide [29]. These results coincide with previously published work by Tamer et al. [35]. The average diameter of synthesized MNPs-Au was equal to 47.6 ± 11.3 nm (Figure 3A). Additionally, it was found that the lattice fringes taken from the surface of MNPs-Au showed 2.38 A interplanar spacing (Figure 3B) attributed to the fcc-structured gold (111) plane, further confirming the formation of a gold shell on the surface of magnetic nanoparticles.

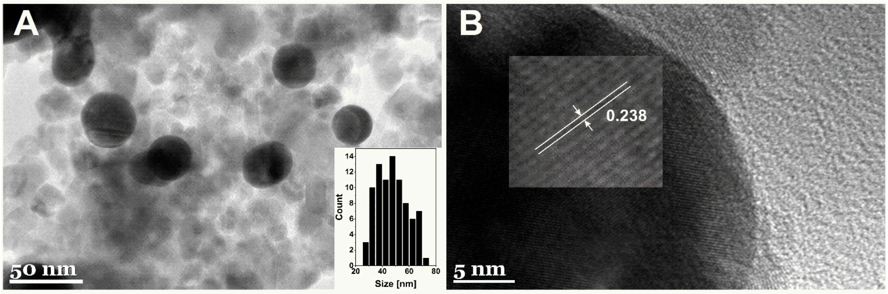

Figure 3. TEM images of synthetized MNPs-Au under different magnification. Insets: (**A**) the particle size distribution histogram and (**B**) HRTEM image demonstrating the Au lattice spacing.

The crystalline structure of synthesized nanoparticles before and after the coating was examined by XRD analysis. The XRD patterns for MNPs and MNPs-Au are presented in Figure 4. It was shown that in the case of MNPs, magnetite (Fe_3O_4) nanoparticles were synthesized. All diffraction peaks match very well with the standard XRD data (ICDD 00-019-0629). As a result of the gold layer coating, the peaks at 38.12°, 44.14°, 64.4°, and 77.38° were observed, which are assigned, respectively, to (111), (200), (220), and (311) reflections of the face-centered cubic structure of metallic gold. It can be observed that (111) plane is the predominant orientation. Some Fe_3O_4 peaks are also seen in the XRD pattern of MNPs-Au. The low intensity of these peaks and the absence of other magnetite peaks can be explained by a heavy atom effect of Au [32].

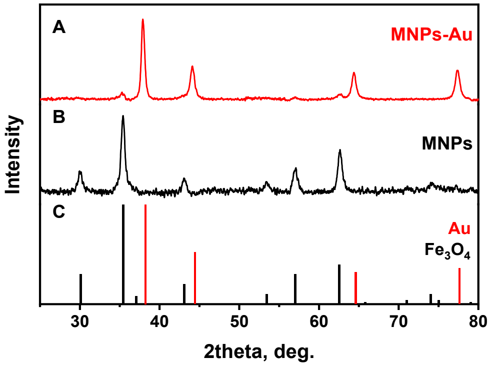

Figure 4. XRD patterns of (**A**) MNPs-Au, (**B**) MNPs, and (**C**) standards of Au (ICDD 00-004-0784) and Fe_3O_4 (ICDD 00-019-0629).

3.2. Magneto-Immunoassay Performance Optimization

The whole procedure for the hGH detection, involving the m-anti-hGH immobilization onto MNPs-Au surface; the interaction with hGH, p-anti-hGH-B, and S-HRP; and followed by the enzymatic reaction and the evaluation using microplate spectrophotometer SpectraMax i3 (Molecular Devices, San Jose, CA, USA), is schematically presented in Figure 1. The first step of this immunoassay optimization involves the selection of the optimal MNPs-Au and m-anti-hGH concentrations ratio.

Thus, in all experiments, 0.2 mg mL^{-1} concentration of MNPs-Au and 200, 330, 660, and 980 nmol L^{-1} concentrations of m-anti-hGH were used for the covalent immobilization onto nanoparticles modified with 11-MUA. Additionally, the 400 nmol L^{-1} of hGH and 990 nmol L^{-1} of p-anti-hGH-B were used in this experiment (Figure 5A). The affinity interactions and immunoconjugate composed of MNPs-Au/m-anti-hGH/hGH/p-anti-hGH-B/S-HRP formation were monitored by the addition of TMB substrate followed by the enzymatic reaction product formation and absorbance registration after the addition of the STOP solution. The absorbance at 450 nm increased by 0.4 when the concentration of m-anti-hGH was increased from 200 to 330 nmol L^{-1}. By further increasing the concentration of m-anti-hGH to 660 and 990 nmol L^{-1}, the absorbance increased by 0.1 and 0.5, respectively. Based on the obtained experimental results and taking into account observations by other authors, better results of analytical systems are achieved using a smaller surface concentration of antibodies [36]; for further experiments, 330 nmol L^{-1} concentration of m-anti-hGH was selected. Additionally, the concentration of p-anti-hGH-B was reduced to 100 nmol L^{-1} in order t to detect lower hGH levels and reduce the non-specific binding of these antibodies.

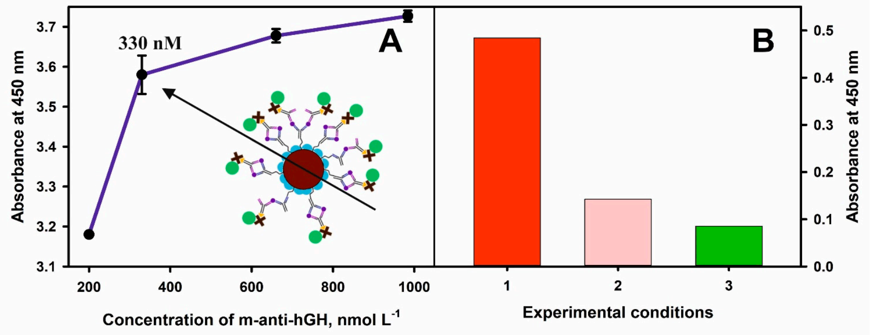

Figure 5. (**A**) Dependence of the optical response at 450 nm on the concentration of m-anti-hGH used for covalent immobilization onto MNPs-Au. (**B**) The reduction in the non-specific interactions during the magneto-immunoassay. The absorbance of the blank samples: 1—using only 10 mmol L^{-1} PBS; 2—after blocking test tubes walls with 1% BSA in 10 mmol L^{-1} PBS; 3—after blocking of test tubes walls with 1% BSA in 10 mmol L^{-1} PBS and using dilution and washing solutions consisting of 0.1% BSA in 10 mmol L^{-1} PBS.

The dilution and washing solution consisting of 0.1% BSA in 10 mmol L^{-1} PBS (pH 7.4) was used to reduce non-specific binding during the indirect detection of hGH. Furthermore, the test tubes were modified with 1% BSA in 10 mmol L^{-1} PBS (pH 7.4) for 1 h. This blocking procedure helped to reduce the absorbance of the blank sample by 5.7 times (Figure 5B). This result is explained by the decrease in the level of non-specific binding of p-anti-hGH and S-HRP. Therefore, the background signal was lowered and subtracted from the experimental results with hGH, and the selected experimental conditions allowed to determine hGH at low concentrations accurately.

3.3. Analytical Characteristics of Sandwich Type Magneto-Immunoassay for hGH Detection Using MNPs-Au

An optical sandwich-type magneto-immunoassay based on the antibody-modified MNPs-Au application for the pre-concentration of hGH present in the solution was developed and optimized. The principal scheme and each step of sandwich magneto-immunoassay followed by the formation of the color enzymatic reaction product is explained in Figure 1. The MNPs-Au/m-anti-hGH were exposed to hGH concentrations of 0.01 to 50 nmol L^{-1}, keeping constant concentrations of other reagents and the duration of the enzymatic reaction. The dependence of absorbance at 450 nm on different concentrations of hGH under optimized conditions is depicted in Figure 6A. The hyperbolic relationship between absorbance and hGH concentrations was obtained (R = 0.9880). The linear dependence (Figure 6B) was registered from 0.1 to 5.0 nmol L^{-1} concentrations of hGH (R^2 = 0.9831). The LOD defined as the lowest concentration of hGH, which gives an analytical signal greater than the background plus 3 σ, was calculated to be 0.082 nmol L^{-1}. The developed magneto-immunoassay is suitable for the determination of hGH in the normal hGH range and at higher concentrations than using standard sandwich-format ELISA. Additionally, LOD was improved from 2.2 times if compared with inhibition SPR-based immunosensor format [37] to 41.6 times [25] if compared with results obtained using direct SPR-based immunosensor format (Table 1).

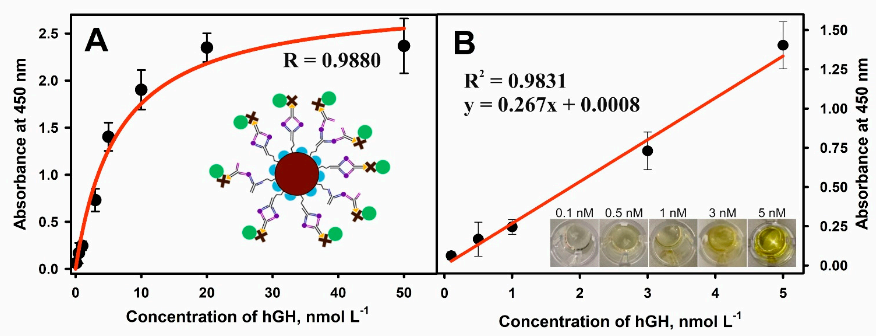

Figure 6. (**A**) Dependence of absorbance at 450 nm on the concentration of hGH. (**B**) The linear range of the developed sandwich-type magneto-immunoassay for hGH detection using MNPs-Au. Conditions: 0.2 mg mL^{-1} of MNPs-Au modified with 330 nmol L^{-1} concentration of m-anti-hGH; 100 nmol L^{-1} concentration of p-anti-hGH-B; 100 µL solution of S-HRP; 100 µL of TMB substrate; 0.1–5.0 nmol L^{-1} concentrations of hGH.

The described system was also used with other non-hGH specific biotinylated antibodies to test the influence of non-specific binding by the affinity interaction with S-HRP. An amount of 5 nmol L^{-1} of hGH and 100 nmol L^{-1} of biotinylated monoclonal mouse antibodies against human cartilage oligomeric matrix protein (clone: 16F12) were used. In this case, the absorbance increased only by 1.7% compared to the control without any hGH, but in the presence of 100 nmol L^{-1} p-anti-hGH-B in the tested analytical system indicating low non-specific interaction for other biotinylated antibodies.

3.4. Determination of hGH in Spiked Serum Samples

In order to demonstrate the utility of the developed sandwich-type magneto-immunoassay using modified MNPs-Au for the detection of hGH in real samples, a human serum sample spiked with 3.5 nmol L^{-1} of hGH was tested. In order to evaluate the impact of the matrix and the possible presence of hGH on the analytical signal, a calibration curve with a known hGH concentration in the serum was constructed. We found the recovery of 3.5 mol L^{-1} of hGH to be 94.9%. Despite a slightly higher concentration of the determined hGH, these results demonstrate the applicability of the developed magneto-immunoassay for the analysis of hGH in real samples of small volume.

Table 1. Comparison of analytical parameters for various formats of optical immunoassays and immunosensors used for hGH detection.

Analytical System for hGH Detection	Linear or Dynamic Range	LOD	Sensitivity	Ref.
SPR-based immunosensors for the direct detection using reduced half antibody fragments	10–720 nmol L^{-1}	3.4 nmol L^{-1}		[25]
SPR-based immunosensors for the direct detection using antibody immobilization via protein G	3–9 nmol L^{-1}	0.99 nmol L^{-1}		[26]
SPR-based inhibition immunosensor format using surface modified with hGH	18–542 ng mL^{-1} (0.82–24.6 nmol L^{-1})	4 ng mL^{-1} (0.18 nmol L^{-1})		[37]
Sandwich ELISA, p-anti-hGH/hGH/anti-hGH-B/S-HRP, absorbance at 450 nm.	1–25 ng mL^{-1} (0.046–1.14 nmol L^{-1})		0.25 ng mL^{-1} (0.0114 nmol L^{-1})	[38]
Sandwich ELISA, anti-hGH/hGH/anti-hGH-B/S-HRP, absorbance at 450 nm.	2.5–600 pg mL^{-1} $1.1 \cdot 10^{-4}$–0.027 nmol L^{-1}		4 pg mL^{-1} ($1.8 \cdot 10^{-4}$ nmol L^{-1})	[13]
Sandwich ELISA, m-anti-hGH/hGH/m-anti-hGH-HRP, absorbance at 450 nm.	0.5–50 ng mL^{-1} (0.023–2.27 nmol L^{-1})		0.5 ng mL^{-1} (0.023 nmol L^{-1})	[39]
Indirect detection, MNPs-Au/m-anti-hGH/hGH/p-anti-hGH-B/S-HRP immunoassay, absorbance at 450 nm.	0.1–5.0 nmol L^{-1}	0.082 nmol L^{-1}		Current work

4. Conclusions

The colorimetric magneto-immunoassay for the determination and quantification of low concentrations of hGH was developed and evaluated. MNPs-Au modified with monoclonal anti-hGH antibodies were successfully applied for the separation of hGH from the relatively high volume sample and concentration in a low volume for further sensitive determination. The coating of MNPs with a gold shell simplifies the antibody immobilization step and allows different antibody immobilization methods to be used. Detection antibody–HRP conjugates were essential for the hGH detection, followed by the analytical signal amplification and registration. Many efforts are now being made to develop methods for the simultaneous detection of multiple biomarkers in a single sample. The proposed magneto-immunoassay methodology can be adapted for this purpose. We can achieve this goal by modifying MNP-Au with antibodies specific for various biomarkers; however, distinct signal amplification tags have to be applied, such as different enzymes or other materials. An ideal tag for the multiplex binding events evaluation and multiple biomarkers detections is QDs. The excited QDs exhibit size and composition-dependent fluorescence emission spectra, allowing simultaneous detection of different biomarkers. In summary, the developed and characterized magneto-immunoassay could be adapted to multiplex biomarker detection using different QDs characterized by a good quantum yield and high photochemical stability.

Author Contributions: Conceptualization, A.R.; methodology, U.T., A.P., A.K.-M. and A.R.; software, A.P., G.K. and E.B. (Eiva Bernotiene); validation, E.B. (Ema Baliunaite) and A.R.; formal analysis, E.B. (Ema Baliunaite), A.P. and B.B.; investigation, E.B. (Ema Baliunaite), B.B. and A.P.; resources, E.B. (Eiva Bernotiene), G.K. and A.R.; writing—original draft preparation, E.B. (Ema Baliunaite), A.P., B.B., A.K.-M., G.K., E.B. (Eiva Bernotiene), A.M. and A.R.; writing—review and editing, A.R., E.B. (Ema Baliunaite), A.P., B.B., A.K.-M., U.T., G.K., E.B. (Eiva Bernotiene) and A.M.; visualization, E.B. (Ema Baliunaite), A.P. and A.R.; supervision, A.R.; project administration, E.B. (Eiva Bernotiene) and G.K.; funding acquisition, A.R. and A.M. All authors have read and agreed to the published version of the manuscript.

Funding: This research was funded by the European Regional Development Fund through the Research Council of Lithuania according to the Programme Attracting Foreign Researchers for Research Implementation, Grant No. 01.2.2-LMT-K-718-02-0022.

Institutional Review Board Statement: Not applicable.

Informed Consent Statement: Not applicable.

Data Availability Statement: The data presented in this study are available on request from the corresponding author.

Conflicts of Interest: The authors declare no conflict of interest.

References

1. Popov, A.; Stirke, A.; Bakute, N.; Brasiunas, B.; Ramanavicius, A.; Ramanaviciene, A. Efficiency of granulocyte colony-stimulating factor immobilized on magnetic microparticles on proliferation of NFS-60 cells. *Colloids Surf. A Physicochem. Eng. Asp.* **2019**, *578*, 123580. [CrossRef]
2. Baniukevic, J.; Hakki Boyaci, I.; Goktug Bozkurt, A.; Tamer, U.; Ramanavicius, A.; Ramanaviciene, A. Magnetic gold nanoparticles in SERS-based sandwich immunoassay for antigen detection by well oriented antibodies. *Biosens. Bioelectron.* **2013**, *43*, 281–288. [CrossRef] [PubMed]
3. Moro, L.; Turemis, M.; Marini, B.; Ippodrino, R.; Giardi, M.T. Better together: Strategies based on magnetic particles and quantum dots for improved biosensing. *Biotechnol. Adv.* **2017**, *35*, 51–63. [CrossRef] [PubMed]
4. Gloag, L.; Mehdipour, M.; Chen, D.; Tilley, R.D.; Gooding, J.J. Advances in the Application of Magnetic Nanoparticles for Sensing. *Adv. Mater.* **2019**, *31*, 1904385. [CrossRef] [PubMed]
5. Poudineh, M.; Aldridge, P.M.; Ahmed, S.; Green, B.J.; Kermanshah, L.; Nguyen, V.; Tu, C.; Mohamadi, R.M.; Nam, R.K.; Hansen, A.; et al. Tracking the dynamics of circulating tumour cell phenotypes using nanoparticle-mediated magnetic ranking. *Nat. Nanotechnol.* **2017**, *12*, 274–281. [CrossRef]
6. Campuzano, S.; de Ávila, B.E.-F.; Yuste, J.; Pedrero, M.; García, J.L.; García, P.; García, E.; Pingarrón, J.M. Disposable amperometric magnetoimmunosensors for the specific detection of Streptococcus pneumoniae. *Biosens. Bioelectron.* **2010**, *26*, 1225–1230. [CrossRef]
7. Tang, C.; He, Z.; Liu, H.; Xu, Y.; Huang, H.; Yang, G.; Xiao, Z.; Li, S.; Liu, H.; Deng, Y.; et al. Application of magnetic nanoparticles in nucleic acid detection. *J. Nanobiotechnol.* **2020**, *18*, 62. [CrossRef]
8. Laube, T.; Kergaravat, S.V.; Fabiano, S.N.; Hernández, S.R.; Alegret, S.; Pividori, M.I. Magneto immunosensor for gliadin detection in gluten-free foodstuff: Towards food safety for celiac patients. *Biosens. Bioelectron.* **2011**, *27*, 46–52. [CrossRef]
9. Lin, P.-C.; Tseng, M.-C.; Su, A.-K.; Chen, Y.-J.; Lin, C.-C. Functionalized Magnetic Nanoparticles for Small-Molecule Isolation, Identification, and Quantification. *Anal. Chem.* **2007**, *79*, 3401–3408. [CrossRef]
10. Jarockyte, G.; Karabanovas, V.; Rotomskis, R.; Mobasheri, A. Multiplexed Nanobiosensors: Current Trends in Early Diagnostics. *Sensors* **2020**, *20*, 6890. [CrossRef]
11. Popov, A.; Brasiunas, B.; Kausaite-Minkstimiene, A.; Ramanaviciene, A. Metal Nanoparticle and Quantum Dot Tags for Signal Amplification in Electrochemical Immunosensors for Biomarker Detection. *Chemosens* **2021**, *9*, 85. [CrossRef]
12. Goldman, E.R.; Clapp, A.R.; Anderson, G.P.; Uyeda, H.T.; Mauro, J.M.; Medintz, I.L.; Mattoussi, H. Multiplexed Toxin Analysis Using Four Colors of Quantum Dot Fluororeagents. *Anal. Chem.* **2004**, *76*, 684–688. [CrossRef] [PubMed]
13. Growth Hormone Human ELISA Kit. Available online: https://www.thermofisher.com/elisa/product/Growth-Hormone-Human-ELISA-Kit/EHGH1 (accessed on 15 November 2021).
14. Popii, V.; Baumann, G. Laboratory measurement of growth hormone. *Clin. Chim. Acta* **2004**, *350*, 1–16. [CrossRef] [PubMed]
15. Saugy, M.; Robinson, N.; Saudan, C.; Baume, N.; Avois, L.; Mangin, P. Human growth hormone doping in sport. *Br. J. Sports Med.* **2006**, *40*, i35–i39. [CrossRef] [PubMed]
16. Baumann, G.P. Growth hormone isoforms. *Growth Horm. IGF Res.* **2009**, *19*, 333–340. [CrossRef] [PubMed]
17. Møller, N.; Jørgensen, J.O.L. Effects of Growth Hormone on Glucose, Lipid, and Protein Metabolism in Human Subjects. *Endocr. Rev.* **2009**, *30*, 152–177. [CrossRef] [PubMed]

18. Rhee, N.; Jeong, K.; Yang, E.M.; Kim, C.J. Gigantism caused by growth hormone secreting pituitary adenoma. *Ann. Pediatr. Endocrinol. Metab.* **2014**, *19*, 96–99. [CrossRef]
19. Fowelin, J.; Attvall, S.; von Schenck, H.; Bengtsson, B.-Å.; Smith, U.; Lager, I. Effect of prolonged hyperglycemia on growth hormone levels and insulin sensitivity in insulin-dependent diabetes mellitus. *Metabolism* **1993**, *42*, 387–394. [CrossRef]
20. Salomon, F.; Cuneo, R.; Sönksen, P.H. Growth Hormone and Protein Metabolism. *Hormones* **1991**, *36* (Suppl. 1), 41–43. [CrossRef]
21. Ayuk, J.; Sheppard, M.C. Growth hormone and its disorders. *Postgrad. Med. J.* **2006**, *82*, 24–30. [CrossRef]
22. Reiter, E.O.; Morris, A.H.; Macgillivray, M.H.; Weber, D. Variable Estimates of Serum Growth Hormone Concentrations by Different Radioassay Systems. *J. Clin. Endocrinol. Metab.* **1988**, *66*, 68–71. [CrossRef] [PubMed]
23. Albertsson-Wikland, K.; Jansson, C.; Rosberg, S.; Novamo, A. Time-resolved immunofluorometric assay of human growth hormone. *Clin. Chem.* **1993**, *39*, 1620–1625. [CrossRef] [PubMed]
24. Iranmanesh, A.; Grisso, B.; Veldhuis, J.D. Low basal and persistent pulsatile growth hormone secretion are revealed in normal and hyposomatotropic men studied with a new ultrasensitive chemiluminescence assay. *J. Clin. Endocrinol. Metab.* **1994**, *78*, 526–535. [CrossRef] [PubMed]
25. Kausaite-Minkstimiene, A.; Ramanavicius, A.; Ruksnaite, J.; Ramanaviciene, A. A surface plasmon resonance immunosensor for human growth hormone based on fragmented antibodies. *Anal. Methods* **2013**, *5*, 4757–4763. [CrossRef]
26. Makaraviciute, A.; Ramanavicius, A.; Ramanaviciene, A. Development of a reusable protein G based SPR immunosensor for direct human growth hormone detection in real samples. *Anal. Methods* **2015**, *7*, 9875–9884. [CrossRef]
27. Rezaei, B.; Khayamian, T.; Majidi, N.; Rahmani, H. Immobilization of specific monoclonal antibody on Au nanoparticles for hGH detection by electrochemical impedance spectroscopy. *Biosens. Bioelectron.* **2009**, *25*, 395–399. [CrossRef]
28. Serafín, V.; Úbeda, N.; Agüí, L.; Yáñez-Sedeño, P.; Pingarrón, J.M. Ultrasensitive determination of human growth hormone (hGH) with a disposable electrochemical magneto-immunosensor. *Anal. Bioanal. Chem.* **2012**, *403*, 939–946. [CrossRef]
29. Tamer, U.; Gündoğdu, Y.; Boyacı, İ.H.; Pekmez, K. Synthesis of magnetic core–shell Fe_3O_4–Au nanoparticle for biomolecule immobilization and detection. *J. Nanoparticle Res.* **2010**, *12*, 1187–1196. [CrossRef]
30. Gupta, A.K.; Gupta, M. Synthesis and surface engineering of iron oxide nanoparticles for biomedical applications. *Biomaterials* **2005**, *26*, 3995–4021. [CrossRef]
31. He, J.; Unser, S.; Bruzas, I.; Cary, R.; Shi, Z.; Mehra, R.; Aron, K.; Sagle, L. The facile removal of CTAB from the surface of gold nanorods. *Colloids Surf. B Biointerfaces* **2018**, *163*, 140–145. [CrossRef]
32. Xu, Z.; Hou, Y.; Sun, S. Magnetic Core/Shell Fe_3O_4/Au and Fe_3O_4/Au/Ag Nanoparticles with Tunable Plasmonic Properties. *J. Am. Chem. Soc.* **2007**, *129*, 8698–8699. [CrossRef] [PubMed]
33. Silva, S.M.; Tavallaie, R.; Sandiford, L.; Tilley, R.D.; Gooding, J.J. Gold coated magnetic nanoparticles: From preparation to surface modification for analytical and biomedical applications. *Chem. Commun.* **2016**, *52*, 7528–7540. [CrossRef] [PubMed]
34. Haiss, W.; Thanh, N.T.K.; Aveyard, J.; Fernig, D.G. Determination of Size and Concentration of Gold Nanoparticles from UV−Vis Spectra. *Anal. Chem.* **2007**, *79*, 4215–4221. [CrossRef] [PubMed]
35. Tamer, U.; Cetin, D.; Suludere, Z.; Boyaci, I.H.; Temiz, H.T.; Yegenoglu, H.; Daniel, P.; Dinçer, İ.; Elerman, Y. Gold-Coated Iron Composite Nanospheres Targeted the Detection of Escherichia coli. *Int. J. Mol. Sci.* **2013**, *14*, 6223. [CrossRef] [PubMed]
36. Makaraviciute, A.; Ruzgas, T.; Ramanavicius, A.; Ramanaviciene, A. Antibody fragment immobilization on planar gold and gold nanoparticle modified quartz crystal microbalance with dissipation sensor surfaces for immunosensor applications. *Anal. Methods* **2014**, *6*. [CrossRef]
37. Treviño, J.; Calle, A.; Rodríguez-Frade, J.M.; Mellado, M.; Lechuga, L.M. Surface plasmon resonance immunoassay analysis of pituitary hormones in urine and serum samples. *Clin. Chim. Acta* **2009**, *403*, 56–62. [CrossRef]
38. Enzyme Immunoassay for Quantitative Determination of Human Growth Hormone. Available online: https://www.ibl-america.com/content/elisa/E02.pdf (accessed on 15 November 2021).
39. Human Growth Hormone ELISA Kit. Available online: https://www.antibodies.com/human-growth-hormone-elisa-kit-a33015 (accessed on 15 November 2021).

Paper 4

Gold nanoparticle based colorimetric sensing strategy for the determination of reducing sugars

B. Brasiunas, A. Popov, A. Ramanavicius, A. Ramanaviciene

Food Chemistry, 2021, 351, 129238
doi.org/10.1016/j.foodchem.2021.129238

Food Chemistry 351 (2021) 129238

Contents lists available at ScienceDirect

Food Chemistry

journal homepage: www.elsevier.com/locate/foodchem

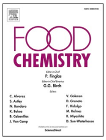

Gold nanoparticle based colorimetric sensing strategy for the determination of reducing sugars

Benediktas Brasiunas, Anton Popov, Arunas Ramanavicius, Almira Ramanaviciene *

NanoTechnas – Center of Nanotechnology and Materials Science, Institute of Chemistry, Faculty of Chemistry and Geosciences, Vilnius University, Naugarduko st. 24, LT-03225 Vilnius, Lithuania

ARTICLE INFO

Keywords:
Fructose
Glucose
Lactose
Mannose
Gold nanoparticles
Optical sensor

ABSTRACT

The colorimetric sensors for reducing sugars based on a redox reaction between $AuCl_4^-$ ions and fructose, glucose, lactose, or mannose are presented. Gold nanoparticles (AuNPs) that formed at room temperature as a product of this reaction were registered using a spectrophotometer. Lengthening reaction time had a positive effect on the sensitivity of the developed sensors. Different reducing sugars exhibited distinct reaction rates for AuNP formation, with the rate decreasing in the order fructose > glucose > lactose > mannose. LOD values after 60 min of the reaction for different sugars followed the same trend of 0.067, 0.081, 0.087, and 0.106 mM, while LOQ was 0.223, 0.270, 0.289, and 0.353 mM, respectively. The linear range 60 min since the start of the reaction varied from 0.3 up to 5.0 mM for different sugars. The colorimetric sensor was evaluated for use in real samples of beverages, milk, and saliva.

1. Introduction

Any monosaccharides and some disaccharides containing aldehyde or ketone group in their molecular structure are classified as reducing sugars and at special conditions they can act like reducing agents. Excessive sugar consumption is considered to be the main factor in global healthcare-related problems, such as diabetes, obesity, tooth decay, heart diseases, weakened immunity and others. Sugars in food and drinks might occur naturally or can be added. Reducing sugars are found in foods in different forms such as crystals, or open-chain or cyclic forms in a solution. Only open-chain sugar form can participate in oxidation–reduction reactions, however, the concentration of this form in reducing sugar solutions is mostly well below 1% (Robyt, 1998). Low open-chain form concentration tends to lead to a slow oxidation–reduction reaction rate. In order to solve this problem, increased temperatures or special catalysts are widely used when performing sugar-based oxidation–reduction reactions (Miljković, 2009). However, during this reaction, open-chain sugar concentration decreases due to it being consumed in the process. This is mitigated by a process called mutarotation, where various reducing sugar forms can turn from one to another, maintaining equilibrium. However, the rate of mutarotation is slow at room temperature and neutral pH (Kaufmann, Krüger, Mügge, & Kroh, 2018), meaning this can be a limiting step in the oxidation–reduction reaction (Miljković, 2009). In order to increase the rate of mutarotation, higher temperatures and acidic or basic conditions are often used. When considering a change in pH, basic conditions are employed more often as the rate of mutarotation is approximately 5000 times (pH 10) faster than in acidic conditions (pH 4) (Robyt, 1998). Another important mechanism of reducing sugar participation in oxidation–reduction reactions is Lobry de Bruyn-Alberda van Eckenstein transformation (Speck, 1958) that can be acid or base catalyzed. The process results in aldose–aldose, ketose–ketose epimerization, and aldose–ketose isomerization through a common enediol intermediate (Miljković, 2009; Speck, 1958). This mechanism allows for a ketose such as fructose to participate in the oxidation–reduction reactions either through the enediol intermediate, or through the conversion to aldoses, such as mannose or glucose.

In analytical chemistry there are various reducing sugar detection methods such as refractometry, polarized light angle measurements, amperometry, potentiometry and conductometry (Buzanovskii, 2015; Magwaza & Opara, 2015). These materials having reducing properties can also be employed in analytical systems based on oxidation and reduction reactions such as Somogyi-Nelson method (Nelson, 1944). However, it needs to be taken into consideration that only open-chain

---

* Corresponding author.
E-mail addresses: benediktas.brasiunas@chgf.vu.lt (B. Brasiunas), anton.popov@chgf.vu.lt (A. Popov), arunas.ramanavicius@chf.vu.lt (A. Ramanavicius), almira.ramanaviciene@chf.vu.lt (A. Ramanaviciene).

https://doi.org/10.1016/j.foodchem.2021.129238
Received 24 July 2020; Received in revised form 4 January 2021; Accepted 25 January 2021

form of reducing sugars participates in the reactions, and reducing sugar sensors based on oxidation–reduction reactions mostly determine total reducing sugar concentration in the sample and rarely distinguish between different sugars (Robyt, 1998). The most common reducing sugar sensors that are specific for an analyte are based on detection using enzymes, such as a glucose biosensor based on glucose oxidase (German, Ramanavicius, Voronovic, & Ramanaviciene, 2012). Despite the selectivity and sensitivity of biosensors they involve enzymes that are sensitive to changes in the detection medium, thus measurements must be performed at conditions optimal for the enzyme.

Nowadays nanomaterials are widely used and are still of growing importance every year in various applications. In analytical chemistry nanomaterials are used for electron transfer (Ramanavicius, German, & Ramanaviciene, 2017) and signal strengthening (Zhang et al., 2015), increasing sensitivity, reproducibility and stability of the sensors (Yan et al., 2019) or as a substrate for molecule immobilization (Kumar, Ahlawat, Kumar, & Dilbaghi, 2015). Additionally, the enlargement of AuNPs in the solution or on the surface in the presence of glucose can be an analytical signal for detecting the desired analyte (Ramanaviciene et al., 2016). When it comes to analytical chemistry there are different ways to detect sugars, mainly acoustically, electrochemically, or optically. Out of all these detection methods, optical methods are attractive due to their non-destructive nature, quick response, and high precision. Methods such as UV–vis spectroscopy, photoluminescence and surface plasmon resonance are the next generation of sensing techniques for everyday use. To combine nanomaterials and optical detection methods in analytical systems, optically active nanomaterials are needed. Most well-known, understood and used optically active nanomaterials are various AuNPs. Due to their unique optical and physical properties AuNPs have been widely used in different analytical systems to strengthen optical signals and improve signal stability (Zhao et al., 2015). Optical methods, such as UV–vis spectroscopy, are useful for the monitoring of AuNP formation or aggregation due to the color change that occurs when AuNPs are present. In addition, local surface plasmon resonance (LSPR) depends on the AuNP shape and size as well as various other factors meaning that variation in LSPR maximum ($LSPR_{max}$) position could also be used as an analytical signal (He, Liu, Kong, & Liu, 2005).

In this work the formation of AuNPs as a result of an oxidation–reduction reaction in the presence of reducing sugars was used as an analytical signal. The reaction is executed at room temperature without the need of AuNP seeds. The aim of this study was to perform a comparative colorimetric study of 4 reducing sugars. As a result, the performance of developed colorimetric sensor was investigated in model samples with glucose, fructose, lactose, and mannose. From this work we aimed to evaluate the viability of using developed colorimetric sensor in real samples containing one analyte or two analyte mixture.

2. Materials and methods

2.1. Materials

Cetyltrimethylammonium bromide (CTAB), D-lactose monohydrate and D-(+)-mannose were purchased from Roth (Karlsruhe, Germany). Sodium hydroxide and D-(−)-fructose were acquired from Merck. Hydrogen tetrachloroaurate(III) trihydrate ($HAuCl_4 \times 3H_2O$) was bought from Sigma-Aldrich (Steinheim, Germany) and D-(+)-glucose was purchased from Alfa Aesar (Karlsruhe, Germany). All aqueous solutions were prepared with deionized water (18 MΩ cm^{-1}).

2.2. Reaction course evaluation

The formation of AuNPs is the result of an oxidation–reduction reaction between $HAuCl_4$ and reducing sugar at room temperature in a basic medium (NaOH) where CTAB acts as a surfactant to stabilize formed nanoparticles. NaOH, CTAB and $HAuCl_4$ concentrations were optimized by changing the concentration of one component while maintaining the same concentrations of other components. In all cases, a constant glucose (reducing sugar) concentration of 0.5 mM was used. The formation of AuNPs was done in polystyrene cuvettes (1 cm in width) and observed using UV – vis spectrometer Lambda 25 (Perkin Elmer) at 20 °C temperature in the range from 400 to 800 nm. The desired outcome of the optimization was to detect the highest absorbance value at LSPR of 525 nm ($LSPR_{525}$), without decreasing the stability of formed AuNP colloid solution.

2.3. Determination of sugar concentrations in model samples

Glucose, fructose, lactose, and mannose were used for the preparation of model samples. Reducing sugar concentrations were tested in the range from 0.3 to 40 mM. Calibration curves were constructed for all reducing sugars using absorbance at $LSPR_{525}$ of model samples as an analytical signal 20, 40, and 60 min since the start of the reaction. Analytical system parameters were calculated from the calibration curves. Limit of detection (LOD) was defined as 3 times the standard deviation of the sample with the lowest reducing sugar concentration while the limit of quantification (LOQ) as 10 times the same standard deviation.

2.4. Evaluation of the developed colorimetric sensor in real samples

Designed sensor was employed for the detection of reducing sugars in real samples. If required, samples were additionally prepared for the analysis. Reaction components were mixed maintaining the same final concentration of CTAB (3.7 mM), $HAuCl_4$ (1 mM) and NaOH (0.1 M), and reaction was carried out for 60 min at a temperature of 20 °C. Absorbance at $LSPR_{525}$ was measured as an analytical signal. The applicability of the developed sensor for the detection of reducing sugars in real samples was investigated.

The samples of lactose-free and ordinary milk were bought at a supermarket and additionally prepared for the analysis. Proteins in the samples were precipitated by adding $CuSO_4$ up to 0.5% mass concentration and waiting for 10 min. The mixture was then centrifuged at 17000×*g* for 15 min. Supernatant was collected and added directly to the reaction mixture. The absorbance at $LSPR_{525}$ was registered, and lactose concentration was evaluated using a calibration curve.

In addition, the sensor was used to detect reducing sugars in beverages. The Coca-Cola and Coca-Cola Zero beverages were chosen for the analysis. These samples were investigated without preliminary preparation. Coca-Cola Zero was used as a known negative control in the analysis.

Lastly, a saliva sample was tested using the developed sensor. The written consent was obtained from the healthy volunteer for this research and publication. Before the sample collection mouth was rinsed with water for 2 min and after that saliva was collected with a cotton roll by chewing on it for 1 min. Saliva was then extracted from the cotton roll with a help of a sterile syringe through a 0.23 μm PVDF filter to separate proteins. The saliva extract was then directly used in the reaction.

3. Results and discussion

In this research the formation of AuNPs was used as a signal for the evaluation of reducing sugar – fructose, glucose, lactose, and mannose, concentration. The synthesis of AuNPs is the result of an oxidation–reduction reaction between $AuCl_4^-$ ions and reducing sugars where CTAB acts as a stabilizer for formed nanoparticles (Scheme 1). The use of surfactant is paramount otherwise AuNPs aggregate and precipitate quickly from the reaction mixture solution. Scampicchio group (Scampicchio, Arecchi, & Mannino, 2009) suggested that reducing sugar based reaction takes place through an open chain aldehyde group and that fructose participates in the reaction only after being converted to glucose or mannose due to Lobry de Bruyn-Alberda van Eckenstein

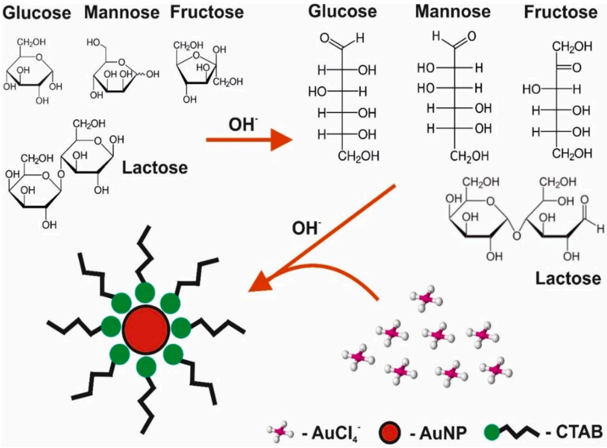

Scheme 1. The principle of gold nanoparticle based colorimetric assay for the determination of reducing sugars.

transformations in highly alkaline medium (pH > 11) (Speck, 1958). However, more investigations are needed to assess whether the reaction takes place through an enediol intermediate or through aldehyde group. Nonetheless, the oxidation–reduction reaction rate in neutral pH is slow, thus the addition of NaOH is required to create a basic medium, which accelerates sugar mutarotation as well as allow for Lobry de Bruyn-Alberda van Eckenstein transformations to take place through proton removal initiated by hydroxide ion (Miljković, 2009). Depending on the reducing sugar concentration the oxidation–reduction reaction rate changes resulting in different amount of AuNPs formed in the same amount of time. This difference was used as an analytical signal for reducing sugar concentration monitoring. The detection was performed using UV–vis spectroscopy in the range from 400 to 800 nm.

3.1. Reaction course evaluation

Optimal CTAB, $HAuCl_4$ and NaOH concentrations were selected by varying the concentration of one of the components while keeping other components concentration constant. In all cases 0.5 mM of glucose was used to carry out the reaction. Later on, the $LSPR_{525}$ was determined to be most relevant for sugar concentration evaluation, thus, when choosing optimal component concentrations, the aim was to detect the highest $LSPR_{525}$ value in the first hour without losing the stability of formed AuNPs. The results of the optimization are provided in Supplementary material (Fig. S1) as well as described in more detail. Here the most important findings are summarized.

CTAB as cationic surfactant is often used in water-based solutions for the stabilization of metal nanoparticles (Moon, Kusunose, & Sekino, 2009). Varying the CTAB concentration allows to control morphology, shape and size of AuNPs (Ahn, Lee, Jin, & Nam, 2013; Gu & Li, 2009; Li et al., 2013). It was found that the increase of CTAB concentration resulted in a lower absorbance value at $LSPR_{525}$ after 1 h. This can be reasoned by increased surface coverage of AuNP with CTAB (Smith & Korgel, 2008) leading to slower AuNPs formation and growth rate. The chosen CTAB concentration for further measurements was 3.7 mM in order to ensure highest stability of formed AuNPs, which is relevant when higher sugar concentrations are used.

In the case of gold precursor – $HAuCl_4$ concentration, as expected, it was observed that increasing $HAuCl_4$ concentration in the reaction mixture leads to stronger absorbance at $LSPR_{525}$ after 1 h, however a further increase in concentration leads to diminishing returns. It was decided to use 1 mM $HAuCl_4$ concentration for further measurements.

When examining NaOH concentration influence on the reaction it was observed that with no NaOH present the reaction does not proceed. This can be explained by a slow mutarotation rate of glucose stereoisomers to an open chain glucose variant in neutral pH solutions (Kaufmann et al., 2018), considering only open form of reducing sugar can be involved in the reaction. It was observed that increasing reaction mixture pH with higher NaOH concentration resulted in faster AuNP formation rate, however, colloidal AuNPs solution was not stable when the concentration of NaOH was too high. The concentration of NaOH chosen for further experiments was 0.1 M as it leads to faster AuNP formation but preserves nanoparticle stability.

The absorbance spectra of the reaction mixture containing 1 mM glucose, 3.7 mM CTAB, 1 mM $HAuCl_4$ and 0.1 M NaOH dependence on the duration of the reaction (Fig. 1) was evaluated. It was observed that LSPR peak first formed at ~ 550 nm. As the reaction proceeds further,

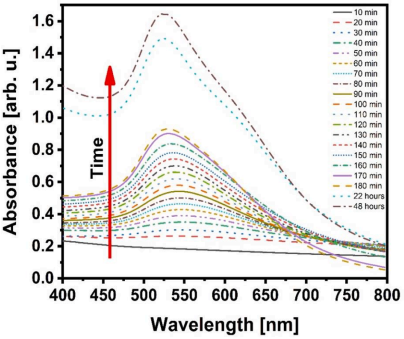

Fig. 1. Absorbance spectra of the reaction mixture with 1 mM glucose dependence on the reaction time. Reaction mixture consists of 3.7 mM CTAB, 1 mM $HAuCl_4$ and 0.1 M NaOH.

after 60 min the blue shift of LSPR peak started until it eventually settled at ~ 525 nm. It was discovered that the starting time and the rate of this shift depended highly on reducing sugar concentration, with the shift starting earlier and the rate of the shift increasing as sugar concentration increases. This blue shift can be explained by the attachment of gold atoms in the electronic double layer of the seed particles as co-ions during the beginning of AuNPs growth (Wuithschick et al., 2015). It can also be seen that almost half of the final absorbance was observed after the first 3 h of the reaction and that AuNPs formation still proceeded after 24 h, albeit significantly slower. The reaction rate could be further increased by accelerating maturation using higher temperatures. For example, glucose solution could be heated up before infusion into reaction mixture (Luo, Ji, Zhuang, & Yang, 2014). It is also worth noting that the reaction is performed in alkaline medium, thus AuNP formation likely occurs through the intermediates of $[AuCl(OH)_3]^-$ or $[Au(OH)_4]^-$. Therefore, nucleation stage is longer and from this point of view reaction rate is slower in comparison with reaction rate in acidic solution (Thanh, Maclean, & Mahiddine, 2014), although the trend is opposite for the rate of mutarotation (Robyt, 1998). Similar system was explored by Panigrahi group (Panigrahi, Kundu, Ghosh, Nath, & Pal, 2005) where the evolution of the reaction at higher temperatures and acidic conditions was investigated focusing on nanoparticle synthesis rather than analytical system development.

3.2. Evaluation of the colorimetric assay performance with various reducing sugars

The analytical system performance was evaluated with 4 different reducing sugars: fructose, glucose, lactose, and mannose. The best linear fit of absorbance dependence on sugar concentration was found at $LSPR_{525}$. Calibration curves for all sugars were created after 20, 40, and 60 min from the start of the reaction. Final sugar concentrations in the sample varied in the range from 0.3 to 40 mM, although in all cases the upper bound of the linear range was found to be from 5 to 10 mM. The results are represented in Fig. 2.

The same tendencies were observed with all sugars, monosaccharides (fructose, glucose, mannose) and disaccharide (lactose). The slope of the calibration curves of the same sugars increased as a function of time meaning that the sensitivity of the system increases, and it is possible to determine lower sugar concentrations. This can be explained by the increase in the amount of formed AuNPs, which yields increased absorbance at $LSPR_{525}$. On the other hand, as the reaction proceeds the linear range of the calibration curve becomes narrower because the samples with higher sugar concentrations deviate from linear correlation. For instance, the linear range of glucose calibration curve 20 min since the start of the reaction was from 0.5 to 10 mM while after 40 min it was from 0.3 to 7 mM. This property of the analytical system allows the creation of calibration curves in different analyte concentration ranges depending on the time of the reaction.

Different sugars displayed distinct slopes for the calibration curves after the same period of time (Fig. 3) indicating different AuNP formation rate depending on the sugar used. The reaction rate decreased in the following order: fructose > glucose > lactose > mannose. Other authors amperometrically determined that the direct oxidation current of reducing sugars followed the trend: fructose > glucose > lactose indicating similar trend (Mohammadia, Amine, Rhazi, & Brett, 2004). Thus, results obtained during the determination of four reducing sugars, can likely be explained by the different concentration of open chain stereoisomer in the reaction mixture (Robyt, 1998; Wrolstad, 2013), and by the specific sugar reduction potential (Mohammadia et al., 2004). The highest reaction rate was determined in the case of fructose. It can be related both with significantly higher concentration of open chain form of fructose in comparison with other investigated reducing sugars (Cui, 2005) and the highest reduction potential (Mohammadia et al., 2004).

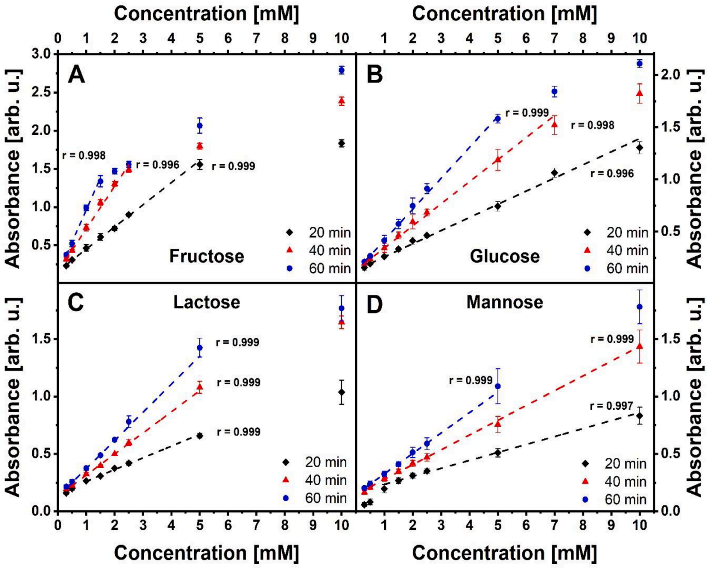

Fig. 2. $LSPR_{525}$ dependence on (A) fructose, (B) glucose, (C) lactose, and (D) mannose concentration in the model samples after the selected duration of AuNPs formation. Reaction mixture consists of 3.7 mM CTAB, 1 mM $HAuCl_4$, 0.1 M NaOH and a corresponding reducing sugar.

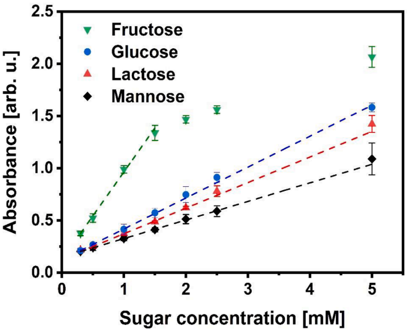

Fig. 3. LSPR$_{525}$ dependence on the concentration of different sugars. Reaction duration was 60 min while the reaction mixture consisted of 3.7 mM CTAB, 1 mM $HAuCl_4$, 0.1 M NaOH and a corresponding reducing sugar.

On the other hand, mannose is practically not present in open chain form in water-based solutions, therefore, the rate of oxidation–reduction reaction was lower than that for the reaction mixtures containing glucose or lactose. Faster AuNPs formation in the case of glucose in comparison with lactose can also be related to higher glucose reducing potential (Mohammadia et al., 2004).

The analytical sensors parameters (LOD, LOQ, Linear range) are provided in Table 1. LOD values are determined for the final sugar concentration in the reaction mixture and thus it should also be considered that real samples would be diluted after the addition, although, this can be prevented by using starting reagents of higher concentrations. Analytical system for the determination of reducing sugars was presented by Palazzo group (Palazzo, Facchini, & Mallardi, 2012). The reported LOD for glucose was 10 μM compared to 81 μM in our case, however, they performed the analysis at 70 °C as well as at pH 3 to kick-start the reaction. The use of higher temperatures in our case would likely lead to improved LOD and LOQ values. We expect this since AuNP synthesis rate increases with temperature resulting in higher absorbance at LSPR$_{525}$ after the same duration of analysis. On the other hand, based on our results it would also most likely lead to a narrower linear range. This reasoning is also supported by Palazzo et. al where the authors report a dynamic range (0.03 to 1.5 mM) that is narrower than the linear range for our analytical system (0.3 to 5.0 mM). For the use case in real samples of foods or blood a wider linear range is likely preferable rather than improved sensitivity considering reducing sugars are present in high concentrations. Pelle et. al. also described a similar system based on AuNPs formation, but they used AuNPs in a different way – for the determination of polyphenols (Della Pelle et al., 2015). A comparison of our analytical sensing strategy with other major detection methods that are used for reducing sugar detection, mainly chromatography and biosensors, strikes a balance in case of sensitivity, linear range, and simplicity. In the case of biosensors, a specific biocomponent is needed for reducing sugar detection, which are enzymes most of the time (Ramanavičius, Kaušaitė, & Ramanavičienė, 2005). Biosensors provide superb specificity, however they suffer from a complex sensor design as well as signal reproducibility and degradation issues. Chromatographic reducing sugar detection methods significantly improve analytical detection parameters with LOD of 1 μM (Jochum et al., 2002), however, sophisticated and expensive lab equipment and personnel training is required. In our case, only a single wavelength spectrophotometer is needed, although with further improvements a visual reducing sugar concentration detection is likely possible since a distinct color change can be observed during the reaction. Another important aspect of this analytical system that should not be overlooked is specificity. The detection strategy is based on the oxidation–reduction reaction meaning that other reducing agents present in the sample could also reduce $HAuCl_4$. However, usually for samples like foods, blood or saliva other reducing agents are present in orders of magnitude lower concentrations compared with the concentration of reducing sugars such as glucose, fructose, or lactose likely leading to minimal interference. On the other hand, the matrix effect, and the behavior of reducing sugar mixtures are more important to assess given that our new research showed that different reducing sugars have distinct AuNP synthesis rates. As such, results described in the next section dealing with real samples further elaborate on this sensing strategy aspect.

Table 1
The analytical parameters of reducing sugar colorimetric sensor based on AuNPs formation.

Reducing sugars, time of the reaction	LOD, mM	LOQ, mM	Linear range after 60 min, mM
Fructose, 60 min	0.067	0.223	0.3–1.5
Glucose, 60 min	0.081	0.270	0.3–5.0
Lactose, 60 min	0.087	0.289	0.3–5.0
Mannose, 60 min	0.106	0.353	0.35–5.0

3.3. Evaluation of the colorimetric sensor performance in real samples

The developed sensor was employed for the detection of reducing sugars in different real samples – beverages, milk, and saliva. Most of the beverages contain sugars, thus, they are a relevant test case considering specific sugars may pose unwanted effects on human health (Bray, Nielsen, & Popkin, 2004). In our case Coca-Cola and Coca-Cola Zero were chosen as known beverages with a reducing sugar mixture and without reducing sugars. The measurements of reducing sugar level in beverages are displayed in Fig. 4A.

For the sample of Coca-Cola Zero there was no LSPR peak registered after 1 h. This is expected considering that the formation of AuNPs should not occur if there are no reducing sugars or other reducing agents present in the sample. On the other hand, Coca-Cola beverage containing high fructose corn syrup (HFCS) participates in the reaction yielding a detectable signal.

Most commonly used HFCS for beverages is HFCS-55 meaning that the ratio between fructose and glucose is 55:45 (Bray et al., 2004). This is a common sample containing a mixture of specific analytes. Considering different AuNPs formation rates for glucose and fructose usually there would be a need for the calibration curve created from a model system with the same reducing sugar ratio in order to determine the concentration of these sugars in a real sample. However, the data presented in Fig. 4B suggests that it might be possible to avoid this problem and create calibration curves for the desired sugar ratios mathematically. Absorbance of LSPR$_{525}$ was monitored and registered every 10 min for 3 different model samples containing 1 mM of fructose (**1**), 1 mM of glucose (**4**) and a sample with overall sugar concentration of 1 mM where the ratio of glucose and fructose was 50:50 (**2**). In addition, the dependency of absorbance average at LSPR$_{525}$ (**3**), calculated from the absorbance spectra of solution containing 1 mM of fructose (**1**) and 1 mM of glucose (**4**), on reaction duration was plotted. As can be seen in Fig. 4B the mathematical averages of LSPR$_{525}$ values (**3**) are very close to measured values of a model sample where sugar ratio is 50:50 (**2**) as long as the averaging is done in the linear range domain for both sugars. In fact, the average percentage error throughout the whole linear absorbance dependence on the reaction time range (from 10 to 60 min) was only 2.3% compared with the model sample. If the same trend holds for samples of different concentrations it could be possible to mathematically construct calibration curves for desired sugar ratios. This idea was tested out for the analysis of beforementioned Coca-Cola sample by applying a combination of linear calibration curves for glucose and fructose (Fig. 3) adjusting for 55:45 ratio of fructose to glucose. Overall sugar concentration calculated from mathematically combined

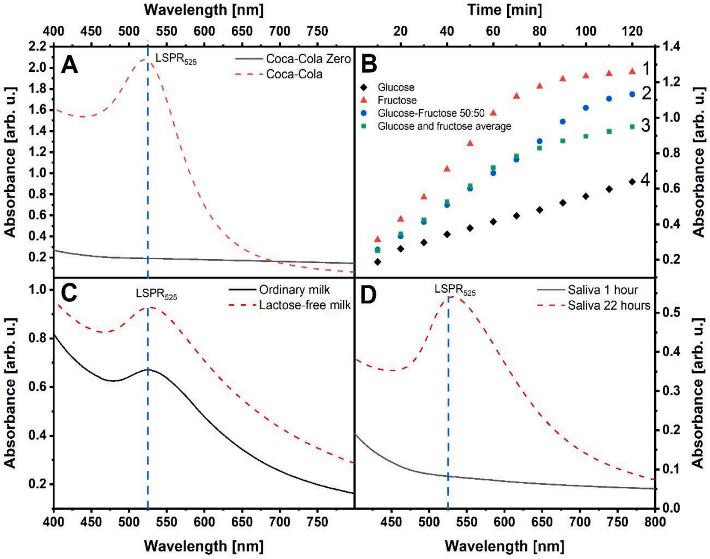

Fig. 4. (A) Absorbance spectra of the reaction mixture containing Coca-Cola and sugar free Coca-Cola Zero after 1 h since the start of the reaction. (B) The dependence of absorbance at $LSPR_{525}$ on the reaction duration in the solution containing 1 mM of fructose (1), 1 mM of glucose (4) and a 1 mM mixture of glucose and fructose at the ratio of 50:50 (2). The mathematical average of $LSPR_{525}$ values (3) was calculated from the absorbance spectra of the solution containing (1) 1 mM of fructose and (4) 1 mM of glucose. (C) Absorbance spectra of the reaction mixture containing ordinary and lactose free milk after 1 h since the start of the reaction. (D) Absorbance spectra of the reaction mixture containing saliva.

calibration curve was 19.7% lower than the concentration provided on a package. This difference could be caused by a non-consistent sugar ratio in the real sample due to variation in the production, which is reported by Ventura group (Ventura, Davis, & Goran, 2011), effect of the matrix, or the presence of other reducing agents. Nonetheless, this is an interesting property of the analytical system, however, more investigations are needed to assert the claim.

Other samples selected for the analysis were ordinary milk with one analyte, and lactose free milk as a reference. Considering the prevalence of lactose intolerance in adult people, milk samples are a relevant test case (Vesa, Marteau, & Korpela, 2000). Since milk samples are opaque a preparation step was needed. For milk samples the procedure of protein separation was successfully performed using a method described in the experimental part. After centrifugation milk samples became clear and supernatant was then used directly in the reaction (Fig. 4C).

In most cases of the lactose free milk lactose is converted to glucose and galactose using enzyme lactase and it was the same in our lactose free milk sample. The absorbance at $LSPR_{525}$ for lactose free milk was higher in comparison with ordinary milk. The conversion of lactose into glucose and galactose leaves overall reducing sugar concentration the same. An increase of absorbance at $LSPR_{525}$ could possibly be explained by a higher AuNPs formation rate due to the presence of glucose and galactose rather than with lactose. This should be the case considering that reaction rate with glucose was higher than with lactose, and in the case of galactose it's expected to be faster than with lactose due to higher open chain concentration (Wrolstad, 2013) and reduction potential (Mohammadia et al., 2004). The calibration curves for lactose after 20, 40, and 60 min were used for the determination of lactose concentration in the ordinary milk sample. The average calculated lactose concentration in the sample differed and was calculated as 0.161 ± 0.014 M after 20 min, 0.153 ± 0.011 M after 40 min, and 0.135 ± 0.010 M after 60 min with the confidence interval of 99%, while the lactose concentration provided on the package was 0.13 M. It can be observed that the accuracy and the precision of the measurement increased as the reaction elapsed further and was the best after 60 min.

As the last test case saliva samples were selected because there is some indication that it can be used to extrapolate glucose concentration in the blood (Swanljung et al., 1992). Saliva possesses a few advantages in comparison with other human biofluids, such as blood and urine. The collection of saliva is a non-invasive and non-intrusive process, which can be easily performed by the patient after a brief training. Therefore, the risk of medical stuff infection is significantly reduced (Piechocka, Wrońska, & Głowacki, 2020). The results obtained measuring glucose in saliva using the developed sensor (Fig. 4D) showed that no LSPR peak appeared after 1 h of the reaction indicating that no AuNPs were formed. Based on literature glucose concentration in saliva varies from 0.03 to 0.07 mM (Zhang, Du, & Wang, 2015) which is below the limit of detection of glucose in the 1st h of the reaction. However, allowing the reaction to take place for a longer period of time produces a measurable signal, which means that a calibration curve for glucose detection in saliva could possibly be created. As mentioned beforehand, almost half of the final analytical signal is recorded in the first 3 h, thus, it is expected that the glucose calibration curve created after 3 h is sufficient to determine glucose concentration in the saliva sample.

4. Conclusion

In this work optimal reaction conditions were selected for the designed colorimetric sensor and calibration curves were created for fructose, glucose, lactose, and mannose detection. The analytical system is based on the formation of gold nanoparticles induced by the analyte itself without the need of seeding, with the reaction taking place at room temperature. A comparative study of 4 different reducing sugars was done showing distinct reaction rates for specific sugars. The developed sensor can be successfully employed to detect reducing sugar in various real samples such as milk, saliva, and beverages. When the sample contains a couple of different reducing sugars, their ratio must be known in order to determine their concentrations, however, the data suggests that it might be possible to use the mathematical averages of the analytical signal of separate sugars for the detection of overall sugar concentration in the mixture. In addition, increasing the reaction time can significantly improve the sensitivity of here reported sensor resulting in the detection of lower sugar concentrations. Finally, the sensing can be easily performed using a single wavelength colorimeter.

CRediT authorship contribution statement

Benediktas Brasiunas: Methodology, Validation, Formal analysis, Software, Visualization, Investigation, Writing - original draft, Writing - review & editing. **Anton Popov:** Formal analysis, Software, Visualization, Investigation, Data curation, Writing - original draft, Writing - review & editing. **Arunas Ramanavicius:** Data curation, Writing - original draft, Writing - review & editing, Funding acquisition. **Almira Ramanaviciene:** Conceptualization, Methodology, Resources, Data curation, Writing - original draft, Writing - review & editing, Supervision, Project administration.

Declaration of Competing Interest

The authors declare that they have no known competing financial interests or personal relationships that could have appeared to influence the work reported in this paper.

Acknowledgement

A. Ramanavicius is acknowledging financial support from Research Council of Lithuania (LMTLT), grant agreement No [S-MIP-20-18].

Appendix A. Supplementary data

Supplementary data to this article can be found online at https://doi.org/10.1016/j.foodchem.2021.129238.

References

Ahn, H. Y., Lee, H. E., Jin, K., & Nam, K. T. (2013). Extended gold nano-morphology diagram: Synthesis of rhombic dodecahedra using CTAB and ascorbic acid. *Journal of Materials Chemistry C, 1*(41), 6861–6868. https://doi.org/10.1039/c3tc31135j.

Bray, G. A., Nielsen, S. J., & Popkin, B. M. (2004). Consumption of high-fructose corn syrup in beverages may play a role in the epidemic of obesity. *The American Journal of Clinical Nutrition, 79*(4), 537–543. https://doi.org/10.1093/ajcn/79.4.537.

Buzanovskii, V. A. (2015). Methods for the determination of glucose in blood. Part 1. *Review Journal of Chemistry, 5*(1), 30–81. https://doi.org/10.1134/s207997801501001x.

Cui, S. W. (Ed.). (2005). *Food Carbohydrates. Food Carbohydrates* (1st ed.). CRC Press. https://doi.org/10.1201/9780203485286.

Della Pelle, F., Vilela, D., González, M. C., Lo Sterzo, C., Compagnone, D., Del Carlo, M., & Escarpa, A. (2015). Antioxidant capacity index based on gold nanoparticles formation. Application to extra virgin olive oil samples. *Food Chemistry, 178*, 70–75. https://doi.org/10.1016/j.foodchem.2015.01.045.

German, N., Ramanavicius, A., Voronovic, J., & Ramanaviciene, A. (2012). Glucose biosensor based on glucose oxidase and gold nanoparticles of different sizes covered by polypyrrole layer. *Colloids and Surfaces A: Physicochemical and Engineering Aspects, 413*, 224–230. https://doi.org/10.1016/j.colsurfa.2012.02.012.

Gu, A., & Li, Z. (2009). Growth of spindle-shaped gold nanoparticles in cetyltrimethylammonium bromide solutions. *Micro & Nano Letters, 4*(3), 142–147. https://doi.org/10.1049/mnl.2009.0047.

He, Y. Q., Liu, S. P., Kong, L., & Liu, Z. F. (2005). A study on the sizes and concentrations of gold nanoparticles by spectra of absorption, resonance Rayleigh scattering and resonance non-linear scattering. *Spectrochimica Acta Part A: Molecular and Biomolecular Spectroscopy, 61*(13), 2861–2866. https://doi.org/10.1016/j.saa.2004.10.035.

Jochum, M., Bakry, R., Wartusch, I., Huck, C. W., Engelhardt, H., & Bonn, G. K. (2002). Analysis of carbohydrates using different quaternized polystyrene-divinylbenzene particles and pulsed amperometric detection. *Chromatographia, 56*(5–6), 263–268. https://doi.org/10.1007/BF02491930.

Kaufmann, M., Krüger, S., Mügge, C., & Kroh, L. W. (2018). General acid/base catalysis of sugar anomerization. *Food Chemistry, 265*, 216–221. https://doi.org/10.1016/j.foodchem.2018.05.101.

Kumar, S., Ahlawat, W., Kumar, R., & Dilbaghi, N. (2015). Graphene, carbon nanotubes, zinc oxide and gold as elite nanomaterials for fabrication of biosensors for healthcare. *Biosensors and Bioelectronics, 70*, 498–503. https://doi.org/10.1016/j.bios.2015.03.062.

Li, C., Fan, F., Yin, B., Chen, L., Ganguly, T., & Tian, Z. (2013). Au+-cetyltrimethylammonium bromide solution: A novel precursor for seed-mediated growth of gold nanoparticles in aqueous solution. *Nano Research, 6*(1), 29–37. https://doi.org/10.1007/s12274-012-0278-2.

Luo, Y., Ji, X., Zhuang, J., & Yang, W. (2014). Controlled formation of gold nanoflowers by reduction of tetrachloroauric acid with thermally treated glucose in alkaline solution. *Colloids and Surfaces A: Physicochemical and Engineering Aspects, 463*, 28–36. https://doi.org/10.1016/J.COLSURFA.2014.09.025.

Magwaza, L. S., & Opara, U. L. (2015). Analytical methods for determination of sugars and sweetness of horticultural products—A review. *Scientia Horticulturae, 184*, 179–192. https://doi.org/10.1016/j.scienta.2015.01.001.

Miljković, M. (2009). Carbohydrates: Synthesis, mechanisms, and stereoelectronic effects. Carbohydrates: Synthesis, Mechanisms, and Stereoelectronic Effects. DOI: 10.1007/978-0-387-92265-2.

Mohammadia, H., Amine, A., Rhazi, M. E., & Brett, C. M. A. (2004). Copper-modified gold electrode specific for monosaccharide detectionUse in amperometric determination of phenylmercury based on invertase enzyme inhibition. *Talanta, 62*(5), 951–958. https://doi.org/10.1016/j.talanta.2003.10.025.

Moon, S. Y., Kusunose, T., & Sekino, T. (2009). CTAB-assisted synthesis of size- and shape-controlled gold nanoparticles in SDS aqueous solution. *Materials Letters, 63*(23), 2038–2040. https://doi.org/10.1016/J.MATLET.2009.06.047.

Nelson, N. (1944). A photometric adaptation of the somogyi method for the determination of glucose. *The Journal of Biological Chemistry, 153*(2), 375–380.

Palazzo, G., Facchini, L., & Mallardi, A. (2012). Colorimetric detection of sugars based on gold nanoparticle formation. *Sensors and Actuators B: Chemical, 161*(1), 366–371. https://doi.org/10.1016/j.snb.2011.10.046.

Panigrahi, S., Kundu, S., Ghosh, S. K., Nath, S., & Pal, T. (2005). Sugar assisted evolution of mono- and bimetallic nanoparticles. *Colloids and Surfaces A: Physicochemical and Engineering Aspects, 264*(1), 133–138. https://doi.org/10.1016/j.colsurfa.2005.04.017.

Piechocka, J., Wrońska, M., & Głowacki, R. (2020). Chromatographic strategies for the determination of aminothiols in human saliva. *TrAC - Trends in Analytical Chemistry, 126*, 115866. https://doi.org/10.1016/j.trac.2020.115866.

Ramanaviciene, A., Voronovic, J., Popov, A., Drevinskas, R., Kausaite-Minkstimiene, A., & Ramanavicius, A. (2016). Investigation of biocatalytic enlargement of gold nanoparticles using dynamic light scattering and atomic force microscopy. *Colloids and Surfaces A: Physicochemical and Engineering Aspects, 510*, 183–189. https://doi.org/10.1016/j.colsurfa.2016.07.078.

Ramanavicius, A., German, N., & Ramanaviciene, A. (2017). Evaluation of electron transfer in electrochemical system based on immobilized gold nanoparticles and glucose oxidase. *Journal of The Electrochemical Society, 164*(4), G45–G49. https://doi.org/10.1149/2.0691704jes.

Ramanavičius, A., Kaušaitė, A., & Ramanavičienė, A. (2005). Polypyrrole-coated glucose oxidase nanoparticles for biosensor design. *Sensors and Actuators B: Chemical, 111–112*, 532–539. https://doi.org/10.1016/j.snb.2005.03.038.

Robyt, J. F. (1998). In *Essentials of Carbohydrate Chemistry* (1st ed.). New York: Springer-Verlag. https://doi.org/10.1007/978-1-4612-1622-3.

Scampicchio, M., Arecchi, A., & Mannino, S. (2009). Optical nanoprobes based on gold nanoparticles for sugar sensing. *Nanotechnology, 20*(13), 135501. https://doi.org/10.1088/0957-4484/20/13/135501.

Smith, D. K., & Korgel, B. A. (2008). The importance of the CTAB surfactant on the colloidal seed-mediated synthesis of gold nanorods. *Langmuir, 24*(3), 644–649. https://doi.org/10.1021/la703625a.

Speck, J. C. (1958). *The Lobry De Bruyn-Alberda Van Ekenstein Transformation* (pp. 63–103). Academic Press. https://doi.org/10.1016/S0096-5332(08)60352-5.

Swanljung, O., Meurman, J. H., Torkko, H., Sandholm, L., Kaprio, E., & Mäenpää, J. (1992). Caries and saliva in 12–18-year-old diabetics and controls. *European Journal of Oral Sciences, 100*(6), 310–313. https://doi.org/10.1111/j.1600-0722.1992.tb01077.x.

Thanh, N. T. K., Maclean, N., & Mahiddine, S. (2014). Mechanisms of nucleation and growth of nanoparticles in solution. *Chemical Reviews. American Chemical Society.* https://doi.org/10.1021/cr400544s.

Ventura, E. E., Davis, J. N., & Goran, M. I. (2011). Sugar content of popular sweetened beverages based on objective laboratory analysis: Focus on fructose content. *Obesity, 19*(4), 868–874. https://doi.org/10.1038/oby.2010.255.

Vesa, T. H., Marteau, P., & Korpela, R. (2000). Lactose intolerance. *Journal of the American College of Nutrition, 19*(2), 165S–175S. https://doi.org/10.1080/07315724.2000.10718086.

Wrolstad, R. E. (2013). In *Food Carbohydrate Chemistry* (1st ed.). Wiley Blackwell. https://doi.org/10.1002/9781118688496.

Wuithschick, M., Birnbaum, A., Witte, S., Sztucki, M., Vainio, U., Pinna, N., … Polte, J. (2015). Turkevich in New Robes: Key questions answered for the most common gold nanoparticle synthesis. *ACS Nano, 9*(7), 7052–7071. https://doi.org/10.1021/acsnano.5b01579.

Yan, Q., Cao, L., Dong, H., Tan, Z., Liu, Q., Zhang, W., … Dong, Y. (2019). Sensitive amperometric immunosensor with improved electrocatalytic Au@Pd urchin-shaped nanostructures for human epididymis specific protein 4 antigen detection. *Analytica Chimica Acta, 1069*, 117–125. https://doi.org/10.1016/j.aca.2019.04.023.

Zhang, W., Du, Y., & Wang, M. L. (2015). Noninvasive glucose monitoring using saliva nano-biosensor. *Sensing and Bio-Sensing Research, 4*, 23–29. https://doi.org/10.1016/j.sbsr.2015.02.002.

Zhang, Y., Zeng, G. M., Tang, L., Chen, J., Zhu, Y., He, X. X., & He, Y. (2015). Electrochemical sensor based on electrodeposited graphene-Au modified electrode and NanoAu carrier amplified signal strategy for attomolar mercury detection. *Analytical Chemistry, 87*(2), 989–996. https://doi.org/10.1021/ac503472p.

Zhao, X., Xue, J., Mu, Z., Huang, Y., Lu, M., & Gu, Z. (2015). Gold nanoparticle incorporated inverse opal photonic crystal capillaries for optofluidic surface enhanced Raman spectroscopy. *Biosensors and Bioelectronics, 72*, 268–274. https://doi.org/10.1016/j.bios.2015.05.036.

Paper 5

Metal nanoparticle and quantum dot tags for signal amplification in electrochemical immunosensors for biomarker detection

A. Popov, **B. Brasiunas**, A. Kausaite-Minkstimiene, A. Ramanaviciene

Chemosensors, 2021, 9(4), 85
doi.org/10.3390/chemosensors9040085

chemosensors

MDPI

Review

Metal Nanoparticle and Quantum Dot Tags for Signal Amplification in Electrochemical Immunosensors for Biomarker Detection

Anton Popov [1,2,†], Benediktas Brasiunas [2,†], Asta Kausaite-Minkstimiene [1,2] and Almira Ramanaviciene [1,2,*]

[1] Department of Immunology, State Research Institute Centre for Innovative Medicine, Santariskiu St. 5, LT-08406 Vilnius, Lithuania; anton.popov@imcentras.lt (A.P.); asta.kausaite@chf.vu.lt (A.K.-M.)
[2] NanoTechnas—Center of Nanotechnology and Materials Science, Faculty of Chemistry and Geosciences, Institute of Chemistry, Vilnius University, Naugarduko St. 24, LT-03225 Vilnius, Lithuania; benediktas.brasiunas@chgf.vu.lt
* Correspondence: almira.ramanaviciene@chf.vu.lt
† Authors contributed equally to this work as first authors.

Abstract: With the increasing importance of healthcare and clinical diagnosis, as well as the growing demand for highly sensitive analytical instruments, immunosensors have received considerable attention. In this review, electrochemical immunosensor signal amplification strategies using metal nanoparticles (MNPs) and quantum dots (Qdots) as tags are overviewed, focusing on recent developments in the ultrasensitive detection of biomarkers. MNPs and Qdots can be used separately or in combination with other nanostructures, while performing the function of nanocarriers, electroactive labels, or catalysts. Thus, different functions of MNPs and Qdots as well as recent advances in electrochemical signal amplification are discussed. Additionally, the methods most often used for antibody immobilization on nanoparticles, immunoassay formats, and electrochemical methods for indirect biomarker detection are overviewed.

Keywords: metal nanoparticles; gold nanoparticles; quantum dots; electrochemical signal amplifying tags; antibody immobilization; biomarkers; electrochemical immunosensors

Citation: Popov, A.; Brasiunas, B.; Kausaite-Minkstimiene, A.; Ramanaviciene, A. Metal Nanoparticle and Quantum Dot Tags for Signal Amplification in Electrochemical Immunosensors for Biomarker Detection. *Chemosensors* **2021**, *9*, 85. https://doi.org/10.3390/chemosensors9040085

Academic Editor: Mehmet Senel

Received: 14 March 2021
Accepted: 15 April 2021
Published: 18 April 2021

1. Introduction

There are many different analytical systems, where the specific affinity-based interaction between antigen and antibody is exploited for analyte detection. In the late 1950s, R. S. Yalow and S. A. Berson developed a radioimmunoassay for endogenous plasma insulin detection [1]. After the replacement of the radioactive label by an enzyme, enzyme-linked immunoassays [2] and enzyme-linked immunosorbent assays (the gold standard of immunoassays [3]) were introduced and are still very popular worldwide in different fields of application, including clinical medicine [4,5]. Further advances in analytical and bioanalytical chemistry and the increasing need for small, easy to use, portable, well operating in small volume of samples and at the same time sensitive, selective, and highly reproducible systems have encouraged the development of alternative technologies and devices already in use. Thus, a special type of affinity biosensor, so-called immunosensor, was developed. The immunosensor differs from other types of biosensors by the biological recognition element, namely, antibodies (or antigens) are coupled to a signal transducer sensor surface (Figure 1). The physicochemical changes occurring on the signal transducer surface after immunorecognition element interaction with the target analyte and immune complex formation are converted by an electronic system to a measurable analytical signal proportional to the analyte concentration in the sample. Due to the high specificity and affinity of antibodies, the analyte separation step from the mixture of different molecules present in the real sample or the pretreatment of the sample is not required. These outstanding advantages of immunosensors over other analytical techniques open up a wide range of applications in a variety of sectors, such as healthcare and clinical diagnosis of biomarkers [6,7], food production and safety [8], the pharmaceutical industry [9], and environmental monitoring [10].

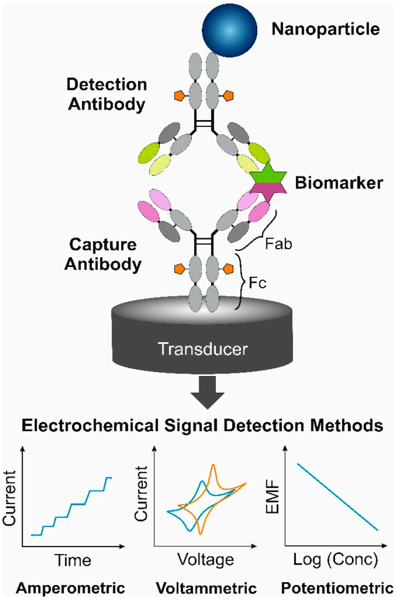

Figure 1. Schema of electrochemical immunosensors based on nanoparticle tags.

The analytical characteristics of immunosensors depend on many factors. The proper antibody immobilization and site-directed orientation on the sensing surface has a high impact on the performance of the immunosensor [11,12]. Analytes can be detected using different immunoassay formats, mainly direct, indirect, sandwich or competitive. The sensitive detection of analytes by the direct method is desirable; however, sandwich or competitive immunoassay formats provide higher sensitivity. Depending on the type and characteristics of the analyte, either the antibody or the antigen can be immobilized on the sensing surface. Additionally, different analytical signal amplification strategies are applied and the impact of nanotechnology is of crucial importance for future immunosensors. There are two main types of signal amplification strategies using nanomaterials. The first employs nanomaterials for modifying the sensing surface, while the second uses nanomaterials as tags, such as nanocarriers, electroactive and catalytically active labels, or labels for analyte preconcentration. On the back of these factors, the selection of the appropriate signal transducer is of high importance. Depending on the type of transducer, immunosensors can be divided into optical, electrochemical, piezoelectric, magnetic, thermometric, and acoustic immunosensors.

In this review, electrochemical immunosensors based on nanomaterials as signal amplifying tags are overviewed, focusing on recently developed strategies for the ultrasensitive detection of biomarkers. Of all the nanomaterials, zero-dimensional metal nanoparticles (MNPs) and quantum dots (Qdots) were selected. Overviewing different MNPs, more attention is given to gold nanoparticles (AuNPs) due to their wide range of advantageous properties, such as chemical stability, excellent biocompatibility, surface chemistry, large surface-to-volume ratio, and easy modification protocols, which are the focus of research and application in electrochemical immunosensors. Another type of powerful nanomaterials well known due to their high quantum yield, stability, and application in optical analytical systems, namely, Qdots, semiconductor nanocrystals, are overviewed as signal amplifying tags in electrochemical immunosensors. The properties of Qdots, such as water solubility, biocompatibility (after appropriate surface modification procedure), catalytic activity, and decomposition reactions upon reduction and oxidation [13,14], were successfully employed in the novel electrochemical immunosensors.

2. Biomarkers

According to the World Health Organization's suggested definition, "a biomarker is any substance, structure, or process that can be measured in the body or its products and influence or predict the incidence of outcome or disease" [15]. The US National Cancer Institute indicates that a biomarker is "a biological molecule found in blood, other body fluids, or tissues that is a sign of a normal or abnormal process, or of a condition or disease and can be tested to see how well the body responds to treatment for a disease or condition" [16]. The US National Institutes of Health's Working Group and the Biomarkers Consortium defined a biomarker as "a characteristic that can be objectively measured and quantitatively evaluated as an indicator of a normal biological and pathological process, or pharmacological responses to a therapeutic intervention" [17].

Biomarkers are classified according to different criteria. Depending on the application, they are generally divided into predictive or early detection biomarkers, diagnostic or staging of disease biomarkers, prognostic biomarkers and monitoring biomarkers. An example of a predictive biomarker in prostate cancer is prostate-specific antigen (PSA) or in breast cancer is the expression of the human epidermal growth factor receptor (HER). Glycated hemoglobin is used as a diagnostic biomarker to identify patients with Type 2 diabetes mellitus [18]. Mutations in breast cancer genes 1 and 2 can be used as prognostic biomarkers in the evaluation of women with breast cancer to assess the likelihood of a second breast cancer [19]. Cancer antigen 125 (CA125) is used as a monitoring biomarker in the assessment of disease status in patients with ovarian cancer during and after treatment [20]. Depending on the characteristics of the biomarkers, molecular and imaging biomarkers can be distinguished. Imaging biomarker is a biomarker which is determined by imaging techniques such as computed tomography, positron emission tomography or magnetic resonance imaging [21]. Meanwhile, molecular biomarkers are biomarkers characterized by biophysical properties that allow them to be measured in biological samples [22,23].

3. Immunoassay Formats Using Nanoparticles as Signal Amplifying Tags

For the biomarker detection with signal amplification using MNPs and Qdots, two main types of immunoassay are used: sandwich and competitive (Figure 2) [24]. The selected format depends on the biomarker size, the presence of different epitopes, concentration in the real sample, and the complexity of the sample. The mentioned immunoassay formats both do not require sample processing before the analysis, which is very convenient and shortens as well as simplifies the analysis.

The sandwich immunoassay format requires two antibodies (capture and detection) specific for different and non-overlapping epitopes of the biomarker to achieve high sensitivity and selectivity as well as accurate results. Capture antibody immobilized on the electrode surface binds the biomarker and then the biomarker can be detected by the detection antibody (in this case, the detection antibody is labeled with nanoparticles) or after the additional binding of the secondary antibody (in this case, the secondary antibody is labeled with nanoparticles) (Figure 2). There is a direct relationship between the magnitude of the registered analytical signal and the biomarker concentration using the sandwich immunoassay format—the registered signal increases with increasing concentration of biomarkers.

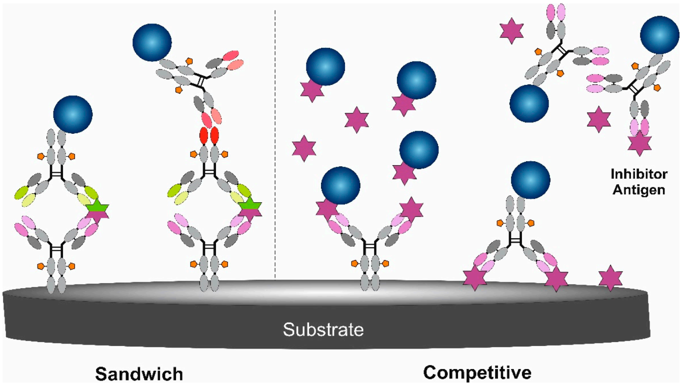

Figure 2. Commonly used immunoassay formats for the detection of biomarkers using nanoparticles as signal amplifying tags.

Competitive/inhibition immunoassay is less sensitive to sample dilution and sample matrix effects in comparison to the sandwich format [24]. Additionally, less variability between two equal samples and assays is specified [25]. The competitive format can be selected for biomarker detection in such cases when only one specific antibody is available or the biomarker is so small that it cannot be bound by two antibodies. There are a few competition options for biomarker detection. When a surface premodified with antibodies is applied in analysis, the biomarker to be determined competes with the reference biomarker labeled with nanoparticles (known and constant concentration) for the free antigen binding sites. A more complex competitive format is performed when antibodies labeled with nanoparticles compete with the biomarker present in the sample and the reference biomarker immobilized on the surface. Only free (not-inhibited) antibodies labeled with metal nanoparticles can interact with the reference biomarker immobilized on the surface. In this case, the biomarker concentration in the sample inversely correlates with the magnitude of the registered signal—the registered signal increases with decreasing concentration of the biomarker.

4. Methods Used for the Modification of MNPs and Qdots by Antibodies

As the purpose of this review is to discuss the performance of immunosensors using nanoparticles as signal amplifying tags, the main methods used for the modification of MNPs and Qdots will be presented. Additionally, these methods might be applied as a reference for antibody immobilization on the electrode surface. The methods used for antibody immobilization might be grouped such as (i) covalent or non-covalent [26], (ii) ensuring random or site-directed antibody orientation [11], (iii) using native antibodies or their reduced fragments [12] (Figure 3). The ability of an immobilized antibody to bind the target biomarker depends on antibody Fab fragment accessibility (orientation on the surface) and the remaining biological activity. Immunosensor performance is based on a specific affinity-based (non-covalent) interaction between the antibody–antigen binding site and the epitope present in the biomarker structure. The selection of the best method also depends on the material of the nanoparticle, surface properties, biocompatibility, and particle size. Since the specific interaction between the antibody and the biomarker as well as the magnitude of the registered signal depend on the selected antibody immobilization method, it is obvious that this step is of crucial importance for developing sensitive immunosensors. Additionally, the optimal concentration of antibodies should be chosen for each individual case [27] before applying MNP–antibody conjugates in immunosensor design.

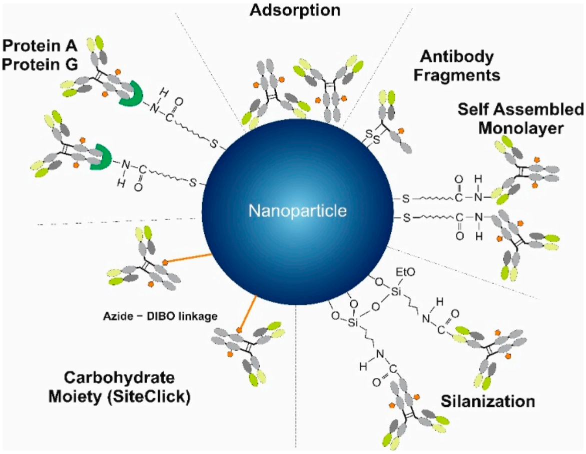

Figure 3. Schematic representation of different methods for antibody immobilization on a nanoparticle.

Noble MNPs (Au, Ag, Pt, Pd), especially AuNPs, can be easily synthesized of different sizes and shapes in aqueous solutions using chemical reductors and metal precursors (bottom-up strategy) [28]; however, nanoparticles without residual toxic compounds can also be synthetized by laser ablation (top-down strategy) in aqueous media [29]. MNPs can be positively or negatively charged. Most often the simple antibody adsorption (due to electrostatic, van der Waals, and hydrophobic interactions, hydrogen bonding) on MNPs is used. Usually, a random orientation of antibodies on the nanoparticle surface is obtained. However, the orientation of antibodies can be regulated by changing the pH of the solution, thus controlling the surface charge distribution of the antibody and affecting the electrostatic interaction with negatively charged AuNPs. It was shown that antigen binding site accessibility to the biomarker increased by decreasing the pH of the solution from 8.5 to 7.5 [30]. Despite the drawbacks of the adsorption method, such as low antibody surface concentration, random orientation, partial denaturation in close contact with the metal, and desorption from the surface due to weak bonds, this method is used for MNP modification and is applied for immunosensor development due to its simplicity and easy procedure. Antibodies with thiol groups present in their structure or reduced antibody fragments maintaining native thiol groups are immobilized on the noble metal surface via chemisorption, forming a noble metal–thiolate bond. Reduced antibody fragments ensure site-directed orientation of antibody's antigen binding sites on the plane surface and MNPs [31,32].

Covalent antibody immobilization on MNPs using self-assembled monolayers (SAMs, n-carbon atom alkyl chains with certain functional groups) is another commonly used method that does not ensure site-directed antibody immobilization. The modification of noble MNPs with SAMs occurs due to thiol head group presence in their structure binding to the surface of MNPs via chemisorption. After that, different functional groups generated on the surface (mainly carboxyl or amine) are directed to the solution and are used for the covalent antibody immobilization. The length of the chain regulates the distance from the antibody to the surface and the mobility on the MNPs. Very often 11-mercaptoundecanoic acid SAM is used for covalent antibody immobilization after carboxyl group activation with a mixture of 1-ethyl-3-(3-diaminopropyl)carbodiimide hydrochloride and N-hydroxysuccinimide (EDC/NHS coupling reaction) [32,33]. Formed functionally active NHS-ester interacts with antibody amine groups and a stable amide bond is formed.

The same protocol might be applied for Qdots with carboxyl groups on their surface [34]. Additionally, chemical linkers (glutaraldehyde, N, N′-carbonyldiimidazole) can also be applied for covalent antibody immobilization on Qdots [35]. SAMs with silane head groups, usually amino silanes, are applied for the metal oxide nanoparticle surface functionalization for further covalent antibody immobilization [36]. Alkyl silanes with amines, aldehydes, thiols, or carboxylic functional groups can be successfully used for covalent antibody immobilization after functional group activation or via cross-linking. Despite the resulting random antibody immobilization on the nanoparticle surface, well-operating electrochemical immunosensors based on this antibody immobilization method were developed [37]. The covalent antibody immobilization via SAMs is well known and is quite simple, thus a stable biolayer is applicable for repeated biomarker detection using a regeneration step. The main drawback of this method is random antibody orientation, which can reduce the sensitivity of immunosensors [26].

Site-directed antibody immobilization might be achieved due to the affinity interaction between bacterial proteins G or A and the antibody Fc region. This favorable method of antibody immobilization on MNPs significantly improves the antibody–biomarker binding ratio due to antigen binding site accessibility and decreased steric hindrance [11,26]. The immobilization of the antibody using protein G or A ensures site-directed orientation. However, for repeated biomarker detection by an immunosensor, cross-linking of the antibody with protein G, which is covalently immobilized to the surface, is required [38]. Affinity interaction between biotinylated antibody and avidin or streptavidin immobilized on the surface is a widely used method for MNPs modification with antibodies, but usually this method does not ensure site-directed orientation of antibodies. The main advantage of this antibody immobilization method is a strong non-covalent interaction between biotin and avidin ($K_d \sim 10^{-15}$ M^{-1}) or streptavidin ($K_d \sim 4 \times 10^{-14}$ M^{-1}) and the resistance of this complex to break down at high temperature, extreme pH and in the presence of a high concentration of chemical agents [39,40]. Additionally, the avidin/streptavidin ability to interact with four biotin molecules ensures high antibody loading on the surface of MNPs.

Branched oligosaccharides present in the Fc fragment of the antibody (CH_2 domain) can be successfully applied for the site-directed antibody immobilization on nanoparticles. Oxidized immunoglobulin G (IgG) class antibodies can be immobilized on the surface of MNPs premodified with amines, hydrazines, hydrazides, and semicarbazides [41,42]. There are commercially available kits (Site-Click^{TM} Antibody Labeling Kits) for antibody labeling with Qdots via a modified antibody carbohydrate moiety present in the Fc fragment [43], unlike the conventional amine-thiol crosslinker method. Although no oxidizing or reducing agents are required, the preparation of the conjugate is a multistep process with a few preconcentration, modification (enzymes are used), and separation steps. It is easy to lose an antibody during the conjugation procedure. Additionally, a limited amount of Qdots per 1 M of IgG was mentioned as one of the disadvantages of this method [34].

5. Electrochemical Immunosensors

Electrochemical immunosensors quantitatively measure an electrical signal generated during a specific antigen and antibody interaction. Depending upon the nature of the electrochemical changes detected during the immunorecognition events, amperometric, voltammetric, potentiometric, conductometric, and impedimetric immunosensors can be distinguished. Electrochemical immunosensors have unique properties such as high sensitivity, which is important for the detection of biomarkers as their concentrations are usually very low, short response time, and high selectivity. In addition, they are characterized by simplicity of fabrication, low cost, relatively simple instrumentation, the possibility of being portable and small in size, suitability for in situ or automated detection of an analyte, as well as adaptability to multiplexing [44]. In addition, they are ideal for the analysis of opaque and optically dense samples [45]. Due to these properties, they are increasingly used in clinical analysis and are becoming a promising alternative to existing laboratory methods [45].

5.1. Amperometric Immunosensors

Amperometric immunosensors are one of the most widely used electrochemical immunosensors [6]. They have been successfully applied to detect many biomarkers, such as carcinoembryonic antigen (CEA) [46], human epididymis protein 4 (HE4) [47], human immunoglobulin G [48] and many others. The amperometric technique is very simple to use, which has the potential for miniaturization and portability. It is based on the measurement of the current resulting from the oxidation or reduction of an electroactive material at the surface of an indicator electrode (otherwise known as a working electrode) as a function of time at a constant potential. In addition to the indicator electrode, the amperometric electrochemical cell consists of reference and auxiliary electrodes. The reference electrode has a constant potential and the potential applied to the indicator electrode is controlled with respect to the reference. Meanwhile, the auxiliary electrode completes the electrical circuit and helps to measure the current flow. The simplest way to design an amperometric immunoassay is direct antibody–antigen interaction. However, most antibodies and antigens are not electrochemically active and therefore their interaction cannot generate an amperometric response. This problem is often solved using additional reversible redox-active substances, called redox probes, whose oxidation or reduction at the indicator electrode surface creates a current signal. The insulating immune complex formed on the working electrode surface during antibody and antigen interaction acts as a kinetic barrier to mass and electron transfer between the electrode and the redox probe. Therefore, when the antigen is present in a solution, a decrease in the current response is observed. At identical redox probe concentrations, the current response obtained is related to the antigen concentration [48]. Soluble redox probes can affect the bioactivity of antibodies or antigens by denaturing them and therefore affect the detection and regeneration of immunosensors [49]. To overcome this drawback, redox-active substances are integrated on a working electrode surface, thus eliminating their direct contact with biomolecules. Another type of amperometric immunosensors are immunosensors that utilize peroxidase-like electroactive materials that have high catalytic activity towards the electroreduction of hydrogen peroxide. The immune complex formed during the antibody–antigen interaction causes both electron transfer resistance and steric resistance to hydrogen peroxide, which reduces the current response [50]. Therefore, although amperometric immunosensors based on the label-free detection format have a short response time, are highly compatible, and repeatable, the use of various indirect detection formats applying electrochemically active or enzymatic labels conjugated with a detection antibody or competitive antigen is often required to achieve an amperometric response [6]. The most commonly used enzymatic labels are horseradish peroxidase (HRP), alkaline phosphatase, glucose oxidase, glucose-6-phosphate dehydrogenase, and laccase. The amperometric enzyme-linked immunoassay format is very popular and commonly used in laboratory practice for the detection of both antigens and antibodies. After the addition of a suitable substrate, an electrochemically active product is formed during the enzymatic reaction. Its oxidation or reduction at the indicator electrode surface generates a current signal that is proportional to the concentration of an analyte [51]. Particular attention is currently focused on electrochemically active labels such as noble metals, metal oxide nanoparticles or Qdots. These materials allow the drastic improvement of the analytical characteristics of amperometric immunosensors and also are very promising in multi-analyte assays, which have many advantages over single-analyte assays, such as the cost of a single test and convenience [52].

5.2. Voltammetric Immunosensors

A three-electrode electrochemical cell is also used for voltammetric measurements, as well as for amperometric. However, unlike in amperometry, in voltammetry the potential is scanned over a range of potentials and the current resulting from the oxidation or reduction of an electroactive material is measured as a function of the applied potential. Due to the variable potential, voltammetric immunosensors, in addition to properties such as high sensitivity and selectivity and short response time, have the ability to simultaneously and quantitatively detect multiple analytes. As three parameters can be controlled in voltammetry: how the potential is changed, how the current is measured, and whether the solution is stirred, there are many different voltammetry techniques that differ in their capabilities. Cyclic voltammetry (CV), linear sweep voltammetry (LSV), differential pulse voltammetry (DPV), square wave voltammetry (SWV), and stripping voltammetry (SV) are the most widely used in the development of immunosensors. Of the techniques mentioned, DPV and SWV are particularly commonly used due to their high sensitivity [53,54]. In addition, due to the narrow peaks in a voltammogram, DPV is a particularly suitable technique for the simultaneous determination of several biomarkers. As a result, false negatives and false positives in clinical diagnoses, more prone to occur when measuring a single molecule, can be minimized [52]. SV, which consists of three related techniques: anodic stripping voltammetry (ASV), cathodic stripping voltammetry and adsorptive stripping voltammetry, is particularly sensitive due to the concentration of an analyte or electroactive label when it is transferred from a larger volume of the solution to a smaller volume near the working electrode. Due to this procedure, the detection limits are much lower than other voltammetric techniques. Voltammetric immunoassay can be performed by direct as well as a variety of indirect formats that were already described for amperometric immunosensors. Among the different types of electrochemical immunosensors, voltammetric immunosensors are very popular and numerous immunosensors for cystatin C [55], Cytokeratin 19 fragment 21-1 [56], CEA [57], C-reactive protein [37] and other biomarkers have been reported over the past decade.

5.3. Potentiometric Immunosensors

Potentiometric immunosensors, whose principle of operation is based on the measurement of the potential difference between an indicator electrode and a reference electrode when a zero or insignificant amount of current flows through the cell, have great potential in clinical immunoassays. According to the Nernst equation, the measured potential difference is proportional to the logarithm of concentration. Potentiometric immunoassay can also be performed by direct as well as by a variety of indirect formats. When a potentiometric immunoassay is performed in a direct format, the change in the recorded potential difference depends on the change in the working electrode potential caused by the antibody–antigen interaction. All proteins are polyelectrolytes and have a positive or a negative electrical charge except for their isoelectric point. When an antibody–antigen interaction occurs, the electrical charge of the resulting immune complex differs from the electrical charge of the immobilized antibody. This interaction causes a change in the surface charge of the indicator electrode, resulting in a change in the registered potential difference. The detection is based on the change in the potentiometric signal before and after the antigen–antibody reaction. An example of a potentiometric immunosensor operating in this format is the IgG immunosensor that was proposed by Feng and co-workers [58]. Despite the simplicity, one of the main disadvantages of this type of potentiometric immunoassay format is a small change in potential difference resulting from the antibody–antigen interaction. Attempts have been made to increase the performance by increasing the amount of immobilized antibodies and maintaining their immunoactivity [59,60]. Nevertheless, direct detection format-based potentiometric immunosensors are often not sensitive and reliable enough [61]. For this reason, the much more commonly used detection format is the potentiometric enzyme-linked immunoassay [62]. The detection of the product obtained by an enzymatic reaction makes it possible to amplify the potentiometric signal corresponding to the immunorecognition event. Potentiometric enzyme-linked immunoassays also have several drawbacks, such as sensitivity to assay conditions at the potentiometric signal generation stage and the instability of enzymes during storage and use. The use of nanomaterials such as noble metal nanoparticles [63] or Qdots [64] as label and ion-selective electrodes avoids these drawbacks and provides new ways to improve the performance of potentiometric immunosensors.

5.4. Photoelectrochemical Immunosensors

Photoelectrochemical (PEC) immunoassay is a newly developed technique, but in recent years it has attracted a great deal of interest from scientists due to its low cost, short response time, high sensitivity, and portable and small PEC devices [65]. The PEC method evolved from electrochemistry, but it differs from traditional electrochemical methods [66]. In addition, due to the lower background signal, the PEC technique has the potential to be more sensitive than conventional electrochemical methods [67,68]. PEC immunoassay converts the immunobinding event into a detectable electrical signal. The principle of PEC immunosensors operation is based on the generation of an electrical signal resulting from the photoelectric conversion of photoactive materials, usually Qdots. PEC immunosensors could be classified into two main groups: potentiometric and amperometric. The most common are amperometric PEC immunosensors, which have been developed rapidly over the past decade. The PEC cell consists of a light-harvesting semiconductor indicator electrode, a counter electrode and a reference electrode. The indicator electrode is initially used for the immobilization of the capture antibody, followed by immunoassay development with different detection formats and signaling strategies. When a photoactive material is illuminated by light with energy higher than that of their band gap, the light excites electron transitions from the valence band to the conduction band, forming electron-hole pairs. The migration of photogenerated charge carriers causes a photocurrent signal, which is proportional to the concentration of an analyte. Depending on the change in photocurrent before and after the interaction with an analyte, PEC immunosensors can be divided into signal-on and signal-off methods. One of the most commonly used signal-on methods is the sandwich-type immunoassay format, in which the antigen is sandwiched between the immobilized captured antibody and the detection antibody. Photoreactive Qdots, such as CdS, CdTe, and CdSe, are most commonly used [69,70]. The disadvantage of signal-off methods is that they suffer from non-specific adsorption of other biological components present with the analyte in the test sample. This leads to erroneously recorded immunosensor signals, resulting in an inaccurate analysis. Nevertheless, a number of PEC immunosensors of this type have also been reported for the analysis of biomarkers [71,72].

6. MNP and Qdot Tags for Electrochemical Signal Amplification

Nanomaterials, including MNPs and Qdots, fulfill various roles in the design of highly sensitive electrochemical immunosensors. The deposition of nanoparticles on the surface of the working electrode permits the enhancement in the surface area, leading to increased molecule loading capacity. Additionally, the deposited nanomaterials could lead to electrical signal amplification due to their unique properties. For instance, the involvement of AuNPs due to high AuNP electrical conductivity accelerates electron transfer to the electrode during reduction-oxidation reactions. However, in this work we focus on the application of MNPs and Qdots as tags for signal amplification in the design of electrochemical immunosensors. MNPs and Qdots can be used separately or in combination with other nanostructures, while the performed functions can be divided as follows (Figure 4):

- Nanocarriers—transport numerous molecules close to the electrode.
- Electroactive labels for biomarker detection.
- Catalytically active labels.

A comprehensive review of the literature about the principles of MNPs and Qdots' application as tags for signal amplification in the electrochemical immunosensors developed for the sensitive detection of biomarkers is provided in the following sections. More detailed information about the analytical characteristics of the developed immunosensors, such as limit of detection (LOD) and linear range, as well as type and size of nanoparticles and electrochemical methods used for the biomarker detection in real samples, is summarized in Table 1, grouping information depending on the function of MNPs and Qdots.

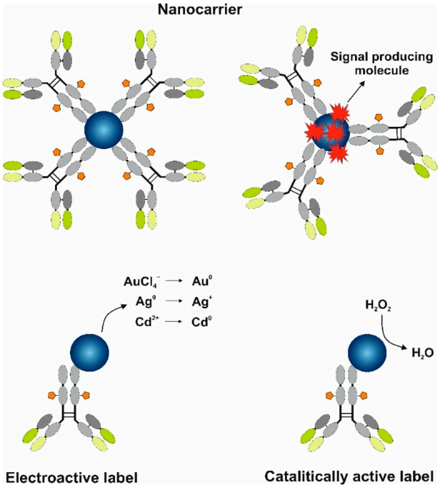

Figure 4. The main functions of metal nanoparticle and quantum dot tags for electrochemical immunosensor signal amplification.

Table 1. The summary of electrochemical immunosensors which employ MNP and Qdot tags for analytical signal amplification.

	Size (nm)	**Technique(s)**	**Biomarker**	**Linear Range ($ng{\cdot}mL^{-1}$)**	**LOD ($pg{\cdot}mL^{-1}$)**	**Real Sample**	**Reference**
Nanocarriers							
AuNPs (MSNP-Thi-Au)	80 (MSN) 5 (AuNPs)	DPV	PSA	10^{-3}–5	0.31	Serum	[73]
Mesoporous Fe_3O_4	25	CA	cTnI	10^{-3}–100	0.39	Serum	[74]
Ni/C@SiO_2	300	DPV	CEA	6×10^{-3}–12	1.56	Serum	[75]
AuNPs	18	DPV	CA-125	20–100 U	3.4 U	Serum	[76]
AuNPs/Thi/MWCNT	15 (AuNPs)	DPV	CYFRA21-1	0.1–150	43	Serum	[56]
AuNPs	30	PT	PSA	0.05–20	13.6	Serum	[63]
NC-AuNPs	30 (NC-AuNPs) 7.5 (AuNPs)	DPV	ALV-J	120–10^4 $TCID_{50}$	95 $TCID_{50}$	–	[77]
MSNP-Fe_3O_4	100 (MSN) 8 (Fe_3O_4)	CV	AFP	0.01–25	4	Serum	[78]
Fe_3O_4/AuNPs	29 (Fe_3O_4/AuNPs) 12 (AuNPs)	DPV	CEA	5×10^{-3}–50	1	Serum	[79]
Electroactive labels							
AuNPs	13	DPV	Mtb	5×10^3–5×10^5	330	Urine	[80]
AuNPs	20	DPV	hMMP9	0.18–23	60	Plasma	[81]
Cu@TiO_2	250	SWV CA	IgG	10^{-4}–100 10^{-5}–100	0.052 4.3×10^{-3}	Serum	[82]
TiNPs-Zn TiNPs-Cd	50 (TiNPs)	SWV	cTnI FABP	5×10^{-5}–50	10^{-3} 3×10^{-3}	Serum	[83]
PbS Qdots	–	SP	HER2	1–100	280	Serum	[84]
CdTe:Ni Qdots	–	DPV	PSA	10^{-3}–100	0.45	Serum	[85]
CdS Qdots	–	DPV	anti-tTG IgA	40–100 U	2.2 U	Serum	[86]
CdS QDots	–	CA	AFP	0.1–500	10	Serum	[87]
CdSe	–	PT	Mouse IgG	0.15–4.0 pM	10 fM	-	[64]
CdS	4	PEC	S100ß	0.25–10	0.15	Serum	[70]

Table 1. *Cont.*

	Size (nm)	Technique(s)	Biomarker	Linear Range ($ng \cdot mL^{-1}$)	LOD ($pg \cdot mL^{-1}$)	Real Sample	Reference
Au@Pt-$MoSe_2$	45 × 16 (Au) 80 × 58 (Au@Pt)	CA	AFP	10^{-5}–200	3.3×10^{-3}	Serum	[88]
PS@PDA−AgNPs	200	LSV	IL-6	10^{-4}–100	0.059	Serum	[89]
Graphene/AgNPs	-	SW ASV	IgE	10–1000	3.6×10^{3}	–	[90]
Au@PAMAM-C_{60}	100	LSV	AFP	10^{-4}–10	0.03	Serum	[91]
Ag@CeO_2-Au	50–100 (Ag@CeO_2)	CV	CEA	10^{-4}–5	3.2×10^{-3}	Serum	[92]
AuNPs/MB/MSNP	80 (MSN)	ASV	Gal-3	5×10^{-7}–500	1.7×10^{-4}	Serum	[93]
AuNPs-PDC-GOx	–	ASV	PCT	5×10^{-7}–500	4×10^{-5}	Serum	[94]
AuNPs	13	ASV	IgG PSA	4×10^{-7}–400 1.8×10^{-7}–450	3×10^{-4} 10^{-4}	Serum	[95]
AuNPs-Fe_3O_4	30 (Fe_3O_4) 25 (AuNPs)	DPV	HER2	5×10^{-4}–50	0.02	Serum	[96]
AuNPs/Au/spiky Au/Ag	250	LSV	PSA	1.9×10^{-3}–0.125 0.125–10	1.2	–	[97]
AuNPs	13	SWE	PDGF	5×10^{-3}–10	2	Serum	[98]
Ag@Au	–	LSV	CEA	0.1–120	55	–	[99]
Catalytically active labels							
$CoSnS_x$–Pd	200 - 600	CA	NT-pro BNP	10^{-4}–50	0.0315	Serum	[100]
$Cu_3(PO_4)_2$	200	SWV	CRP	5×10^{-4}–1	0.13	Serum	[101]
PtPd-Fe_3O_4	10	CA	CA72-4	10^{-3}–10 U	0.3 mU	Serum	[102]
Mesoporous Pt NPs	30	DPV	CEA CA-125 CA-153	0.05–20 U 8×10^{-3}–24 U 0.02–20	2 mU 1 mU 7	Serum	[103]
PdNi NPs/ graphene nanoribbon	10 (PdNi NPs)	CA	AFP	10^{-4}–16	0.03	Serum	[104]
Au@Pd NDs/NH_2–MoO_2 NSs	20 (Au@Pd NDs)	CA	HBsAg	10^{-5}–100	3.3×10^{-3}	Serum	[105]
Zn_2SiO_4-PdNPs	100–200 (Zn_2SiO_4)	SWV	Insulin	10^{-4}–50	2.5×10^{-4}	Serum	[106]

Abbreviations: AFP: Alpha fetoprotein, **ALV-J:** Avian leukosis virus subgroup J, **anti-tTG IgA:** anti-tissue transglutaminase antibody, **CA:** chronoamperometry, **CA-125:** carcinoma antigen 125, **CA-153:** carbohydrate antigen 153, **CA72-4:** Gastric cancer biomarker CA72-4, **CEA:** Carcinoembryonic antigen, **CRP:** C-reactive protein, **cTnI:** cardiac troponin I, **CYFRA21-1:** Cytokeratin 19 fragment 21-1, **FABP:** human heart-type fatty-acid-binding protein, **Gal-3:** Galectin-3, **GOx:** Glucose Oxidase, **GQdots:** Graphene quantum dots, **HBsAg:** Hepatitis B surface antigen, **HER2:** Human epidermal growth factor receptor 2, **hMMP9:** human matrix metallopeptidase-9, **IL-6:** Human interleukin-6, **MB:** Methylene blue, **MSNP:** Mesoporous silica nanoparticles, **Mtb:** Mycobacterium tuberculosis antigen, **MWCNT:** Multi-walled carbon nanotubes, **NC:** Nanocellulose, **NDs:** nanodendrites, **NPs:** nanoparticles, **NSs:** nanosheets, **NT-pro BNP:** N-terminal prohormone of brain natriuretic peptide, **PAMAM:** Polyamidoamine, **PCT:** Procalcitonin, **PDA:** Polydopamine, **PD_C:** Poly(L-DOPA), **PDGF:** Platelet-derived growth factor BB, **PPy:** Polypyrrole, **PT:** Potentiometry, **PS:** Polystyrene, **PSA:** Prostate-specific antigen, **S100ß:** S100 calcium-binding protein β, **SW ASV:** Square wave anodic stripping voltammetry, **TCID50:** 50% tissue culture infective dose, **Thi:** Thionine.

6.1. MNPs and Qdots as Nanocarriers

MNPs and Qdots are excellent candidates to be used as nanocarriers for antibodies together with numerous electroactive substances [73,107] and especially enzymes [77,78]. The involvement of nanocarriers in the design of electrochemical immunosensors provides significant amplification of the analytical signal by handling an increased number of carried molecules close to the electrode surface. Numerous possible MNPs and Qdots surfaces containing functional groups permit various single molecule immobilization scenarios facilitating the design of the immunosensor. MNPs possess good electron transfer properties [108] and if used as nanocarriers can improve or provide direct electron transfer between the active site of the immobilized enzyme and the electrode.

If at first scientists used various nanostructures as carriers separately, now the usage of different types of nanomaterials together while trying to find the optimal combination for signal amplification prevails. One of the possible benefits is an increase in the loading capacity due to the increase in surface area for single molecule immobilization provided by nanocarriers. The deposition of graphene quantum dots (GQdots) on the surface of Fe_3O_4/Ag core-shell nanostructures allows an increase in the antibody loading capacity for the detection of Mycobacterium tuberculosis antigen [80]. GQdots were also used for nanocarrier design together with multiwalled carbon nanotubes (MWCNTs) [109,110]. Moreover, the enhancement of electron transfer can be achieved. The usage of Au/Pt nanorods loaded with $MoSe_2$ nanosheets enhances the electron transfer capability from the label to the electrode, resulting in the increase in the analytical signal intended for monitoring alpha fetoprotein (AFP) concentration [88].

A joint use of AuNPs and mesoporous silica nanoparticles (MSNPs) allows for the design of a controlled system of label release (Figure 5) [73]. The immunosensor was designed for the detection of PSA. For this purpose, the electroactive substance thionine was encapsulated in the MSNPs' pores, which were capped with AuNPs. After the formation of an immune complex between detection antibodies conjugated with AuNPs-MSNPs and analyte solution, the pH was lowered to 3.5. Under acidic conditions, the hydrolysis of acid-labile acetal linker liberates AuNPs, resulting in the controlled release of thionine molecules, which were detected using DPV.

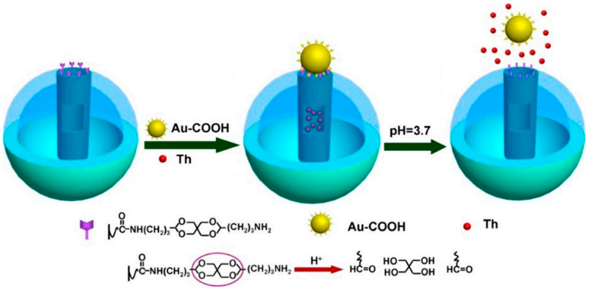

Figure 5. Schematic representation of pH controlled release of thionine for monitoring of PSA concentration using sandwich format immunosensor. Adapted from [73] with permission from Elsevier.

Metal-based nanoparticles can also act as a transport medium aimed to enhance electrochemical immunosensor response and stability or to capture the analyte from the sample. The aim usually is to concentrate the signal producing molecules towards the electrode to improve the detected analytical signal, and for this reason some immunosensor component is labeled using nanomaterials, usually the capture antibody [79,100]. The most common nanomaterials for this use case are magnetic nanoparticles, such as Fe_3O_4, where a strong magnet is placed near the electrode or other types of magnetic electrodes are used to draw antibodies with magnetic nanoparticle labels towards the electrode [100]. Magnetic nanoparticles are usually bimetallic with a magnetic core and a noble metal or polymer shell [79,100]. The use of magnetic labels with magnetic electrodes allows for increased antibody density near the electrode, which in turn leads to a higher density of signal producing molecules. In addition to signal enhancement, magnetic labels also act as substrates that can be easily removed from the electrode by removing the magnetic field, allowing for simple reuse of the electrode surface. Furthermore, magnetic labels improve and shorten immunosensing procedures by simplifying antibody washing and collection steps. Examples of such systems are provided for N-terminal prohormone of brain natriuretic peptide [100] and carcinoembryonic antigen detection [79]. In both cases, Fe_3O_4@PPy-Au and Fe_3O_4@Au-Au magnetic bimetallic nanoparticles were used, respectively, while the capture antibody was immobilized on the surface. Magnetic labels with capture antibodies can also be used to extract and concentrate the analyte from the sample solution. Soelberg et al. used magnetic nanoparticles with immobilized monoclonal antibodies to capture the staphylococcal enterotoxin B from a sample and then used a magnet to extract and concentrate the analyte [111]. Although the authors used an optical detection method, in principle, electrochemical detection could be performed by using the described analyte concentration method in conjunction with magnetic electrodes.

6.2. MNPs and Qdots as Electroactive Labels in Electrochemical Immunosensors

The action of an electrochemical immunosensor implies the presence of an electroactive substance whose concentration should be proportional to the concentration of the analyte. One of the feasible strategies of immunosensor design is based on the involvement of electroactive labels. This role can be played excellently by MNPs and Qdots. Such a strategy typically leads to the usage of sandwich immunoassay formats, although applications of the competitive electrochemical immunoassay format can also be found in the literature [89]. Moreover, a further enhancement of signal amplification already provided by electroactive labels can be achieved by the additional involvement of other nanostructures such as carbon nanomaterials [90,91], metal oxides [92], etc., that serve the role of nanocarriers. High loading capacity caused by their large surface area allows the deposition of a higher amount of electroactive labels to the electrode, amplifying the analytical signal. In addition, MNPs and Qdots do not have specific limitations such as loss of activity and operational stability, which are inherent for popular biological labels—enzymes.

MNPs are composed of hundreds or even millions of atoms, which can be electrochemically oxidized. The monitoring of electrochemical oxidation is the most often applied operating principle of electrochemical immunosensors containing MNPs as labels, while AuNPs are one of the most commonly used. AuNPs, as well as the majority of other MNPs, possess good stability. As a result, the application of a high potential is necessary for AuNPs' electrooxidation, which leads to decreased sensitivity due to high background level [112]. Such a limitation is bypassed by a two-step process (Figure 6A). The first step includes the formation of $AuCl_4^-$ ions from AuNPs to the solution, while various voltammetry types such as DPV, ASV and LSV are used for the detection of Au^0 atom formation caused by the reduction during the second step. Metal ions can be released to the solution due to the dissolution in HBr/Br_2 mixture [113]. However, the toxicity of HBr/Br_2 solution limits the application of this method [114]. It was shown that diluted 30% aqua regia could be an alternative and provides the same detection level of the heart failure biomarker galectin-3 [93]. This solvent change provides a well-shaped anodic Au-stripping peak, which is not affected by the oxidation process of bromine [94]. However, the most common method of AuNP oxidation is electrochemical oxidation in HCl solution. Electrochemical oxidation at +1.2 +1.4 V is performed for no longer than 3 min. The reduction of formed $AuCl_4^-$ ions to Au^0 is monitored by voltammetry during the second step [115]. Applying the $NaNO_3/NaCl$ mixture instead of HCl as a more ecofriendly oxidant provides a comparable immunosensor response to human matrix metallopeptidase 9 [81]. Such a detection strategy enables performing the detection of biomarkers at the $fg \cdot mL^{-1}$ concentration levels for human immunoglobulin G or human PSA [95].

Silver nanoparticles (AgNPs) are also quite popular labels for electrochemical immunosensors. The oxidation of AgNPs is performed at a noticeably lower potential in comparison with AuNPs, wherein the lower background signal is achieved by controlling the Ag deposition on the surface of the electrode [116,117]. As an alternative, permanganate or sodium hypochlorite can be used for the peroxidation of AgNPs [118]. Moreover, the detection of AgNPs can be performed in KCl solution through the monitoring of the solid-state Ag/AgCl process. Ag^+ ions oxidized from AgNPs during the anodic potential scan form solid AgCl, which reduces to Ag^0 and Cl^- ions during the cathodic potential scan. The return to the anodic part of the scan is accompanied with the reoxidation of metallic Ag to AgCl. This experiment design allows the detection of AgNP labels without the peroxidation-dissolving step and reaches the $fg \cdot mL^{-1}$ detection level of PSA [119,120].

Metal deposition on MNP labels can also be used for signal amplification (Figure 6B). The metal is deposited on the surface of MNPs, where MNPs act as nucleation sites [121]. After the deposition, the amount of deposited metal is quantified by the stripping potential. The susceptibility of Ag to oxidation makes it a perfect candidate for this purpose, wherein the most common formation of bimetallic Au/Ag particles is used [96]. Such particles formed using the seed-mediated growth approach are normally more electroactive, and the enlarged particles are located closer to the electrode. It is important to reiterate that Ag reduction demands lower potential. Additional enhancement of the analytical signal can be reached by the enlargement of AuNP labels and by the optimization of AuNP shapes [97]. Au/Ag bimetallic particles [98,99] as well as other MNPs [122] can be used as electron migration enhancers and mediate the redox response of the electroactive molecules.

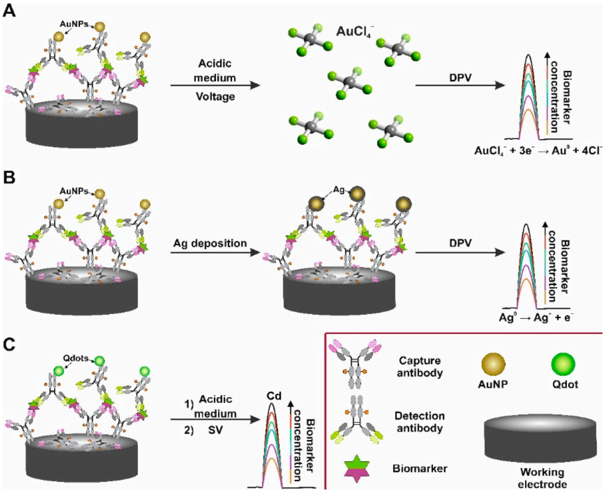

Figure 6. Schematic representation of sandwich format electrochemical immunosensor based on AuNP and Qdot labels. (**A**) Electrochemical oxidation of AuNPs in acidic medium. (**B**) Deposition of Ag on AuNPs. (**C**) Electrochemical oxidation of Qdots in acidic medium.

The metal dissolution approach in acidic medium such as HCl or HNO_3 solutions with the further monitoring of released metal ion concentration can also be effectively utilized with Qdots labels (Figure 6C), which as well as MNPs are typically used in sandwich format immunoassay [123]. Qdots typically have a core-shell structure and consist of heavy metals such as Cd, Pb, and Zn, which can be released from Qdots and quantified by sweeping the potential of the electrode. Such an approach allows the measurement of the concentration at the pg·mL^{-1} level for different biomarkers such as PSA, HE4 and HER2 [84,85,124]. Qdots are also suitable for the application as labels in electrochemical immunosensors aimed at microorganism detection (for instance, Escherichia coli [125]). However, the primary benefit of Qdots is the difference in oxidation potential allowing Qdots to be applied for multiplexed simultaneous detection of biomarkers. Heavy metal oxidation peaks are quite narrow, whereby the cross talk issue is less prevalent [126,127]. The oxidation potentials of the commonly used MNPs (based on Ag, Au, Cu), in contrast, are located close to each other, which leads to a possible cross talk. This issue can be solved using electrochemical systems with multiple working electrodes, permitting spatial separation and ensuring multiplex biomarkers detection.

The design of photoelectrochemical immunosensors commonly implies the deposition of Qdots on the surface of the electrode. Enzymes can be involved as labels and are conjugated with detection antibodies. The generation of the analytical signal in these instances can be based on the interaction of immobilized Qdots with chemical and biological molecules, such as O_2 and H_2O_2, which can be a substrate or a product for enzymatic reaction. Moreover, the principle of an immunosensor can be based on steric hindrance arising from immunocomplex formation, resulting in a reduced redox probe diffusion towards the Qdots [65]. Furthermore, Qdots can also be applied as labels in photoelectrochemical immunosensors. For instance, "signal off" sandwich type immunoassay for the detection of CEA at pg·mL^{-1} level was proposed by Fan et al. [128]. The operating principle was based on the immunorecognition event between CEA and the detection antibody. The decrease in the analytical signal was proportional to the concentration of the Qdot–antibody conjugate. This can be explained by the competitive absorption of photons and the consumption of electron donors performed by Qdots while accompanied by reduced electron transfer. The competitive immunoassay format can also be adapted for Qdots photochemical immunosensors [87]. Another interesting detection strategy is based on the involvement of noble metal nanoparticles as labels. Such nanoparticles possess high extinction coefficient and a wide absorption spectrum, which allows the design of immunosensors based on energy transfer from nanoparticles to Qdots and/or on steric hindrance [129,130].

6.3. MNPs as Catalytically Active Labels

Metal-based nanomaterial labels can also be used as catalysts that facilitate reactions or even mimic enzymes. Electrochemical immunosensors employing this type of labeling strive to use MNPs to initiate chemical reactions that would otherwise not occur or to increase chemical reaction rates, in turn, enhancing registered electrical signals or shortening the analysis time. Noble metal nanoparticles are most commonly used for this type of electrochemical immunosensors since noble metals are stable, biocompatible, and exhibit strong catalytic activity as well as high electrical conductivity. Bimetallic nanomaterials are also used, usually consisting of a magnetic or noble metal core with a shell made from noble metals. The use of catalytically active nanomaterial tags replaces the need for traditional enzymatic labels, providing multiple advantages such as high surface area, reduced cost, immunosensor design complexity, compatibility with biomolecules, longer sensor shelf life, and improved reproducibility and repeatability [104,131,132]. Additionally, catalytically active nanomaterials are significantly easier to obtain compared with biomolecules such as enzymes. Finally, it is possible to select for desired physical, chemical, and catalytic properties by varying nanomaterial size/composition.

The most common subtype of these electrochemical immunosensors employ nanoparticles to directly catalyze H_2O_2 reduction [104,131,132], replacing the use of enzymes such as catalase [133] or HRP [134,135]. Typically, H_2O_2 is added to the sandwich immunoassay format immunosensor where the detection antibody is labeled with nanomaterials that catalyze H_2O_2 reduction. Usually, the current produced during H_2O_2 reaction is measured as an analytical signal. Several factors should be taken into consideration when designing these types of electrochemical immunosensors. Firstly, the highest nanomaterial electroactive surface area should be pursued so as to not hinder the reaction that is being catalyzed on the nanomaterial surface. As such, the step of antibody immobilization onto the nanoparticle plays a significant role. Secondly, high electrical conductivity of the material is desired in order to facilitate faster electron transfer kinetics. Lastly, the catalytic activity of the material should be taken into consideration. Many different materials are employed in immunosensor design for the purpose of H_2O_2 reduction catalysis; however, the most common are Pt and Pd. A comprehensive comparative study of immunosensors with different nanomaterials is difficult to attain since changing the nanomaterial usually results in nanoparticles of different sizes and shapes, rendering a comparison difficult. For example, Guo et al. [131] presented an electrochemical immunosensor based on the catalysis of H_2O_2 reduction for CA125 detection. The authors presented the comparison of an analytical signal with three different labels—gold, palladium, and bimetallic Au@Pd nanoparticles—modified with immobilized detection antibody. The results showed that the Au-antibody label produced almost no response; Pd-Ab facilitated a much larger current response, while the Au@Pd-antibody label displayed the highest current change. However, it is difficult to assess whether the signal enhancement was solely due to catalytic improvements since nanoparticles were of different sizes and antibody immobilization efficiency or electroactive surface area measurements were not presented for Au-antibody and Pd-antibody labels. Pourbaix diagrams can be employed as an aid for selecting the material to be used for nanoparticle labels [136]. Nonetheless, the replacement of traditional enzyme labels such as HRP [134,135] with catalytic nanomaterial tags can lead to significant sensitivity improvements, resulting in a 2000 times lower LOD for CA125 detection. Other examples of catalytic H_2O_2 reduction-based electrochemical immunosensors for the detection of AFP [104,132] also exhibit similar sensitivity and LOD improvements compared to enzymatic labels [137,138].

Furthermore, various catalytic labels can be combined to further increase analytical signals. For example, Yang et al. reported an electrochemical immunosensor for hepatitis B surface antigen detection where detection antibodies were labeled with nanostructures consisting of amino-functionalized molybdenum dioxide nanosheets, Au@Pd nanostructures (Figure 7) [105]. The analytical signal enhancement can be attributed to higher surface area and improved electron transfer kinetics.

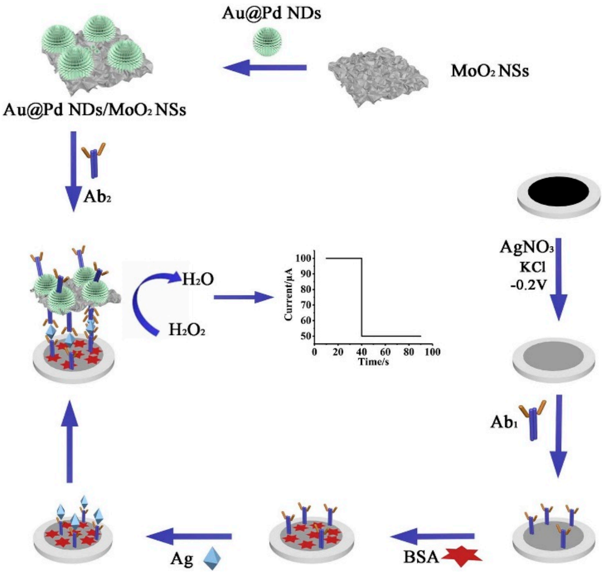

Figure 7. Schematic representation of the sandwich-type electrochemical immunosensor based on Au@Pd nanodendrite functionalized MoO_2 nanosheet for the detection of HBsAg. Adapted from [105] with permission from Elsevier.

7. Conclusions

Immunosensors based on different signal transducers can be used for biomarker detection. Among them, electrochemical immunosensors are increasingly used in clinical analysis and are becoming a promising alternative to existing laboratory methods. Electrochemical immunosensors possess unique properties such as high sensitivity, simplicity of fabrication, low cost, and applicability to perform the analysis of opaque and optically dense samples. However, the analytical parameters of electrochemical immunosensors can be improved using nanomaterials in their development. Zero-dimensional MNPs and Qdots were selected for this review due to their unique properties. MNPs (single metal or bimetallic) can be easily synthesized in various sizes. MNPs are chemically stable and possess a large surface-to-volume ratio. The availability of various modification methods enhances the ability of biomolecule immobilization. Therefore, MNPs and Qdots have found wide practical application, including as a tag for the immunosensor signal amplification. Qdots are commonly used in optical analytical systems; however, the application in electrochemical sensors is insufficiently studied. In this review, different strategies for electrochemical signal amplification using MNPs and Qdots as tags are discussed. Even though this review focused mainly on the single biomarker assays, MNPs and Qdots are also very promising nanomaterials for the design of electrochemical immunosensors intended for the simultaneous detection of multiple biomarkers.

Author Contributions: Conceptualization, A.P., B.B., A.K.-M. and A.R.; writing—original draft preparation, A.P., B.B., A.K.-M., A.R.; writing—review and editing, A.P., B.B., A.K.-M., A.R.; supervision A.K.-M. and A.R.; project administration, A.P.; funding acquisition, A.P. All authors have read and agreed to the published version of the manuscript.

Funding: This project has received funding from the European Social Fund (project no. 09.3.3-LMT-K-712-19-0170) under grant agreement with the Research Council of Lithuania (LMTLT).

Institutional Review Board Statement: Not applicable.

Informed Consent Statement: Not applicable.

Data Availability Statement: Not applicable.

Conflicts of Interest: The authors declare no conflict of interest.

References

1. Yalow, R.S.; Berson, S.A. Immunoassay of endogenous plasma insulin in man. *J. Clin. Investig.* **1960**, *39*, 1157–1175. [CrossRef] [PubMed]
2. Nakane, P.K.; Pierce, G.B. Enzyme-labeled antibodies: Preparation and application for the localization of antigens. *J. Histochem. Cytochem.* **1966**, *14*, 929–931. [CrossRef] [PubMed]
3. Evtugyn, G.; Hianik, T. Electrochemical immuno- and aptasensors for mycotoxin determination. *Chemosensors* **2019**, *7*, 10. [CrossRef]
4. Engvall, E.; Perlmann, P. Enzyme-linked immunosorbent assay (ELISA) quantitative assay of immunoglobulin G. *Immunochemistry* **1971**, *8*, 871–874. [CrossRef]
5. Van Weemen, B.K.; Schuurs, A.H.W.M. Immunoassay using antigen-enzyme conjugates. *FEBS Lett.* **1971**, *15*, 232–236. [CrossRef]
6. Mollarasouli, F.; Kurbanoglu, S.; Ozkan, S.A. The Role of Electrochemical Immunosensors in Clinical Analysis. *Biosensors* **2019**, *9*, 86. [CrossRef]
7. Ramanavicius, A.; Oztekin, Y.; Ramanaviciene, A. Electrochemical formation of polypyrrole-based layer for immunosensor design. *Sens. Actuators B Chem.* **2014**, *197*. [CrossRef]
8. Duffy, G.F.; Moore, E.J. Electrochemical Immunosensors for Food Analysis: A Review of Recent Developments. *Anal. Lett.* **2017**, *50*, 1–32. [CrossRef]
9. Pollap, A.; Kochana, J. Electrochemical Immunosensors for Antibiotic Detection. *Biosensors* **2019**, *9*, 61. [CrossRef] [PubMed]
10. Cho, I.-H.; Lee, J.; Kim, J.; Kang, M.-S.; Paik, J.K.; Ku, S.; Cho, H.-M.; Irudayaraj, J.; Kim, D.-H. Current Technologies of Electrochemical Immunosensors: Perspective on Signal Amplification. *Sensors* **2018**, *18*, 207. [CrossRef]
11. Makaraviciute, A.; Ramanaviciene, A. Site-directed antibody immobilization techniques for immunosensors. *Biosens. Bioelectron.* **2013**, *50*, 460–471. [CrossRef]
12. Baniukevic, J.; Kirlyte, J.; Ramanavicius, A.; Ramanaviciene, A. Application of oriented and random antibody immobilization methods in immunosensor design. *Sens. Actuators B Chem.* **2013**, *189*. [CrossRef]
13. Huang, H.; Zhu, J.-J. The electrochemical applications of quantum dots. *Analyst* **2013**, *138*, 5855–5865. [CrossRef]
14. Varghese, R.J.; Oluwafemi, O.S. The photoluminescence and biocompatibility of cuins2-based ternary quantum dots and their biological applications. *Chemosensors* **2020**, *8*, 101. [CrossRef]
15. WHO. *Biomarkers in Risk Assessment: Validity and Validation*; World Health Organization: Geneva, Switzerland, 2001.
16. Website for the National Cancer Institute (NCI), the U.S. Government's Principal Agency for Cancer Research. Available online: https://www.cancer.gov/publications/dictionaries/cancer-terms/def/biomarker (accessed on 13 March 2021).

17. Atkinson, A.J.; Colburn, W.A.; DeGruttola, V.G.; DeMets, D.L.; Downing, G.J.; Hoth, D.F.; Oates, J.A.; Peck, C.C.; Schooley, R.T.; Spilker, B.A.; et al. Biomarkers and surrogate endpoints: Preferred definitions and conceptual framework. *Clin. Pharmacol. Ther.* **2001**, *69*, 89–95.
18. Sherwani, S.I.; Khan, H.A.; Ekhzaimy, A.; Masood, A.; Sakharkar, M.K. Significance of HbA1c Test in Diagnosis and Prognosis of Diabetic Patients. *Biomark. Insights* **2016**, *11*, 95–104. [CrossRef]
19. Basu, N.N.; Ingham, S.; Hodson, J.; Lalloo, F.; Bulman, M.; Howell, A.; Evans, D.G. Risk of contralateral breast cancer in BRCA1 and BRCA2 mutation carriers: A 30-year semi-prospective analysis. *Fam. Cancer* **2015**, *14*, 531–538. [CrossRef] [PubMed]
20. Gundogdu, F.; Soylu, F.; Erkan, L.; Tatli, O.; Mavi, S.; Yavuzcan, A. The role of serum CA-125 levels and CA-125 tissue expression positivity in the prediction of the recurrence of stage III and IV epithelial ovarian tumors (CA-125 levels and tissue CA-125 in ovarian tumors). *Arch. Gynecol. Obstet.* **2011**, *283*, 1397–1402. [CrossRef] [PubMed]
21. Mitterhauser, M.; Wadsak, W. Imaging biomarkers or biomarker imaging? *Pharmaceuticals* **2014**, *7*, 765–778. [CrossRef]
22. Huss, R. Biomarkers. In *Translational Regenerative Medicine*; Atala, A., Allickson, J.G.B.T.-T.R.M., Eds.; Academic Press: Boston, MA, USA, 2015; pp. 235–241. ISBN 9780124104570.
23. Laterza, O.F.; Hendrickson, R.C.; Wagner, J.A. Molecular Biomarkers. *Drug Inf. J.* **2007**, *41*, 573–585. [CrossRef]
24. Darwish, I.A. Immunoassay Methods and their Applications in Pharmaceutical Analysis: Basic Methodology and Recent Advances. *Int. J. Biomed. Sci.* **2006**, *2*, 217–235.
25. Website for Bio-Rad Company. Available online: https://www.bio-rad-antibodies.com/elisa-types-direct-indirect-sandwich-competition-elisa-formats.htm (accessed on 14 March 2021).
26. Kausaite-Minkstimiene, A.; Ramanaviciene, A.; Kirlyte, J.; Ramanavicius, A. Comparative study of random and oriented antibody immobilization techniques on the binding capacity of immunosensor. *Anal. Chem.* **2010**, *82*. [CrossRef]
27. Byzova, N.A.; Safenkova, I.V.; Slutskaya, E.S.; Zherdev, A.V.; Dzantiev, B.B. Less is More: A Comparison of Antibody–Gold Nanoparticle Conjugates of Different Ratios. *Bioconjug. Chem.* **2017**, *28*, 2737–2746. [CrossRef]
28. Mühlpfordt, H. The preparation of colloidal gold particles using tannic acid as an additional reducing agent. *Experientia* **1982**, *38*, 1127–1128. [CrossRef]
29. Correard, F.; Maximova, K.; Estève, M.-A.; Villard, C.; Roy, M.; Al-Kattan, A.; Sentis, M.; Gingras, M.; Kabashin, A.V.; Braguer, D. Gold nanoparticles prepared by laser ablation in aqueous biocompatible solutions: Assessment of safety and biological identity for nanomedicine applications. *Int. J. Nanomed.* **2014**, *9*, 5415–5430. [CrossRef]
30. Ruiz, G.; Tripathi, K.; Okyem, S.; Driskell, J.D. pH Impacts the Orientation of Antibody Adsorbed onto Gold Nanoparticles. *Bioconjug. Chem.* **2019**, *30*, 1182–1191. [CrossRef]
31. Makaraviciute, A.; Ruzgas, T.; Ramanavicius, A.; Ramanaviciene, A. Antibody fragment immobilization on planar gold and gold nanoparticle modified quartz crystal microbalance with dissipation sensor surfaces for immunosensor applications. *Anal. Methods* **2014**, *6*. [CrossRef]
32. Baniukevic, J.; Hakki Boyaci, I.; Goktug Bozkurt, A.; Tamer, U.; Ramanavicius, A.; Ramanaviciene, A. Magnetic gold nanoparticles in SERS-based sandwich immunoassay for antigen detection by well oriented antibodies. *Biosens. Bioelectron.* **2013**, *43*. [CrossRef]
33. Kaminiaris, M.D.; Mavrikou, S.; Georgiadou, M.; Paivana, G.; Tsitsigiannis, D.I.; Kintzios, S. An Impedance Based Electrochemical Immunosensor for Aflatoxin B1 Monitoring in Pistachio Matrices. *Chemosensors* **2020**, *8*, 121. [CrossRef]
34. Dvorakova, V.; Cadkova, M.; Datinska, V.; Kleparnik, K.; Foret, F.; Bilkova, Z.; Korecka, L. An advanced conjugation strategy for the preparation of quantum dot-antibody immunoprobes. *Anal. Methods* **2017**, *9*, 1991–1997. [CrossRef]
35. Sahoo, S.L.; Liu, C.-H.; Kumari, M.; Wu, W.-C.; Wang, C.-C. Biocompatible quantum dot-antibody conjugate for cell imaging, targeting and fluorometric immunoassay: Crosslinking, characterization and applications. *RSC Adv.* **2019**, *9*, 32791–32803. [CrossRef]
36. Thomas, J.A.; Schnell, F.; Kaveh-Baghbaderani, Y.; Berensmeier, S.; Schwaminger, S.P. Immunomagnetic Separation of Microorganisms with Iron Oxide Nanoparticles. *Chemosensors* **2020**, *8*, 17. [CrossRef]
37. Jampasa, S.; Siangproh, W.; Laocharoensuk, R.; Vilaivan, T.; Chailapakul, O. Electrochemical detection of c-reactive protein based on anthraquinone-labeled antibody using a screen-printed graphene electrode. *Talanta* **2018**, *183*, 311–319. [CrossRef] [PubMed]
38. Makaraviciute, A.; Ramanavicius, A.; Ramanaviciene, A. Development of a reusable protein G based SPR immunosensor for direct human growth hormone detection in real samples. *Anal. Methods* **2015**, *7*. [CrossRef]
39. Bodanszky, A.; Bodanszky, M. Sepharose-avidin column for the binding of biotin or biotin-containing peptides. *Experientia* **1970**, *26*, 327. [CrossRef] [PubMed]
40. Deng, L.; Kitova, E.N.; Klassen, J.S. Dissociation Kinetics of the Streptavidin–Biotin Interaction Measured Using Direct Electrospray Ionization Mass Spectrometry Analysis. *J. Am. Soc. Mass Spectrom.* **2013**, *24*, 49–56. [CrossRef]
41. Melnyk, O.; Duburcq, X.; Olivier, C.; Urbès, F.; Auriault, C.; Gras-Masse, H. Peptide Arrays for Highly Sensitive and Specific Antibody-Binding Fluorescence Assays. *Bioconjug. Chem.* **2002**, *13*, 713–720. [CrossRef] [PubMed]
42. Quash, G.; Roch, A.-M.; Niveleau, A.; Grange, J.; Keolouangkhot, T.; Huppert, J. The preparation of latex particles with covalently bound polyamines, IgG and measles agglutinins and their use in visual agglutination tests. *J. Immunol. Methods* **1978**, *22*, 165–174. [CrossRef]
43. Website for Thermo Fisher Scientific Company. Available online: https://www.thermofisher.com/order/catalog/product/S10469#/S10469 (accessed on 14 March 2021).

44. Kondzior, M.; Grabowska, I. Antibody-Electroactive Probe Conjugates Based Electrochemical Immunosensors. *Sensors* **2020**, *20*, 2014. [CrossRef] [PubMed]
45. Warsinke, A.; Benkert, A.; Scheller, F.W. Electrochemical immunoassays. *Fresenius. J. Anal. Chem.* **2000**, *366*, 622–634. [CrossRef]
46. Li, Y.; Zhang, Y.; Li, F.; Li, M.; Chen, L.; Dong, Y.; Wei, Q. Sandwich-type amperometric immunosensor using functionalized magnetic graphene loaded gold and silver core-shell nanocomposites for the detection of Carcinoembryonic antigen. *J. Electroanal. Chem.* **2017**, *795*, 1–9. [CrossRef]
47. Yan, Q.; Cao, L.; Dong, H.; Tan, Z.; Liu, Q.; Zhang, W.; Zhao, P.; Li, Y.; Liu, Y.; Dong, Y. Sensitive amperometric immunosensor with improved electrocatalytic Au@Pd urchin-shaped nanostructures for human epididymis specific protein 4 antigen detection. *Anal. Chim. Acta* **2019**, *1069*, 117–125. [CrossRef]
48. Thunkhamrak, C.; Reanpang, P.; Ounnunkad, K.; Jakmunee, J. Sequential injection system with amperometric immunosensor for sensitive determination of human immunoglobulin G. *Talanta* **2017**, *171*, 53–60. [CrossRef]
49. Shi, W.; Ma, Z. A novel label-free amperometric immunosensor for carcinoembryonic antigen based on redox membrane. *Biosens. Bioelectron.* **2011**, *26*, 3068–3071. [CrossRef]
50. Yang, Y.; Liu, Q.; Liu, Y.; Cui, J.; Liu, H.; Wang, P.; Li, Y.; Chen, L.; Zhao, Z.; Dong, Y. A novel label-free electrochemical immunosensor based on functionalized nitrogen-doped graphene quantum dots for carcinoembryonic antigen detection. *Biosens. Bioelectron.* **2017**, *90*, 31–38. [CrossRef] [PubMed]
51. Martínez-García, G.; Sánchez-Tirado, E.; González-Cortés, A.; Yáñez-Sedeño, P.; Pingarrón, J.M. Amperometric immunoassay for the obesity biomarker amylin using a screen printed carbon electrode functionalized with an electropolymerized carboxylated polypyrrole. *Microchim. Acta* **2018**, *185*, 323. [CrossRef]
52. Yáñez-Sedeño, P.; Campuzano, S.; Pingarrón, J.M. Multiplexed Electrochemical Immunosensors for Clinical Biomarkers. *Sensors* **2017**, *17*, 965. [CrossRef] [PubMed]
53. Mansuriya, B.D.; Altintas, Z. Graphene Quantum Dot-Based Electrochemical Immunosensors for Biomedical Applications. *Materials* **2019**, *13*, 96. [CrossRef] [PubMed]
54. Cui, F.; Zhou, Z.; Zhou, H.S. Review—Measurement and Analysis of Cancer Biomarkers Based on Electrochemical Biosensors. *J. Electrochem. Soc.* **2020**, *167*, 37525. [CrossRef]
55. Trindade, E.K.G.; Silva, B.V.M.; Dutra, R.F. A probeless and label-free electrochemical immunosensor for cystatin C detection based on ferrocene functionalized-graphene platform. *Biosens. Bioelectron.* **2019**, *138*, 111311. [CrossRef] [PubMed]
56. Zeng, Y.; Bao, J.; Zhao, Y.; Huo, D.; Chen, M.; Qi, Y.; Yang, M.; Fa, H.; Hou, C. A sandwich-type electrochemical immunoassay for ultrasensitive detection of non-small cell lung cancer biomarker CYFRA21-1. *Bioelectrochemistry* **2018**, *120*, 183–189. [CrossRef] [PubMed]
57. Sun, X.; Hui, N.; Luo, X. Reagentless and label-free voltammetric immunosensor for carcinoembryonic antigen based on polyaniline nanowires grown on porous conducting polymer composite. *Microchim. Acta* **2017**, *184*, 889–896. [CrossRef]
58. Feng, C.; Xu, Y.; Song, L. Study on highly sensitive potentiometric IgG immunosensor. *Sens. Actuators B Chem.* **2000**, *66*, 190–192. [CrossRef]
59. Tang, D.P.; Yuan, R.; Chai, Y.Q.; Zhong, X.; Liu, Y.; Dai, J.Y.; Zhang, L.Y. Novel potentiometric immunosensor for hepatitis B surface antigen using a gold nanoparticle-based biomolecular immobilization method. *Anal. Biochem.* **2004**, *333*, 345–350. [CrossRef]
60. Ibupoto, Z.H.; Jamal, N.; Khun, K.; Willander, M. Development of a disposable potentiometric antibody immobilized ZnO nanotubes based sensor for the detection of C-reactive protein. *Sens. Actuators B Chem.* **2012**, *166–167*, 809–814. [CrossRef]
61. Fowler, J.M.; Wong, D.K.Y.; Brian Halsall, H.; Heineman, W.R. Recent developments in electrochemical immunoassays and immunosensors. In *Electrochemical Sensors, Biosensors and their Biomedical Applications*; Elsevier Inc.: Amsterdam, The Netherlands, 2008; pp. 115–143. ISBN 9780123737380.
62. Cao, Y.; Zheng, M.; Cai, W.; Wang, Z. Enzyme-loaded liposome with biocatalytic precipitation for potentiometric immunoassay of thyroid-stimulating hormone in thyroid carcinoma. *Chinese Chem. Lett.* **2020**, *31*, 463–467. [CrossRef]
63. Lv, S.; Lin, Z.; Zhang, K.; Lu, M.; Tang, D. Polyion oligonucleotide-decorated gold nanoparticles with tunable surface charge density for amplified signal output of potentiometric immunosensor. *Anal. Chim. Acta* **2017**, *964*, 67–73. [CrossRef]
64. Thürer, R.; Vigassy, T.; Hirayama, M.; Wang, J.; Bakker, E.; Pretsch, E. Potentiometric immunoassay with quantum dot labels. *Anal. Chem.* **2007**, *79*, 5107–5110. [CrossRef]
65. Shu, J.; Tang, D. Current Advances in Quantum-Dots-Based Photoelectrochemical Immunoassays. *Chem. Asian J.* **2017**, *12*, 2780–2789. [CrossRef]
66. Li, R.; Gao, J.; Gao, P.; Zhang, S.; Liu, Y.; Du, B.; Wei, Q. A sensitive photoelectrochemical immunoassay based on mesoporous carbon/core–shell quantum dots as donor–acceptor light-harvesting architectures. *New J. Chem.* **2015**, *39*, 731–738. [CrossRef]
67. Liang, M.; Liu, S.; Wei, M.; Guo, L.-H. Photoelectrochemical Oxidation of DNA by Ruthenium Tris(bipyridine) on a Tin Oxide Nanoparticle Electrode. *Anal. Chem.* **2006**, *78*, 621–623. [CrossRef] [PubMed]
68. Zhao, W.-W.; Xu, J.-J.; Chen, H.-Y. Photoelectrochemical bioanalysis: The state of the art. *Chem. Soc. Rev.* **2015**, *44*, 729–741. [CrossRef] [PubMed]
69. Chen, J.; Zhao, G.-C. A novel signal-on photoelectrochemical immunosensor for detection of alpha-fetoprotein by in situ releasing electron donor. *Biosens. Bioelectron.* **2017**, *98*, 155–160. [CrossRef]

70. Tabrizi, M.A.; Ferré-Borrull, J.; Kapruwan, P.; Marsal, L.F. A photoelectrochemical sandwich immunoassay for protein S100β, a biomarker for Alzheimer's disease, using an ITO electrode modified with a reduced graphene oxide-gold conjugate and CdS-labeled secondary antibody. *Microchim. Acta* **2019**, *186*, 117. [CrossRef] [PubMed]
71. Zhang, N.; Wang, Y.; Zhao, G.; Wang, C.; Li, Y.; Zhang, Y.; Wang, H.; Wei, Q. A photoelectrochemical immunosensor based on CdS/CdTe-cosensitized SnO2 as a platform for the ultrasensitive detection of amyloid β-protein. *Analyst* **2020**, *145*, 619–625. [CrossRef]
72. Sun, X.; Li, C.; Zhu, Q.; Chen, J.; Li, J.; Ding, H.; Sang, F.; Kong, L.; Chen, Z.; Wei, Q. A novel ultrasensitive sandwich-type photoelectrochemical immunoassay for PSA detection based on dual inhibition effect of Au/MWCNTs nanohybrids on N-GQDs/CdS QDs dual sensitized urchin-like TiO2. *Electrochim. Acta* **2020**, *333*, 135480. [CrossRef]
73. Fan, D.; Li, N.; Ma, H.; Li, Y.; Hu, L.; Du, B.; Wei, Q. Electrochemical immunosensor for detection of prostate specific antigen based on an acid cleavable linker into MSN-based controlled release system. *Biosens. Bioelectron.* **2016**, *85*, 580–586. [CrossRef]
74. Ma, N.; Zhang, T.; Yan, T.; Kuang, X.; Wang, H.; Wu, D.; Wei, Q. Novel electrochemical immunosensor for sensitive monitoring of cardiac troponin I using antigen–response cargo released from mesoporous Fe3O4. *Biosens. Bioelectron.* **2019**, *143*, 111608. [CrossRef]
75. Song, D.; Zheng, J.; Myung, N.V.; Xu, J.; Zhang, M. Sandwich-type electrochemical immunosensor for CEA detection using magnetic hollow Ni/C@SiO2 nanomatrix and boronic acid functionalized CPS@PANI@Au probe. *Talanta* **2021**, *225*, 122006. [CrossRef]
76. Kumar, N.; Sharma, S.; Nara, S. Dual gold nanostructure-based electrochemical immunosensor for CA125 detection. *Appl. Nanosci.* **2018**, *8*, 1843–1853. [CrossRef]
77. Liu, C.; Dong, J.; Waterhouse, G.I.N.; Cheng, Z.; Ai, S. Electrochemical immunosensor with nanocellulose-Au composite assisted multiple signal amplification for detection of avian leukosis virus subgroup J. *Biosens. Bioelectron.* **2018**, *101*, 110–115. [CrossRef] [PubMed]
78. Wang, H.; Li, X.; Mao, K.; Li, Y.; Du, B.; Zhang, Y.; Wei, Q. Electrochemical immunosensor for α-fetoprotein detection using ferroferric oxide and horseradish peroxidase as signal amplification labels. *Anal. Biochem.* **2014**, *465*, 121–126. [CrossRef] [PubMed]
79. Li, J.; Gao, H.; Chen, Z.; Wei, X.; Yang, C.F. An electrochemical immunosensor for carcinoembryonic antigen enhanced by self-assembled nanogold coatings on magnetic particles. *Anal. Chim. Acta* **2010**, *665*, 98–104. [CrossRef]
80. Tufa, L.T.; Oh, S.; Tran, V.T.; Kim, J.; Jeong, K.J.; Park, T.J.; Kim, H.J.; Lee, J. Electrochemical immunosensor using nanotriplex of graphene quantum dots, Fe_3O_4 and Ag nanoparticles for tuberculosis. *Electrochim. Acta* **2018**, *290*, 369–377. [CrossRef]
81. López-Marzo, A.M.; Hoyos-De-La-Torre, R.; Baldrich, E. NaNO3/NaCl Oxidant and Polyethylene Glycol (PEG) Capped Gold Nanoparticles (AuNPs) as a Novel Green Route for AuNPs Detection in Electrochemical Biosensors. *Anal. Chem.* **2018**, *90*, 4010–4018. [CrossRef] [PubMed]
82. Zhang, S.; Ma, H.; Yan, L.; Cao, W.; Yan, T.; Wei, Q.; Du, B. Copper-doped titanium dioxide nanoparticles as dual-functional labels for fabrication of electrochemical immunosensors. *Biosens. Bioelectron.* **2014**, *59*, 335–341. [CrossRef]
83. Feng, L.N.; Bian, Z.P.; Peng, J.; Jiang, F.; Yang, G.H.; Zhu, Y.D.; Yang, D.; Jiang, L.P.; Zhu, J.J. Ultrasensitive multianalyte electrochemical immunoassay based on metal ion functionalized titanium phosphate nanospheres. *Anal. Chem.* **2012**, *84*, 7810–7815. [CrossRef]
84. Lah, Z.M.A.N.H.; Ahmad, S.A.A.; Zaini, M.S.; Kamarudin, M.A. An Electrochemical Sandwich Immunosensor for the Detection of HER2 using Antibody-Conjugated PbS Quantum Dot as a label. *J. Pharm. Biomed. Anal.* **2019**, *174*, 608–617. [CrossRef]
85. Ehzari, H.; Amiri, M.; Safari, M. Enzyme-free sandwich-type electrochemical immunosensor for highly sensitive prostate specific antigen based on conjugation of quantum dots and antibody on surface of modified glassy carbon electrode with core–shell magnetic metal-organic frameworks. *Talanta* **2020**, *210*, 120641. [CrossRef]
86. Martín-Yerga, D.; González-García, M.B.; Costa-García, A. Electrochemical immunosensor for anti-tissue transglutaminase antibodies based on the in situ detection of quantum dots. *Talanta* **2014**, *130*, 598–602. [CrossRef] [PubMed]
87. Xu, R.; Jiang, Y.; Xia, L.; Zhang, T.; Xu, L.; Zhang, S.; Liu, D.; Song, H. A sensitive photoelectrochemical biosensor for AFP detection based on ZnO inverse opal electrodes with signal amplification of CdS-QDs. *Biosens. Bioelectron.* **2015**, *74*, 411–417. [CrossRef]
88. Zhang, S.; Zhang, C.; Jia, Y.; Zhang, X.; Dong, Y.; Li, X.; Liu, Q.; Li, Y.; Zhao, Z. Sandwich-type electrochemical immunosensor based on Au@Pt DNRs/NH 2 -MoSe 2 NSs nanocomposite as signal amplifiers for the sensitive detection of alpha-fetoprotein. *Bioelectrochemistry* **2019**, *128*, 140–147. [CrossRef]
89. Lou, Y.; He, T.; Jiang, F.; Shi, J.J.; Zhu, J.J. A competitive electrochemical immunosensor for the detection of human interleukin-6 based on the electrically heated carbon electrode and silver nanoparticles functionalized labels. *Talanta* **2014**, *122*, 135–139. [CrossRef]
90. Song, W.; Li, H.; Liu, H.; Wu, Z.; Qiang, W.; Xu, D. Fabrication of streptavidin functionalized silver nanoparticle decorated graphene and its application in disposable electrochemical sensor for immunoglobulin e. *Electrochem. Commun.* **2013**, *31*, 16–19. [CrossRef]
91. Chen, P.; Wang, T.; Zheng, X.; Tian, D.; Xia, F.; Zhou, C. An ultrasensitive electrochemical immunosensor based on C60-modified polyamidoamine dendrimers and Au NPs for co-catalytic silver deposition. *New J. Chem.* **2018**, *42*, 4653–4660. [CrossRef]

92. Chen, S.; Yang, Y.; Li, W.; Song, Y.; Shi, L.; Hong, C. A sandwich-type electrochemical immunosensor using Ag@CeO2-Au as a lable for sensitive detection of carcinoembryonic antigen. *Microchem. J.* **2020**, *159*, 105415. [CrossRef]
93. Liu, H.; Cheng, Y.; Chen, Y.; Xiao, H.; Sui, Y.; Xie, Q.; Liu, R.; Yang, X. Dual-signal sandwich-type electrochemical immunoassay of galectin-3 using methylene blue and gold nanoparticles biolabels. *J. Electroanal. Chem.* **2020**, *861*, 113952. [CrossRef]
94. Sui, Y.; Xu, A.; Jin, X.; Zheng, J.; He, X.; Cheng, Y.; Xie, Q.; Liu, R. In situ enzymatic generation of gold for ultrasensitive amperometric sandwich immunoassay of procalcitonin. *Biosens. Bioelectron.* **2018**, *117*, 422–428. [CrossRef]
95. Qin, X.; Xu, A.; Liu, L.; Deng, W.; Chen, C.; Tan, Y.; Fu, Y.; Xie, Q.; Yao, S. Ultrasensitive electrochemical immunoassay of proteins based on in situ duple amplification of gold nanoparticle biolabel signals. *Chem. Commun.* **2015**, *51*, 8540–8543. [CrossRef]
96. Shamsipur, M.; Emami, M.; Farzin, L.; Saber, R. A sandwich-type electrochemical immunosensor based on in situ silver deposition for determination of serum level of HER2 in breast cancer patients. *Biosens. Bioelectron.* **2018**, *103*, 54–61. [CrossRef]
97. Duangkaew, P.; Wutikhun, T.; Laocharoensuk, R. Triple signal amplification strategy based on size and shape transformation of ultrasmall sub-10 nm gold nanoparticles tag towards sensitivity improvement of electrochemical immunosensors. *Sens. Actuators B Chem.* **2017**, *239*, 430–437. [CrossRef]
98. Wang, C.; Ding, L.; Qu, F. Sensitive electrochemical immunosensor for platelet-derived growth factor in serum with electron transfer mediated by gold nanoparticles initiated silver enhancement. *Measurement* **2013**, *46*, 279–283. [CrossRef]
99. Yang, G.; Lai, Y.; Xiao, Z.; Tang, C.; Deng, Y. Ultrasensitive electrochemical immunosensor of carcinoembryonic antigen based on gold-label silver-stain signal amplification. *Chinese Chem. Lett.* **2018**, *29*, 1857–1860. [CrossRef]
100. Li, Y.; Wang, Y.; Zhang, N.; Fan, D.; Liu, L.; Yan, T.; Yang, X.; Ding, C.; Wei, Q.; Ju, H. Magnetic electrode-based electrochemical immunosensor using amorphous bimetallic sulfides of CoSnSx as signal amplifier for the NTpro BNP detection. *Biosens. Bioelectron.* **2019**, *131*, 250–256. [CrossRef]
101. Tan, X.; Zhang, L.; Deng, X.; Miao, L.; Li, H.; Zheng, G. Redox active molybdophosphate produced by $Cu_3(PO_4)_2$ nanospheres for enhancing enzyme-free electrochemical immunoassay of C-reactive protein. *New J. Chem.* **2017**, *41*, 11867–11871. [CrossRef]
102. Wu, D.; Guo, Z.; Liu, Y.; Guo, A.; Lou, W.; Fan, D.; Wei, Q. Sandwich-type electrochemical immunosensor using dumbbell-like nanoparticles for the determination of gastric cancer biomarker CA72-4. *Talanta* **2015**, *134*, 305–309. [CrossRef]
103. Cui, Z.; Wu, D.; Zhang, Y.; Ma, H.; Li, H.; Du, B.; Wei, Q.; Ju, H. Ultrasensitive electrochemical immunosensors for multiplexed determination using mesoporous platinum nanoparticles as nonenzymatic labels. *Anal. Chim. Acta* **2014**, *807*, 44–50. [CrossRef] [PubMed]
104. Li, N.; Ma, H.; Cao, W.; Wu, D.; Yan, T.; Du, B.; Wei, Q. Highly sensitive electrochemical immunosensor for the detection of alpha fetoprotein based on PdNi nanoparticles and N-doped graphene nanoribbons. *Biosens. Bioelectron.* **2015**, *74*, 786–791. [CrossRef]
105. Yang, Q.; Wang, P.; Ma, E.; Yu, H.; Zhou, K.; Tang, C.; Ren, J.; Li, Y.; Liu, Q.; Dong, Y. A sandwich-type electrochemical immunosensor based on Au@Pd nanodendrite functionalized MoO2 nanosheet for highly sensitive detection of HBsAg. *Bioelectrochemistry* **2021**, *138*, 107713. [CrossRef]
106. Li, Y.; Tian, L.; Liu, L.; Khan, M.S.; Zhao, G.; Fan, D.; Cao, W.; Wei, Q. Dual-responsive electrochemical immunosensor for detection of insulin based on dual-functional zinc silicate spheres-palladium nanoparticles. *Talanta* **2018**, *179*, 420–425. [CrossRef]
107. Kang, J.; Li, Z.; Wang, G. A novel signal amplification strategy electrochemical immunosensor for ultra-sensitive determination of p53 protein. *Bioelectrochemistry* **2021**, *137*, 107647. [CrossRef]
108. Brasiunas, B.; Popov, A.; Ramanavicius, A.; Ramanaviciene, A. Gold nanoparticle based colorimetric sensing strategy for the determination of reducing sugars. *Food Chem.* **2021**, *351*, 129238. [CrossRef]
109. Serafín, V.; Valverde, A.; Martínez-García, G.; Martínez-Periñán, E.; Comba, F.; Garranzo-Asensio, M.; Barderas, R.; Yáñez-Sedeño, P.; Campuzano, S.; Pingarrón, J.M. Graphene quantum dots-functionalized multi-walled carbon nanotubes as nanocarriers in electrochemical immunosensing. Determination of IL-13 receptor A2 in colorectal cells and tumor tissues with different metastatic potential. *Sens. Actuators B Chem.* **2019**, *284*, 711–722. [CrossRef]
110. Serafín, V.; Valverde, A.; Garranzo-Asensio, M.; Barderas, R.; Campuzano, S.; Yáñez-Sedeño, P.; Pingarrón, J.M. Simultaneous amperometric immunosensing of the metastasis-related biomarkers IL-13Rα2 and CDH-17 by using grafted screen-printed electrodes and a composite prepared from quantum dots and carbon nanotubes for signal amplification. *Microchim. Acta* **2019**. [CrossRef]
111. Soelberg, S.D.; Stevens, R.C.; Limaye, A.P.; Furlong, C.E. Surface Plasmon Resonance Detection Using Antibody-Linked Magnetic Nanoparticles for Analyte Capture, Purification, Concentration, and Signal Amplification. *Anal. Chem.* **2009**, *81*, 2357–2363. [CrossRef]
112. Lara, S.; Perez-Potti, A. Applications of Nanomaterials for Immunosensing. *Biosensors* **2018**, *8*, 104. [CrossRef]
113. Ozsoz, M.; Erdem, A.; Kerman, K.; Ozkan, D.; Tugrul, B.; Topcuoglu, N.; Ekren, H.; Taylan, M. Electrochemical Genosensor Based on Colloidal Gold Nanoparticles for the Detection of Factor V Leiden Mutation Using Disposable Pencil Graphite Electrodes. *Anal. Chem.* **2003**, *75*, 2181–2187. [CrossRef] [PubMed]
114. Rasheed, P.A.; Sandhyarani, N. Electrochemical DNA sensors based on the use of gold nanoparticles: A review on recent developments. *Microchim. Acta* **2017**, *184*, 981–1000. [CrossRef]
115. Kokkinos, C.; Economou, A.; Prodromidis, M.I. Electrochemical immunosensors: Critical survey of different architectures and transduction strategies. *TrAC Trends Anal. Chem.* **2016**, *79*, 88–105. [CrossRef]
116. Lim, S.A.; Ahmed, M.U. Electrochemical immunosensors and their recent nanomaterial-based signal amplification strategies: A review. *RSC Adv.* **2016**, *6*, 24995–25014. [CrossRef]

117. Szymanski, M.; Porter, R.; Dep, G.V.; Wang, Y.; Haggett, B.G.D. Silver nanoparticles and magnetic beads with electrochemical measurement as a platform for immunosensing devices. *Phys. Chem. Chem. Phys.* **2011**, *13*, 5383–5387. [CrossRef]
118. Cunningham, J.C.; Scida, K.; Kogan, M.R.; Wang, B.; Ellington, A.D.; Crooks, R.M. Paper diagnostic device for quantitative electrochemical detection of ricin at picomolar levels. *Lab Chip* **2015**, *15*, 3707–3715. [CrossRef]
119. Ting, B.P.; Zhang, J.; Khan, M.; Yang, Y.Y.; Ying, J.Y. The solid-state Ag/AgCl process as a highly sensitive detection mechanism for an electrochemical immunosensor. *Chem. Commun.* **2009**, *0*, 6231–6233. [CrossRef]
120. Iglesias-Mayor, A.; Amor-Gutiérrez, O.; Costa-García, A.; de la Escosura-Muñiz, A. Nanoparticles as emerging labels in electrochemical immunosensors. *Sensors* **2019**, *19*, 5137. [CrossRef]
121. Ramanaviciene, A.; Voronovic, J.; Popov, A.; Drevinskas, R.; Kausaite-Minkstimiene, A.; Ramanavicius, A. Investigation of biocatalytic enlargement of gold nanoparticles using dynamic light scattering and atomic force microscopy. *Colloids Surf. A Physicochem. Eng. Asp.* **2016**, *510*, 183–189. [CrossRef]
122. Jiang, P.; Wang, Y.; Zhao, L.; Ji, C.; Chen, D.; Nie, L. Applications of gold nanoparticles in non-optical biosensors. *Nanomaterials* **2018**, *8*, 977. [CrossRef]
123. Prodromidis, M.I.; Economou, A. New Trends in Antibody-Based Electrochemical Biosensors. *Compr. Anal. Chem.* **2017**, *77*, 55–100. [CrossRef]
124. Cadkova, M.; Kovarova, A.; Dvorakova, V.; Metelka, R.; Bilkova, Z.; Korecka, L. Electrochemical quantum dots-based magneto-immunoassay for detection of HE4 protein on metal film-modified screen-printed carbon electrodes. *Talanta* **2018**, *182*, 111–115. [CrossRef]
125. Zhong, M.; Yang, L.; Yang, H.; Cheng, C.; Deng, W.; Tan, Y.; Xie, Q.; Yao, S. An electrochemical immunobiosensor for ultrasensitive detection of Escherichia coli O157:H7 using CdS quantum dots-encapsulated metal-organic frameworks as signal-amplifying tags. *Biosens. Bioelectron.* **2019**, *126*, 493–500. [CrossRef]
126. Zupančič, U.; Rainbow, J.; Flynn, C.; Aidoo-Brown, J.; Estrela, P.; Moschou, D. *Strategies for Multiplexed Electrochemical Sensor Development*; Springer: Singapore, 2021; pp. 63–93.
127. Tang, D.; Hou, L.; Niessner, R.; Xu, M.; Gao, Z.; Knopp, D. Multiplexed electrochemical immunoassay of biomarkers using metal sulfide quantum dot nanolabels and trifunctionalized magnetic beads. *Biosens. Bioelectron.* **2013**, *46*, 37–43. [CrossRef]
128. Fan, G.C.; Zhu, H.; Du, D.; Zhang, J.R.; Zhu, J.J.; Lin, Y. Enhanced Photoelectrochemical Immunosensing Platform Based on CdSeTe@CdS:Mn Core-Shell Quantum Dots-Sensitized TiO_2 Amplified by CuS Nanocrystals Conjugated Signal Antibodies. *Anal. Chem.* **2016**, *88*, 3392–3399. [CrossRef] [PubMed]
129. Zhao, W.W.; Wang, J.; Xu, J.J.; Chen, H.Y. Energy transfer between CdS quantum dots and Au nanoparticles in photoelectrochemical detection. *Chem. Commun.* **2011**, *47*, 10990–10992. [CrossRef]
130. Dong, Y.X.; Cao, J.T.; Liu, Y.M.; Ma, S.H. A novel immunosensing platform for highly sensitive prostate specific antigen detection based on dual-quenching of photocurrent from CdSe sensitized TiO2 electrode by gold nanoparticles decorated polydopamine nanospheres. *Biosens. Bioelectron.* **2017**, *91*, 246–252. [CrossRef] [PubMed]
131. Guo, A.; Wu, D.; Ma, H.; Zhang, Y.; Li, H.; Du, B.; Wei, Q. An ultrasensitive enzyme-free electrochemical immunosensor for CA125 using Au@Pd core–shell nanoparticles as labels and platforms for signal amplification. *J. Mater. Chem. B* **2013**, *1*, 4052–4058. [CrossRef]
132. Zhao, L.; Li, S.; He, J.; Tian, G.; Wei, Q.; Li, H. Enzyme-free electrochemical immunosensor configured with Au–Pd nanocrystals and N-doped graphene sheets for sensitive detection of AFP. *Biosens. Bioelectron.* **2013**, *49*, 222–225. [CrossRef]
133. Dong, S.; Wang, S.; Gyimah, E.; Zhu, N.; Wang, K.; Wu, X.; Zhang, Z. A novel electrochemical immunosensor based on catalase functionalized AuNPs-loaded self-assembled polymer nanospheres for ultrasensitive detection of tetrabromobisphenol A bis(2-hydroxyethyl) ether. *Anal. Chim. Acta* **2019**, *1048*, 50–57. [CrossRef]
134. Wu, L.; Chen, J.; Du, D.; Ju, H. Electrochemical immunoassay for CA125 based on cellulose acetate stabilized antigen/colloidal gold nanoparticles membrane. *Electrochim. Acta* **2006**, *51*, 1208–1214. [CrossRef]
135. Wu, L.; Yan, F.; Ju, H. An amperometric immunosensor for separation-free immunoassay of CA125 based on its covalent immobilization coupled with thionine on carbon nanofiber. *J. Immunol. Methods* **2007**, *322*, 12–19. [CrossRef]
136. Gu, L.; Luo, N.; Miley, G.H. Cathode electrocatalyst selection and deposition for a direct borohydride/hydrogen peroxide fuel cell. *J. Power Sources* **2007**, *173*, 77–85. [CrossRef]
137. Yuan, Y.; Li, S.; Xue, Y.; Liang, J.; Cui, L.; Li, Q.; Zhou, S.; Huang, Y.; Li, G.; Zhao, Y. A Fe_3O_4@Au-basedpseudo-homogeneous electrochemical immunosensor for AFP measurement using AFP antibody-GNPs-HRP as detection probe. *Anal. Biochem.* **2017**, *534*, 56–63. [CrossRef]
138. Li, Y.; Yuan, R.; Chai, Y.; Zhuo, Y.; Su, H.; Zhang, Y. Horseradish peroxidase-loaded nanospheres attached to hollow gold nanoparticles as signal enhancers in an ultrasensitive immunoassay for alpha-fetoprotein. *Microchim. Acta* **2014**, *181*, 679–685. [CrossRef]

Paper 6

ZnO nanostructures: A promising frontier in immunosensor development

B. Brasiunas, A. Popov, V. Lisyte, A. Kausaite-Minkstimiene, A. Ramanaviciene

Biosensors and Bioelectronics, 2024, 246, 115848
doi.org/10.1016/j.bios.2023.115848

Biosensors and Bioelectronics 246 (2024) 115848

Contents lists available at ScienceDirect

Biosensors and Bioelectronics

journal homepage: www.elsevier.com/locate/bios

ZnO nanostructures: A promising frontier in immunosensor development

Benediktas Brasiunas [a], Anton Popov [a], Viktorija Lisyte [a], Asta Kausaite-Minkstimiene [a], Almira Ramanaviciene [a,*]

[a] *NanoTechnas - Nanotechnology and Materials Science Center, Faculty of Chemistry and Geosciences, Vilnius University, Naugarduko St. 24, LT 03225, Vilnius, Lithuania*

ARTICLE INFO

Keywords:
ZnO
Semiconducting metal oxides
Optical immunosensor
Electrochemical immunosensor
ZnO immobilization
Protein immobilization

ABSTRACT

This review addresses the design of immunosensors, which employ ZnO nanostructures. Various methods of modifying ZnO nanostructures with antibodies or antigens are discussed, including covalent and non-covalent approaches and cross-linking techniques. Immunosensors based on different properties of ZnO nanomaterials are described and compared. This article provides a comprehensive review of electrochemical immunosensors based on ZnO nanostructures and various detection techniques, including cyclic voltammetry (CV), differential pulse voltammetry (DPV), photoelectrochemical (PEC) detection, electrochemical impedance spectroscopy (EIS), and other electrochemical methods. In addition, this review article examines the application of optical detection techniques, including photoluminescence (PL) and electrochemiluminescence (ECL), in the development of immunosensors based on ZnO nanostructures.

1. Introduction

Semiconducting metal oxides are non-stoichiometric compounds with strong ionic bonds between positive metal ions and negative oxygen ions. These materials exhibit various desirable properties such as low cost, excellent chemical and thermal stability, the ability to tune energy band gaps based on the materials used, high dielectric constants as well as unique optical properties (Liustrovaite et al., 2023; Zhang and Zhou, 2020). For example, indium tin oxide (ITO), a doped n-type semiconductor, is electrically conductive while at the same time has a high transmittance in the visible range, which makes it possible to create transparent electrodes (Farhan et al., 2013). Furthermore, semiconducting metal oxides can be fabricated in a variety of nanostructured forms or different crystalline structures, allowing control over the final material properties (Afzal et al., 2012; Zhang and Zhou, 2020). This variety facilitates extensive use of semiconducting metal oxides in numerous fields, one of the most common of which is gas sensors (Wang et al., 2010).

One of the most widely used semiconductor metal oxide is ZnO. This material is very versatile and exhibits a wide range of useful properties. With a density of 5.6 g cm^{-1}, among the group II–VI semiconductors, it is the hardest at about 5 on the Mohs scale (Singh et al., 2007). Due to the lack of a center of symmetry in hexagonal wurtzite crystalline structure (*C6mc*, a = 0.3296 nm, c = 0.52065 nm) and the presence of significant electromechanical coupling, ZnO exhibits robust piezoelectric and pyroelectric characteristics, making it suitable for applications such as production of mechanical actuators and piezoelectric sensors (Molarius et al., 2003; Wang, 2004a). With a band gap of 3.37 eV at room temperature and excitation energy of 60 meV, ZnO also exhibits luminescent properties (Özgür et al., 2005). At an excitation wavelength of 325 nm, the PL spectrum of ZnO contains two most notable emission bands, one in the UV region close to the band edge, as well as deep-level emission in the visible light region (Liustrovaite et al., 2023). Different emission bands can also be observed based on the defects in the ZnO crystal structure (Rai et al., 2022). In addition, information regarding the amount of defects present in ZnO samples can be obtained by analyzing the intensity ratio between the UV and visible peaks (Serrano et al., 2017). Furthermore, ZnO thin films are highly transparent in the visible light region (Janotti and Van de Walle, 2009; Lima et al., 2007; Natsume and Sakata, 2003). ZnO is an n-type semiconductor with electrical conductivity arising mainly from intrinsic defects such as interstitial zinc atoms and oxygen vacancies. Electrical conductivity can be improved by doping with various group III or group VII elements (Jeong et al., 2006). Doping levels of up to $n = 10^{21}$ cm^{-3} can be achieved (Klingshirn et al., 2010). The electrical conductivity can also be adjusted by annealing, depending on the atmosphere and annealing temperature (Natsume and Sakata, 2003). The electrical conductivity of the ZnO thin film is also sensitive to the presence of adsorbed species,

---

* Corresponding author.
E-mail address: almira.ramanaviciene@chf.vu.lt (A. Ramanaviciene).

https://doi.org/10.1016/j.bios.2023.115848
Received 1 August 2023; Received in revised form 1 November 2023; Accepted 15 November 2023
Available online 19 November 2023
0956-5663/

which facilitates the development of conductivity-based gas sensors (Chatterjee et al., 1999; Si et al., 2006; Wan et al., 2004). Doping ZnO with magnetic properties exhibiting metal ions like Mn, Fe, Co, V, can make ZnO semimagnetic exhibiting ferromagnetism up to room temperature (Klingshirn, 2007). Another property of ZnO is photocurrent generation when exposed to UV light, as well as visible light if additional materials are employed (Han et al., 2017; Sun et al., 2014a; Wang et al., 2011). In addition, ZnO exhibits excellent photocatalytic properties, facilitating the option of using this material for water treatment (Bizarro, 2010; Hariharan, 2006; Kansal et al., 2008; Wang et al., 2011; Xiao and Ouyang, 2009). Electroluminescence is possible when voltage is applied to ZnO nanostructures (Lima et al., 2007; Neshataeva et al., 2009; Wong et al., 2008). ZnO has also found extensive use in biosensing and biomedical applications due to the high biocompatibility and antimicrobial properties (Kumar, et al., 2017; Nair et al., 2009; Padmavathy and Vijayaraghavan, 2008; Rekha et al., 2010; Zhang et al., 2008). Isoelectric point (IEP) and the point of zero charge for ZnO nanostructures varies in the range of 8.8–9.5 (Bahnemann et al., 1987; Degen and Kosec, 2000; Huang et al., 2005; Kittaka and Morimoto, 1980; Mohd Omar et al., 2014; Ray et al., 1978; Venu Rajendran et al., 2022; Zyoud et al., 2019, 2023). Finally, these various properties can be tuned and improved as required by synthesizing ZnO in nanostructured form or as a composite with other materials. Many different methods of synthesizing ZnO can be used to produce ZnO in the form of nanorods, nanowires, nanobelts, nanocombs, nanosaws, nanosprings, nanospirals, and various other shapes (Djurišić et al., 2010; Kołodziejczak-Radzimska and Jesionowski, 2014; Wang, 2004a, 2004b, 2009).

A biosensor is an analytical device designed to detect a desired analyte by measuring a signal, which is proportional to the analyte concentration (Ramanaviciene et al., 2012; Ramanaviciene and Ramanavicius, 2004; Sakalauskiene et al., 2022). In the biosensor design, the recognition of the analyte is performed with various biomolecules, such as enzymes, antigens, antibodies, DNA, or cells. A transducer that converts a biorecognition event into a measurable signal is also needed. When the biorecognition element is antibodies or antigens, the biosensor is called an immunosensor (Ramanaviciene et al., 2022). In immunosensors, the analyte biorecognition is based on immunocomplex formation between antibodies and antigens. The immune complex formation is based on multiple non-covalent bonds forming between the complementary sites of the antibody and the antigen. Immunosensing strategies can be of different types, which can be divided into label-free and labelled. In the case of label-free detection, the analyte is detected directly after the immune complex formation. The sensitivity of such strategies is limited because the formation of immune complexes not always has a high effect on the overall electrochemical or optical properties of the immunsensor, especially at low analyte concentration. On the other hand, label-based detection strategies are designed to detect the absence or presence of the label and are generally more sensitive, but they require the use of either labelled detection or secondary antibodies (Popov et al., 2021).

Combining nanomaterials into immunosensor design can help to significantly improve the sensitivity, stability, and other analytical sensor parameters. This is especially important in the case of label-free immunosensor design, where the incorporation of nanomaterials is critical to achieve sufficient sensitivity. Nanomaterials being employed in the design of immunosensors can be divided into the 3 main groups (de la Escosura-Muñiz et al., 2010; Lara and Perez-Potti, 2018; Zhang et al., 2019). Carbon-based nanomaterials such as graphene oxide or carbon nanotubes, given their superior electrical properties, can be employed in the design of both electrochemical and optical sensors, however, synthesizing such nanomaterials is usually more expensive, and obtaining homogeneous structures is more difficult. (Kaur et al., 2019; Sharma et al., 2020). Another group consists of metal-based nanomaterials, which can be synthesized in a range of shapes and sizes. For example, due to superb electrical properties and unique plasmonic effects noble metal nanoparticles can be used to enhance electrochemical and optical sensor response (Malekzad et al., 2017). Furthermore, additional ways to immobilize antibodies or antigens on the sensor surface can be explored using such nanomaterials. For instance, thiol functional group containing self-assembled monolayers can be formed on gold surfaces (Kausaite-Minkstimiene et al., 2010). The third group of nanomaterials are semiconductor structures like quantum dots, silicon-based nanoparticles, and metal oxides. As mentioned beforehand, semiconducting nanomaterials, including ZnO, are highly suitable for the development of optical sensors and can be employed for electrochemical sensor creation. Other nanomaterial groups like metal-organic frameworks, and polymeric nanostructures are less commonly used. These nanomaterials usually exhibit limited electrical or optical properties, or might not be stable for a long period of time (Liu et al., 2018; Zhang et al., 2021).

ZnO being an affordable semiconducting metal oxide is a surprisingly versatile material for the design of immunosensors. It can be produced in the range of shapes and sizes and due to the wide variety of material properties, ZnO nanomaterials can be adopted for the design of voltammetric, potentiometric, electrochemical impedance spectroscopy (EIS), photoelectrochemical (PEC), electrochemiluminescence (ECL), and photoluminescence (PL) based immunosensors. The nanostructures of ZnO can be used to modify the underlying immunosensor surface or to label antibodies. In addition, ZnO nanostructures can be combined with other nanomaterials in order to further enhance analytical sensor parameters. As such, the purpose of this article is to review, categorize, and compare the immunosensors that employ ZnO nanostructures in their design.

2. Modification of ZnO with biomolecules

Over the years, many comprehensive biomolecule immobilization methods have been developed and applied for the modification of various nanomaterials. The development of precise immunosensors based on different signal transducers with surface-functionalized metal oxide nanostructures is a complex process which depends on different surface preparation steps and selected sensing techniques. The proper immobilization of antibodies on solid-liquid interfaces is a critical step in the development of well-operating immunosensors (Baniukevic et al., 2013a, 2013b; Kausaite-Minkstimiene et al., 2010; Makaraviciute and Ramanaviciene, 2013). Many different methods have been successfully applied for the functionalization of ZnO nanostructures by antibodies or antigens. However, the selected method for ZnO nanostructure biofunctionalization must not suppress desired material properties such as PL, conductivity, catalytic efficiency, transparency in the visible range, plasmonic properties, or biocompatibility. Meanwhile, it is equally important not to disturb the conformation and biological activity of biomolecules after ZnO nanostructure biofunctionalization by the selected immobilization strategy. The type, amount, and the orientation of antibodies on the sensing surface are key parameters for the sensitive detection of the analyte.

The main methods used for ZnO nanostructure modification with biomolecules and the development of the surface serving to capture targeted analyte are physical and electrostatic adsorption, as well as covalent immobilization. For this purpose, a high IEP ~8.8–9.5 of ZnO nanostructures can be successfully used or the surface of nanostructures could be pre-modified with required functional groups using organic compounds, mainly carboxylic acids, thiols, and amines, facilitating the attachment of biomolecules. When ZnO nanostructures are immobilized on the transducer surface, the functionalization ensures nanostructure stabilization and reduces the chance for agglomeration during other immunosensor preparation steps. This is especially important when performing measurements in aqueous media where agglomeration can significantly affect the electric and luminescent properties of ZnO. In the next sections, the most common ZnO biofunctionalization methods are described.

2.1. Adsorption on ZnO nanostructures

The simplest method for ZnO nanostructure biofunctionalization is adsorption due to the electrostatic interaction between the positively charged ZnO and negatively charged biomolecules, such as DNA (Ma et al., 2016), bovine serum albumin (BSA), or fibrinogen (Wang et al., 2015), at physiological pH of 7.4. Hydrophobic interaction also plays an important role in the immobilization of some proteins i.e., fibrinogen exhibits slightly higher affinity to hydrophobic surfaces than BSA (Wang et al., 2015). Usually IEP of IgG class antibodies is in the range from 6.1 to 8.5 (7.3 ± 1.2) (Isoelectric point of IgG class antibodies), thus they can also be adsorbed on ZnO nanostructures. For example, monoclonal antibodies specific to interferon gamma (IFN-γ) were adsorbed on suspended ZnO nanoparticles. Biofunctionalized ZnO nanoparticles were drop casted on the surface of the graphite electrode, and Nafion was used to hinder the desorption of antibodies. The immunosensor was used for the EIS determination of IFN-γ and tuberculosis diagnosis (Wang et al., 2017). In another case, monoclonal antibodies specific for cortisol were electrostatically adsorbed on ZnO nanorods (ZnO NRs) and two-dimensional ZnO nanoflakes creating label-free, highly sensitive, and selective electrochemical immunosensors for the determination of cortisol (Vabbina et al., 2015). Furthermore, rabbit IgG antibodies together with BSA were immobilized on the nanostructured ZnO film, which was formed on the ITO electrode, and the developed immunosensor was applied for the EIS detection of ochratoxin A (OTA). It was determined that antibodies bind to Zn–O–Zn inorganic network by the hydrogen bonding and electrostatic interactions (Ansari et al., 2010). Another EIS immunosensor was developed for the fast detection of Severe acute respiratory syndrome coronavirus 2 (SARS-CoV-2) spike protein-specific antibodies in convalescent and vaccinated patients. In this case, the recombinant trimeric spike protein was physically adsorbed on ZnO NR-modified fluorine-doped tin oxide substrate due to electrostatic interactions (Nunez et al., 2023b). Moreover, antibodies that specifically recognize carbohydrate antigen 19–9 (CA19-9) were immobilized on ZnO quantum dots (ZnO QDs) by electrostatic attraction. The obtained conjugate was successfully applied as an electrochemical and fluorescent label in a sandwich-type immunoassay to sensitively detect CA19-9, which is a preferred maker for pancreatic cancer (Gu et al., 2011). Antibodies specific to grapevine virus A-type (GVA) proteins from the serum sample were physically adsorbed of ZnO NRs present on silicon surface. ZnO NRs modified in this way were applied for the detection of GVA proteins registering changes in PL intensity (Tereshchenko et al., 2020). The same specific antibody immobilization method was performed with different ZnO NRs and PL-based immunosensors were used for the detection of *Salmonella antigens* (Viter et al., 2014), human chorionic gonadotropin (hCG) (Rodrigues et al., 2020), and CD5 biomarker present on leukemic cells (T-lymphoblasts cell line MOLT-4) (Tamashevski et al., 2020).

2.2. Covalent cross-linking of adsorbed biomolecules by homobifunctional cross-linkers

Glutaraldehyde (GA) is a homobifunctional cross-linker containing an aldehyde residue at both ends of its 5-carbon chain. Thus, a second method for the immobilization is a covalent cross-linking of antibodies or antigens, which are adsorbed on ZnO nanostructures. Both aldehyde functional groups of GA can interact with primary amine groups of adsorbed biomolecules creating a mesh-type structure in turn reducing the chance of desorption. An EIS immunosensor for the determination of a new pancreatic cancer biomarker UL16 binding protein 2 (ULBP2) was developed using ZnO nanoparticles modified by antibodies. For this purpose, a mixture of ZnO nanoparticles and GA (2.5%) was dropped on the screen-printed carbon electrode and then antibodies specific to ULBP2 were added. Covalent cross-linking was performed overnight in the dark at 4 °C (Yang et al., 2020). In another example, the sandwich luminol ECL immunosensor for the detection of carcinoembryonic antigen (CEA) was developed using ZnO nanoparticles and glucose oxidase decorated graphene labelled antibody specific to CEA (detection antibody). For the immunosensing probe preparation, antibody specific to CEA and GA (0.5%) solution were added to the suspension of ZnO nanoparticles/graphene nanocomposite and allowed to react while slightly stirring for 6 h at 4 °C. Afterwards the biofunctionalized nanocomposite was removed by centrifugation. Based on the information provided in the publication, detection antibodies were adsorbed on the ZnO nanoparticle/graphene nanocomposite and cross-linked by GA. ECL of luminol was enhanced by the presence of ZnO nanoparticles (Cheng et al., 2012). Moreover, for the detection of CD19 biomarker present on cancer cells (B-lymphoblastoid cell line IM9), fluorescein isothiocyanate (FITC)-conjugated mouse monoclonal antibodies specific to human CD19 were adsorbed on ZnO NRs and secured using 1% solution of paraformaldehyde (Tamashevski et al., 2019). Potentiometric immunosensors based on ZnO nanotubes and ZnO NRs for the determination of D-dimer, a biomarker detectable in patients with deep venous thrombosis disorders, were developed. The electrode modified with ZnO nanotubes decorated with silver nanoparticles (AgNPs) was immersed in mouse antibody specific to D-dimer and GA solution for 3 min and then dried at room temperature for 3 h (Ibupoto et al., 2013). The same antibody immobilization protocol was applied for ZnO NRs modified by a lipid layer (Ibupoto et al., 2014).

2.3. Covalent linking of biomolecules to ZnO nanoparticles or nanocomposites via self-assembled monolayers

When an additional self-assembled monolayer (SAM) is formed on ZnO nanostructures or it's nanocomposites, GA or a mixture of N-(3-(dimethylamino)propyl)-N-ethylcarbodiimide hydrochloride (EDC) and N-hydroxysuccinimide (NHS) can be used to covalently immobilize biomolecules on the modified nanostructure surface. For example, arrays of nanocomposite (nanohybrids) consisting of ZnO NRs and gold nanoparticles (AuNPs) modified by specific antibodies were used for the direct electrochemical detection of ovarian 0. AuNPs and ZnO NRs created favorable conditions (a higher surface area) for efficient loading of specific antibodies. For this purpose, nanocomposite, mainly AuNPs, was modified by the self-assembled monolayer via thiol group and gold surface interaction. Primary amine groups present on the SAM were then activated with GA and dried in air. After that CA125 specific antibodies were covalently linked to the nanocomposite via the covalent bond between amino groups of the antibody and the aldehyde residue present on the surface of the nanocomposite (Gasparotto et al., 2017). Another research paper describes an electrochemical immunosensor based on the electrode modified by ZnO NRs designed for the early diagnosis of Zika infection. ZnO NRs were modified by antibodies specific to Zika non-structural protein 1 (ZIKV-NS1, antigen). In this case, specific monoclonal antibodies were immobilized on the surface of ZnO nanostructures via the SAM with amine functional groups and the GA (2.5%) solution (Faria and Mazon, 2019). Furthermore, a sandwich-type ECL immunosensor for the detection of prostate specific antigen (PSA) was developed based on ZnO NRs-L-cysteine-luminol nanocomposites and the biotin-streptavidin system for the amplification of the analytical signal. ZnO NRs were modified by L-cysteine and then a mixture of EDC and NHS was used for the activation of carboxyl functional groups followed by the covalent immobilization of luminol. Then GA solution (5%) was added and the covalent immobilization of the detection antibodies specific to PSA was performed overnight at 4 °C. In this case, ZnO NRs served two functions. Firstly, it acted as a nanocarrier that increased the amount of secondary antibodies and luminol molecules. Secondly, it enhanced the ECL signal by promoting the H_2O_2 decomposition, further increasing ECL intensity (Zhang et al., 2020). In the last example, a near-infrared light PEC immunosensor based on Au-paper electrode and functionalized ZnO NRs was developed for CEA detection. 4-Aminothiophenol was used for the functionalization of the electrode surface by amine functional groups. Then the tetra-carboxyl naphthalocyanine zinc

(ZnNc-COOH) containing EDC was used for the sensitization of ZnO NRs. The EDC/NHS coupling reaction was applied for the surface activation and antibodies specific to the CEA were immobilized (Sun et al., 2014a).

2.4. *Covalent linking of biomolecules to ZnO nanoparticles or nanocomposites via organo-functional alkoxysilanes*

Silanization can also be performed on ZnO nanostructures usually providing amino or carboxyl functional groups which can be used to covalently immobilize biomolecules using GA or EDC and NHS chemistry. For instance, label-free electrochemical biosensors based on ZnO nanoparticles and ZnO NRs were developed for the detection of the matrix metalloproteinase 9 (MMP-9). (3-Aminopropyl)triethoxysilane (APTES) was attached to hydroxyl groups present on ZnO nanomaterials prepared in slightly alkaline solutions. Then, the electrode containing ZnO nanoparticles functionalized with amine groups was immersed in a GA solution (2.5%) to convert surface amine groups to aldehyde groups. The mouse monoclonal antibodies specific to the matrix metalloproteinase 9 (MMP-9) were covalently immobilized on the electrode surface due to the reaction of amine groups present in antibody structure with aldehyde groups present on the ZnO nanostructures (Shabani et al., 2020). Furthermore, APTES was also used for the functionalization of nanotextured ZnO thin film. Antibodies specific to the cardiac biomarker troponin-T were covalently immobilized. For this purpose, carboxyl functional groups present in the antibody structure were activated using EDC/NHS mixture and the formed NHS-esters could then bind to amine groups of APTES (Munje et al., 2015). Moreover, the nanogapped EIS sensor with ZnO doped gold surface was fabricated for the 16 kDa heat shock protein (HSP) detection. It is an immuno-dominant antigen used in the diagnosis of infectious *Mycobacterium tuberculosis* causing tuberculosis. In this case, the surface after the modification by APTES was reacted with a GA solution (2.5%) and then antibodies specific to HSP were covalently immobilized (Gopinath et al., 2016). Furthermore, ECL immunosensor for the detection of carbohydrate antigen 15–3 (CA15-3), one of the main breast cancer-related specific biomarkers, employing polyamidoamine (PAMAM)-functionalized ZnO NRs as carriers was developed. APTES was used for the surface modification by amine functional groups while PAMAM dendrimers were employed for the covalent co-immobilization of luminol and CA15-3 detection antibodies via carboxyl functional groups using EDC/NHS as coupling agents. PAMAM dendrimers were additionally activated by EDC/NHS, and luminol together with specific antibodies were covalently bound (Jiang et al., 2015). For the last example, the PL-based immunosensor for aflatoxin B1 (AFB1) detection was developed using a microfluidic device with integrated polyacrylonitrile (PAN)/ZnO nanofibers. For this purpose, nanofibers were modified by APTES, and reacted with GA followed by the covalent immobilization of monoclonal antibodies specific to AFB1 (Myndrul et al., 2021).

2.5. *Site directed immobilization of antibodies using bacterial protein A*

Antibodies can also be immobilized with proper orientation using a bacterial protein A. After the protein A is immobilized on the surface, it can bind to the Fc part of the antibody ensuring that antigen binding sites are orientated towards the liquid interface. For instance, the PL immunosensor for the determination of OTA was developed based on ZnO NRs functionalized by antibodies in a site-directed manner. For this purpose, ZnO NRs were modified by APTES, activated with GA solution (10%) at room temperature for 20 min, and then protein A was covalently immobilized. Furthermore, antibodies specific to OTA were attached to the protein A via the affinity interaction in a site-directed orientation (Viter et al., 2018).

2.6. *Summary of methods used to immobilize biomolecules on ZnO*

A review of studies of ZnO biofunctionalization methods shows that the most commonly used methods do not ensure the site directed antibody orientation on the surface. Simple physical and electrostatic adsorption is often used since the high IEP of ZnO can help to somewhat alleviate the problem of biomolecule desorption from the surface during further immunosensor design steps and analyte detection. Glutaraldehyde can be employed to cross-link adsorbed biomolecules to further stabilize the surface and prevent desorption, however the activity of antibodies can be negatively affected. In order to perform covalent biomolecule immobilization extra linkers need to be used, for example SAMs or silanes. To facilitate the covalent immobilization using linkers, GA is used as a co-linker for materials with amino functional groups, while EDC/NHS chemistry is used for carboxyl functional groups. Nevertheless, the application of ZnO nanostructures not only enhances the surface area for antibody immobilization, but can also ensure better spatial orientation, resulting in better availability of antibody binding sites for the biomarker detection. Although most of previously mentioned biomolecule immobilization methods do not ensure the site directed immobilization, these methods combined with ZnO nanostructure-based signal amplification still lead to a design of sufficiently sensitive electrochemical and optical immunosensors. The schematic showing the most often used ZnO biofunctionalization methods is provided in Fig. 1.

3. Application of ZnO in immunosensor design

ZnO nanostructures can be employed in various ways for the design of electrochemical and optical immunosensors. ZnO nanostructures are being used to modify the surfaces of other materials to achieve the desired properties or are employed as labels for the detection antibodies. In some cases, the properties of ZnO such as PL are used as a basis for immunosensor design, however, ZnO nanostructures can also be used to enhance the analytical signals, due to improvements in electrochemical characteristics, increased surface area, or the high IEP of the material.

In order to produce surfaces modified with ZnO nanostructures various immobilization methods can be employed. One of the common

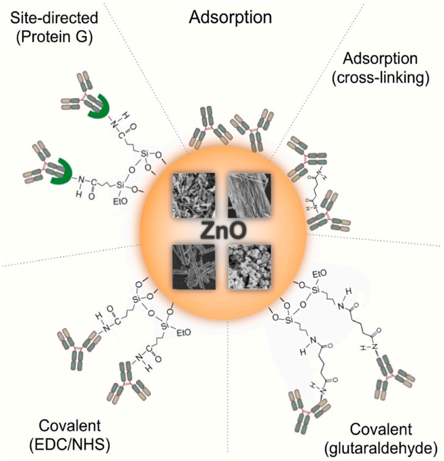

Fig. 1. Commonly used biomolecules immobilization methods on various ZnO nanostructures.

methods is the hydrothermal growth of ZnO onto the underlying electrode surface (Faria and Mazon, 2019; Gasparotto et al., 2017; Ibupoto et al., 2013, 2014; Nunez et al., 2023a; Shabani et al., 2020; Sun et al., 2015a; Zhou et al., 2023a, 2023b). This method provides good contact between the electrode and the grown ZnO, which is usually of nanorod morphology. Other ZnO immobilization methods are based on screen-printing (Khan et al., 2021), spin coating (Mutlaq et al., 2021), electrodeposition (Patella et al., 2022; Saxena et al., 2022), and sonochemical immobilization involving ultrasound (Alam et al., 2019; Vabbina et al., 2015). In addition, simple drop casting of ZnO suspension with water (Fang et al., 2017), phosphate buffered saline solution (Dong et al., 2019), N,N-dimethylformamide (Paul et al., 2017), Nafion (Liustrovaite et al., 2023), and chitosan (Lu et al., 2008; Wang et al., 2006; Zhan et al., 2021) is reported. Various analytical detection methods can be used for the development of ZnO nanostructure based immunosensors. The detection can also be label-free or employ additional labelled biomolecules. The main detection methods for ZnO based immunosensors are presented in Fig. 2.

3.1. *Electrochemical detection methods*

Electrochemical immunosensors employing ZnO nanostructures can be divided into two main groups, labelled and label-free. ZnO nanostructures can be employed as a label for detection antibodies, however, much more often ZnO is being used to modify the electrode surface. Electrode modifications with ZnO due to the semiconductor nature and resulting lower electrical conductivity can hinder the sensitivity of analytical systems which employ popular techniques like CV or DPV, where the oxidation or reduction current of the redox probe is measured. On the other hand, the semiconductor nature of ZnO does not necessarily negatively affect analytical systems that employ electrochemical techniques like EIS, potentiometry or conductometry.

3.1.1. *Label-free electrochemical immunosensors*

One type of label-free electrochemical immunosensors employs additional redox probes which help to assess the changes that happen at the surface of the electrode during immunosensor design. The formation of the immune complex, which happens during the detection of the analyte, results in the hindrance of the redox probe diffusion and electron transfer rate. The most common redox probe, used for label-free electrochemical immunosensors containing ZnO, is $[Fe(CN)_6]^{-3/-4}$. For this immunosensor type, an increase in the analyte concentration results in the decrease of registered oxidation/reduction current of the redox probe. Various electrochemical detection techniques like chronoamperometry, CV, and DPV can be used. However, as previously mentioned, due to the semiconducting nature of ZnO, the use of this material can reduce the electrical conductivity and decrease the observed oxidation/reduction current of the redox probe after the immobilization of ZnO on the electrode (Alam et al., 2019; Gasparotto et al., 2017; Paul et al., 2017; Shabani et al., 2020; Vabbina et al., 2015). Although, if the electrical conductivity or kinetics of electron transfer for the underlying electrode are poor to begin with, the immobilization of ZnO on the electrode surface can improve these characteristics (Garg et al., 2023; Liustrovaite et al., 2023). In addition, shortcomings of ZnO can be alleviated when ZnO is used in specific nanostructure form (Zhan et al., 2021), or by employing ZnO nanocomposites with other materials which have superior electrical characteristics like porous carbon matrix (Dong et al., 2019), carbon nanotubes (CNTs) (Paul et al., 2017), copper (Martins et al., 2021), copper oxide (Khan et al., 2021), graphitic carbon nitride (Saxena et al., 2022). Furthermore, the research by Vabbina et al. (2015) indicated that the developed electrochemical immunosensor exhibited sharp and distinct $[Fe(CN)_6]^{-3/-4}$ redox probe oxidation/reduction peaks indicating a much better surface controlled process when 2D ZnO nanoflakes were used compared with 1D ZnO NRs. Schematics of a typical label-free electrochemical immunosensor employing electrodes modified with ZnO, reported by Dong et al. (2019) and Liustrovaite et al. (2023), are presented in Fig. 3. In the work by Dong et al. a hybrid ZnO/porous carbon matrix nanomaterial was synthesized and used to modify the carbon paste electrode surface. The high surface area and excellent electrical conductivity of this material allowed for almost

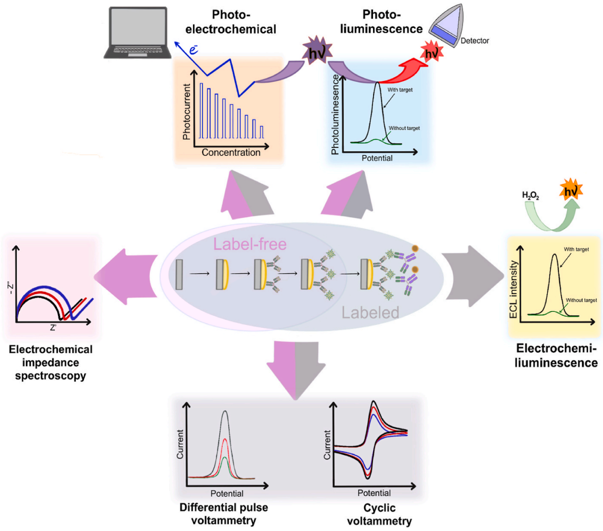

Fig. 2. Commonly used detection methods in the design of ZnO based immunosensors.

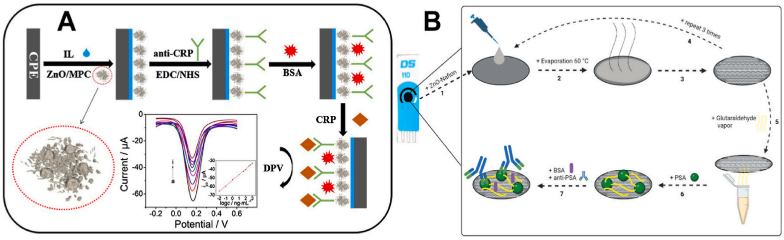

Fig. 3. Schematic diagram of the preparation process of a label-free immunosensor used to detect CRP (**A**) (Dong et al., 2019; Copyright, 2018; Elsevier) and anti-PSA (**B**) (Liustrovaite et al., 2023, under the terms of CC BY 4.0 license, http://creativecommons.org/licenses/by/4.0/).

10-fold increase in the detected reduction current of $[Fe(CN)_6]^{-3/-4}$ redox probe compared to the unmodified carbon paste electrode. The developed immunosensor was used for the detection of C-reactive protein (CRP) in a wide linear concentration range from 0.01 to 1000 ng mL^{-1} with the limit of detection (LOD) of 5 pg mL^{-1} (Dong et al., 2019). The label-free immunosensor design can also be used for the detection of antibodies (Liustrovaite et al., 2023). In this work, screen printed electrodes were modified with various ZnO nanostructures by drop casting ZnO-nafion suspension on the electrode surface. The use of ZnO nanostructures improved electron transfer kinetics for $[Fe(CN)_6]^{-3/-4}$ redox probe oxidation. PSA was adsorbed on the surface of the modified electrode and GA vapor was used to cross-link the adsorbed PSA. Modified electrodes were applied for the detection of antibodies against PSA in the linear concentration range from 10 to 50 nM. The LOD for antibodies against PSA varied based on the ZnO morphology and was 1.35 nM for the sensor using ZnO NRs and 2.36 nM for rod-like nanoparticles.

Reviewing the research on label-free electrochemical immunosensors which employ electrodes modified with ZnO nanostructures and redox probes, it can be observed that although the inclusion of ZnO itself can sometimes lead to improvements of electrochemical characteristics, usually the main function of ZnO is to provide increased surface area for the immobilization of other electrically superior materials and to improve biocompatibility of the electrode surface in order to preserve the activity of immobilized antibodies or antigens. In addition, the use of ZnO can allow for employment of simpler antibody immobilization techniques like electrostatic adsorption since the high IEP of ZnO can facilitate electrostatic adsorption of antibodies (Alam et al., 2019).

Another type of label-free electrochemical immunosensors which employ ZnO nanostructures is based on EIS detection method. The modification of the electrode as well as the immune complex formation between antibody and antigen alter the impedimetric response of the electrode due to changes in capacitance and electron transfer kinetics at the interface. The high sensitivity of EIS allows for the label-free detection of the analyte. EIS can be used for the detection of faradaic and non-faradaic processes. Faradaic EIS utilizes an additional redox probe to monitor the change in the insulation of the electrode surface. In this case, the binding of the analyte inhibits charge transfer of the redox probe and is registered as an increase in the real component of the impedance data (R_{CT}). Since faradaic EIS registers the charge transfer of the redox probe oxidation or reduction, the modifications to the electrode surface during immunosensor design must either be conductive or have sufficient gaps to allow for electron transfer. On the other hand, non-faradaic EIS does not employ redox probes and instead is usually performed in buffer solutions. Without the presence of the redox probe, EIS measurements register the capacitance effects resulting from the immune complex formation. Capacitance based immunosensors usually employ an insulating layer on the electrode surface and the antibodies are instead immobilized on the insulating layer itself. The formation of the immune complex produces a change in capacitance which can be related to the analyte concentration (Prodromidis, 2010). Reviewing the literature, both faradaic (Ansari et al., 2010; Haghayegh et al., 2022; Nunez et al., 2023a, 2023b; Shabani et al., 2020; Wang et al., 2017) and non-faradaic EIS (Gopinath et al., 2016; Sanguino et al., 2014; Yang et al., 2020) immunosensors using ZnO nanostructures can be found. Furthermore, due to the non-destructive nature of EIS method measurements can be performed after each electrode modification step during immunosensor design, providing additional information about the processes happening on the electrode surface. Research using EIS method also shows that modification of various electrodes with ZnO nanostructures can hinder electron transfer kinetics due to semiconductor nature of ZnO (Haghayegh et al., 2022; Nunez et al., 2023b; Sanguino et al., 2014; Wang et al., 2017). Although research by Shabani et al. (2020) revealed, that electrode with ZnO NRs showed lower R_{CT} compared to electrode modified with ZnO nanoparticles attributing the effect to increased interface for ZnO nanorod electrode between the electrolyte and the electrode. The use of interdigitated electrodes can help to improve the sensitivity of non-faradaic EIS with Gopinath et al. (2016) reporting gold/ZnO composite nanogapped sensing electrode and Sanguino et al. (2014) describing ZnO NRs modified microgapped gold electrode. Research by Yang et al. (2020) showed that the use of screen printed electrodes modified with ZnO, can result in an order of magnitude increased sensitivity for ULBP2 biomarker detection in addition displaying that electrode arrays can be used to further enhance the analytical parameters.

An example faradaic EIS immunosensor reported by Ansari et al. (2010) is used to detect OTA in the linear concentration range from 6 to 10 pM with LOD being 6 pM (Fig. 4A). Fig. 4B shows the design of interdigitated electrode reported by Sanguino et al. (2014).

Reviewing the research on EIS based immunosensors which employ electrodes modified with ZnO nanostructures it can be observed that faradaic EIS is more commonly used than non-faradaic EIS. The main function of ZnO is similar as for other types of electrochemical detection methods, that is to provide increased surface area with improved biocompatibility for protein immobilization as a result preserving the activity of immobilized biomolecules. However, capacitive effects of ZnO nanostructures can be helpful for the design of non-faradaic EIS immunosensors.

Other types of electrochemical detection methods can also be used to quantify the analyte without using additional labelled detection antibodies. In the literature ZnO nanostructure based immunosensors can employ potentiometric and conductometric detection, however, these methods are used more rarely. Ibupoto et al. have published research in which different ZnO nanostructures were used for the development of two different potentiometric immunosensors designed to detect D-dimer (Ibupoto et al., 2013, 2014). ZnO nanostructures in both cases were used due to the high surface to volume ration, especially for etched ZnO nanotubes (Ibupoto et al., 2013), as well as, superb biocompatibility and

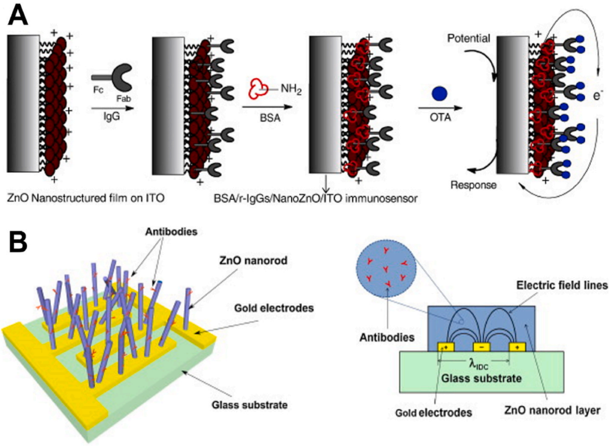

Fig. 4. Schematic diagram of (**A**) faradaic (Ansari et al., 2010, Copyright, 2009; Elsevier) and (**B**) non-faradaic (Sanguino et al., 2014, Copyright, 2014; Elsevier) EIS immunosensor design.

high isoelectric point of ZnO allowing for improved immobilization of antibodies. Research by Mutlaq et al. reports a conductometric electrochemical immunosensor which employs polyaniline/ZnO composite for the detection of *Escherichia coli*. Although the lower electrical conductivity of ZnO would likely harm the sensitivity for conductometric detection, the high surface area of ZnO nanostructures and a composite formation with a more conductive polyaniline results in a highly sensitive analytical system (Mutlaq et al., 2021). Lastly, ZnO can also be employed for the design of field effect transistors (FET) with Koike et al. using Indium-doped ZnO channel for the detection of human immunoglobulin G (Koike et al., 2014). In addition, Reyes et al. using ZnO channel as a sensing surface for the detection of epidermal growth factor receptor (Reyes et al., 2011) managed to achieve the LOD of 10 fM.

3.1.2. Labelled electrochemical immunosensors

ZnO nanostructures can also be employed for the design of labelled electrochemical immunosensors. For this immunosensor type, a labelled detection antibody is used for the detection of the desired analyte. The label itself can be electrochemically active, or it can require additional materials for activation, for example, substrates for enzyme labels. Usually, a sandwich type immunoassay format is chosen, where specific capture antibodies are immobilized on the electrode surface in order to catch and/or pre-concentrate the analyte from the sample. The labelled detection antibodies are then introduced in order to facilitate the detection of the analyte or to improve the sensitivity of the analytical system. ZnO nanostructures or their composites can be employed in the design of sandwich type electrochemical immunosensors by employing these materials for the modification of the electrode surface (Lu et al., 2008; Patella et al., 2022; Sun et al., 2015a; Wang et al., 2006), for the conjugation with detection antibodies (Cao et al., 2013; Jing et al., 2019; Yang et al., 2016), or in some cases can be used for both in the same immunosensor design (Fang et al., 2017). The semiconductor nature and a lower electrical conductivity of ZnO matters less for labelled than for label-free electrochemical immunosensors, since the analytical signal is usually produced by the label or enhanced by its presence near the electrode. Nevertheless, for labelled electrochemical immunosensors, after the modification of the electrode with ZnO nanostructures an impediment to electron transfer kinetics and decreased electrical conductivity have also been reported (Fang et al., 2017; Sun et al., 2015a). On the other hand, in some cases a synergistic effect is observed when ZnO nanostructures are used in composites with other materials like gold nanowires enhancing the analytical signal more than expected from the combination of analytical signal when these materials are used alone (Lu et al., 2008). Reviewing the research on labelled electrochemical immunosensors, which employ electrodes modified with ZnO nanostructures, it is reported that the main function of ZnO nanomaterials is to provide biocompatible surface with increased surface area in order to achieve higher immobilized antibody density and improve the availability of the capture antibody active center. Furthermore, when ZnO nanostructures are used for conjugation with detection antibodies, the main function is also the same. ZnO based nanostructures are used as nanocarriers allowing for significantly higher detection antibody or other electrocatalytic material loading. However, research by Gu et al. (2011) presented an immunosensor for CA19-9, in which ZnO QDs were used as an electroactive label allowing for the direct detection using square wave stripping voltammetry (SWSV). In addition, the use of ZnO QDs label allowed not only for electrochemical detection using SWSV method, but also for optical detection due to PL of the ZnO although electrochemical detection method was more sensitive providing a wider linear range from 0.1 to 180 U·mL^{-1} and 6 times lower LOD of 0.04 U·mL^{-1}. A schematic of a typical labelled electrochemical immunosensor employing ZnO labels is reported by Yang et al. (2016) and is presented in Fig. 5. In this work, porous ZnO nanoparticles (pZnO) were synthesized and used as a platform for hydrothermal growth of platinum nanoparticles and immobilization of hemin and alkaline phosphatase (ALP). This nanocomposite was then used as a label for detection antibodies facilitating electrochemical detection based on two catalytic processes: ALP catalyzed conversion of 1-naphthyl acid phosphate to 1-naphthol, as well as hemin and Pt nanoparticle (PtNPs) catalyzed conversion of 1-naphthol to 2-hydroxy-1,4-naphthoquinone in the presence of H_2O_2. Labelled antibodies were used for the detection of influenza in the linear range from 0.001 to 60 ng mL^{-1} with the LOD of 0.76 pg mL^{-1}.

3.1.3. Photoelectrochemical immunosensors

PEC detection method employs photoactive materials and measures the photocurrent resulting after the illumination of the electrode with light. The immobilization of biomolecules including antibodies or

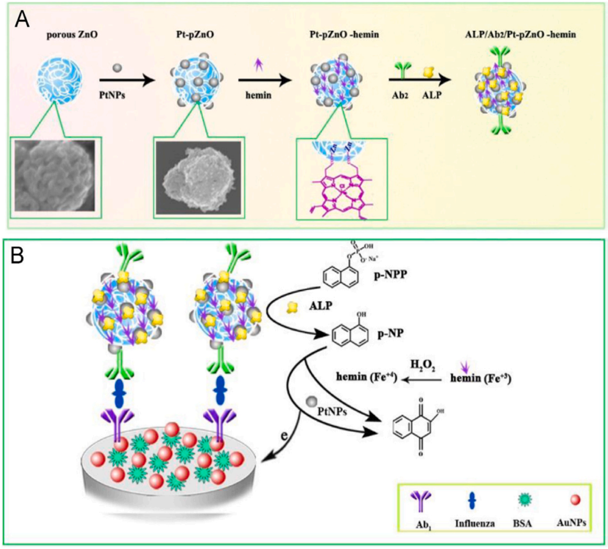

Fig. 5. Schematic illustration of ALP and Pt–pZnO–hemin as catalyst for signal amplification (Yang et al., 2016, Copyright, 2015; Elsevier).

antigens reduces the registered photocurrent in part due to absorbance of light by the biomolecules, the hindrance to charge transfer, and changes in the band gap of photoactive material. PEC immunosensors can employ detection antibodies labelled with photoactive materials, resulting in an increase of registered photocurrent after the immune complex formation. On the other hand, a label-free detection can be performed, in which the photoactive material is immobilized on the electrode and the immune complex formation results in a decrease of registered photocurrent. ZnO is a suitable material for constructing PEC immunosensors due to the photoactive properties resulting from the semiconductor nature of the material. However, electric and in turn photoactivity properties of ZnO are significantly affected by the phase structure, specific surface area and crystallinity of the material (Lee et al., 2010; Loh et al., 2015; Tong et al., 2018). For example, the use of 1D ZnO nanostructures can help to improve electron mobility almost 3 fold compared to bulk (Zhang et al., 2009). Nevertheless, ZnO suffers from low photogenerated electron-hole pair separation efficiency while the wide band gap of ZnO results in a weak visible wavelength absorption (Sun et al., 2015b). As such, usually nanocomposites of ZnO with noble metal nanoparticles or narrow band gap semiconductors are used in order to overcome these limitations and enhance photovoltaic conversion efficiency or facilitate the conversion of visible light. Reviewing PEC immunosensors that employ ZnO nanostructures, various nanocomposites can be found with gold nanostructures (Han et al., 2017), AuPd/CdS/CuO (Sun et al., 2015b), naphthalocyanine dye (Sun et al., 2014a), MWCNTs/CdS (Wang et al., 2013), CdS/CeS (Fan et al., 2019) Ni/CdS (Qileng et al., 2022), CdS/Ag (Zhou et al., 2023a), CdS (Zhu et al., 2021), MXenes/Ag_2S (Zhou et al., 2023b), or ZnO alone can be immobilized on the gold electrode (Sun et al., 2014b). ZnO nanostructures and nanocomposites can be found in the design of both label-free (Han et al., 2017; Sun et al., 2014a, 2015b; Wang et al., 2013; Zhou et al., 2023a, 2023b) and labelled (Fan et al., 2019; Qileng et al., 2022; Sun et al., 2014b; Zhu et al., 2021) PEC immunosensors. However, for labelled PEC immunosensors, ZnO nanocomposites are only being employed for modifying the electrode instead of labelling detection antibodies. A typical example of a label-free PEC immunosensor provided in Fig. 6 is reported by (Zhou et al., 2023a). In this case, ZnO nanowires were grown on an ITO working electrode using hydrothermal method. The PEC response of the ITO/ZnO modified electrode was increased more than 2 times by incorporating CdS QDs and AgNPs on the electrode surface. Monoclonal antibodies against fibroin were covalently immobilized with the help of polydopamine employing electrostatic binding and Michael addition and/or Schiff-base reactions (Li et al., 2011). To reduce non-specific interactions blocking of the remaining free surface was done using BSA. The designed PEC immunosensor was used for the detection of fibroin, a protein present in silk, in the linear range of 1–1000 ng mL^{-1} with LOD of 0.56 ng mL^{-1}.

3.1.4. *Summary of electrochemical detection methods*

As can be seen, ZnO nanostructures are widely used in the design of electrochemical immunosensors, both as electrode modification material, and for labelling of antibodies. This allows the development of both label-free and labelled detection systems based on various electrochemical methods, such as CV, DPV and PEC detection. In the case of label-free immunosensors, additional methods such as EIS, potentiometry and conductometry are being employed. Table 1 provides a summary of immunosensors utilizing electrochemical detection methods, which are classified into two categories: labelled and label-free detection.

3.2. *Optical detection methods*

3.2.1. *Photoluminescence immunosensors*

PL spectroscopy is a great method for immunosensor development. Sensitive and selective detection can be achieved using this technique. The current technological level allows to fabricate miniature PL immunosensors, which can be easily operated by an inexperienced user (Gao et al., 2022; Lee et al., 2020; Tereshchenko et al., 2016). PL

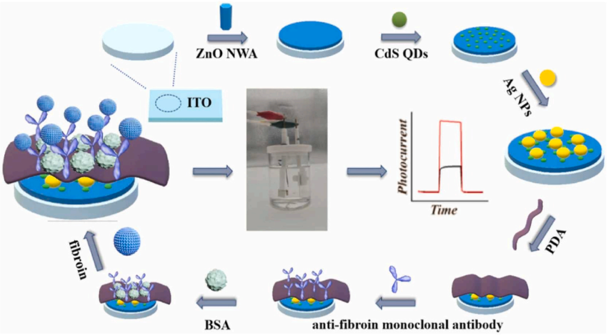

Fig. 6. Schematic representation of a typical label-free PEC immunosensor based on ZnO nanostructures (Zhou et al., 2023a, Copyright, 2022; Elsevier).

properties make ZnO nanostructures an ideal candidate for the fabrication of optical immunosensors. These immunosensors based on PL measurements can be divided into two types. The first is based on ZnO QDs labels facilitating PL signal generation after immune complex formation. The second type is based on the monitoring of PL quenching, which occurs due to antibody-antigen interaction when either of them is immobilized on the surface. In addition, ZnO nanostructures can be used as a nanocarrier increasing the number of molecules that can be available for immune interaction (Medawar-Aguilar et al., 2019).

ZnO QDs are a promising alternative to Cd-based QDs. Low toxicity and chemical stability allow their use in bioimaging and *in-vivo* diagnostics (Gulia and Rita Kakkar, 2013). QDs are widely used as labels for optical sensing and imaging due to the broad absorption spectra, tunable narrow emission band, high extinction coefficient and fluorescent quantum yield (Popov et al., 2021). The determination of carbohydrate antigen 19–9 (CA 19–9) was performed using a sandwich type immunoassay based on ZnO QDs (Gu et al., 2011). The detection antibodies were adsorbed on the surface of ZnO QDs and the interaction of the conjugates with CA 19–9 was assessed using PL spectroscopy. In addition, SWSV was used in parallel. Optical and electrochemical immunosensors showed a linear response in the ranges of 1–180 U·mL^{-1} and 0.1–180 U·mL^{-1}, respectively. Meanwhile, the LOD was lower in the case of electrochemical detection (0.04 U·mL^{-1}), compared to PL detection (0.25 U·mL^{-1}). In another example, a direct immunosensor based on Cd-doped ZnO QDs was proposed for the detection of bisphenol A (Zhang et al., 2014). Antibodies were covalently immobilized on the surface of QDs. The wells of the microliter plate were coated with antigen and blocked with 3 % skim milk. After incubation of conjugates in the wells and subsequent washing, PL spectroscopy was used for the detection. The linear range was 20.8–330.3 ng mL^{-1} with an LOD of 13.1 ng mL^{-1}.

ZnO is a semiconductor, and even a slight change on its surface causes a change in the PL signal. Thus, a slight change in analyte concentration can result in a measurable PL response (Rodrigues et al., 2020). PL changes can possibly be associated with ZnO band gap modification due to the interaction with charged biomolecules. According to this theory, due to the interaction between two proteins, when one of them is immobilized on surface of ZnO, the charge near ZnO surface changes, resulting in the change of PL intensity (Myndrul et al., 2021). The PL intensity of ZnO NRs was measured as an analytical signal for OTA detection (Viter et al., 2018). Oriented immobilization of anti-OTA antibody was performed through protein A, which was covalently fixed on ZnO NRs pre-modified by APTES using GA as a cross-linking agent. The decrease in PL intensity was linearly proportional to the OTA concentration, ranging from 0.1 to 1 ng mL^{-1} with LOD of 0.01 ng mL^{-1}. Tereshchenko et al. (2020) proposed the use of ZnO NRs formed on the surface of silicon as a whispering gallery mode resonator, which was applied to the optical detection of GVA proteins. The interaction of GVA antigens with anti-GVA antibodies immobilized on the surface of ZnO NRs resulted in a UV-shift of the PL emission. The sensitivity of the developed immunoanalytical system has been shown to range from 1 to 200 ng mL^{-1}. In addition, ZnO nanostructures have been used for the detection of bigger structures such as *Salmonella* (Viter et al., 2014), T-lymphoblast cells (Tamashevski et al., 2020) and human leukemic cells (Tamashevski et al., 2019). In the case of cancer cell detection, ZnO NRs were formed on the surface of glass substrate. The detection was organized using antibodies against biomarkers expressed on the surface of cancer cells. Measurable PL quenching was registered even in the presence of 3–10 cells per 1 mm^2 of immunosensing platform.

Optical immunosensors can also be based on the use of ZnO in combination with other nanomaterials. For instance, 1D ZnO nanostructures can be formed by atomic layer deposition on the surface of electrospun PAN substrate (Viter et al., 2015). Such synthesis provides an opportunity to control the morphology and thickness of ZnO nanostructures. This is especially important because morphology and thickness affect immunosensor performance and the PL properties of ZnO (Damberga et al., 2020; Sang et al., 2016). Proposed nanostructures were applied for the detection of AFB1 (Myndrul et al., 2021). Anti-AFB1 antibodies were immobilized on PAN/ZnO pre-modified with APTES and GA. After blocking remaining active sites with BSA, the immunosensor was suitable for detection of AFB1 in the range from 0.1 to 20 ng mL^{-1} with LOD of 39 pg mL^{-1}. The summary of photoluminescence based immunosensors which employ ZnO nanostructures is provided in Table 2.

3.2.2. *Electrochemiluminescence immunosensors*

ECL also called electrogenerated chemiluminescence is the process of generating highly reactive species on the electrode surface followed by emission of light due to the formation of excited states of generated species undergoing electron-transfer reactions between them (Richter, 2004). As a combination of electrochemistry and spectroscopy, ECL has the advantages of both methods. ECL is a sensitive and selective method with a fast response time. Intensity can be controlled by an external supply voltage, and there is no need for an external light source, which would introduce background noise and decrease sensitivity (Du et al., 2021; Parracino et al., 2019). This makes ECL a good choice for immunosensing with the ability to detect an individual cell (Wang et al., 2020) or even a single biomolecule (Liu et al., 2021). The enhancement of ECL intensity can be done by the use of nanostructures, and a possible

Table 1
Electrochemical immunosensors that use ZnO nanostructures.

Material	Analyte	Antibody immobilization method	Electrochemical detection method	Linear range	LOD	Reference
Label-free electrochemical immunosensors						
ZnO NRs and AuNPs	CA125	GA (covalent)	CV	–	0.25 ng μL^{-1}	Gasparotto et al. (2017)
ZnO–CuO nanocomposite	*E. coli*	Adsorption	DPV	1 10^{3}–8 10^{4} CFU mL^{-1}	2 CFU mL^{-1}	Khan et al. (2021)
g-C3N4/ZnO nanocomposite	*H. pylori* secretory protein VacA	EDC/NHS (covalent)	DPV	0.1–12.8 ng mL^{-1}	0.1 ng mL^{-1}	Saxena et al. (2022)
ZnO/porous carbon matrix nanocomposite	C-reactive protein	EDC/NHS (covalent)	DPV	0.01–1000 ng mL^{-1}	5 pg mL^{-1}	Dong et al. (2019)
1D ZnO NRs and 2D ZnO nanoflakes	Cortisol	Adsorption	CV	0.01–100 nM	1 pM	Vabbina et al. (2015)
ZnO nanostructures	ZIKV-NS1 antigen	GA (covalent)	CV	0.1–100 ng mL^{-1}	1 pg mL^{-1}	Faria and Mazon (2019)
ZnO nanoflakes	Ethyl-glucuronide	Adsorption	CV	0.001–100 μg mL^{-1}	1 ng mL^{-1}	Alam et al. (2019)
ZnO nanocrystals decorated with Cu	Human salivary alpha-amylase	Adsorption	CV	–	0.00196 U·mL^{-1}	Martins et al. (2021)
ZnO nanoparticles	Clenbuterol	Adsorption	DPV	0.3–1000 ng mL^{-1}	0.12 ng mL^{-1}	Zhan et al. (2021)
ZnO/rGO nanocomposite	BSA	EDC/NHS (covalent)	DPV	0.001–30 ng mL^{-1}	1 pg mL^{-1}	Garg et al. (2023)
CNTs embedded on ZnO nanowire	CA125	EDC/NHS (covalent)	DPV	0.001 U mL^{-1} – 1 kU·mL^{-1}	0.00113 U·mL^{-1}	Paul et al. (2017)
ZnO/MoS$_2$ nanocomposite	IL8	Adsorption	DPV	0.5–4.5 ng mL^{-1}	11.6 fM	Vetrivel et al. (2023)
ZnO nanoparticles and ZnO NRs	MMP-9	GA (covalent)	CV/EIS	1–1000 ng mL^{-1}	0.15 ng mL^{-1}	Shabani et al. (2020)
ZnO nanotubes decorated with AgNPs	D-dimer	GA (cross-linking)	Potentiometric	10^{-5} – 1 μg mL^{-1}	10^{-6} μg mL^{-1}	Ibupoto et al. (2013)
ZnO NRs	D-dimer	GA (cross-linking)	Potentiometric	10^{-6} – 10^{-3} mg L^{-1}	100 pg mL^{-1}	Ibupoto et al. (2014)
ZnO/polyaniline composite	*E. coli*	GA (covalent)	Conductometric	10–10^{4} CFU mL^{-1}	4.8 CFU mL^{-1}	Mutlaq et al. (2021)
ZnO	EGFR	Covalent	FET	0.01–10 000 pM	10 fM	Reyes et al. (2011)
In-doped ZnO	Human IgG	GA (covalent)	FET	–	0.35 μM	Koike et al. (2014)
ZnO NRs	HRP	Sulfo-MBS (covalent)	EIS	–	–	Sanguino et al. (2014)
ZnO nanoparticles	ULBP2	GA (cross-linking)	EIS	1–1000 pg mL^{-1}	1 pg mL^{-1}	Yang et al. (2020)
ZnO nanoparticles	IFN-γ	Adsorption	EIS	0.1–100 pg mL^{-1}	0.1 pg mL^{-1}	Wang et al. (2017)
ZnO nanostructures	OTA	Adsorption	EIS	6–10 pM	6 pM	Ansari et al. (2010)
ZnO	HSP	GA (covalent)	EIS	0.1–1000 pM	0.1 pM	Gopinath et al. (2016)
ZnO/rGO nanocomposite	SARS-CoV-2	Adsorption	EIS	1–10 000 pg mL^{-1}	21 fg mL^{-1}	Haghayegh et al. (2022)
ZnO NRs	Anti−SARS-CoV-2	Adsorption	EIS	200–1200 ng mL^{-1}	19.34 ng mL^{-1}	Nunez et al. (2023b)
ZnO NRs	Anti−SARS-CoV-2	Adsorption	EIS	200–1200 ng mL^{-1}	52.55 ng mL^{-1}	Nunez et al. (2023a)
Au–ZnO flower-rods	α-fetoprotein	Adsorption	PEC	0.005–50 ng mL^{-1}	0.56 pg mL^{-1}	Han et al. (2017)
ZnO NRs	CEA	EDC/NHS (covalent)	PEC	0.005–100 ng mL^{-1}	1.6 pg mL^{-1}	Sun et al. (2014a)
ZnO spheres	PSA	GA (covalent)	PEC	0.005–150 ng mL^{-1}	2.3 pg mL^{-1}	Sun et al. (2014b)
MWCNTs/ZnO/CdS	CEA	Adsorption	PEC	0.01–50 ng mL^{-1}	4 pg mL^{-1}	Wang et al. (2013)
ZnO NRs/MXenes/Ag$_2$S	Silk fibroin	Michael addition (covalent)	PEC	0.005–50 ng mL^{-1}	1.51 pg mL^{-1}	Zhou et al. (2023b)
ZnO nanowires/CdS/Ag	Silk fibroin	Michael addition (covalent)	PEC	1–1000 ng mL^{-1}	0.56 ng mL^{-1}	Zhou et al. (2023a)
Labelled electrochemical immunosensors						
ZnO NRs/Au nanowire composite	α-fetoprotein	Adsorption	Chronoamperometric	0.5–160 ng mL^{-1}	0.1 ng mL^{-1}	Lu et al. (2008)
ZnO NRs-modified rGO-paper electrode	hCG PSA; CEA	Adsorption	Chronoamperometric	0.002–120 mIU·mL^{-1} (hCG); 0.001–110 ng mL^{-1} (PSA);	0.0007 mIU·mL^{-1} (hCG); 0.35 pg mL^{-1} (PSA); 0.33 pg mL^{-1} (CEA)	Sun et al. (2015a)

(*continued on next page*)

Table 1 (*continued*)

Material	Analyte	Antibody immobilization method	Electrochemical detection method	Linear range	LOD	Reference
				0.001–100 ng mL^{-1} (CEA)		
Porous ZnO spheres decorated with PtNPs and hemin	Influenza	Adsorption	DPV	0.001–60 ng mL^{-1}	0.76 pg mL^{-1}	Yang et al. (2016)
ZnO nanostructures	Human IgG	EDC/NHS (covalent)	Chronoamperometric	10–1000 ng mL^{-1}	1.25 ng mL^{-1}	Patella et al. (2022)
ZnO/chitosan	Human IgG	Adsorption	Chronoamperometric	2.5–500 ng mL^{-1}	1.2 ng mL^{-1}	Wang et al. (2006)
AuNPs/ZnO NRs/ Hybridized rG nanosheet	α-fetoprotein	Adsorption	DPV	0.02–10 000 pg mL^{-1}; 10 000–1 000 000 pg mL^{-1}	0.01 pg mL^{-1}	Fang et al. (2017)
ZnO/Au	CEA	Adsorption	DPV	0.001–100 ng mL^{-1}	0.6 pg mL^{-1}	Jing et al. (2019)
(TH)-doped MP-ZnO	Human IgG	Adsorption	DPV	0.01–200 ng mL^{-1}	4 pg mL^{-1}	Cao et al. (2013)
ZnO QDs	CA19-9	Adsorption	SWSV	0.1–180 U·mL^{-1}	0.04 U·mL^{-1}	Gu et al. (2011)
ZnO/CdS/CeS	β-amyloid protein	EDC/NHS (covalent)	PEC	0.001–100 ng mL^{-1}	0.37 pg mL^{-1}	Fan et al. (2019)
AuPd/ZnO/CdS/CuO	CA125; PSA; α-fetoprotein	Adsorption	PEC	0.005–80 U·mL^{-1}; 0.001–50 ng mL^{-1}; 0.002–50 ng mL^{-1};	0.0013 U·mL^{-1}; 0.3 pg mL^{-1}; 0.7 pg mL^{-1};	Sun et al. (2015b)
ZnO/Ni/CdS	Rosiglitazone	EDC/NHS (covalent)	PEC	1–1000 ng L^{-1}	0.97 ng L^{-1}	Qileng et al. (2022)
ZnO/CdS	PSA	–	PEC	0.05–50 ng mL^{-1}	0.018 ng mL^{-1}	Zhu et al. (2021)

g-C3N4 – graphitic carbon nitride; **rGO** – reduced graphene oxide; **rG** – reduced graphene; **TH** – thionine; **MP-ZnO** - mesoporous ZnO nanostrawberries; **IL8** – interleukin-8; **MMP-9** – matrix metalloproteinase 9; **EGFR** – epidermal growth factor receptor; **HRP** – horseradish peroxidase; **ULBP2** – UL16 binding protein 2; **IFN-γ** – interferon gamma; **OTA** – ochratoxin A; **HSP** – heat shock protein; **CEA** – carcinoembryonic antigen; **CA 19–9** – carbohydrate antigen 19–9; **BSA** – bovine serum albumin; **CA125** – cancer antigen 125; **PSA** – prostate specific antigen; **MWCNTs** – multi-walled carbon nanotubes; **anti−SARS-CoV-2** – antibodies against SARS-CoV-2; **ZIKV-NS1** – Zika non-structural protein 1 (antigen); **GA** – glutaraldehyde.

Table 2
Photoluminescence immunosensors which employ ZnO nanostructures.

Material	Analyte	Antibody immobilization method	Linear range	LOD	Reference
Chitosan-ZnO-nanoparticles	*T. gondii*	GA (cross-linking)	0–200 U·mL^{-1}	3.9×10^{-4} U·mL^{-1}	Medawar-Aguilar et al. (2019)
ZnO QDs	CA 19-9	Adsorption	1–180 U·mL^{-1}	0.25 U·mL^{-1}	Gu et al. (2011)
Cd-doped ZnO QDs	Bisphenol A	EDC/NHS (covalent)	20.8–330.3 ng mL^{-1}	13.1 ng mL^{-1}	Zhang et al. (2014)
PAN/ZnO nanofibers	AFB1	APTES and GA (covalent)	0.1–20 ng mL^{-1}	39 pg mL^{-1}	Myndrul et al. (2021)
ZnO NRs	OTA	APTES and GA (covalent) Protein A (site-directed)	–	0.01 ng mL^{-1}	Viter et al. (2018)
ZnO NRs	GVA	Adsorption	–	–	Tereshchenko et al. (2020)
ZnO NRs	*Salmonella typhimurium*	Adsorption	10^2 - 10^5 cell mL^{-1}	–	Viter et al. (2014)
ZnO NRs	Human leukemic T-cells	Adsorption	–	–	Tamashevski et al. (2020)
ZnO NRs	B-lymphoblastoid cells	Adsorption	–	–	Tamashevski et al. (2019)

PAN – polyacrylonitrile; **CA 19–9** – carbohydrate antigen 19–9; **AFB1** – aflatoxin B1; **OTA** – ochratoxin A; **GVA** – grapevine virus A-type; **GA** – glutaraldehyde; **APTES** – (3-Aminopropyl) triethoxysilane.

Table 3
Electrochemiluminescence immunosensors which employ ZnO nanostructures.

Material	Analyte	Antibody immobilization method	Linear range	LOD	Reference
ZnO NRs-L-cysteine-luminol	PSA	EDC/NHS (covalent)	0.03 pg mL^{-1} – 30 ng mL^{-1}	10 fg mL^{-1}	Zhang et al. (2020)
ZnO NRs and AuNPs	Brombuterol	Adsorption	0.001–500 ng mL^{-1}	0.3 pg mL^{-1}	Zhu et al. (2016)
PAMAM functionalized ZnO NRs	CA15-3	EDC/NHS (covalent)	0.1–120 U·mL^{-1}	0.033 U·mL^{-1}	Jiang et al. (2015)
CdS-coated-ZnO NRs	HepG2 cell	Adsorption	300–10 000 cells mL^{-1}	256 cells mL^{-1}	Liu et al. (2015)
ZnO QDs dotted CNTs	PSA	Adsorption	0.001–500 ng mL^{-1}	0.61 pg mL^{-1}	Liu et al. (2014)

PAMAM – polyamidoamine; **PSA** – prostate specific antigen; **CA15–3** – carbohydrate antigen 15–3; **HepG2 cell** – liver cancer cell line.

candidate is ZnO nanostructures, such as nanoparticles (Haghighi and Bozorgzadeh, 2011) or nanowires (Guerrero-Esteban et al., 2019). Zhang and coworkers (Zhang et al., 2020) proposed an immunosensor based on ZnO NRs-L-cysteine-luminol nanocomposite for PSA detection (Fig. 7). ZnO NRs pre-modified with L-cysteine were covalently conjugated to luminol, and detection antibodies were applied to the surface of the conjugates using GA as a cross-linking agent. Streptavidin-modified AuNPs were deposited on the surface of Au electrode via a 1,3-dimercaptopropane SAM. After the biotinylated capture antibody was attached to streptavidin, sequential interactions were performed with PSA of different concentrations and with prepared conjugates to form a sandwich-type ECL immunosensor, which possessed good analytical

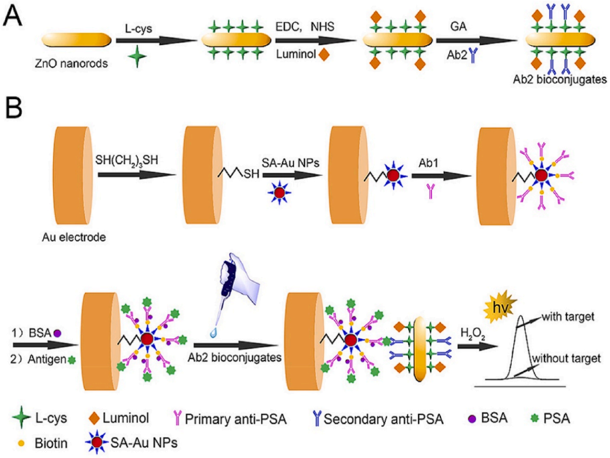

Fig. 7. Schematic illustration of a sandwich-type ECL immunosensor fabrication based on signal amplification using a ZnO NRs -L-cysteine-luminol nanocomposite (Zhang et al., 2020, Copyright, 2015; Elsevier).

characteristics. A wide linear range from 0.03 pg mL^{-1} to 30 ng mL^{-1} with a LOD of 0.01 pg mL^{-1} was achieved.

ZnO NRs have also been used to make sensitive immunosensors designed to detect brombuterol (Zhu et al., 2016), CA15-3 (Jiang et al., 2015) and the liver cancer line (HepG2 cell) (Liu et al., 2015). Moreover, ZnO QDs were used for the fabrication of PSA immunosensor with LOD of 0.61 pg mL^{-1} (Liu et al., 2014). The increase of ECL intensity due to the use of ZnO nanostructures is in part due to the increased surface area for immobilization of the antigen or antibody when they act as nanocarrier (Zhu et al., 2016). Moreover, in ECL systems ZnO acts as a catalyst for the formation of highly reactive species. For instance, it has been suggested that H_2O_2 decomposition is catalyzed by ZnO in luminol-H_2O_2 based ECL systems (Cui et al., 1998; Zhang et al., 2003). Thus, the superoxide anion ($O_2^{\bullet-}$) and hydroxyl radical ($OH^{\bullet}$) formed as reactive intermediates were assumed to participate in the oxidation of luminol (Merényi and Lind, 1980) and react with the anion radicals with subsequent light emission. Thus, a significant increase in ECL intensity is observed in the presence of ZnO nanostructures (Cheng et al., 2012). The summary of electrochemiluminescence based immunosensors which employ ZnO nanostructures is provided in Table 3.

4. Conclusion

Because of its extensive properties, ZnO can be widely used in the design of immunosensors. PL, ECL, PEC, EIS, potentiometric, voltammetric, conductometric and other types of immunosensors have been reported in the literature. In addition to the unique electrical and optical properties, ZnO nanostructures are also used due to the biocompatible nature of the material, which is crucial in order to preserve antibody and antigen biological activity. The high IEP of ZnO nanostructures can also help improve the stability of biomolecule immobilization process through electrostatic attraction if proteins with low IEP are used. In the immunosensor design, ZnO nanostructures are being used to modify the underlying immunosensing surface or to label antibodies. ZnO nanomaterial labels can either be directly detected by the chosen detection method or, alternatively, they can be employed as scaffolds for immobilizing other molecules, thanks to their high surface area. The use of ZnO nanomaterials for the design of electrochemical immunosensors has been widely established, with ZnO being used mainly to increase the electrode surface area and improve the biocompatibility of the electrode material, although in some cases, ZnO can also improve electrochemical characteristics. On the other hand, ZnO can also be the basis for the immunosensor design, due to the unique material properties, allowing the development of PEC, PL and ECL sensors.

CRediT author statement

Benediktas Brasiunas: Conceptualization, Investigation, Writing – original draft, Writing – review & editing, Visualization. Anton Popov: Conceptualization, Investigation, Writing – original draft, Writing – review & editing. Viktorija Lisyte: Conceptualization, Investigation, Data curation, Writing – review & editing. Asta Kausaite-Minkstimiene: Conceptualization, Investigation, Writing – original draft, Writing – review & editing. Almira Ramanaviciene: Conceptualization, Investigation, Writing – original draft, Writing – review & editing, Supervision, Funding acquisition.

Declaration of competing interest

The authors declare that they have no known competing financial interests or personal relationships that could have appeared to influence the work reported in this paper.

Data availability

No data was used for the research described in the article.

Acknowledgements

This work is part of a project that has received funding from the European Union's Horizon 2020 research and innovation programme under grant agreement No 778157 CanBioSe.

References

Afzal, A., Cioffi, N., Sabbatini, L., Torsi, L., 2012. NO sensors based on semiconducting metal oxide nanostructures: progress and perspectives. Sensor. Actuator. B Chem. 171–172, 25–42. https://doi.org/10.1016/j.snb.2012.05.026.

Alam, F., Jalal, A.H., Pala, N., 2019. Selective detection of alcohol through ethyl-glucuronide immunosensor based on 2D zinc oxide nanostructures. IEEE Sensor. J. 19, 3984–3992. https://doi.org/10.1109/JSEN.2019.2898869.

Ansari, A.A., Kaushik, A., Solanki, P.R., Malhotra, B.D., 2010. Nanostructured zinc oxide platform for mycotoxin detection. Bioelectrochemistry 77, 75–81. https://doi.org/10.1016/j.bioelechem.2009.06.014.

Bahnemann, D.W., Kormann, C., Hoffmann, M.R., 1987. Preparation and characterization of quantum size zinc oxide: a detailed spectroscopic study. J. Phys. Chem. 91, 3789–3798. https://doi.org/10.1021/j100298a015.

Baniukevic, J., Hakki Boyaci, I., Goktug Bozkurt, A., Tamer, U., Ramanavicius, A., Ramanaviciene, A., 2013a. Magnetic gold nanoparticles in SERS-based sandwich immunoassay for antigen detection by well oriented antibodies. Biosens. Bioelectron. 43, 281–288. https://doi.org/10.1016/j.bios.2012.12.014.

Baniukevic, J., Kirlyte, J., Ramanavicius, A., Ramanaviciene, A., 2013b. Application of oriented and random antibody immobilization methods in immunosensor design. Sensor. Actuator. B Chem. 189, 217–223. https://doi.org/10.1016/j.snb.2013.03.126.

Bizarro, M., 2010. High photocatalytic activity of ZnO and ZnO:Al nanostructured films deposited by spray pyrolysis. Appl. Catal. B Environ. 97, 198–203. https://doi.org/10.1016/j.apcatb.2010.03.040.

Cao, X., Liu, S., Feng, Q., Wang, N., 2013. Silver nanowire-based electrochemical immunoassay for sensing immunoglobulin G with signal amplification using strawberry-like ZnO nanostructures as labels. Biosens. Bioelectron. 49, 256–262. https://doi.org/10.1016/j.bios.2013.05.029.

Chatterjee, A.P., Mitra, P., Mukhopadhyay, A.K., 1999. Chemically deposited zinc oxide thin film gas sensor. J. Mater. Sci. 34, 4225–4231. https://doi.org/10.1023/A:1004694501646.

Cheng, Y., Yuan, R., Chai, Y., Niu, H., Cao, Y., Liu, H., Bai, L., Yuan, Y., 2012. Highly sensitive luminol electrochemiluminescence immunosensor based on ZnO nanoparticles and glucose oxidase decorated graphene for cancer biomarker detection. Anal. Chim. Acta 745, 137–142. https://doi.org/10.1016/j.aca.2012.08.010.

Cui, H., Li, Q., Meng, R., Zhao, H., He, C., 1998. Flow injection analysis of tannic acid with inhibited chemiluminescent detection. Anal. Chim. Acta 362, 151–155. https://doi.org/10.1016/S0003-2670(98)00031-2.

Damberga, D., Viter, R., Fedorenko, V., Iatsunskyi, I., Coy, E., Graniel, O., Balme, S., Miele, P., Bechelany, M., 2020. Photoluminescence study of defects in ZnO-coated polyacrylonitrile nanofibers. J. Phys. Chem. C 124, 9434–9441. https://doi.org/10.1021/acs.jpcc.0c00326.

de la Escosura-Muñiz, A., Parolo, C., Merkoçi, A., 2010. Immunosensing using nanoparticles. Mater. Today 13, 24–34. https://doi.org/10.1016/S1369-7021(10)70125-5.

Degen, A., Kosec, M., 2000. Effect of pH and impurities on the surface charge of zinc oxide in aqueous solution. J. Eur. Ceram. Soc. 20, 667–673. https://doi.org/10.1016/S0955-2219(99)00203-4.

Djurišić, A.B., Ng, A.M.C., Chen, X.Y., 2010. ZnO nanostructures for optoelectronics: material properties and device applications. Prog. Quant. Electron. 34, 191–259. https://doi.org/10.1016/j.pquantelec.2010.04.001.

Dong, S., Zhang, D., Cui, H., Huang, T., 2019. ZnO/porous carbon composite from a mixed-ligand MOF for ultrasensitive electrochemical immunosensing of C-reactive protein. Sensor. Actuator. B Chem. 284, 354–361. https://doi.org/10.1016/j.snb.2018.12.150.

Du, F., Chen, Y., Meng, C., Lou, B., Zhang, W., Xu, G., 2021. Recent advances in electrochemiluminescence immunoassay based on multiple-signal strategy. Curr. Opin. Electrochem. https://doi.org/10.1016/j.coelec.2021.100725.

Fan, D., Liu, X., Bao, C., Feng, J., Wang, H., Ma, H., Wu, D., Wei, Q., 2019. A novel sandwich-type photoelectrochemical immunosensor based on Ru(bpy)32+ and Ce-CdS co-sensitized hierarchical ZnO matrix and dual-inhibited polystyrene@CuS-Ab2 composites. Biosens. Bioelectron. 129, 124–131. https://doi.org/10.1016/j.bios.2019.01.029.

Fang, X., Liu, J., Wang, J., Zhao, H., Ren, H., Li, Z., 2017. Dual signal amplification strategy of Au nanopaticles/ZnO nanorods hybridized reduced graphene nanosheet and multienzyme functionalized Au@ZnO composites for ultrasensitive electrochemical detection of tumor biomarker. Biosens. Bioelectron. 97, 218–225. https://doi.org/10.1016/j.bios.2017.05.055.

Farhan, M.S., Zalnezhad, E., Bushroa, A.R., Sarhan, A.A.D., 2013. Electrical and optical properties of indium-tin oxide (ITO) films by ion-assisted deposition (IAD) at room temperature. Int. J. Precis. Eng. Manuf. 14, 1465–1469. https://doi.org/10.1007/s12541-013-0197-5.

Faria, A.M., Mazon, T., 2019. Early diagnosis of Zika infection using a ZnO nanostructures-based rapid electrochemical biosensor. Talanta 203, 153–160. https://doi.org/10.1016/j.talanta.2019.04.080.

Gao, P., Xie, Z., Zheng, M., 2022. Small nanoparticles bring big prospect: the synthesis, modification, photoluminescence and sensing applications of carbon dots. Chin. Chem. Lett. 33, 1659–1672. https://doi.org/10.1016/j.cclet.2021.09.085.

Garg, P., Thakur, D., Verma, S., Jalil, O., Pandey, C.M., Kumar, D., 2023. Biosynthesized rGO@ZnO-based ultrasensitive electrochemical immunosensor for bovine serum albumin detection. J. Appl. Electrochem. 53, 1449–1459. https://doi.org/10.1007/s10800-023-01848-5.

Gasparotto, G., Costa, J.P.C., Costa, P.I., Zaghete, M.A., Mazon, T., 2017. Electrochemical immunosensor based on ZnO nanorods-Au nanoparticles nanohybrids for ovarian cancer antigen CA-125 detection. Mater. Sci. Eng. C 76, 1240–1247. https://doi.org/10.1016/j.msec.2017.02.031.

Gopinath, S.C.B., Perumal, V., Kumaresan, R., Lakshmipriya, T., Rajintraprasad, H., Rao, B.S., Arshad, M.K.M., Chen, Y., Kotani, N., Hashim, U., 2016. Nanogapped impedimetric immunosensor for the detection of 16 kDa heat shock protein against. Mycobacterium Tuberculosis. Microchim. Acta 183, 2697–2703. https://doi.org/10.1007/s00604-016-1911-7.

Gu, B., Xu, C., Yang, C., Liu, S., Wang, M., 2011. ZnO quantum dot labeled immunosensor for carbohydrate antigen 19-9. Biosens. Bioelectron. 26, 2720–2723. https://doi.org/10.1016/j.bios.2010.09.031.

Guerrero-Esteban, T., Gutiérrez-Sánchez, C., Revenga-Parra, M., Pau, J.L., Pariente, F., Lorenzo, E., 2019. Enhanced electrochemiluminescence by ZnO nanowires for taurine determination. Talanta 204, 63–69. https://doi.org/10.1016/j.talanta.2019.05.090.

Gulia, Rita Kakkar, S., 2013. ZnO quantum dots for biomedical applications. Adv. Mater. Lett. 4, 876–887. https://doi.org/10.5185/amlett.2013.3440.

Haghayegh, F., Salahandish, R., Hassani, M., Sanati-Nezhad, A., 2022. Highly stable buffer-based zinc oxide/reduced graphene oxide nanosurface chemistry for rapid immunosensing of SARS-CoV-2 antigens. ACS Appl. Mater. Interfaces 14, 10844–10855. https://doi.org/10.1021/acsami.1c24475.

Haghighi, B., Bozorgzadeh, S., 2011. Fabrication of a highly sensitive electrochemiluminescence lactate biosensor using ZnO nanoparticles decorated multiwalled carbon nanotubes. Talanta 85, 2189–2193. https://doi.org/10.1016/j.talanta.2011.07.071.

Han, Z., Luo, M., Chen, L., Chen, J., Li, C., 2017. A photoelectrochemical immunosensor for detection of α-fetoprotein based on Au-ZnO flower-rod heterostructures. Appl. Surf. Sci. 402, 429–435. https://doi.org/10.1016/j.apsusc.2017.01.137.

Hariharan, C., 2006. Photocatalytic degradation of organic contaminants in water by ZnO nanoparticles: revisited. Appl. Catal. Gen. 304, 55–61. https://doi.org/10.1016/j.apcata.2006.02.020.

Huang, W.-J., Fang, G.-C., Wang, C.-C., 2005. A nanometer-ZnO catalyst to enhance the ozonation of 2,4,6-trichlorophenol in water. Colloids Surfaces A Physicochem. Eng. Asp. 260, 45–51. https://doi.org/10.1016/j.colsurfa.2005.01.031.

Ibupoto, Z.H., Jamal, N., Khun, K., Liu, X., Willander, M., 2013. A potentiometric immunosensor based on silver nanoparticles decorated ZnO nanotubes, for the selective detection of d-dimer. Sensor. Actuator. B Chem. 182, 104–111. https://doi.org/10.1016/j.snb.2013.02.084.

Ibupoto, Z.H., Mitrou, N., Nikoleli, G.-P., Nikolelis, D.P., Willander, M., Psaroudakis, N., 2014. The development of highly sensitive and selective immunosensor based on antibody immobilized ZnO nanorods for the detection of D-dimer. Electroanalysis 26, 292–298. https://doi.org/10.1002/elan.201300580.

Isoelectric point of IgG class antibodies [WWW Document], n.d. URL https://www.agrisera.com/en/info/igg.html (accessed 7.26.23).

Janotti, A., Van de Walle, C.G., 2009. Fundamentals of zinc oxide as a semiconductor. Rep. Prog. Phys. 72, 126501 https://doi.org/10.1088/0034-4885/72/12/126501.

Jeong, W.J., Kim, S.K., Park, G.C., 2006. Preparation and characteristic of ZnO thin film with high and low resistivity for an application of solar cell. Thin Solid Films 506 (507), 180–183. https://doi.org/10.1016/j.tsf.2005.08.213.

Jiang, X., Wang, H., Yuan, R., Chai, Y., 2015. Sensitive electrochemiluminescence detection for CA15-3 based on immobilizing luminol on dendrimer functionalized ZnO nanorods. Biosens. Bioelectron. 63, 33–38. https://doi.org/10.1016/j.bios.2014.07.009.

Jing, A., Xu, Q., Feng, W., Li, Y., Liang, G., 2019. New electrochemical immunosensor of Au/holey graphene oxide and Au/ZnO for sensitive detection of carcinoembryonic antigen. Int. J. Electrochem. Sci. 14, 11212–11224. https://doi.org/10.20964/2019.12.29.

Kansal, S.K., Singh, M., Sud, D., 2008. Studies on TiO2/ZnO photocatalysed degradation of lignin. J. Hazard Mater. 153, 412–417. https://doi.org/10.1016/j.jhazmat.2007.08.091.

Kaur, R., Sharma, S.K., Tripathy, S.K., 2019. Advantages and limitations of environmental nanosensors. In: Deep, A., Kumar, S.B.T.-A., N. for B, E.A (Eds.), Advances in Nanosensors for Biological and Environmental Analysis. Elsevier, pp. 119–132. https://doi.org/10.1016/B978-0-12-817456-2.00007-3.

Kausaite-Minkstimiene, A., Ramanaviciene, A., Kirlyte, J., Ramanavicius, A., 2010. Comparative study of random and oriented antibody immobilization techniques on the binding capacity of immunosensor. Anal. Chem. 82, 6401–6408. https://doi.org/10.1021/ac100468k.

Khan, S., Akrema, Qazi, S., Ahmad, R., Raza, K., Rahisuddin, 2021. In silico and electrochemical studies for a ZnO–CuO-based immunosensor for sensitive and selective detection of E. coli. ACS Omega 6, 16076–16085. https://doi.org/10.1021/acsomega.1c01959.

Kittaka, S., Morimoto, T., 1980. Isoelectric point of metal oxides and binary metal oxides having spinel structure. J. Colloid Interface Sci. 75, 398–403. https://doi.org/10.1016/0021-9797(80)90464-6.

Klingshirn, C., 2007. ZnO: from basics towards applications. Phys. Status Solidi 244, 3027–3073. https://doi.org/10.1002/pssb.200743072.

Klingshirn, C., Fallert, J., Zhou, H., Sartor, J., Thiele, C., Maier-Flaig, F., Schneider, D., Kalt, H., 2010. 65 years of ZnO research – old and very recent results. Phys. Status Solidi 247, 1424–1447. https://doi.org/10.1002/pssb.200983195.

Koike, K., Mukai, K., Onaka, T., Maemoto, T., Sasa, S., Yano, M., 2014. A potentiometric immunosensor based on a ZnO field-effect transistor. Jpn. J. Appl. Phys. 53, 05FF04 https://doi.org/10.7567/JJAP.53.05FF04.

Kołodziejczak-Radzimska, A., Jesionowski, T., 2014. Zinc oxide—from synthesis to application: a review. Materials 7, 2833–2881. https://doi.org/10.3390/ma7042833.

Kumar, R., Umar, A., Kumar, G., Nalwa, H.S., 2017. Antimicrobial properties of ZnO nanomaterials: a review. Ceram. Int. 43, 3940–3961. https://doi.org/10.1016/j.ceramint.2016.12.062.

Lara, S., Perez-Potti, A., 2018. Applications of nanomaterials for immunosensing. Biosensors 8, 104. https://doi.org/10.3390/bios8040104.

Lee, H., Lee, D.Y., Kang, M.G., Koo, Y., Kim, T., Park, K.-D., 2020. Tip-enhanced photoluminescence nano-spectroscopy and nano-imaging. Nanophotonics 9, 3089–3110. https://doi.org/10.1515/nanoph-2020-0079.

Lee, S.-H., Han, S.-H., Jung, H.S., Shin, Hyunjung, Lee, J., Noh, J.-H., Lee, S., Cho, I.-S., Lee, J.-K., Kim, J., Shin, Hyunho, 2010. Al-doped ZnO thin film: a new transparent conducting layer for ZnO nanowire-based dye-sensitized solar cells. J. Phys. Chem. C 114, 7185–7189. https://doi.org/10.1021/jp1008412.

Li, F., Feng, Y., Yang, L., Li, L., Tang, C., Tang, B., 2011. A selective novel non-enzyme glucose amperometric biosensor based on lectin–sugar binding on thionine modified electrode. Biosens. Bioelectron. 26, 2489–2494. https://doi.org/10.1016/j.bios.2010.10.040.

Lima, S.A.M., Cremona, M., Davolos, M.R., Legnani, C., Quirino, W.G., 2007. Electroluminescence of zinc oxide thin-films prepared via polymeric precursor and via sol–gel methods. Thin Solid Films 516, 165–169. https://doi.org/10.1016/j.tsf.2007.06.106.

Liu, D., Wang, L., Ma, S., Jiang, Z., Yang, B., Han, X., Liu, S., 2015. A novel electrochemiluminescent immunosensor based on CdS-coated ZnO nanorod arrays for HepG2 cell detection. Nanoscale 7, 3627–3633. https://doi.org/10.1039/c4nr06946c.

Liu, F., Deng, W., Zhang, Y., Ge, S., Yu, J., Song, X., 2014. Application of ZnO quantum dots dotted carbon nanotube for sensitive electrochemiluminescence immunoassay based on simply electrochemical reduced Pt/Au alloy and a disposable device. Anal. Chim. Acta 818, 46–53. https://doi.org/10.1016/j.aca.2014.01.047.

Liu, L., Zhou, Y., Liu, S., Xu, M., 2018. The applications of Metal−Organic frameworks in electrochemical sensors. Chemelectrochem 5, 6–19. https://doi.org/10.1002/celc.201700931.

Liu, Y., Zhang, H., Li, B., Liu, J., Jiang, D., Liu, B., Sojic, N., 2021. Single biomolecule imaging by electrochemiluminescence. J. Am. Chem. Soc. 143, 17910–17914. https://doi.org/10.1021/jacs.1c06673.

Liustrovaite, V., Karoblis, D., Brasiunas, B., Popov, A., Katelnikovas, A., Kareiva, A., Ramanavicius, A., Viter, R., Giardi, M.T., Erts, D., Ramanaviciene, A., 2023. Electrochemical immunosensor for the determination of antibodies against prostate-specific antigen based on ZnO nanostructures. Int. J. Mol. Sci. 24, 5803. https://doi.org/10.3390/ijms24065803.

Loh, L., Briscoe, J., Dunn, S., 2015. Chemical protection of ZnO nanorods at ultralow pH to form a hierarchical BiFeO 3/ZnO core–shell structure. ACS Appl. Mater. Interfaces 7, 152–157. https://doi.org/10.1021/am505019p.

Lu, X., Bai, H., He, P., Cha, Y., Yang, G., Tan, L., Yang, Y., 2008. A reagentless amperometric immunosensor for α-1-fetoprotein based on gold nanowires and ZnO nanorods modified electrode. Anal. Chim. Acta 615, 158–164. https://doi.org/10.1016/j.aca.2008.03.054.

Ma, L., Liu, B., Huang, P.-J.J., Zhang, X., Liu, J., 2016. DNA adsorption by ZnO nanoparticles near its solubility limit: implications for DNA fluorescence quenching and DNAzyme activity assays. Langmuir 32, 5672–5680. https://doi.org/10.1021/acs.langmuir.6b00906.

Makaraviciute, A., Ramanaviciene, A., 2013. Site-directed antibody immobilization techniques for immunosensors. Biosens. Bioelectron. 50, 460–471. https://doi.org/10.1016/j.bios.2013.06.060.

Malekzad, H., Sahandi Zangabad, P., Mirshekari, H., Karimi, M., Hamblin, M.R., 2017. Noble metal nanoparticles in biosensors: recent studies and applications. Nanotechnol. Rev., Nanotechnology Reviews 6, 301–329. https://doi.org/10.1515/ntrev-2016-0014.

Martins, B.R., Sampaio, T.M., de Farias, A.K.S.R., de Paula Martins, R., Teixeira, R.R., Oliveira, R.T.S., Oliveira, C.J.F., da Silva, M.V., Rodrigues, V., Dantas, N.O., Espindola, F.S., Silva, A.C.A., Alves-Balvedi, R.P., 2021. Immunosensor based on zinc oxide nanocrystals decorated with copper for the electrochemical detection of human salivary alpha-amylase. Micromachines 12, 657. https://doi.org/10.3390/mi12060657.

Medawar-Aguilar, V., Jofre, C.F., Fernández-Baldo, M.A., Alonso, A., Angel, S., Raba, J., Pereira, S.V., Messina, G.A., 2019. Serological diagnosis of Toxoplasmosis disease using a fluorescent immunosensor with chitosan-ZnO-nanoparticles. Anal. Biochem. 564–565, 116–122. https://doi.org/10.1016/j.ab.2018.10.025.

Merényi, G., Lind, J.S., 1980. Role of a peroxide intermediate in the chemiluminescence of luminol. A mechanistic study. J. Am. Chem. Soc. 102, 5830–5835. https://doi.org/10.1021/ja00538a022.

Mohd Omar, F., Abdul Aziz, H., Stoll, S., 2014. Aggregation and disaggregation of ZnO nanoparticles: influence of pH and adsorption of Suwannee River humic acid. Sci. Total Environ. 468, 195–201. https://doi.org/10.1016/j.scitotenv.2013.08.044. –469.

Molarius, J., Kaitila, J., Pensala, T., Ylilammi, M., 2003. Piezoelectric ZnO films by r.f. sputtering. J. Mater. Sci. Mater. Electron. 14, 431–435. https://doi.org/10.1023/A:1023929524641.

Munje, R.D., Jacobs, M., Muthukumar, S., Quadri, B., Shanmugam, N.R., Prasad, S., 2015. A novel approach for electrical tuning of nano-textured zinc oxide surfaces for ultra-sensitive troponin-T detection. Anal. Methods 7, 10136–10144. https://doi.org/10.1039/C5AY02052B.

Mutlaq, S., Albiss, B., Al-Nabulsi, A.A., Jaradat, Z.W., Olaimat, A.N., Khalifeh, M.S., Osaili, T., Ayyash, M.M., Holley, R.A., 2021. Conductometric immunosensor for Escherichia coli O157:H7 detection based on polyaniline/zinc oxide (PANI/ZnO) nanocomposite. Polymers 13, 3288. https://doi.org/10.3390/polym13193288.

Myndrul, V., Coy, E., Bechelany, M., Iatsunskyi, I., 2021. Photoluminescence label-free immunosensor for the detection of Aflatoxin B1 using polyacrylonitrile/zinc oxide nanofibers. Mater. Sci. Eng. C 118, 111401. https://doi.org/10.1016/j.msec.2020.111401.

Nair, Shantikumar, Sasidharan, A., Divya Rani, V.V., Menon, D., Nair, Seema, Manzoor, K., Raina, S., 2009. Role of size scale of ZnO nanoparticles and microparticles on toxicity toward bacteria and osteoblast cancer cells. J. Mater. Sci. Mater. Med. 20, 235–241. https://doi.org/10.1007/s10856-008-3548-5.

Natsume, Y., Sakata, H., 2003. Electrical and optical properties of zinc oxide films post-annealed in H2 after fabrication by sol–gel process. Mater. Chem. Phys. 78, 170–176. https://doi.org/10.1016/S0254-0584(02)00314-0.

Neshataeva, E., Kümmell, T., Bacher, G., Ebbers, A., 2009. All-inorganic light emitting device based on ZnO nanoparticles. Appl. Phys. Lett. 94, 91115 https://doi.org/10.1063/1.3093675.

Nunez, F.A., Castro, A.C.H., Daher, I.P., Cunha-Neto, E., Kalil, J., Boscardin, S.B., Lanfredi, A.J.C., Oliveira, V.L. de, Alves, W.A., 2023a. ZnO-based electrochemical immunosensor to assess vaccine-induced antibody-mediated immunity against wild-type and gamma SARS-CoV-2 strains. Biosensors 13, 371. https://doi.org/10.3390/bios13030371.

Nunez, F.A., Castro, A.C.H., de Oliveira, V.L., Lima, A.C., Oliveira, J.R., de Medeiros, G. X., Sasahara, G.L., Santos, K.S., Lanfredi, A.J.C., Alves, W.A., 2023b. Electrochemical immunosensors based on zinc oxide nanorods for detection of antibodies against SARS-CoV-2 spike protein in convalescent and vaccinated individuals. ACS Biomater. Sci. Eng. 9, 458–473. https://doi.org/10.1021/acsbiomaterials.2c00509.

Özgür, Ü., Alivov, Y.I., Liu, C., Teke, A., Reshchikov, M.A., Doğan, S., Avrutin, V., Cho, S.-J., Morkoç, H., 2005. A comprehensive review of ZnO materials and devices. J. Appl. Phys. 98, 41301 https://doi.org/10.1063/1.1992666.

Padmavathy, N., Vijayaraghavan, R., 2008. Enhanced bioactivity of ZnO nanoparticles—an antimicrobial study. Sci. Technol. Adv. Mater. 9, 035004 https://doi.org/10.1088/1468-6996/9/3/035004.

Parracino, M.A., Martín, B., Grazú, V., 2019. State-of-the-art strategies for the biofunctionalization of photoactive inorganic nanoparticles for nanomedicine. In: Prieto, J.P., Béjar, M.G. (Eds.), Photoactive Inorganic Nanoparticles. Elsevier, pp. 211–257. https://doi.org/10.1016/B978-0-12-814531-9.00009-9.

Patella, B., Moukri, N., Regalbuto, G., Cipollina, C., Pace, E., Di Vincenzo, S., Aiello, G., O'Riordan, A., Inguanta, R., 2022. Electrochemical synthesis of zinc oxide nanostructures on flexible substrate and application as an electrochemical immunoglobulin-G immunosensor. Materials 15, 713. https://doi.org/10.3390/ma15030713.

Paul, K.B., Singh, V., Vanjari, S.R.K., Singh, S.G., 2017. One step biofunctionalized electrospun multiwalled carbon nanotubes embedded zinc oxide nanowire interface for highly sensitive detection of carcinoma antigen-125. Biosens. Bioelectron. 88, 144–152. https://doi.org/10.1016/j.bios.2016.07.114.

Popov, A., Brasiunas, B., Kausaite-Minkstimiene, A., Ramanaviciene, A., 2021. Metal nanoparticle and quantum dot tags for signal amplification in electrochemical immunosensors for biomarker detection. Chemosensors 9, 85. https://doi.org/10.3390/chemosensors9040085.

Prodromidis, M.I., 2010. Impedimetric immunosensors—a review. Electrochim. Acta 55, 4227–4233. https://doi.org/10.1016/j.electacta.2009.01.081.

Qileng, A., Liu, W., Sun, Z., Zhou, W., Fang, Y., Lei, H., Liu, Y., Zhang, S., 2022. Portable dual-modular immunosensor constructed from bimetallic metal–organic framework heterostructure grafted with enzyme-mimicking label for rosiglitazone detection. Adv. Funct. Mater. 32, 2203244 https://doi.org/10.1002/adfm.202203244.

Rai, H., Choudhary, P., Kondal, N., 2022. A review on defect related emissions in undoped ZnO nanostructures. Mater. Today Proc. 48, 1320–1324. https://doi.org/10.1016/j.matpr.2021.08.343.

Ramanaviciene, A., German, N., Kausaite-Minkstimiene, A., Voronovic, J., Kirlyte, J., Ramanavicius, A., 2012. Comparative study of surface plasmon resonance, electrochemical and electroassisted chemiluminescence methods based immunosensor for the determination of antibodies against human growth hormone. Biosens. Bioelectron. 36, 48–55. https://doi.org/10.1016/j.bios.2012.03.036.

Ramanaviciene, A., Kausaite-Minkstimiene, A., Popov, A., Brasiunas, B., Ramanavicius, A., 2022. Design of immunosensors for rapid and sensitive detection of biomarkers. In: Ozkan, S.A., Bakirhan, N.K., Mollarasouli, F. (Eds.), The Detection of Biomarkers. Elsevier, pp. 303–333. https://doi.org/10.1016/B978-0-12-822859-3.00009-2.

Ramanaviciene, A., Ramanavicius, A., 2004. Pulsed amperometric detection of DNA with an ssDNA/polypyrrole-modified electrode. Anal. Bioanal. Chem. 379, 287–293. https://doi.org/10.1007/s00216-004-2573-6.

Ray, K.C., Roy, S.K., Khan, S., 1978. Electrochemical properties of zinc oxide-aqueous electrolyte solution interface. Indian J. Chem. 16, 675–678.

Rekha, K., Nirmala, M., Nair, M.G., Anukaliani, A., 2010. Structural, optical, photocatalytic and antibacterial activity of zinc oxide and manganese doped zinc oxide nanoparticles. Phys. B Condens. Matter 405, 3180–3185. https://doi.org/10.1016/j.physb.2010.04.042.

Reyes, P.I., Ku, C.-J., Duan, Z., Lu, Y., Solanki, A., Lee, K.-B., 2011. ZnO thin film transistor immunosensor with high sensitivity and selectivity. Appl. Phys. Lett. 98, 173702 https://doi.org/10.1063/1.3582555.

Richter, M.M., 2004. Electrochemiluminescence (ECL). Chem. Rev. 104, 3003–3036. https://doi.org/10.1021/cr020373d.

Rodrigues, J., Pereira, S.O., Santos, N.F., Rodrigues, C., Costa, F.M., Monteiro, T., 2020. Insights on luminescence quenching of ZnO tetrapods in the detection of hCG. Appl. Surf. Sci. 527, 146813 https://doi.org/10.1016/j.apsusc.2020.146813.

Sakalauskiene, L., Popov, A., Kausaite-Minkstimiene, A., Ramanavicius, A., Ramanaviciene, A., 2022. The impact of glucose oxidase immobilization on dendritic gold nanostructures on the performance of glucose biosensors. Biosensors 12, 320. https://doi.org/10.3390/bios12050320.

Sang, C.H., Chou, S.J., Pan, F.M., Sheu, J.T., 2016. Fluorescence enhancement and multiple protein detection in ZnO nanostructure microfluidic devices. Biosens. Bioelectron. 75, 285–292. https://doi.org/10.1016/j.bios.2015.08.050.

Sanguino, P., Monteiro, T., Bhattacharyya, S.R., Dias, C.J., Igreja, R., Franco, R., 2014. ZnO nanorods as immobilization layers for interdigitated capacitive immunosensors. Sensor. Actuator. B Chem. 204, 211–217. https://doi.org/10.1016/j.snb.2014.06.141.

Saxena, K., Kumar, A., Chauhan, N., Khanuja, M., Malhotra, B.D., Jain, U., 2022. Electrochemical immunosensor for detection of H. pylori secretory protein VacA on g-C 3 N 4/ZnO nanocomposite-modified Au electrode. ACS Omega 7, 32292–32301. https://doi.org/10.1021/acsomega.2c03627.

Serrano, A., Arana, A., Galdámez, A., Dutt, A., Monroy, B.M., Güell, F., Santana, G., 2017. Effect of the seed layer on the growth and orientation of the ZnO nanowires: consequence on structural and optical properties. Vacuum 146, 509–516. https://doi.org/10.1016/j.vacuum.2017.03.010.

Shabani, E., Abdekhodaie, M.J., Mousavi, S.A., Taghipour, F., 2020. ZnO nanoparticle/nanorod-based label-free electrochemical immunoassay for rapid detection of MMP-9 biomarker. Biochem. Eng. J. 164, 107772 https://doi.org/10.1016/j.bej.2020.107772.

Sharma, S., Shekhar, S., Gautam, S., Sharma, B., Kumar, A., Jain, P., 2020. Carbon-based nanomaterials as novel nanosensors. In: Pal, K., Gomes, F.B.T.-N., for, S.N.A. (Eds.), Nanofabrication for Smart Nanosensor Applications. Elsevier, pp. 323–347. https://doi.org/10.1016/B978-0-12-820702-4.00014-3.

Si, S., Li, C., Wang, X., Peng, Q., Li, Y., 2006. Fe2O3/ZnO core–shell nanorods for gas sensors. Sensor. Actuator. B Chem. 119, 52–56. https://doi.org/10.1016/j.snb.2005.11.050.

Singh, S., Thiyagarajan, P., Mohan Kant, K., Anita, D., Thirupathiah, S., Rama, N., Tiwari, B., Kottaisamy, M., Ramachandra Rao, M.S., 2007. Structure, microstructure and physical properties of ZnO based materials in various forms: bulk, thin film and nano. J. Phys. D Appl. Phys. 40, 6312–6327. https://doi.org/10.1088/0022-3727/40/20/S15.

Sun, G., Wang, P., Zhu, P., Ge, L., Ge, S., Yan, M., Song, X., Yu, J., 2014a. A near-infrared light photoelectrochemical immunosensor based on a Au-paper electrode and naphthalocyanine sensitized ZnO nanorods. J. Mater. Chem. B 2, 4811–4817. https://doi.org/10.1039/C4TB00623B.

Sun, G., Zhang, L., Zhang, Y., Yang, H., Ma, C., Ge, S., Yan, M., Yu, J., Song, X., 2015a. Multiplexed enzyme-free electrochemical immunosensor based on ZnO nanorods modified reduced graphene oxide-paper electrode and silver deposition-induced signal amplification strategy. Biosens. Bioelectron. 71, 30–36. https://doi.org/10.1016/j.bios.2015.04.007.

Sun, G., Zhang, Y., Kong, Q., Ma, C., Yu, J., Ge, S., Yan, M., Song, X., 2014b. Chemiluminescence excited paper-based photoelectrochemical competitive immunosensing based on porous ZnO spheres and CdS nanorods. J. Mater. Chem. B 2, 7679–7684. https://doi.org/10.1039/C4TB01119H.

Sun, G., Zhang, Y., Kong, Q., Zheng, X., Yu, J., Song, X., 2015b. CuO-induced signal amplification strategy for multiplexed photoelectrochemical immunosensing using CdS sensitized ZnO nanotubes arrays as photoactive material and AuPd alloy nanoparticles as electron sink. Biosens. Bioelectron. 66, 565–571. https://doi.org/10.1016/j.bios.2014.12.020.

Tamashevski, A., Harmaza, Y., Slobozhanina, E., Viter, R., Iatsunskyi, I., 2020. Photoluminescent detection of human T-lymphoblastic cells by ZnO nanorods. Molecules 25, 3168. https://doi.org/10.3390/molecules25143168.

Tamashevski, A., Harmaza, Y., Viter, R., Jevdokimovs, D., Poplausks, R., Slobozhanina, E., Mikoliunaite, L., Erts, D., Ramanaviciene, A., Ramanavicius, A., 2019. Zinc oxide nanorod based immunosensing platform for the determination of human leukemic cells. Talanta 200, 378–386. https://doi.org/10.1016/j.talanta.2019.03.064.

Tereshchenko, A., Bechelany, M., Viter, R., Khranovskyy, V., Smyntyna, V., Starodub, N., Yakimova, R., 2016. Optical biosensors based on ZnO nanostructures: advantages and perspectives. A review. Sensor. Actuator. B Chem. 229, 664–677. https://doi.org/10.1016/j.snb.2016.01.099.

Tereshchenko, A., Yazdi, G.R., Konup, I., Smyntyna, V., Khranovskyy, V., Yakimova, R., Ramanavicius, A., 2020. Application of ZnO nanorods based whispering gallery mode resonator in optical immunosensors. Colloids Surf. B Biointerfaces 191, 110999. https://doi.org/10.1016/j.colsurfb.2020.110999.

Tong, Y., Jiang, T., Qiu, S., Koshmak, K., Giglia, A., Kubsky, S., Bendounan, A., Chen, L., Pasquali, L., Esaulov, V.A., Hamoudi, H., 2018. ZnO functionalization: metal–dithiol superstructures on ZnO(0001) by self-assembly. J. Phys. Chem. C 122, 2880–2889. https://doi.org/10.1021/acs.jpcc.7b12071.

Vabbina, P.K., Kaushik, A., Pokhrel, N., Bhansali, S., Pala, N., 2015. Electrochemical cortisol immunosensors based on sonochemically synthesized zinc oxide 1D nanorods and 2D nanoflakes. Biosens. Bioelectron. 63, 124–130. https://doi.org/10.1016/j.bios.2014.07.026.

Venu Rajendran, M., Ganesan, S., Sudhakaran Menon, V., Raman, R.K., Alagumalai, A., Ashok Kumar, S., Krishnamoorthy, A., 2022. Manganese dopant-induced isoelectric point tuning of ZnO electron selective layer enable improved interface stability in cesium–formamidinium-based planar perovskite solar cells. ACS Appl. Energy Mater. 5, 6671–6686. https://doi.org/10.1021/acsaem.2c00170.

Vetrivel, C., Sivarasan, G., Durairaj, K., Ragavendran, C., Kamaraj, C., Karthika, S., Lo, H.-M., 2023. MoS2-ZnO nanocomposite mediated immunosensor for non-invasive electrochemical detection of IL8 oral tumor biomarker. Diagnostics 13, 1464. https://doi.org/10.3390/diagnostics13081464.

Viter, R., Abou Chaaya, A., Iatsunskyi, I., Nowaczyk, G., Kovalevskis, K., Erts, D., Miele, P., Smyntyna, V., Bechelany, M., 2015. Tuning of ZnO 1D nanostructures by atomic layer deposition and electrospinning for optical gas sensor applications. Nanotechnology 26, 105501. https://doi.org/10.1088/0957-4484/26/10/105501.

Viter, R., Khranovskyy, V., Starodub, N., Ogorodniichuk, Y., Gevelyuk, S., Gertnere, Z., Poletaev, N., Yakimova, R., Erts, D., Smyntyna, V., Ubelis, A., 2014. Application of room temperature photoluminescence from ZnO nanorods for salmonella detection. IEEE Sensor. J. 14, 2028–2034. https://doi.org/10.1109/JSEN.2014.2309277.

Viter, R., Savchuk, M., Iatsunskyi, I., Pietralik, Z., Starodub, N., Shpyrka, N., Ramanaviciene, A., Ramanavicius, A., 2018. Analytical, thermodynamical and kinetic characteristics of photoluminescence immunosensor for the determination of Ochratoxin A. Biosens. Bioelectron. 99, 237–243. https://doi.org/10.1016/j.bios.2017.07.056.

Wan, Q., Li, Q.H., Chen, Y.J., Wang, T.H., He, X.L., Li, J.P., Lin, C.L., 2004. Fabrication and ethanol sensing characteristics of ZnO nanowire gas sensors. Appl. Phys. Lett. 84, 3654–3656. https://doi.org/10.1063/1.1738932.

Wang, C., Yin, L., Zhang, L., Xiang, D., Gao, R., 2010. Metal oxide gas sensors: sensitivity and influencing factors. Sensors 10, 2088–2106. https://doi.org/10.3390/s100302088.

Wang, P., Sun, G., Ge, L., Ge, S., Song, X., Yan, M., Yu, J., 2013. Paper-based photoelectrochemical immunosensing based on CdS QD sensitized multidimensional porous ZnO spheres promoted by carbon nanotubes. Chem. Commun. 49, 10400–10402. https://doi.org/10.1039/C3CC45856C.

Wang, X., Han, X., Ma, A., Chen, L., Liang, H., Litifu, A., Xue, F., 2017. Fabrication of electrochemical immunosensor for interferon-γ determination and its application of tuberculosis diagnosis. Int. J. Electrochem. Sci. 12, 7262–7271. https://doi.org/10.20964/2017.08.67.

Wang, Y., Deng, H., Huangfu, C., Lu, Z., Wang, X., Zeng, X., He, H., Rao, H., 2015. Research of protein adsorption on the different surface topography of the zinc oxide. Surf. Interface Anal. 47, 245–252. https://doi.org/10.1002/sia.5698.

Wang, Y., Jin, R., Sojic, N., Jiang, D., Chen, H.Y., 2020. Intracellular wireless analysis of single cells by bipolar electrochemiluminescence confined in a nanopipette. Angew. Chem. Int. Ed. 59, 10416–10420. https://doi.org/10.1002/anie.202002323.

Wang, Y., Shi, R., Lin, J., Zhu, Y., 2011. Enhancement of photocurrent and photocatalytic activity of ZnO hybridized with graphite-like C3N4. Energy Environ. Sci. 4, 2922–2929. https://doi.org/10.1039/C0EE00825G.

Wang, Z., Yang, Y., Li, J., Gong, J., Shen, G., Yu, R., 2006. Organic–inorganic matrix for electrochemical immunoassay: detection of human IgG based on ZnO/chitosan composite. Talanta 69, 686–690. https://doi.org/10.1016/j.talanta.2005.11.004.

Wang, Z.L., 2009. ZnO nanowire and nanobelt platform for nanotechnology. Mater. Sci. Eng. R Rep. 64, 33–71. https://doi.org/10.1016/j.mser.2009.02.001.

Wang, Z.L., 2004a. Zinc oxide nanostructures: growth, properties and applications. J. Phys. Condens. Matter 16, R829–R858. https://doi.org/10.1088/0953-8984/16/25/R01.

Wang, Z.L., 2004b. Nanostructures of zinc oxide. Mater. Today 7, 26–33. https://doi.org/10.1016/S1369-7021(04)00286-X.

Wong, C.-Y., Lai, L.-M., Leung, S.-L., Roy, V.A.L., Pun, E.Y.-B., 2008. Ambipolar charge transport and electroluminescence properties of ZnO nanorods. Appl. Phys. Lett. 93, 23502 https://doi.org/10.1063/1.2957671.

Xiao, Q., Ouyang, L., 2009. Photocatalytic photodegradation of xanthate over Zn1−xMnxO under visible light irradiation. J. Alloys Compd. 479 https://doi.org/10.1016/j.jallcom.2008.12.085. L4–L7.

Yang, W.-C., Liao, S.-Y., Phan, T.L., Van Hieu, N., Chu, P.-Y., Yi, C.-C., Wu, H.-J., Chang, K.-M., Ching, C.T.-S., 2020. An immunosensor for the detection of ULBP2 biomarker. Micromachines 11, 568. https://doi.org/10.3390/mi11060568.

Yang, Z.-H., Zhuo, Y., Yuan, R., Chai, Y.-Q., 2016. A nanohybrid of platinum nanoparticles-porous ZnO–hemin with electrocatalytic activity to construct an amplified immunosensor for detection of influenza. Biosens. Bioelectron. 78, 321–327. https://doi.org/10.1016/j.bios.2015.10.073.

Zhan, B., Zhang, Y., Zhao, X., 2021. High sensitive sol-gel based electrochemical immunosensor for Clenbuterol Determination. Int. J. Electrochem. Sci. 16, 211124 https://doi.org/10.20964/2021.11.23.

Zhang, J., Zhao, S.Q., Zhang, K., Zhou, J.Q., 2014. Cd-doped ZnO quantum dots-based immunoassay for the quantitative determination of bisphenol A. Chemosphere 95, 105–110. https://doi.org/10.1016/j.chemosphere.2013.08.039.

Zhang, L.-T., Zhou, Y., Han, S.-T., 2021. The role of metal–organic frameworks in electronic sensors. Angew. Chem. Int. Ed. 60, 15192–15212. https://doi.org/10.1002/anie.202006402.

Zhang, L., Ding, Y., Povey, M., York, D., 2008. ZnO nanofluids – a potential antibacterial agent. Prog. Nat. Sci. 18, 939–944. https://doi.org/10.1016/j.pnsc.2008.01.026.

Zhang, Q., Dandeneau, C.S., Zhou, X., Cao, G., 2009. ZnO nanostructures for dye-sensitized solar cells. Adv. Mater. 21, 4087–4108. https://doi.org/10.1002/adma.200803827.

Zhang, S.-R., Zhou, Y., 2020. Introduction to semiconducting metal oxides. In: Semiconducting Metal Oxide Thin-Film Transistors. IOP Publishing, pp. 1–9. https://doi.org/10.1088/978-0-7503-2556-1ch1.

Zhang, Y., Zhang, Z., Rong, S., Yu, H., Gao, H., Sha, Q., Ding, P., Pan, H., Chang, D., 2020. A sandwich-type ECL immunosensor based on signal amplification using a ZnO nanorods-L-cysteine-luminol nanocomposite for ultrasensitive detection of prostate specific antigen. Anal. Chim. Acta 1109, 98–106. https://doi.org/10.1016/j.aca.2020.02.056.

Zhang, Z., Berg, A., Levanon, H., Fessenden, R.W., Meisel, D., 2003. On the interactions of free radicals with gold nanoparticles. J. Am. Chem. Soc. 125, 7959–7963. https://doi.org/10.1021/ja034830z.

Zhang, Z., Cong, Y., Huang, Y., Du, X., 2019. Nanomaterials-based electrochemical immunosensors. Micromachines 10, 397. https://doi.org/10.3390/mi10060397.

Zhou, Q., Chen, H., Wang, K., Zhang, H., Pan, L., Zheng, H., Zhou, Y., Hu, Z., Peng, Z., Wan, J., Wang, B., 2023a. Photoelectrochemical immunosensor for archaeological silk microtrace detection based on tailored monoclonal antibody and ZnO nanowires array. Sensor. Actuator. B Chem. 374, 132804 https://doi.org/10.1016/j.snb.2022.132804.

Zhou, Q., Liu, Y., Wang, L., Wang, K., Chen, H., Zheng, H., Zhou, Y., Hu, Z., Peng, Z., Wan, J., Wang, B., 2023b. A visible and near-infrared light dual-responsive PEC immunosensor for archaeological silk microtrace detection based on in situ growth of Ag2S on ZnO-MXene nanocomposites. Chem. Eng. J. 469, 143926 https://doi.org/10.1016/j.cej.2023.143926.

Zhu, L., Yin, Z., Lv, Z., Li, M., Tang, D., 2021. Ultrasensitive photoelectrochemical immunoassay for prostate-specific antigen based on silver nanoparticle-triggered ion-exchange reaction with ZnO/CdS nanorods. Analyst 146, 4487–4494. https://doi.org/10.1039/D1AN00822F.

Zhu, Q., Cai, F., Zhang, J., Zhao, K., Deng, A., Li, J., 2016. Highly sensitive electrochemiluminescent immunosensor based on gold nanoparticles-functionalized zinc oxide nanorod and poly(amidoamine)-graphene for detecting brombuterol. Biosens. Bioelectron. 86, 899–906. https://doi.org/10.1016/j.bios.2016.07.091.

Zyoud, A., Zyoud, A.H., Zyoud, Shaher H., Nassar, H., Zyoud, Samer H., Qamhieh, N., Hajamohideen, A., Hilal, H.S., 2023. Photocatalytic degradation of aqueous methylene blue using ca-alginate supported ZnO nanoparticles: point of zero charge role in adsorption and photodegradation. Environ. Sci. Pollut. Res. 30, 68435–68449. https://doi.org/10.1007/s11356-023-27318-1.

Zyoud, A.H., Zubi, A., Zyoud, S.H., Hilal, M.H., Zyoud, S., Qamhieh, N., Hajamohideen, A., Hilal, H.S., 2019. Kaolin-supported ZnO nanoparticle catalysts in self-sensitized tetracycline photodegradation: zero-point charge and pH effects. Appl. Clay Sci. 182, 105294 https://doi.org/10.1016/j.clay.2019.105294.

NOTES

NOTES

Vilniaus universiteto leidykla
Saulėtekio al. 9, III rūmai, LT-10222 Vilnius
El. p. info@leidykla.vu.lt, www.leidykla.vu.lt
bookshop.vu.lt, journals.vu.lt
Tiražas 25 egz.